Influence of metallurgical phase transformation on crack propagation of 15-5PH stainless steel and 16MND5 low carbon steel

Jikai Liu

N° d'ordre: 2012ISAL0120 Année 2012

THESE

présentée devant

L'INSTITUT NATIONAL DES SCIENCES APPLIQUEES DE LYON

pour obtenir

LE GRADE DE DOCTEUR

Spécialité :Mécanique -Génie Mécanique - Génie Civil

ECOLE DOCTORALE DES SCIENCES DE L'INGENIEUR DE LYON:
Mécanique, Energétique, Génie civil, Acoustique (MEGA)

par

Jikai LIU

Influence of metallurgical phase transformation on crack propagation of 15-5PH stainless steel and 16MND5 low carbon steel

Soutenue le 7 Décembre 2012, devant la Commission d'Examen:

Jury:

MM.	Stéphane MARIE	CEA	Rapporteur
	Hervé LOUCHE	Université Montpellier 2	Rapporteur
MM.	Alain COMBESCURE	INSA de Lyon	Directeur de thèse
	Hervé KLOCKER	ENSMSE	Examinateur
	Jean-Yves GUEDOU	SAFRAN	Examinateur
	Michel CORET	Ecole Centrale de Nantes	Co-directeur de thèse
	Philippe GILLES	AREVA-NP	Examinateur
	René BILLARDON	ENS de Cachan	Examinateur

LaMCoS (Laboratoire de Mécanique des Contacts et des Structures)

CNRS UMR5259, INSA-Lyon.

20, avenue Albert Einstein, 69621 Villeurbanne Cedex, France

INSA DE LYON
Service Scolarité

Année Universitaire 2012-2013
Mise à jour le 25 Juin 2012

ECOLES DOCTORALES

L'INSA est l'établissement principal pour les Ecoles Doctorales (vert)

ECOLES DOCTORALES n° code national	RESPONSABLE PRINCIPAL	CORRESPONDANT INSA	LABORATOIRES RATTACHES	DIRECTEUR LABORATOIRE
ED CHIMIE DE LYON **(Chimie, Procédés, Environnement)** *http://sakura.cpe.fr/ED206* **EDA206**	M. Jean-Marc LANCELIN CPE LYON 04.72.43.13.95 directeur@edchimie-lyon.fr secretariat@edchimie-lyon.fr Directrice Adjointe : Mme Bernadette CHARLEUX Bernadette.charleux@lcpp.cpe.fr	M. Rémy GOURDON 04.72.43.81.70 Patrick.germain@insa-lyon.fr	**Matériaux : Ingénierie et Science – MATEIS** Bât Blaise Pascal **Laboratoire de Génie Civil et d'Ingénierie Environnementale - LGCIE** Bât J.C.A. Coulomb **Institut de Chimie et de Biochimie Moléculaires et Supramoléculaires – ICBMS** Bât Jules Verne	M. Joël COURBON Joel.courbon@insa-lyon.fr M. Ali LIMAM ali.limam@insa-lyon.fr M. Loïc BLUM **INSA :** M. Yves QUENEAU yves.queneau@insa-lyon.fr
HISTOIRE, GEOGRAPHIE, AMENAGEMENT, URBANISME, ARCHEOLOGIE, SCIENCE POLITIQUE, SOCIOLOGIE, ANTHROPOLOGIE **(ScSo)** **EDA483**	M. Lionel OBADIA Lionel.obadia@univ-lyon2.fr LYON 2 04.78.77.23.86 ou 04.78.69.72.76	Mme Chantal BERDIER 04.72.43.83.07 Chantal.berdier@insa-lyon.fr	Environnement, Ville, Société - EVS **Bât Eugène Freyssinet**	M. Jean-Yves TOUSSAINT Jean-yves.Toussaint@insa-lyon.fr
ELECTRONIQUE, ELECTROTECHNIQUE, AUTOMATIQUE **(E.E.A.)** **EDA160** ***http://edeea.ec-lyon.fr***	M. Gérard SCORLETTI ECL 04.72.18.60.97 gerard.scorletti@ec-lyon.fr ecole-doctorale.eea@ec-lyon.fr		**Génie Electrique, Electromagnétisme, Automatique, Microbiologie Environnementale et Applications - AMPERE** Bât Léonard de Vinci **Centre de Recherche en Acquisition et Traitement d'Images pour la santé - CREATIS** Bât Blaise Pascal Laboratoire de Génie Electrique et Ferroélectricité – LGEF **Bât Gustave Ferrié** Institut des Nanotechnologies de Lyon - INL Bât Blaise Pascal **Unité mixte internationale en Nanotechnologies et Nanosystèmes –**	M. Laurent NICOLAS **INSA :** M. Bruno ALLARD Bruno.Allard@insa-lyon.fr Mme Isabelle MAGNIN isabelle.magnin@insa-lyon.fr M. Daniel GUYOMAR Daniel.Guyomar@insa-lyon.fr M. Guy HOLLINGER Guy.hollinger@insa-lyon.fr M. Abdelkader SOUIFI Abdelkader.souifi@insa-lyon.fr

			UMI/LN2 Bât Blaise Pascal	
EVOLUTION, ECOSYSTEMES, MICROBIOLOGIE , MODELISATION *http://biomserv.univ-lyon1.fr/E2M2* **(E2M2)** EDA 341	Mme Gudrun BORNETTE UCBL 1 04.72.43.12.94 e2m2@univ-lyon1.fr	M. CHARLES Hubert 04.72.43.80.85 Hubert.charles@insa-lyon.fr	**Biologie Fonctionnelle, Insectes et Interactions – BF2I** Bât Louis Pasteur	M. Yvan RAHBE Yvan.rahbe@isna-lyon.fr
INTERDISCIPLINAIRE SCIENCES-SANTE *http://www.ibcp.fr/ediss* **(EDISS)** **EDA205**	M. Didier REVEL UCBL 1 04.72.68.49.09 didier.revel@creatis.univ-lyon1.fr Directrice Adjointe : Mme Emmanuelle CANET-SOULAS Emmanuelle.canet@univ-lyon1.fr	M. Michel LAGARDE 04.72.43.82.40 Michel.Lagarde@insa-lyon.fr	**Centre de Recherche en Acquisition et Traitement d'Images pour la santé - CREATIS** Bât Blaise Pascal Cardiovasculaire, Métabolisme, Diabétologie et Nutrition - CARMEN Bât Louis Pasteur **Institut de Chimie et de Biochimie Moléculaires et Supramoléculaires - ICBMS** Bât Jules Verne *Microbiologie, Adaptation et Pathogénie - MAP* Bât Louis Pasteur	Mme Isabelle MAGNIN isabelle.magnin@insa-lyon.fr M. Hubert VIDAL **INSA :** Mme Isabelle VANDENBROUCKE isabelle.vandenbroucke@insa-lyon.fr M. Loïc BLUM **INSA :** M. Yves QUENEAU yves.queneau@insa-lyon.fr Mme Nicole COTTE-PATTAT Nicole.Cotte-Pattat@insa-lyon.fr
ED MATERIAUX DE LYON http://ed34.universite-lyon.fr **EDA 034**	M. Jean-Yves BUFFIERE 04.72.43.71.70 Jean-Yves.buffiere@insa-lyon.fr		Ingénierie des Matériaux Polymères - IMP **Bât Jules Verne** **Matériaux : Ingénierie et Science - MATEIS** Bât Blaise Pascal Institut des Nanotechnologies de Lyon - INL Bât Blaise Pascal **Unité mixte internationale en Nanotechnologie et Nanosystèmes – UMI/LN2** Bât Blaise Pascal	M. Philippe CASSAGNAU **INSA. :** M. Etienne FLEURY Etienne.fleury@insa-lyon.fr M. Joël COURBON Joel.courbon@insa-lyon.fr M. Guy HOLLINGER Guy.hollinger@insa-lyon.fr M. Abdelkader SOUIFI Abdelkader.souifi@insa-lyon.fr
INFORMATIQUE ET MATHEMATIQUES DE LYON *http://Infomaths.univ-lyon1.fr* **(InfoMath)**	M. Johannes KELLENDONK UCBL 1 04.72.43.19.05 Secrétariat : 04.72.44.82.94 kellendonk@math.univ-lyon1.fr		Institut Camille Jordan - ICJ **Bât Léonard de Vinci** **Centre d'Innovation en Télécommunications et Intégration de services – CITI** Bât Claude Chappe	Mme Elisabeth ROUY-MIRONESCU **INSA :** M.Jérôme POUSIN jerome.pousin@insa-lyon.fr M. Jean-Marie GORCE jean-marie.gorce@insa-lyon.fr

EDA 512			Décision et Information pour les Systèmes de Production - DISP **Bât Léonard de Vinci** Laboratoire d'InfoRmatique en Images et Systèmes d'information - LIRIS Bât Blaise Pascal	Mme Valérie BOTTA-GENOULAZ Valerie.botta-genoulaz@insa-lyon.fr M. Attila BASKURT Attila.baskurt@insa-lyon.fr
MEGA DE LYON (MECANIQUE, ENERGETIQUE, GENIE CIVIL, ACOUSTIQUE) *http://www.lmfa.ec-lyon.fr/autres/MEGA/index.html* **(MEGA)** EDA162	M. Philippe BOISSE 04.72.43.63.96 ou 04.72.43.71.70 philippe.boisse@insa-lyon.fr mega@insa-lyon.fr		Centre de Thermique de Lyon - CETHIL **Bât Sadi Carnot** **Centre de Recherche en Acquisition et Traitement d'Images pour la santé - CREATIS** Bât Blaise Pascal ***Laboratoire de Mécanique des Contacts et des Structures - LaMCoS*** **Bât Jean d'Alembert** Laboratoire de Génie Electrique et Ferroélectricité - LGEF Bât Gustave Ferrié **Laboratoire de Mécanique des Fluides et d'Acoustique - LMFA** Bât Joseph Jacquard **Laboratoire Vibrations et Acoustique - LVA** Bât Antoine de Saint Exupéry Laboratoire de Génie Civil et d'Ingénierie Environnementale - LGCIE Bât J. C.A. Coulomb **Matériaux : Ingénierie et Science – MATEIS** Bât Blaise Pascal	Mme Dany ESCUDIE Dany.Escudie@insa-lyon.fr Mme Isabelle MAGNIN isabelle.magnin@insa-lyon.fr **M. David DUREISSEIX** david.dureisseix@insa-lyon.fr M. Daniel GUYOMAR Daniel.Guyomar@insa-lyon.fr M. Michel LANCE INSA : M. Jean Yves CHAMPAGNE Jean-Yves.Champagne@insa-lyon.Fr M. Jean-Louis GUYADER Jean-louis.guyader@insa-lyon.fr M. Ali LIMAM ali.limam@insa-lyon.fr M. Joël COURBON Joel.courbon@insa-lyon.fr

Acknowledgments

There is an old saying in China: all good things will come to an end. In the last three years, I spent one wonderful life on research here, Lyon of France. Maybe it’s time to say goodbye. But before the farewell, I'm delighted to give my heartfelt acknowledgments.

First of all, I am very grateful to my supervisor, Professor Alain Combescure. Millions thanks for his persistent encouragement, patience, mercifulness and creative advices. He is not only one of the best supervisors with profound understanding of numerical simulation of mechanical problems especially crack propagation, but also one of the best advisers on problem-solving and team management. I feel that I am very lucky to have an opportunity to work with him and I surly couldn't finish my thesis without his help.

I also would like to express my appreciation to my lovely co-supervisor: Professor Michel Coret who shared his knowledge in the thermal, metallurgical and mechanical aspects and taught me how to do the thermal and mechanical experiments with high quality and then process the data statistically. His solid theoretical foundation and wealth of experimental experience helped me a lot during this thesis.

Appreciation should be also going to CHAUDET Philippe, GUILHERMOND Jean-Pascal, SAINSOT Philippe, DESCARTES Sylvie, GODEAU Claude, LAFARGE Lionel, HUGUENY Georges for their help on my experimental studies such as specimen machinery, apparatus installation and microstructure observation etc.

Prof. Yves Bréchet, Prof. H. K. D. H. Bhadeshia are acknowledged for their inspired discussions on bainite transformation. Prof. Anthony Gravouil also helped me with understanding the operators from CAST3M simulation software. Besides, I also shall thank Dr. MORESTIN Fabrice for his training on digital image correlation which has played an important role in my thesis.

I also can't forget the encouragement from my former supervisor Prof. X. Hong (ECUST) and Prof. Ye Yifu. It was them who make me be full of confidence for this research project. Meanwhile I appreciate the supports from my colleagues, they are Dr. Zh. Yancheng, X. Jing, C. Jing, Q. Jichao, Y. Hexiang, Dr. C. Thibaut, Dr. C. Cedric, Dr. D. Emilien, Dr. B. Gauthier, Dr. Alexandre, Dr. M. Daniel, B. Caroline, B. Didier, M. Romains, R. Clément, T. Benoit etc. They showed me their warm welcome and friendship to me.

And of course, the financial support from China Scholarship Council (CSC) is also appreciated.

Finally, heartfelt gratitude must go to my family especially my parents for their teachings by personal example with verbal instruction and my wife for her understanding and caring. They are always with me absolutely, I love them so much!

Abstract

This thesis focuses on the influence of solid-solid phase transformations on the crack propagation. We want to understand well the changes in material's fracture toughness during the welding process of the crack reparation. In this work, crack propagation resistance ability is characterized by critical *J*-integral based fracture toughness. There are many experimental methods to obtain the critical toughness J_{IC}, but they are impractical for our investigation during the phase transformation. That is the reason why we have proposed a method coupling mechanical tests, digital image correlation and finite element simulation. The fracture tests are implemented on pre-cracked single edge notched plate sample which is easy for machining and heat transfer during phase transformation. The tests are conducted at different temperatures until rupture. Digital image correlation gives us the displacement and deformation information on every sample's surface. Each test is then simulated by finite element where the fracture toughness is evaluated by the method G-Theta at the crack propagation starting moment found by potential drop method and digital image correlation technical. Previous simulations incorporate the boundary conditions obtained by correlation and mechanical behavior considered is that we have identified from characterization tests.

Two materials have been studied with this method, one is 15Cr-5Ni martensitic precipitation hardening stainless steel (15-5PH) and another one is 16MND5 ferritic low carbon steel. There is always the martensite transformation in 15-5PH no matter how quickly it is cooled after austenitization. While 16MND5 has pearlitic, bainitic or martensitic phase transformation during cooling which depends on the cooling rate. Notice that the time and temperature dependent bainitic transformation in 16MND5 is shown to be more complex than the study for 15-5PH. For these two materials, different test temperatures were chosen before, during and after phase transformation for material and failure characterization of the mechanical behavior.

Investigation result shows that metallurgical phase transformation has an influence on the fracture toughness and further crack propagation. For 15-5PH, the result of J_{1C} value shows that the pure martensitic 15-5PH has higher fracture toughness at room temperature than the one at 200°C. The toughness is also higher than the original material after one cycle heat treatment, this is probably caused by some residual austenite. Meanwhile, pure austenite 15-5PH at 200°C has a higher fracture toughness than pure martensitic 15-5PH at the same temperature. The J_{1C} value of the dual phase 15-5PH during the martensitic transformation

also shows that possibly austenite can enhance the ductility of the material as well as fracture toughness. For 16MND5 low carbon steel, the result also proves that the heat treatment and metallurgic phase transformation have an influence on the mechanical properties and fracture toughness. 16MND5 low carbon steel after one cycle bainite transformation has nearly 40% higher strength than the as-received condition. The material at as received condition has bigger J_{1C} value than the one heated to 600°C. On the other hand, the material at 600°C just before continuous cooling bainite transformation after the austenitization during cooling process also has higher fracture toughness than the one at 600°C before austenitization. These two conclusions are consistent with the result of 15-5PH. But the final situation of 16MND5 after one cycle heat treatment has a slightly smaller J_{1C} value than the as-received situation. It means that one cycle heat treatment hasn't a significant influence on the fracture toughness of the bainitic 16MND5 low carbon steel. For 16MND5, the J_{1C} value is nearly constant during the cooling bainite transformation.

Conclusions of our study show that one should pay attention to the heating period before austenitization of the base material when people weld for crack reparation as the higher temperature will bring the lower fracture toughness during this process. While the fracture toughness doesn't change a lot during, before or after the cooling induced phase transformation.

Key words

Crack propagation, Fracture toughness, Martensite transformation, Bainite transformation, Critical *J*-integral, Boundary condition, Digital image correlation, Finite element analysis

Résumé

Cette thèse porte sur l'influence des transformations de phases solide-solide sur la propagation de fissure. On souhaite ainsi mieux comprendre les variations de ténacité en cours de soudage par exemple, ou bien pendant la réparation d'une fissure. Dans ce travail, la ténacité est obtenue à partir de l'intégrale *J*. Il existe de nombreuses méthodes expérimentales permettant d'obtenir la ténacité critique J_{IC} mais qui sont difficilement applicables pour des essais se déroulant pendant une transformation de phase. C'est pourquoi nous avons proposé une méthode couplant essai mécanique et mesure par corrélation d'images avec de la simulation par éléments finis. Les essais sont réalisés sur de simples éprouvettes plates pré fissurées, faciles à usiner et simple à chauffer par induction. Les essais sont conduits pour différentes températures et jusqu'à rupture. En sus des mesures d'efforts et déplacements de traverse, la corrélation d'images nous fournit également les champs de déplacement sur chaque face de l'éprouvette. Chaque essai est ensuite simulé par éléments finis où la ténacité critique est calculée par la méthode G-Theta au maximum de la charge supportée par l'éprouvette. Les simulations précédentes intègrent les conditions aux limites obtenues par corrélation et le comportement mécanique considéré est celui que nous avons identifié sur des essais de caractérisation.

Deux nuances de matériau ont été étudiées avec cette méthode: l'acier inoxydale 15-5PH ainsi que l'acier ferritique 16MND5. L'acier 15-5PH est toujours sous forme martensitique alors que le 16MND5 peut être bainitique ou martensitique selon le traitement thermique. On notera que l'étude sur la transformation bainitique du 16MD5 dépendant du temps et de la température s'est révélée dans notre cas plus complexe que l'étude sur le 15-5PH dont la transformation martensitique ne dépend que de la température. Pour ces deux matériaux, différentes températures d'essai ont été choisies avant, pendant et après la transformation pour effectuer les essais de rupture ainsi que de caractérisation du comportement mécanique.

Les résultats de cette étude montrent que la transformation de phase peut avoir un impact non négligeable sur la ténacité. Ainsi, pour le 15-5PH, le taux d'austénite résiduelle est un facteur important et les essais pendant la transformation martensitique montrent que la ténacité critique peut être inférieure pendant celle ci à celle du matériau purement austénitique.

Dans le cas du 16MND5, la ténacité est beaucoup plus faible à 600°C (et bainitique) qu'à température ambiante ce qui est assez logique. Par contre, lors du refroidissement, depuis

600° (austénitique) jusqu'à la température ambiante (bainitique), nous avons obtenu une ténacité critique relativement constante.

En conclusion, cette étude apporte une solution quant à la mesure de la ténacité critique de matériau pendant des transformations de phases, ce que ne permettent pas forcément les essais normalisés. Pour le 15-5PH, la ténacité critique semble évoluer pendant la transformation martensitique et est assez dépendante du taux d'austénite résiduelle. Il semble par contre que pour le 16MND5, la ténacité critique soit assez peu dépendante de la fraction volumique d'austénite et la valeur obtenue varie peu au cours du refroidissement du matériau depuis 600°C.

Mots clés

Propagation de fissure, Ténacité à la rupture, Transformation martensitique, Transformation bainitique, Intégrale *J* Critique, Condition limite, Corrélation d'image numérique, Analyse par éléments finis

Contents

List of figures

List of tables

Nomenclature and Abbreviation

Nomenclature

a	Fatigue crack length
α'	Material constant
a_0	Notch length of the fracture specimen
A_3	Transition point from γ-Fe to α-Fe
A_4	Transition point from δ-Fe to γ-Fe
Ac_1	Austenitic transformation start temperature
Ac_3	Austenitic transformation finish temperature
α	Martensite phase
α_2	Primary Ti_3Al
α_α	Dilatation coefficient of martensite phase
α_γ	Dilatation coefficient of austenite phase
A_{pl}	Area of plastic part under the force versus displacement curve
B	Thickness of the fracture specimen
B_1	Starting temperature of bainite transformation during constant cooling rate
B_3	Ending temperature of bainite transformation during constant cooling rate
B_c	Starting temperature of bainite transformation in non-equilibrium situation
b_0	Uncracked ligament length
β	Geometric coefficient of the stress intensity factor
C_γ	Carbon content in austenite
d	Mean free path of dislocation motion in ferrite
da	Crack length difference between two fracture specimens
ΔM	The surface of the pattern in the initial image
ΔM^*	The subset in the deformed image
ΔW	Different work between two fracture tests
ε_0	Yield strain
$\Delta\varepsilon_{\alpha,\gamma}^{T_{ref}}$	Different of compactness of phase α compared to phase γ at T_{ref}
E	Elastic modulus
$\mathbf{E}$	Green-Lagrange tensor
ε^{thm}	Thermo metallurgical microscopic strain
F	Force
$\mathbf{F}$	Transformation gradient
φ	Geometric function for calculating the stress intensity factor
ψ	Orientation angle
G	Strain energy release rate
G_c	Critical strain energy release rate
G_θ	Energetic domain parameter
h_1	Function of a/W and n in EPRI solution of J-integral
J_3	The third invariant of the deviatoric stress
J_{1C}	Critical J-integral in model I
J_{el}	Elastic component of J
J^{far}	Far field J-integral

J_{pl}	Plastic component of *J*
J^{tip}	Crack tip *J*-integral
ΔJ	Amount of transformation toughening
ΔJ_{te}	Toughness enhancement factor
K	Stress intensity factor
K_{∞}	Stress intensity factor in the infinite plane
K^{far}	Stree intensity factor near the crack tip
K^{far}	Stree intensity factor in the far field
K_{1C}	Critical stress intensity factor
ΔK	Toughness enhancement due to transformation
M_1	Starting temperature of martensite transformation during constant cooling rate
M_3	Ending temperature of martensite transformation during constant cooling rate
n	Hardening exponent of material
$\vec{n}$	Normal to the *J*-integral path
∂a	Crack length difference between two fracture samples
∂W	Different potential energy in the loading line displacement curves of two fracture tests
P	Applied load per unit thickness in EPRI solution of *J*-integral
P_Q	The critical load
P_1	Starting temperature of pearlite transformation during constant cooling rate
P_3	Ending temperature of pearlite transformation during constant cooling rate
ψ	Constant parameter in EPRI solution of *J*-integral
γ	Austenite phase
Ω	Integration domain of modified G_theta method
σ_0	Yield stress
σ_Y	Effective yield stress
dS	Surface element in modified G_theta method
t	Time
t_{shift}	Shift time from continuous cooling temperature to constant
T	Temperature
$\vec{T}$	The traction vector defined in *J*-integral
T_{ref}	Reference temperature
Tc	Curie temperature
Γ	Any contour surrounding the crack tip
$\Theta_{k,j}$	Theta component in modified G_theta method
$U_{(a)}$	Potential after the fatigue test
$U_{(a_0)}$	Potential before the fatigue test
$\vec{U}$	Displacement vector defined in *J*-integral
η	Geometrical parameter in EPRI solution of *J*-integral
η_{pl}	Geometrical parameter of ASTM *J*-integral estimation method
ν	Poisson ratio

Abbreviation

15-5PH	15%Cr - 5%Ni Precipitation Hardening stainless steel
16MND5	0.16%C-Mn-N-D-5
ASME	American Society of Mechanical Engineers
ASTM	American Society for Testing and Materials
AT	Austenite Transformation
APT	Atom Probe Tomography
BT	Bainite Transformation
BC	Boundary Conditions
BCC	Body Centered Cubic
CC	Continuous Cooling
CCD	Charge Coupled Device
CCP	Centre Cracked Plate specimen
CCT	Centre Cracked Tension specimen
CT	Compact Tension specimen
CTOA	Crack Tip Opening Angle
CTOD	Crack Tip Opening Displacement
DECP	Double Edge Cracked Plate
DC	Direct Current
DIC	Digital Image Correlation
EPRI	Electric Power Research Institute
FCC	Face Centered Cubic
FEA	Finite Element Analysis
LLD	Loading Line Displacement
LVDT	Linear Variable Differential Transformer
MT	Martensite Transformation
MT1	Anisothermal Martensite Transformation
MT2	Isothermal Martensite Transformation
PD	Potential Drop
PT	Phase Transformation
PTE	Periodic Table of Elements
RAW	Relative Atomic Weight
SEM	Scanning Electron Micrograph
SENB	Single Edge Notched Bending specimen
SENP	Single Edge Notched Plate specimen
SMAs	Shape Memory Alloys
SIF	Stress Intensity Factor
SIMT	Stress Induced Martensitic Transformation
TRIP	TRansformation Induced Plasticity
TTT	Time-Temperature-Transformation
X-DIC	eXtended Digital Image Correlation
X-FEM	eXtended Finite Element Method
XRD	X-Ray Diffraction
VL	Void Linkage
ZOI	Zone Of Interest

Chapter 1 Introduction

The research presented in my thesis is linked to the basic problem of life extension for expensive components. The following problem is often encountered by the industry: a critical defect or crack is detected during the life of a component, what is the decision to take for metallic components: change the component or repair the crack? This is a recurrent question for aerospace parts and nuclear components as well as for railways carriages.

Crack reparation is attractive because it is less expensive, but it is very often not chosen for important components, because people fear the consequences of this reparation on the future safety of the repaired component. The main reason is that there is a lack of understanding of the effects of reparation in this type of situation. If the crack root is still present after reparation, what happens to this initial damage during the repair (filling with welding material)?

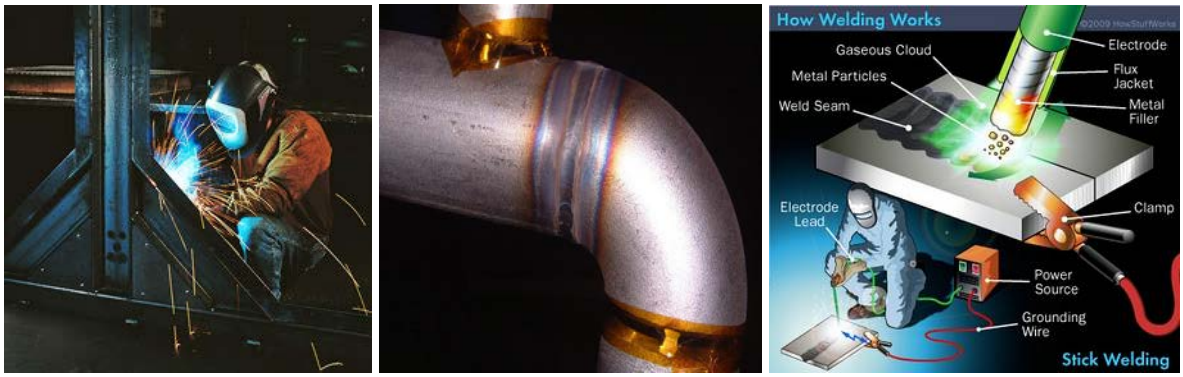

Fig. 1.1 Industrial crack reparation: welding [1-3]

This research is devoted to the acquisition of basic understanding of what happens in such cases. It is focussed on getting basic information on the material fracture properties in case of typical repair and refilling temperature histories. Mechanics, metallurgy and thermal, these three aspects always have a complex relationship between each other which is summarized in the following figure.

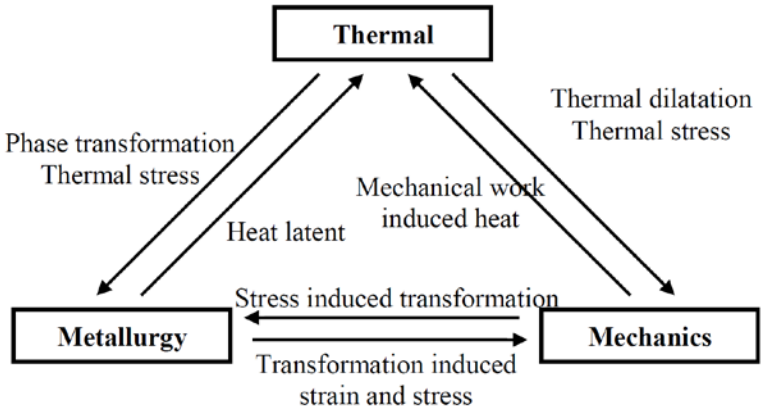

Fig. 1.2 Relation between Thermal, metallurgy and mechanics

Metallurgy is always accompanied with the thermal treatment which will change the microstructure, and in consequence change the mechanical properties of the material. More simply, the heat treatment induced by the repair process may introduce the phase transformation which makes the material have different composition such as different phase proportion, different Fe_3C content and different carbon distribution etc. All these could bring different mechanical properties. In our thesis here, we simply want to find quantitatively the effect on fracture toughness of one material at different temperature and different status during one cycle heat treatment period, and also look for the reason why this kind of heat treatment will bring the change of the fracture toughness to the material we study.

We implement our investigation in two kinds of materials: 15-5PH martensitic precipitation stainless steel and 16MND5 low carbon steel. 15-5PH stainless steel is a dual phase material which experiences martensite phase transformation during continuous cooling, there is no isothermal transformation in 15-5PH. 16MND5 low carbon steel is more complex, three transformations will occur during cooling: martensite transformation in a very high cooling rate, pearlite transformation in a very slow cooling rate and bainite transformation in a medium cooling rate. What should be emphasized is that there is also isothermal transformation in 16MND5 when we keep a constant temperature during cooling with an appropriate cooling rate. Dilatometry technology permits to see the effects of this kind of transformations and study the kinetics of the transformations.

The mechanism of bainite transformation is not yet well understood, but they have an important effect on the material properties and toughness. We hence study a little bit more deeply the anisothermal (Continuous Cooling or CC)-isothermal bainite transformation in 16MND5, carbon movement during the bainite transformation and its effect on the martensite

transformation starting temperature will be quantitatively estimated. The TTT curve which is also called C-curve will also be drawn.

Once the transformation kinetics, mechanism in 15-5PH stainless steel and 16MND5 low carbon steel are better understood, we will perform mechanical experimental tests. A fatigue crack side is initiated in a thin Single Edge Notched Plate (SENP) specimen. This plate is submitted to a typical uniform thermal history and the monotonic load crack propagation tests are performed on the plate. The objective of our thesis is to evaluate how much the toughness is affected by the temperature history. We briefly illustrate the chosen method to evaluate the critical *J*-integral based fracture toughness (see figure 1.3). The usual CT specimen can't be used to evaluate the toughness directly, because they are rather thick and it is clear that the temperature history is not uniform along the crack front during fast cooling. Consequently the J_{1C} estimation would apply to a heterogeneous material. We have decided to use these flat specimens which ensure an uniform material state along crack front even for fast cooling. We first of all apply Digital Image Correlation (DIC) technique to find the boundary conditions of the fracture tests, in the other hand, round bar tests will be done to find the mechanical properties of the material such as yield stress or Young's modulus under the related same thermal history, then the *J*-integral based fracture toughness will be computationally estimated by CAST3M simulation.

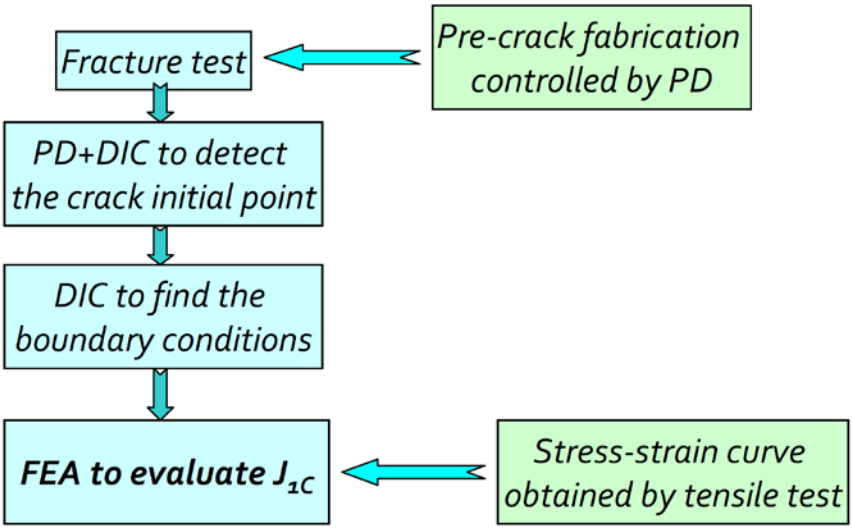

Fig. 1.3 Methodology to get J_{1C} from experiments

The structure followed this introduction of this thesis is summarized as below:

Chapter 2 will introduce the basic research methods we have known before, and then we will talk about the materials we will study. DIC and X-DIC will be introduced first of all and consequently we will introduce the well known dilatometry technique, Direct Current Potential Drop (PD) technology and Johnson's formula for fabricating the pre-crack. Then we will separately talk about our studied materials 15-5PH and 16MND5, together with their transformations during heat treatment. Meanwhile, the investigated effect of phase transformation on fracture toughness is introduced. On the other hand, the introduction and comparison of current methods to evaluate the *J*-integral based fracture toughness is discussed in the end of this chapter.

Chapter 3, after the analysis of advantages and disadvantages of nowadays J_{1C} estimation methods, we propose a method coupling PD, DIC and CAST3M to evaluate the *J*-integral of the studied materials. The Boundary Conditions (BC) will be extracted by DIC method for numerical simulation. The re-programmed G_theta method provided in CAST3M will give us the critical *J*-integral value.

Chapter 4, the effect of martenstic transformation on fracture toughness of 15-5PH stainless steel will be given in this chapter. At first, we will present stress-strain properties of the 15-5PH under the different thermal history. The round bar tests for materials are submitted to the same temperature history as the fracture tests with the SENP samples. The J_{1C} value is then calculated by our method. The fractography of fracture surface is also analyzed to study the fracture mechanism and the relation with fracture toughness.

Chapter 5, 16MND5 low carbon steel is studied at this chapter. More metallurgical investigation is done for this material as bainite transformation is more complex. Continuous cooling bainite transformation as well as isothermal bainite transformation was studied in this chapter. The continuous cooling-isothermal bainite transformation will be especially discussed. More microstructure investigation will be involved also. After all these, mechanical tests will be done and further the J_{1C} will be detected by our method. Like what we have done for 15-5PH martensitic stainless steel, we will also study the fracture mechanism by the fractography.

Chapter 6 contains the conclusions and perspectives.

Chapter 2 Methods and Materials

This chapter will introduce the methods and materials in our investagation. Our research is a combination of materials science, thermomechanics and fracture mechanics, so some basic knowledge will be mentioned such as metallurgical phase transformation and the dilatometry technique for studying the transformation kinetics. Digital image correlation technology and direct current potential drop method will be involved also. Our research is implemented on 15-5PH stainless steel and 16MND5 low carbon steel, two well-known materials. The later one has more complex transformation kinetics than 15-5PH, not only the transformation types but also the transformation mechanism. Back to our research purpose, the already invesgated effects of metallurgical phase transformation on crack propagation ability which is charactered by fracture toughness will be recalled and the current J_{1C} estimation methods will be introduced briefly in the end of this chapter.

2.1 DIC and X-DIC

Local displacement and strain measurement is always an important task for mechanical investigation especially when the thermomechanics will be also taken into account. So here we make a brief introduction of a whole-field and non-contact strain & displacement measuring method called Digital Image Correlation (DIC) and its improved version eXtended-DIC.

2.1.1 Digital Image Correlation (DIC)

The Digital Image Correlation (DIC) method was firstly introduced by Peters and Ranson [4] in the early 80s. It is widely used in nowadays as it is an optical whole-field and non-contact strain & displacement measuring method. First of all, researchers will do a painting on the surface of the specimen, and then use the digital cameras to take some photos during the test, Zone Of Interest (ZOI) will be processed based on the matching pixel gray level values [5-7] of these photos to detect the strain and displacement etc. during the mechanical test.

2.1.2 Principle of digital image correlation

Consider an object that is illuminated by a light source. The light-intensity patterns are reflected from the undeformed and deformed object surfaces. Intensity patterns $f(x, y)$ and $f^*(x^*, y^*)$ corresponds to the reflected light from the undeformed and deformed object

configurations. Relative to the intensity patterns, $f(x,y)$ and $f^*(x^*,y^*)$, respectively, they are assumed to be in unique, one-to-one correspondence with the respective object surfaces.

$$f^*(x^*,y^*) - f(x+u(x,y), y+v(x,y)) = 0 \tag{2-1}$$

Where $u(x,y)$ and $v(x,y)$ represent the displacement components of the reference subset center in x and y directions. Therefore, using this basic assumption, one may measure the deformations of small subsets of the image and thereby obtain deformations of small subsets of the actual object surface [8][9].

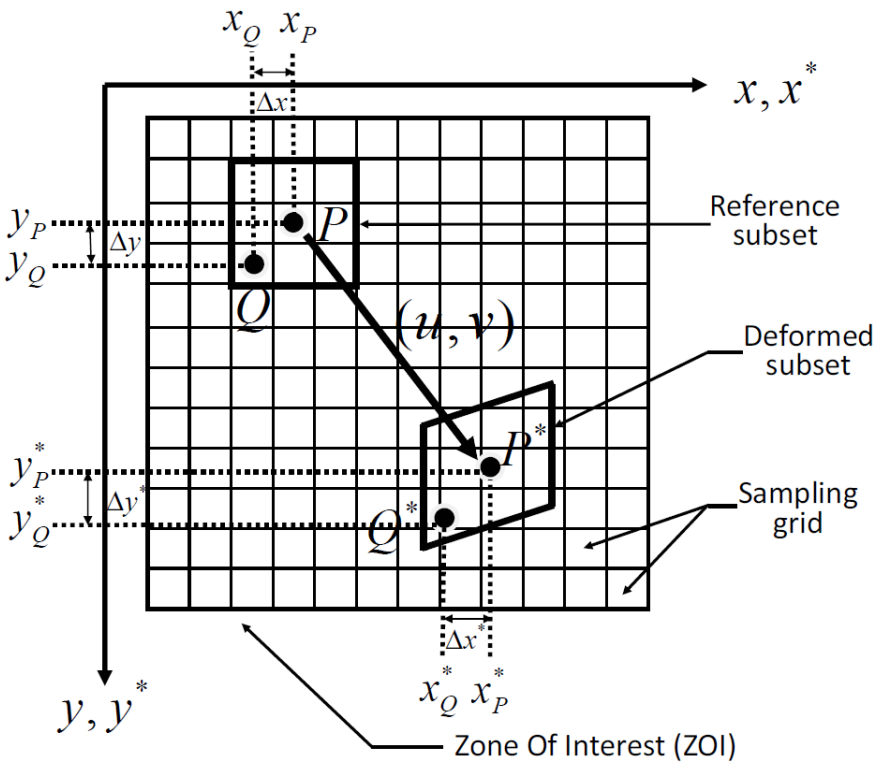

Fig. 2.1 Schematic for the principle of digital image correlation

As shown in Fig. 2.1, in the reference image, a square reference subset centered at point P is picked. The matching procedure is to find the corresponding subset centered at point P^* in the deformed image, which has the maximum similarity with the reference subset. Consequently [10], the two central points P and P^* are a couple of corresponding points of the two images. Before deformation,

$$Q = (x_i, y_i) = (x_0 + \Delta x, y_0 + \Delta y) \tag{2-2}$$

In which Δx and Δy are the distances from the subset central *P* to point *Q*. After the deformation, we have equation (2-3),

$$\begin{aligned} x_i^{'} &= x_0 + \Delta x + u + u_x \Delta x + u_y \Delta y \\ y_i^{'} &= y_0 + \Delta y + v + v_x \Delta x + v_y \Delta y \end{aligned} \tag{2-3}$$

In which, u_x, u_y, v_x and v_y are the first-order displacement gradients of the reference subset. [10].

The most used correlation parameter for a correlation technique are the least square and the crossed parameters [9][11] :

$$C_1 = \int_{\Delta M} (f(x,y) - f^*(x^*, y^*))^2 \cdot dx \cdot dy \tag{2-4}$$

and:

$$C_2 = 1 - \frac{\int_{\Delta M^*} f(x,y) \cdot f^*(x^*, y^*) \cdot dx \cdot dy}{\sqrt{\int_{\Delta M} f(x,y)^2 \cdot dx \cdot dy \cdot \int_{\Delta M^*} f^*(x^*, y^*)^2 \cdot dx \cdot dy}} \tag{2-5}$$

Where, ΔM represents the surface of the pattern in the initial image and ΔM^* denotes the subset in the deformed image.

The strains calculation on the plane could be done for one pattern or for a group of patterns. This calculation uses the gradient of the transformation **F** and the Green-Lagrange tensor **E** [12] :

$$[\mathbf{F}] = \begin{bmatrix} F_{11} & F_{12} \\ F_{21} & F_{22} \end{bmatrix} \text{ and } [\mathbf{E}] = \frac{1}{2} \cdot ({}^T\mathbf{F} \cdot \mathbf{F} - \mathrm{I}) \tag{2-6}$$

With this components, the principal strains are given by:

$$\begin{cases} \varepsilon_{\mathrm{I}} = \ln(E_{11} + E_{22} + \sqrt{(E_{11} - E_{22})^2 + (2 \cdot E_{12})^2} + 1) \\ \varepsilon_{\Pi} = \ln(E_{11} + E_{22} - \sqrt{(E_{11} - E_{22})^2 + (2 \cdot E_{12})^2} + 1) \end{cases} \tag{2-7}$$

More details about the principle of DIC could be found in the references [4][8-12].

2.1.3 eXtended Digital Image Correlation (X-DIC)

However, one drawback [13][14] of DIC is when localized phenomena arises such as cracks, shear-bands, sliding or frictional interfaces. They are not smooth and continuous in the selected zone of interest, or may simply prevent the convergence of the correlation procedure when the displacement jump across the discontinuity is large. Alternative approaches require the partitioning of the domain into different parts that are further reassembled to estimate the discontinuity.

But real deformation fields of the crack tip and the crack face are difficult to be precisely obtained. Consequently, an algorithm named eXtended Digital Image Correlation (X-DIC) [15-17] has been raised to measure the full-field displacements by using the partition of unity method as the eXtended Finite Element Method (X-FEM)[18][19]. This technique allows for very efficient modelling of discontinuities within the finite element framework and without any demand for a remeshing element. More details could be found in the references [16].

2.1.4 Icasoft, one software to process DIC

The softwares for DIC and image capturing equipment can be found as followed [20]:

1). The ARAMIS_ software (http://www.gom.com) for DIC with 2D and 3D registration with image size 1280 × 1024 pixels.

2). The LIMESS software (VIC 2D) (http://www.limess.com) for DIC with 2D and 3D registration with image size 1392 × 1040 pixels.

3). The ICASOFT software (http://www.techlab.fr/Strain.htm#Icasoft) for DIC with 2D registration with CCD 8 bits (1024 · 1024 pixels) Kodak Mega+ Cameras. This software has been developed at LaMCoS in INSA de Lyon [19][21].

As it says in [20], all these hardwares and softwares are not difficult to use. Preparation of the optical system is not so difficult (even calibration is not needed for 2D measurements) and does not produce experimental 'overheads'. Processing of the images (calculation of the displacement/strain fields) may take few minutes, following processing of the displacement/strain fields (e.g., calculation of local shear angles, statistical parameters of the field, etc.) is done automatically (either using internal commands of the DIC software, or external processing of output ASCII files).

2.2 Dilatometry technique

Dilatometry technique is very important and easy-command for learning the phase transformation kinetics. There is expansion during heating period and contraction during cooling period, the dilatometry can give us the expansion rate and transformation starting/ending temperature from the dilatation curve versus temperature. The device for this technique is extensometer or dilatometer with LVDT etc.

Figure 2.2 is an ideal schematic of the free dilatation curve during a whole heat treatment process. If there is a specimen which is heated under a constant rate to a certain meximum temperature for austenitization, after that it is cooled down by a constant rate until to room temperature or held at one isothermal temperature for a certain time, the dilatation curve will always look like figure 2.7 except there is no transformation in this kind of material or we failed to get the transformation under this heat treatment condition.

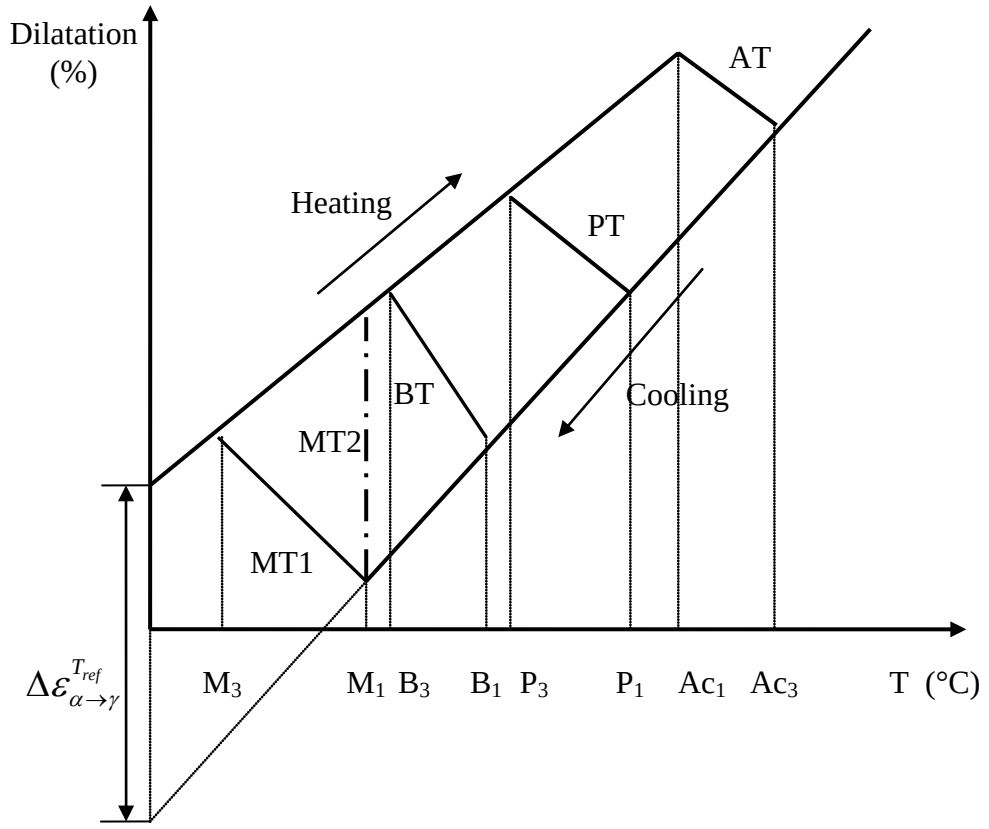

Fig. 2.2 Ideal schematic of dilatation curve during all kinds of transformations

In figure 2.2, the specimen is first of all heated to Ac_1 temperature, and it happens the austenite transformation (AT) until Ac_3 temperature, after heating to the designed maximum temperature, the specimen is cooling down. During the cooling period, as mentioned before,

the transformation could be Continuous Cooling Transformation (CCT) and also Time-Temperature-Transformation (TTT). You can find in fig. 2.2, the PT, BT and MT1 separately means the pearlite transformation, bainite transformation and martensite transformation during the continuous cooling process, while the MT2 lines shows you the isothermal transformation induced dilatation. Whether or not the MT2 line can touch the heating line? It depends on whether or not the isothermal transformation will finish completely. As widely accepted, isothermal or anisothermal bainite transformation is an un-completed transformation, it tells us that it couldn't touch the heating line (or expansion line) if there is a similar BT2 line in Figure 2.2. About the temperature parameters in abscissa, the lower temperature is the transformation finish temperature and the corresponded higher one is relatively the transformation starting temperature during the cooling period.

We can also investigate the transformation kinetics by dilatometry technique. From fig. 2.2, we can first of all easily get the expansion coefficient of every phase by the slope and further the difference of compactness between two phases $\Delta\varepsilon_{\alpha\to\gamma}^{T_{ref}}$. By the following equation, we can calculate the transformed phase fraction [22].

$$Z_\gamma(T) = \frac{\varepsilon^{thm} - \alpha_\alpha(T - T_{ref})}{(\alpha_\gamma - \alpha_\alpha)(T - T_{ref}) + \Delta\varepsilon_{\alpha,\gamma}^{T_{ref}}} \tag{2-8}$$

where:

ε^{thm} : *dilatation or strain measured in the phase transformation*

$\Delta\varepsilon_{\alpha,\gamma}^{T_{ref}}$: *difference of compactness of phase* α *compared to phase* γ *at* $T_{ref} = 20°C$

α_α: *dilatation coefficient of phase* α;

α_γ: *dilatation coefficient of phase* γ;

$Z = 1$ *pure* γ, $= 0$ *pure* α

2.3 DC potential drop method and Johnson's formula

The non-destructive Potential Drop (PD) method has been widely used to detect the crack length and control the fatigue crack since it was introduced by H. H. Johnson in September 1965 [23]. In this method, a constant Direct Current (DC) is passed through the specimen. The electrical potential is measured across the crack mouth and is related to the crack length. The electric potential across the crack mouth can be related to the unbroken crack ligament

resistance. The change of the crack length will change the resistance of the unbroken ligament and further the potential drop between the mouths of the crack.

It has now been developed to Alternating Current (AC) PD and even for the non-conductive specimen by so many researchers later [24-27]. The crack length measurement and fatigue crack fabrication control is based on Johnson's formula (see Eq.2-9), this equation is very convenient because it is independent of the material characteristics. Eq.2-9 gives a simple estimation of the fatigue crack length a using simply the comparison of the potential drop $U_{(a)}$ of the present crack with the one associated with the original known crack length a_0 (in our case a_0 is the notch length which is measured by microscope observation, see figure 2.4).

$$\frac{U_{(a)}}{U_{(a_0)}} = \frac{\arccos h\left[\dfrac{\cosh\dfrac{\pi \cdot y}{2W}}{\cos\dfrac{\pi \cdot a}{2W}}\right]}{\arccos h\left[\dfrac{\cosh\dfrac{\pi \cdot y}{2W}}{\cos\dfrac{\pi \cdot a_0}{2W}}\right]} \tag{2-9}$$

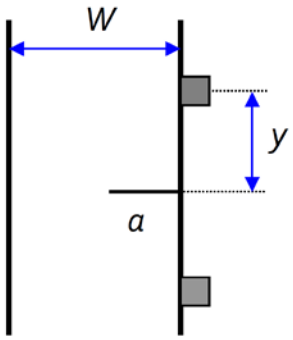

Fig. 2.3 Schematic definition of geometrical parameters of Johnson's formula

In Eq. 2-9, W is the width of the specimen and the y is the distance between the wires welded on two sides of the crack (figure 2.3). This method can give an accuracy of about 0.05mm.

With this equation, during the fatigue crack fabrication, we know the beginning potential $U_{(a_0)}$ and original crack length a_0 which is calculated by the mean value measured by optical microscope as followed picture shows. When we design one expected fatigue crack length,

we take it into equation (2-9) to get the destination potential $U_{(a)}$, when the potential arrives the expected value, we stop the fatigue experiment.

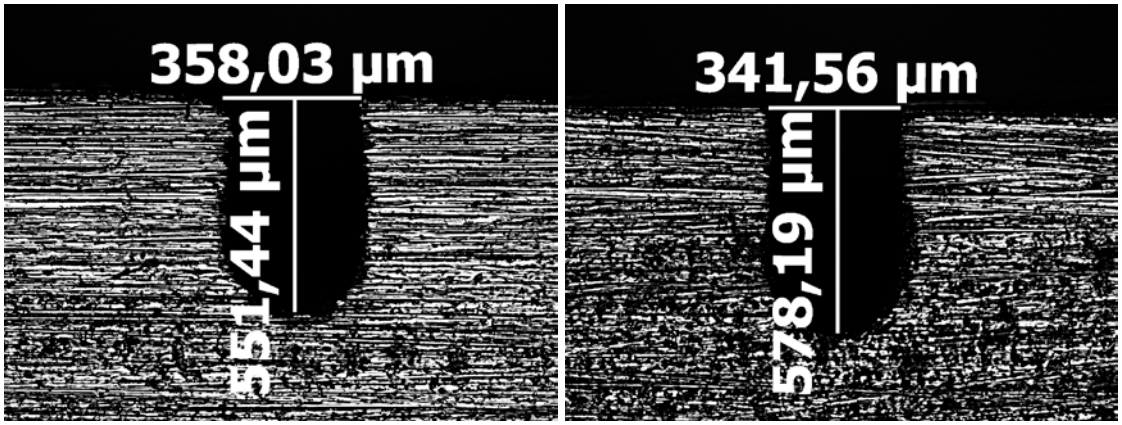

Fig. 2.4 The notch size from the views of two faces

Then we transfer equation (2-9) to equation (2-10) and we can calculate the fatigue crack length with the acquired true potential.

$$a = \frac{2W}{\pi} \cdot \cos^{-1} \frac{\cosh \frac{\pi \cdot y}{2W}}{\cosh \left(\frac{U_{(a)}}{U_{(a_0)}} \cdot \cos h^{-1} \frac{\cosh \frac{\pi \cdot y}{2W}}{\cos \frac{\pi \cdot a_0}{2W}} \right)} \tag{2-10}$$

Following figure 2.5 shows the set-up of the DC potential drop method for the fatigue test or fracture test. The red and blue wires are used to input the DC current, two small wires welded on two sides of the notch are applied to measure the potential drop. The distance from the two small wires to the notch must be the same to each other.

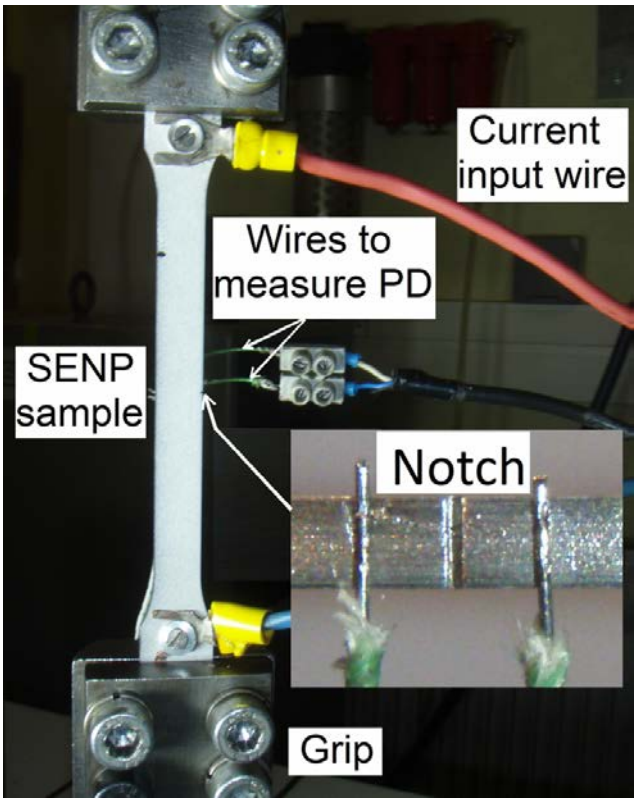

Fig. 2.5 Set-up of DC potential drop method

However, we need to pay attention that this formula has the following limitations.

(1) The parameter of y and W must be clearly constant when one applies the load

The load must remain small such that plastic zone at crack tip is very limited. The thickness of the specimen must not change.

(2) The change of temperature must be avoided

The variation of the temperature will bring the variation of electrical conductivity and expansion or shrinking which also affect the strain and the value of y and W. This influence will be big when the temperature changes a lot. More details could be found in annexes (4). Hence this method will only be used for room temperature in our study.

(3) The conductivity of crack tip

When the loading relaxed during the fatigue test, two sides of the crack tips maybe also connect physically which can also conduct electricity.

(4) The choice of starting / ending point

As Johnson suggested, the sample starter geometry strongly influences the calibration between measured potential and crack length. Similarly, the crack-after propagation geometry also influences the calibration between measured potential and crack length. So it is important to choose an appropriate starting point and ending point.

So in our study, we need to take these four aspects into account for getting a better result of fatigue crack length. Taking the following figure for example, it is acquired during a fatigue test. We take the potential when the force arrives at the mean value of the sinus force designed as $U_{(a_0)}$, and take the final potential when the force decreases from the mean value to zero as $U_{(a)}$. Then we can calculate the fatigue crack length by equation (2-10).

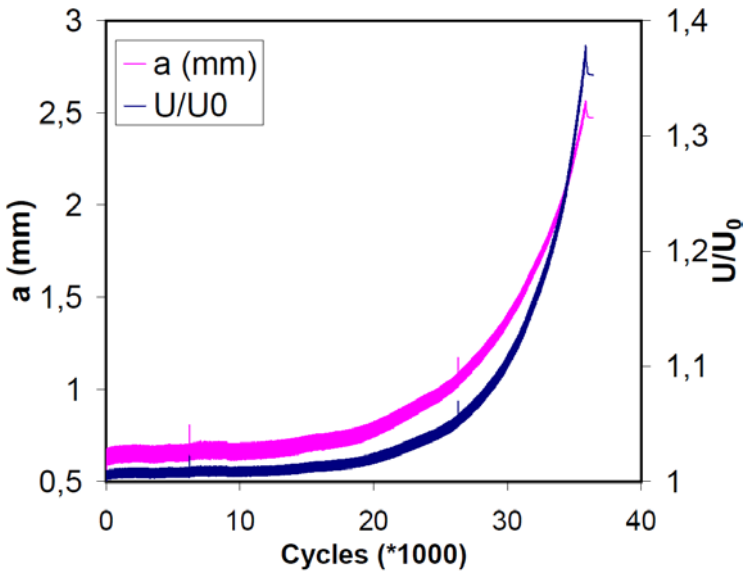

Fig. 2.6 Fatigue crack controlled by potential drop technique

Finally this method will only be used for the control of initiation of fatigue crack length and for the room temperature J_{1C} test.

2.4 Materials studied and phase transformation

2.4.1 Metallurgical phase transformation phenomenon

2.4.1.1 Pure iron and crystal lattice

Fe is the 26th element in the Periodic Table of Elements (PTE) with the Relative Atomic Weight (RAW) 56. Its melting point at 1 atm is 1538°C. It has different lattice during the cooling period. When it is cooled to 1538°C but higher than 1394°C, it is δ-Fe who is Body

Centered Cubic (BCC, see Fig. 2.7), while it transforms to Face Centered Cubic (FCC) γ-Fe when temperature is cooling to lower than 1394°C. This transformation is normally called A_4 transformation. When it cools to 912°C, here goes the A_3 transition to α-Fe which is BCC also. The α-Fe will re-obtain its magnetism if cooled to lower than 770°C which is the Curie temperature (Tc), or Curie point [28].

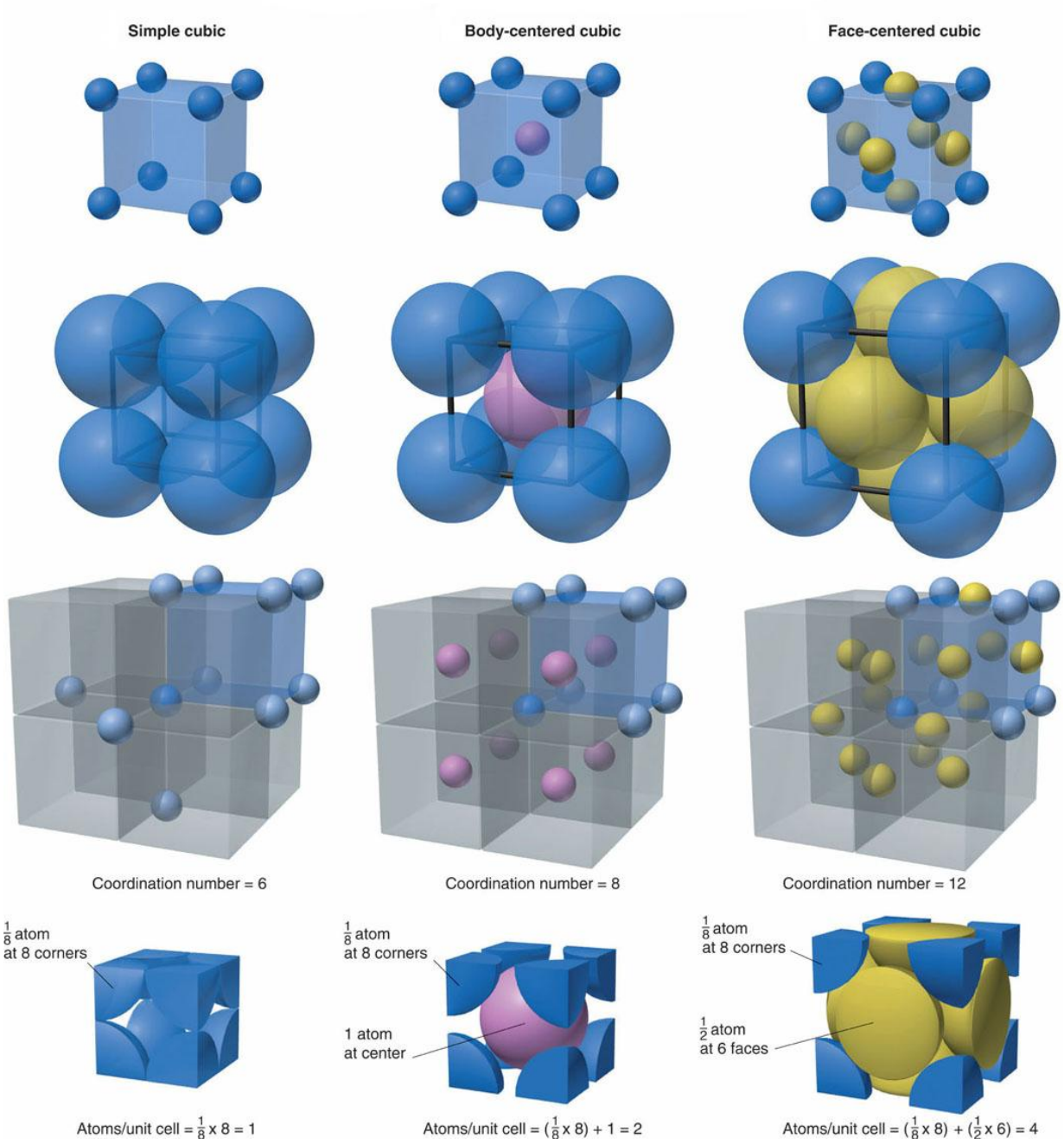

Fig. 2.7 Crystal lattice form [29]

2.4.1.2 Metallurgical phase transformation

Normally there is phase transformation phenomenon in the alloy during the heat treatment process. We here take the famous Fe-Fe_3C phase diagram (Fig. 2.8) for the explanation.

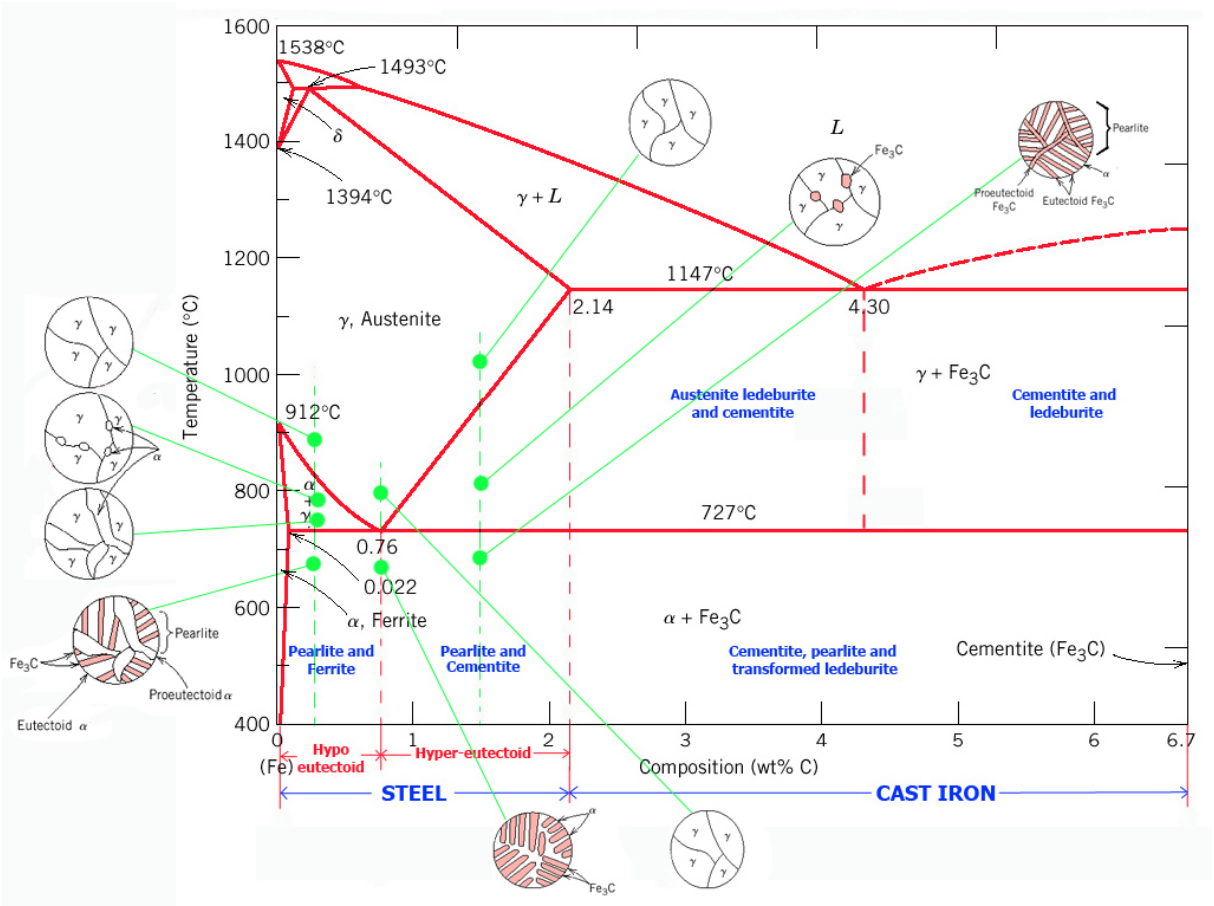

Fig. 2.8 Fe-Fe_3C phase diagram [30]

In figure 2.8, when the alloy has less carbon than 2.14% (wt), it is steel, while it is cast iron when it has more carbon content. Hypo eutectoid steel has less than 0.76% carbon while hyper eutectoid steel has more carbon than this value. We take hypo eutectoid steel for example, it is liquid above 1538°C, when it continues cooling, it crystallizes partly into single-phase δ-solid solution which has 0.09% carbon, and then becomes austenite (γ, Carbon dissolves in γ-Fe, FCC structure) by peritectic transformation at 1493°C. The ferrite (Carbon dissolves in α-Fe, BCC structure) will appear along the austenite grain boundary by eutectoid reaction when temperature is cooling below than 912°C. The microstructure of hypo eutectoid at room temperature is composed of pearlite and ferrite.

Generally speaking, metallurgy people will heat the steel to a predetermined temperature and keep at this temperature for a certain time, after that there will be kinds of cooling methods,

this process is called heat treatment. During this process, it will bring several phase transformations. They are austenite (FCC structure) transformation during heating and pearlite transformation at very high temperature, martensite (BBC structure) transformation at lower temperature, bainite transformation at an intermediate temperature (upper bainite in 400°C-550°C and lower bainite in 250°C-400°C) during cooling. By appropriate heat treatment method, people can get better material properties and improve the microstructure. Figure 2.9 shows you the typical metallographics of martensite, pearlite and bainite [31-33].

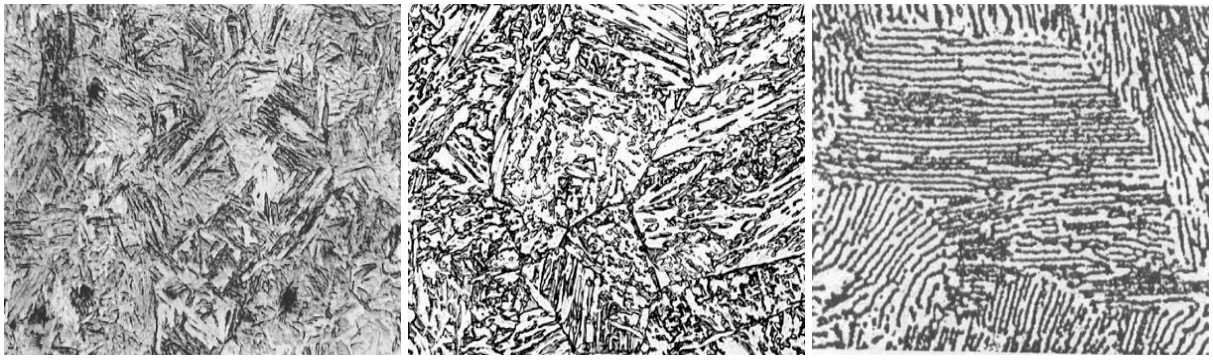

Fig. 2.9 Typical metallographics of martensite (left), bainite (middle) and pearlite (right)

2.4.1.3 Diffusive and Displacive: transformation mechanism

As we know, there are two phase transformation mechanisms, one is diffusive or reconstructive such as pearlite transformation. Another one is diffusionless or displacive such as martensite transformation. The mechanism of bainite transformation is much more complex and it will be discussed in chapter 6.

As illustrated in Figure 2.10, the austenite consists of a mixture of square atoms and round atoms, and has the unit cell outlined in red rectangle. One way of changing the crystal structure is to do so without disrupting the relative order of the atoms. This can be done by generating the unit cell of ferrite by a homogeneous deformation of the parent austenite. For displacive mechanism, the overall shape of the sample must change in a manner consistent with the change in crystal structure. When this shape deformation occurs in the bulk of polycrystalline steel, its accommodation brings plenty of strain energy. This energy can be minimised if the ferrite adopts a thin-plate shape. Since transformation occurs by a deformation, the atoms maintain the sequence which existed in the parent phase. There is therefore, no change in the chemical composition during displacive transformation. There is also a one-to-one atomic correspondence between the ferrite and austenite, which is the basis of the shape memory effect.

The change in crystal structure can also be achieved in effect by breaking the bonds in the austenite and rearranging the atoms into the structure of ferrite while maintaining the overall shape. This requires atoms to diffuse over distances compared to the size of the transformation product. Thus, although the strain energy associated with displacive transformations is avoided, this reconstructive mechanism can only occur at temperatures where atoms get sufficient mobility. Given that atoms are mobile, certain species which are more soluble in a particular phase (ferrite or austenite) will tend to migrate preferentially into that phase, leading to a difference in the chemical composition between them. The atomic correspondence between the parent and product phases is lost in a reconstructive transformation. The shape of the transformation product is either determined by growth circumstances, or as equilibrium is approached, by a minimisation of the overall interfacial energy per unit volume.

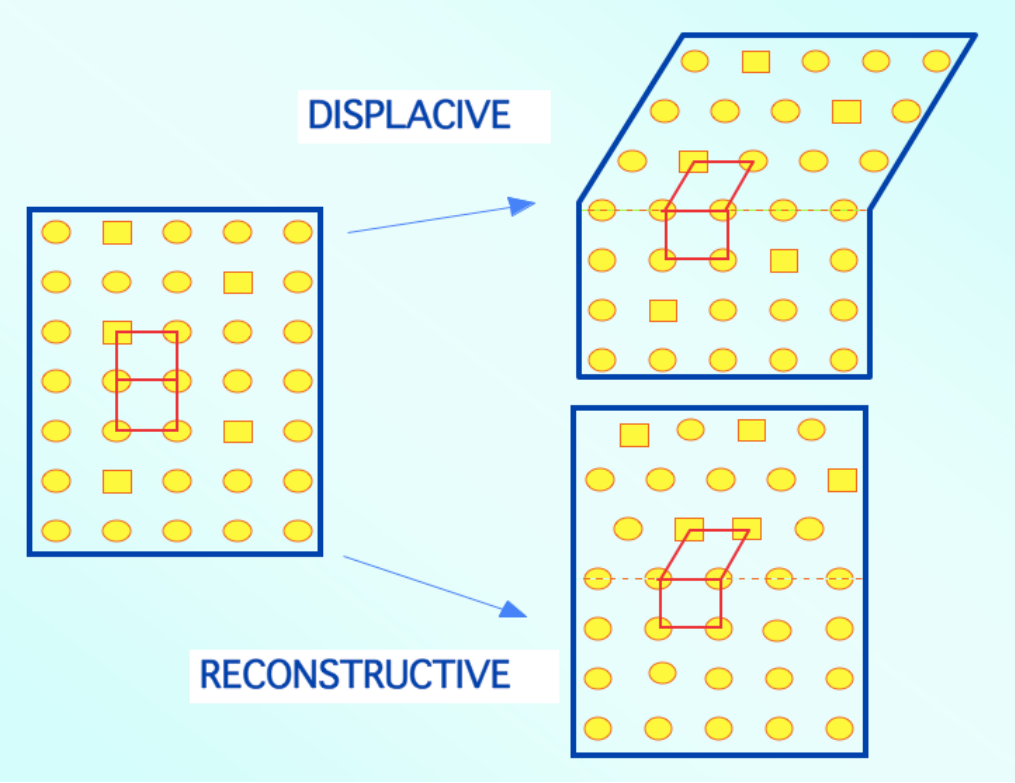

Fig. 2.10 The displacive and reconstructive mechanisms [34]

2.4.1.4 CCT and TTT curves

Hereinbefore we mentioned the different cooling methods in the heat treatment process, actually the most normal two transformation types are Continuous Cooling Transformation (CCT) and Time-Temperature Transformation (TTT). CCT diagrams are generally more appropriate for engineering applications as components are cooled (air cooled, furnace cooled,

quenched etc.) more economically than transferring to a separate furnace for an isothermal heat treatment [35].

Continuous cooling transformation (CCT) diagrams: measure the extent of transformation as a function of time for a continuously decreasing temperature with a constant cooling rate. Figure 2.11 given below is a typical CCT diagram of a steel (Chemical composition in *wt*% of: 0.95 C, 0.25 Si, 1.2 Mn, 0.48 Cr, 0.13 V, 0.55 W, Fe for balance) [36].

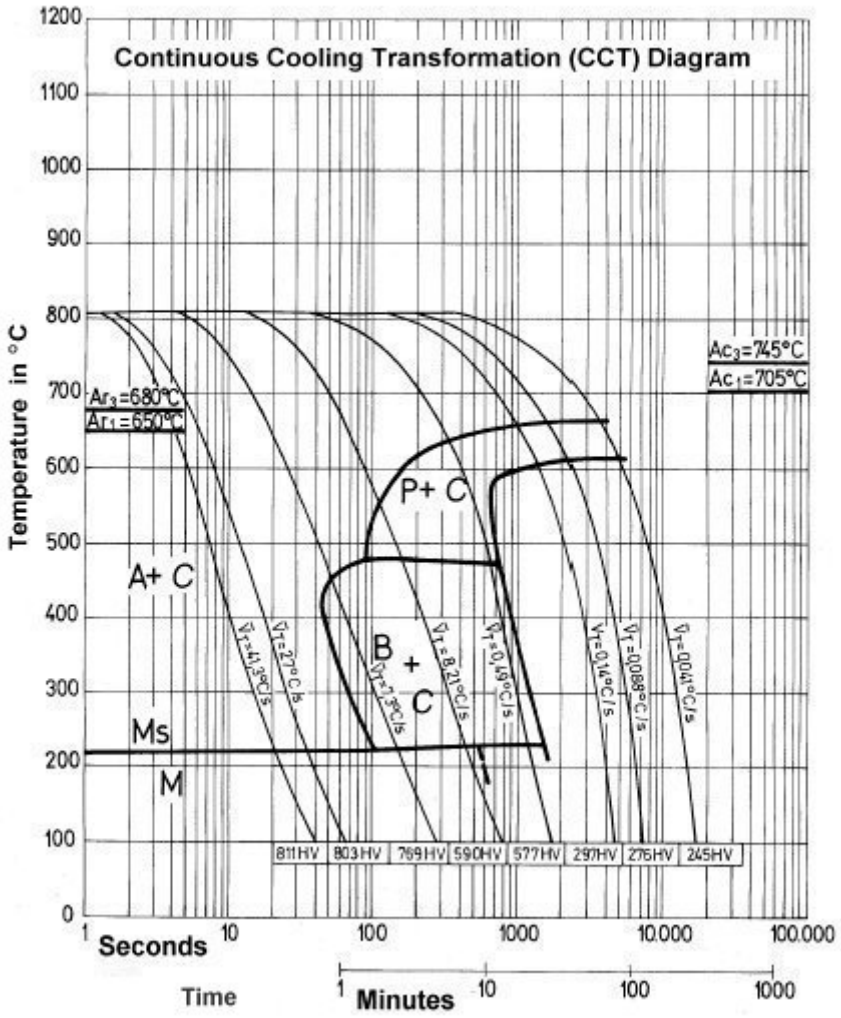

Fig. 2.11 CCT Diagram of one high carbon steel [36]

Time-temperature transformation (TTT) diagrams: measure the rate of transformation at a constant temperature. The sample is austenitised and then cooled rapidly to a certain temperature and held at that temperature isothermally. TTT diagram is also named C-curve as it's shape looks quite like C. Figure 2.12 given below is a typical TTT diagram (steel: 80WCrV8) [37].

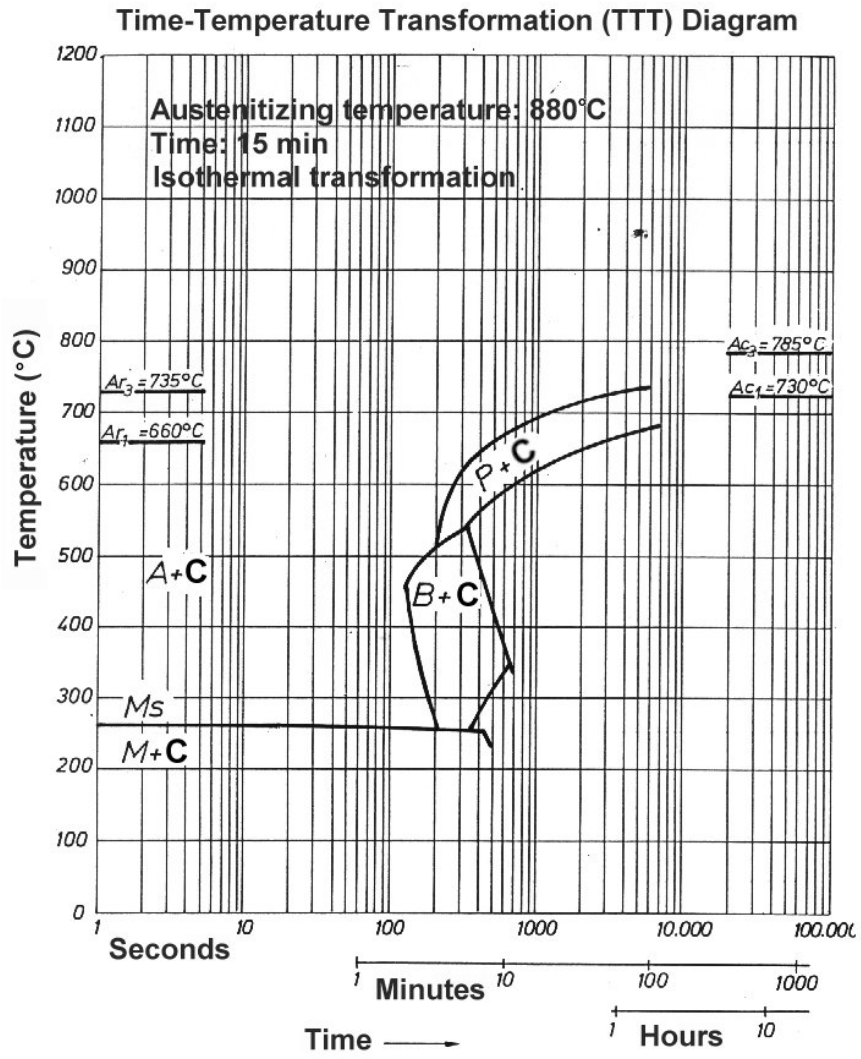

Fig. 2.12 TTT Diagram of 80WCrV8 alloy steel [37]

Obviously a large number of experiments is required to build up either a complete CCT diagram or a TTT curve.

2.4.2 Martensitic precipitation hardening stainless steel: 15-5PH

The material 15-5PH (Condition H1025) is a martensitic precipitation hardening stainless steel which is a precipitation of age hardened and heat solution-treated material at 1025°F for 4 hours and then air cooling. It is widely used in aerospace and nuclear areas due to its toughness and hardness are high and it has a good corrosion resistance due to some alloy elements were added such as Mo, Ti, Si and Cu [22]. The following table 2.1 shows the chemical composition of 15-5PH. You can easily find 15-5PH is named by the weight percent of element chromium and nickel. Table 2.2 gives the basic mechanical properties of receiving condition 15-5PH. Figure 2.13 gives the micrography of as received 15-5PH stainless steel.

Table. 2.1 Chemical composition of 15-5PH

Element	Cr	Ni	Cu	C	Mn	Si	Other alloys	Fe
wt%	15.440	4.500	3.160	0.020	0.660	1.00	*N/A*	Balance

Table. 2.2 Basic mechanical properties of 15-5PH at room temperature

Property	Young's Modulus	Yield stress	Ultimate stress	Hardening exponent *n*	Material constant α'
Quantity	205 GPa	900 MPa	1148 MPa	30	0.0014

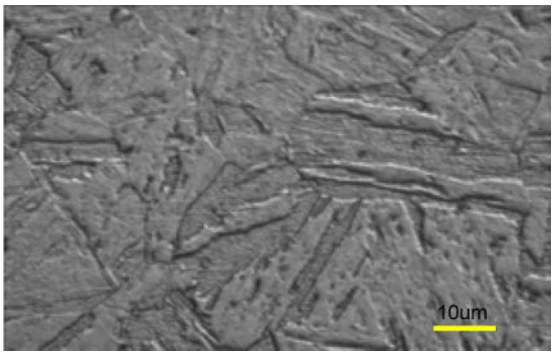

Fig. 2.13 Micrography of as received 15-5PH stainless steel [22]

2.4.3 Phase transformation in 15-5PH

Like others metals, 15-5PH experiences phase transformation during specific heat treatment. This material is in the family of dual phase ones because it only experiences austenite and martensitic transformation but no ferrite or pearlite transformation. The research on phase transformation effects on toughness is then easier. Figure 2.14 displays the dilatation curve of 15-5PH with a whole heat treatment cycle.

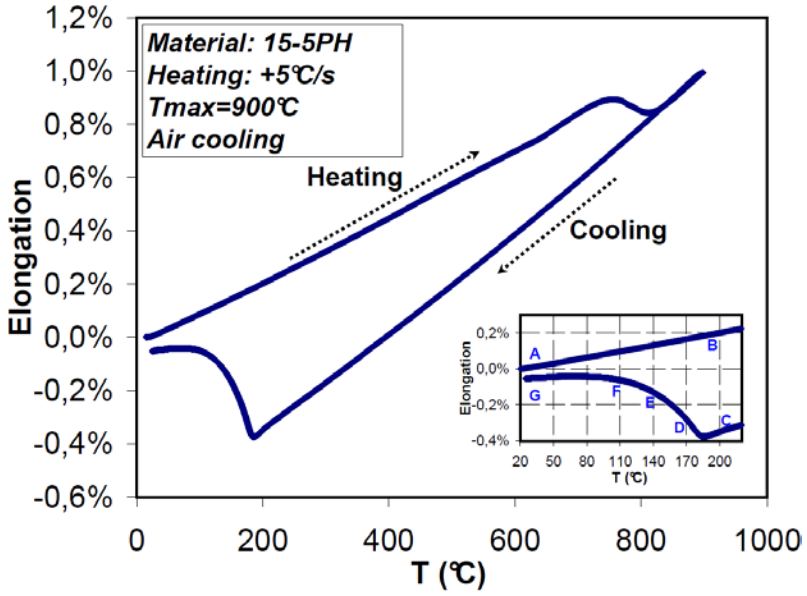

Fig. 2.14 Elongation during a heat loading cycle, heating rate: +5°C/s, max T is 900°C and air cooling

The test is done with an initial heating rate of +5°C/s until the maximum temperature which is 900°C. The first linear response is the expansion of martensite. At about 770°C the austenite transformation starts and is finished at about 815°C. After the maximum temperature 900°C is reached the specimen is air-cooled. The first part of the decreasing curve is the linear contraction of austenite which stops at about 185°C where martensitic transformation starts. The transformation is over at about 80°C. Figure 2.15 displays the measured temperatures loading during the test. The cooling rate is between 0.6°C/s and 0.2°C/s during the martensitic transformation.

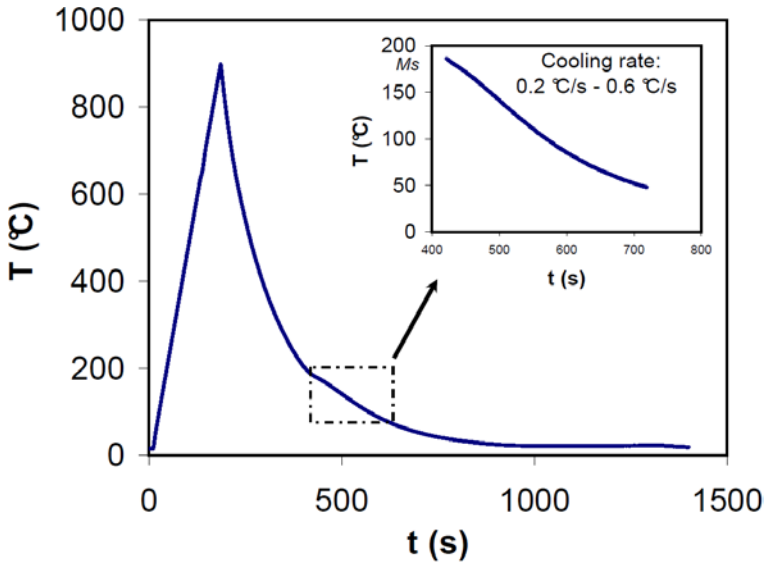

Fig. 2.15 Temperature history and cooling rate during the martensitic transformation

We will focus on the continuous cooling martensitic transformation of 15-5PH to study the effect of metallurgical phase transformation on mechanical behaviour. One can read in [38] that the martensitic transformation of 15-5PH is temperature driven, that is to say, once the temperature stops decreasing the transformation will also stop. Our experimental results are consistent with this observation. This means that one can keep a constant phase proportion if the temperature is changed to be constant during the continuous cooling martensitic transformation and do the corresponding mechanical tests.

In the lower right corner of figure 2.14, seven points (A to G) are marked which means that we will study the mechanical behaviour for these seven states. For example points A and G are two tests performed at room temperature one before the heat treatment as received condition (A) and one after a whole cycle heat treatment (G). Point B is fully martensite at 200°C while point C is totally austenite at the same temperature just before the martensitic

transformation; Point D, E and F are three points during the martensitic transformation at respectively 170, 140 and 110°C.

By the dilatometer technique, we can get:

$\Delta\varepsilon_{\alpha,\gamma}^{T_{ref}} = -0.00686$

α_α: *expansion coefficient of martensite*, $\alpha_\alpha = 1.23\times10^{-5}$

α_γ: *expansion coefficient of austenite*, $\alpha_\gamma = 1.89\times10^{-5}$

And consequently, equation 2-8 can give us the phase fraction during the martensite transformation. Table 2.3 shows the phase proportion at each point [37][39][40][41].

Table. 2.3 Analysis points related to the phase

Point	A	B	C	D	E	F	G
Phase	α	α	γ	α/γ	α/γ	α/γ	α
% of α	100%	100%	≈0%	25%	60%	80%	≈100%

Notice: α presents martensite, γ presents austenite, α/γ means martensite and austenite mixed. The reason why there are two approximately equal symbol ≈ is that the phase transformation may be not finished completely, for example there may be some residual austenite exists at point G.

The fraction curve versus continuous cooling temperature is also given below. From figure 2.16, we can find that there is some residual austenite exists in the final material after one cycle heat treatment. Actually it can also be found by the dilatation curve in figure 2.14, when the temperature arrived at the room temperature, the final dilatation curve didn't meet the beginning of the dilatation curve which means that there is some retained austenite at point G. The gap between the final dilatation curve and the beginning of the dilatation curve in figure 2.14 depends on the amount of the residual austenite.

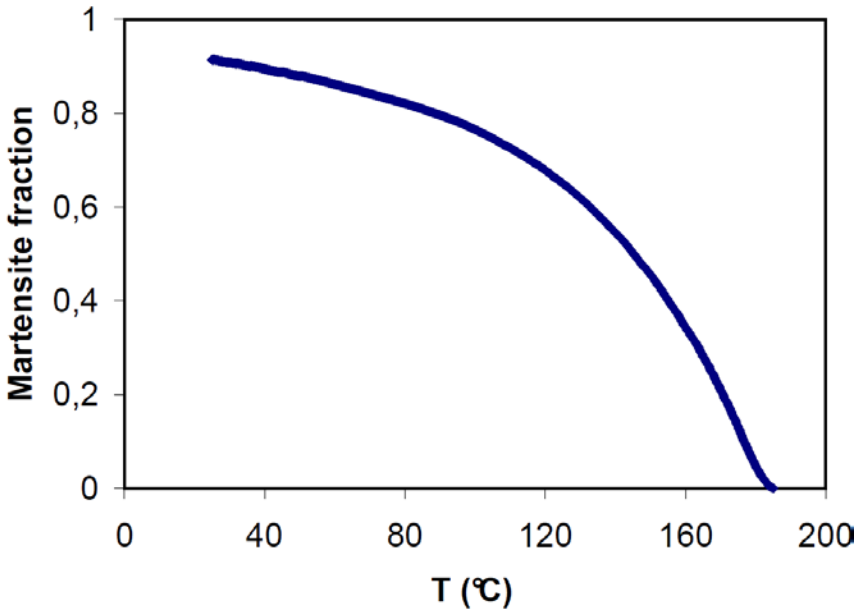

Fig. 2.16 Phase fraction versus time in the 15-5PH martensite transformation

2.4.4 16MND5 low carbon steel

Our research is also implemented on the 16MND5 low carbon steel whose chemical composition is given in table 2.4. 16MND5 (Also called A508 Cl3) is used widely in France for PWR (Pressure Water Reactor) vessels. It was heat treated by two austenitizations at 880°C for 4 hours and 40 minutes followed by water quenching, tempering at 640°C for 7.5 hours, and final stress relief annealing at 610 ℃/8 h. After this series of heat treatment process, 16MND5 has a tempered bainitic microstructure [42][43].

Table. 2.4 Chemical composition of 16MND5

Element	C	Mn	Ni	Mo	Si	Other alloys	Fe
wt%	0.16	1.30	0.74	0.48	0.015	*N/A*	Balance

Table 2.5 shows basic mechanical properties of 16MND5 low carbon steel at room temperature. Figure 2.17 shows the typical microstructure of 16MND5 low carbon steel. Figure 2.18 gives an example of experimental PWR sample [44] which has the same structure to the real PWR but has been minified by 10 times.

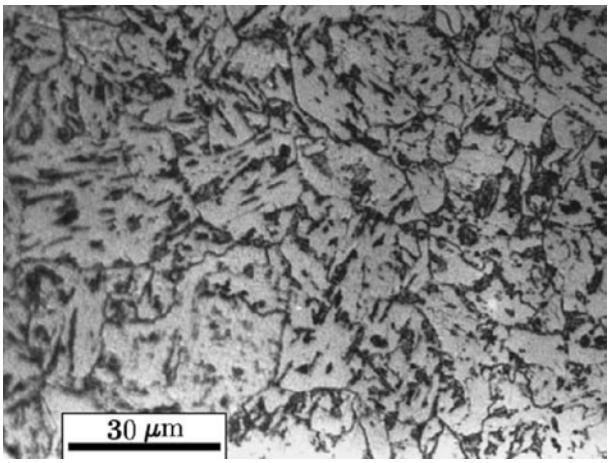

Fig. 2.17 Typical microstructure of as received 16MND5 low carbon steel [42]

Table. 2.5 Mechanical properties of receiving 16MND5

Property	Young's Modulus	Yield stress	Ultimate stress	Hardening exponent n	Material constant α'
Quantity	191 GPa	450 MPa	610 MPa	19.62	0.031

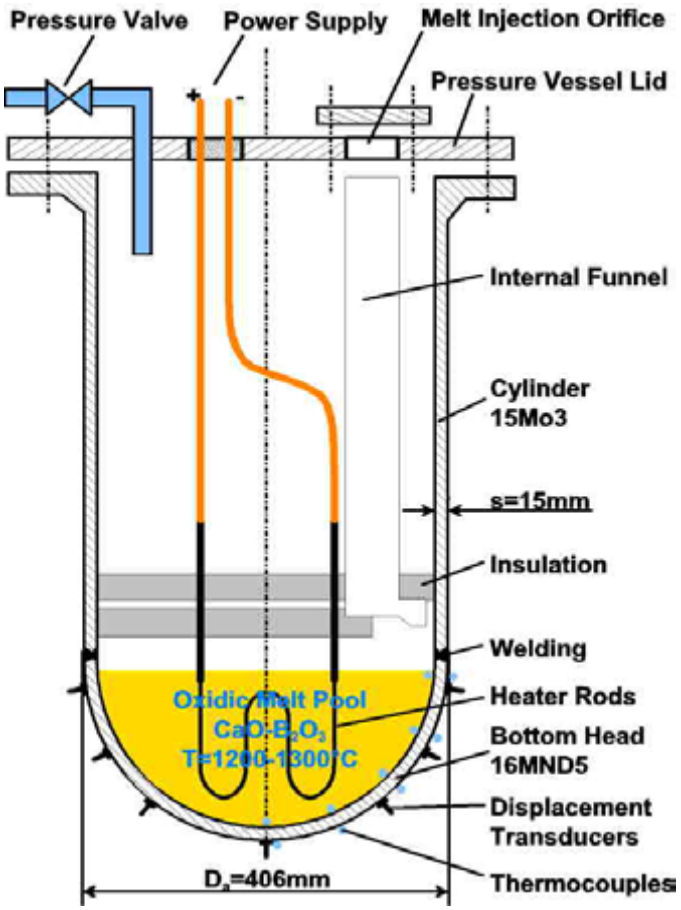

Fig.2.18 16MND5 in a pressure water reactor vessel sample (scale 1:10) [44]

2.4.5 Phase transformation in 16MND5

Like other metals or alloys, 16MND5 also has several phase transformations during the heat treatment process. M.Martinez did a lot of experiments and plotted the following CCT (Continuous-Cooling- Transformation) curve of 16MND5 [45]. As it shows, 16MND5 will start austenitization around 730°C (Ac1) and finish at about 830°C (Ac3), martensitic transformation begins at 415 °C (Ms) under a cooling rate quicker than 30°C/s., bainite transformation goes with a cooling rate quicker than 3°C/s and slower than 30°C/s.

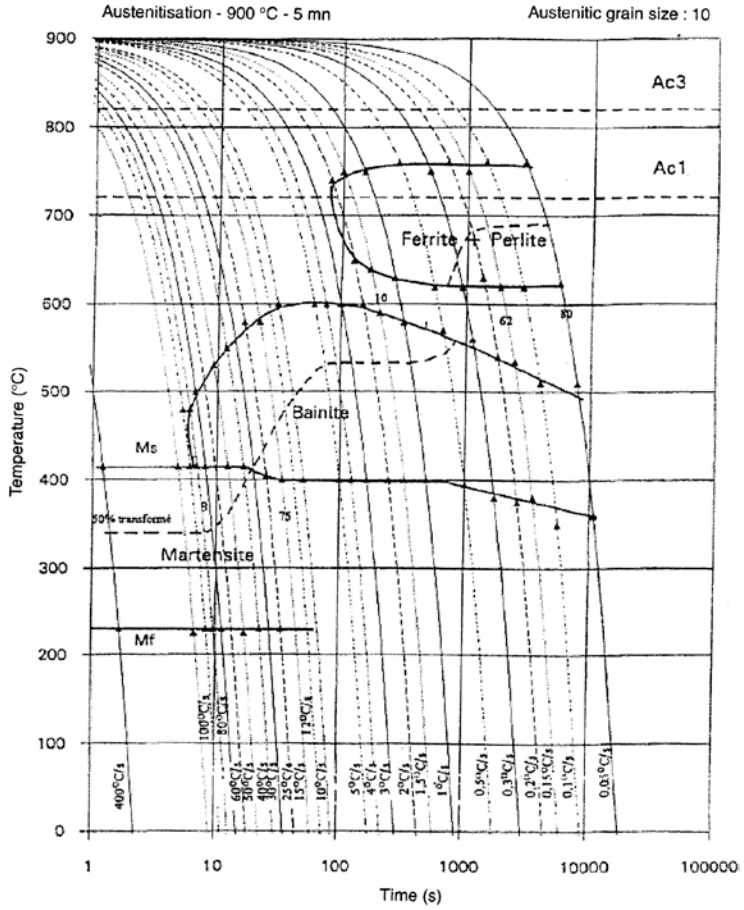

Fig. 2.19 CCT diagram of 16MND5 steel [44]

If we want to investigate the effects of phase transformation on the mechanical properties of 16MND5, two aspects must be studied. First, the appropriate cooling rate for pure bainite transformation; Second, when the temperature is kept as isothermal where the mechanical test is expected to be done, is there any isothermal bainite transformation or not. If there is, the mechanical tests should be launched after the end of isothermal bainite transformation. So, the investigation of bainite transformation kinetics in 16MND5 is meaningful to us.

2.4.5.1 Review of bainite transformation investigation

Bainite transformation is formed between the martensite transformation in lower temperature and the pearlite transformation in higher temperature. Normally from 250°C to 550°C is the bainite transformation region which contains the upper bainite from 400°C to 550°C and lower bainite from 250°C to 400°C [46]. Since E. S. Davenport and Edgar Bain first introduced the bainite which is originally described as being similar to tempered martensite in the 1920s, So many investigations have been done to research the bainite transformation and transformation kinetics in kinds of materials. However the controversy on the bainite transformation mechanism is still unresoloved [47][48]. Undoubtedly, bainite transformation is the most complex decomposition of austenite under Ac1. A lot of people think that the displacive theory is reasonable for the bainite transformation just like martensite transformation, but some other people agree more with the diffusion theory [49-52]. So many bainite transformation models have been also presented to study the kinetics and the following point has been agreed: the bainite transformation is the evaluation of carbon atom [49][53-56]. And researchers are also searching the basic understanding that why bainite transformation is an incomplete transformation [57][58]. F.G. Caballero et al. presented that the diffusionless growth of bainite subunits can explain the incomplete bainite transformation by some experimental evidence [59]. Meanwhile, the effects on bainite transformations of alloy elements and external stress are also widely studied to potentially produce some high proporties steels such as carbide-free banitic steel [60-65]. For example, P. Jacques et al. [62] and D. Quidort with Y. Bréchet [63] all experimentally proved the silicon can strongly prevent the cementite precipitation. L.C. Chang presented that carbide precipitates in ferrite component of lower bainite can align single or multiple variants under the influence of stress created by the formation of bainite [64]. In 1999, Mr. Bhadeshia summarized the research achievement and discussed the unresolved issues of bainite transformation [65], he presented his theory which can explain a lot of observations and make a number of predictions. The theory tells us that there is an invariant plane strain shape deformation during the bainite transformation and the shape deformation induces plastic accommodation which causes a loss of coherency and brings the growth process to a premature halt. His opinion on the bainite transformation mechanism can be illustrated in Fig. 2.20, some comments are marked on the figure for better understanding. Detail description can be found in reference [66]. In 2010, F.G. Caballero et al. effectively monitored the decarburization of super-saturated bainitic ferrite during the bainite transformation for the first time with Atom Probe Tomography (APT)

and provided strong evidence of carbon supersaturation in bainitic ferrite at the early stage of transformation. Based of this, they stated that the bainite transformation is essentially displacive in nature [67].

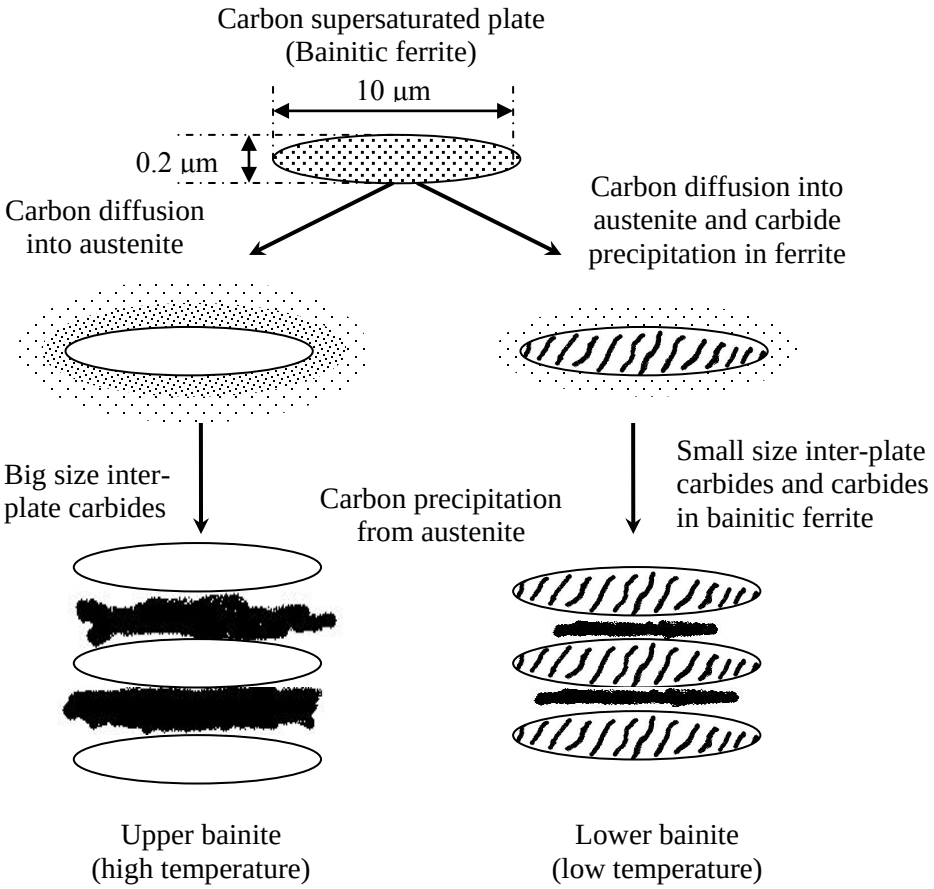

Fig. 2.20 Illustration of bainite transformation mechanism [65]

2.4.5.2 Pure continuous cooling bainite transformation in 16MND5

With the help of 16MND5 CCT diagram from M.Martinez's thesis [68], we imposed a heat rate 5°C/s to maximum temperature of 900°C and stayed there for 30 seconds. Consequently it was cool down by -5°C/s. The free dilatation curve is given as below. It shows us the austenitization temperature is from 750°C to 840°C, the continuous cooling bainite transformation begins at 585°C. These data agree well with the result of M.Martinez's thesis. It is 100% bainite transformation without any pearlite or martensite transformation.

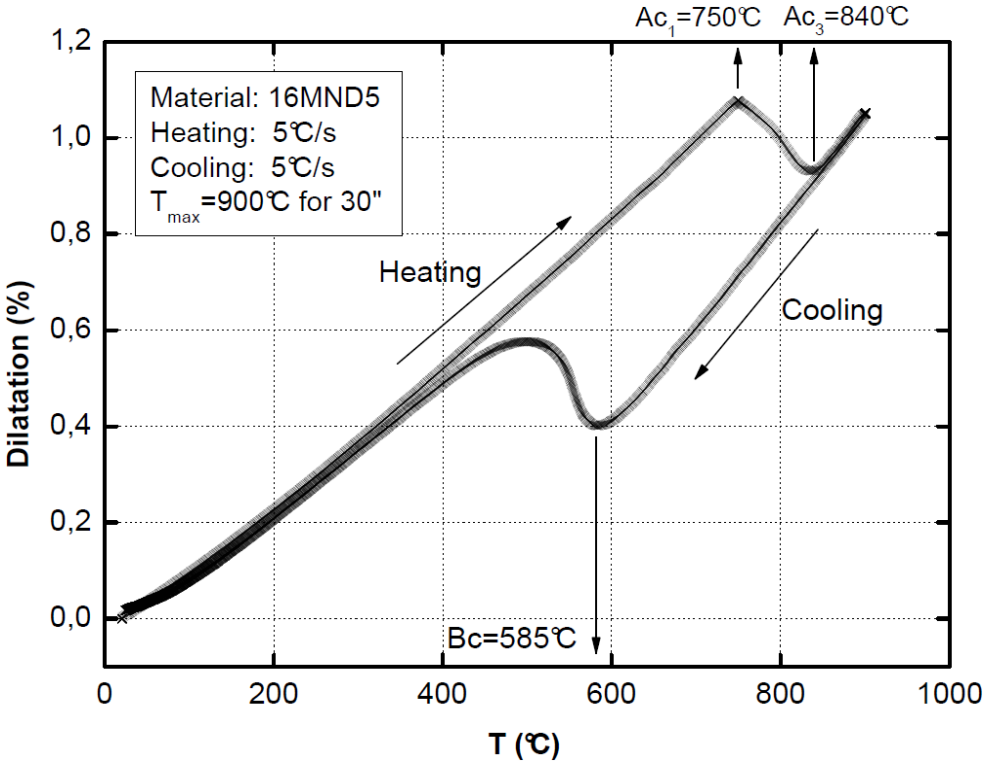

Fig. 2.21 Free dilatation curve of continuous cooling bainite transformation in 16MND5

From the above free dilatation curve, we can get the expansion coefficients of bainite and austenite, the compactness difference between them is also calculated.

$\Delta\varepsilon_{\alpha,\gamma}^{T_{ref}} = -0.00865$

α_α: *expansion coefficient of bainite*, $\alpha_\alpha = 1.472\times10^{-5}$

α_γ: *expansion coefficient of austenite*, $\alpha_\gamma = 2.186\times10^{-5}$

And equation 2-8 can give us the phase fraction versus time during the continuous cooling bainite transformation (see figure 2.22).

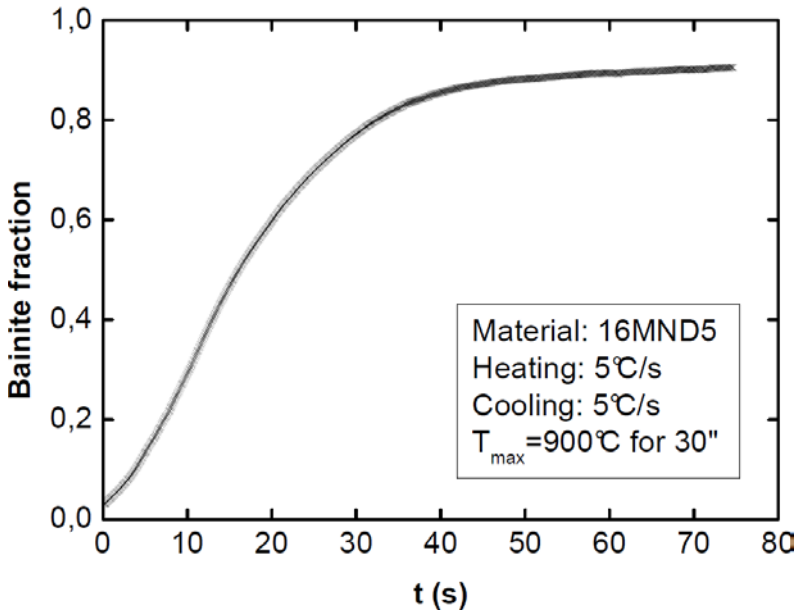

Fig. 2.22 Bainite fraction transformed during the continuous cooling bainite transformation

2.5 Effect of phase transformation on fracture toughness

2.5.1 Fracture toughness, an important material property

Fracture toughness is a property which describes the ability of a cracked component to resist the fracture, and is one of the important properties of any material. From energy side, the ability of a metal to deform plastically and to absorb energy in the process before fracture is termed toughness. The emphasis of this definition should be placed on the ability to absorb energy before fracture [69]. It is a very basic characterization of materials applied in such as aerospace, automotive, water pressure reactor and other engineering components. Whether one material has a good fracture toughness or not is a standard to evaluate the material for engineering application. Following picture 2.23 is one example to show the engineering issue when there is fracture. A crack was found on the axle of a train type used on the Shanghai-Beijing high-speed line and finally the cracked axle has to be replaced.

Fig. 2.23 Cracked axle was found on a CRH380BL train in 2011 [70]

As a consequence, the experimental measurement and estimation of fracture toughness play an important role in fracture mechanics for the damage tolerance evaluation, structure integrity assessment and residual strength analysis etc. for these usual components. There are two traditional parameters to quantitatively express the material fracture toughness, one is the stress intensity factor K which is proposed in 1957 by Dr. George Irwin, the father of fracture mechanics [71-73]. Another one is *J*-integral introduced by James R. Rice in 1968 [74]. The stress intensity factor is normally applied for the elastic crack tip field, while the later *J*-integral is usually used for the elastic-plastic mechanics.

So many aspects can affect the fracture toughness of material, such as the grain size, microstructure, material composition, alloy elements and phase proportion etc. All these aspects are also offen affected by the metallurgical heat treatment.

2.5.2 Effect of phase transformation on fracture toughness

A lot of work has been done on the effect of phase transformation on material properties especially fracture toughness in the last half century. Greenwood, Johnson and Magee respectively worked on the effect of an applied stress during the phase transformation, they showed that this stress could lead to an additional irreversible strain [75][76], described by the phase TRansformation Induced Plasticity (TRIP). Furthermore, J.P. Bressanelli and A. Moskowitz presented that TRIP can increase the strain-hardening rate which results in an overall increase of tensile strength and uniform ductility [77]. Consequently the TRIP high strength steel came out [78]. Subsequently many papers appeared dealing with the influence of mechanically-induced martensitic transformation on the general mechanical behaviour of

metastable austenitic steels under monotonic and cyclic loading [79]. For example, Gerberich *et al.* [80] and Singh [81] have researched the enhancement of fracture toughness due to TRIP phenomenon. Many constitutive equations and kinetic theories of isothermal martensitic transformation have been also presented [82][83]. Bhadeshia also found large regions of untransformed austenite in the microstructure is detrimental to toughness as they can transform to corresponding large regions of untempered and brittle martensite under the influence of external stress [84][85]. Sun and Hwang established a micromechanics constitutive model based on an internal variable theory to describe the stress–strain–temperature relations during forward and reverse transformation processes [86]. Hannink *et a.*, Kelly and Rose found that the stress-induced martensitic transformation in zirconia ceramics involves predominately positive volumetric change, resulting in a reduction in the crack-tip stress-intensity factor [87], which in turn leads to an increase in the material fracture toughness. Sung yi *et a.* analysed the fracture toughening of Shape Memory Alloys (SMAs) with a macro-crack under mixed mode loads [88]. The analytical results also show that the martensite transformation reduces the crack tip energy release rate and increases the toughness. The toughness of SMAs is enhanced by the transformation strain, which tends to limit or prevent crack growth.

By contrast, the phase transformation in SMAs involves negative volumetric change, which would result in an increase in the crack-tip stress-intensity factor and thus a decrease in fracture toughness [89]. P. Yan *et al.* found that Steel line pipes produced by high frequency induction welding can result in a low-toughness zone at the weld junction [90].

Now let's review the investigation in the last decade about the influences of phase transformation on the fracture toughness with more details.

In 2001, the influence of austempering temperature on the microstructure and the mechanical properties of high carbon and high silicon (HCHS) steel at room temperature and ambient atmosphere were examined by Susil K. Putatunda [91].The influence of microstructure on the plane strain fracture toughness of this HCHS steel was also investigated. Figure 2.24 shows that fracture toughness of the HCHS steel increases with austempering temperature, reaching a peak value at 350°C and then starts to decrease.

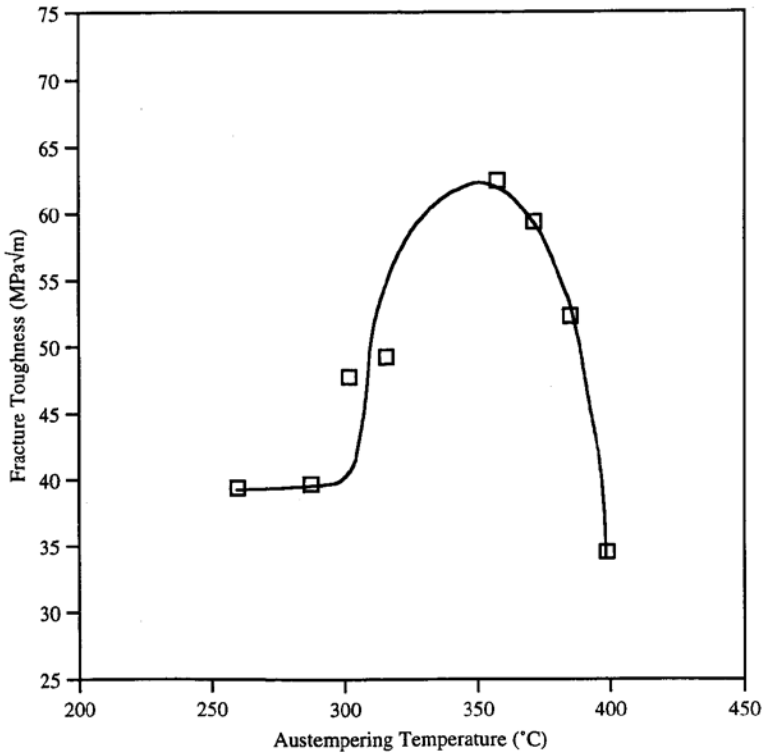

Fig. 2.24 Influence of austempering temperature on the fracture toughness of HCHS steel [91]

Figure 2.25 denotes that the maximum fracture toughness is obtained in this steel with a upper bainitic microstructure when the microstructure contains about 35% austenite.

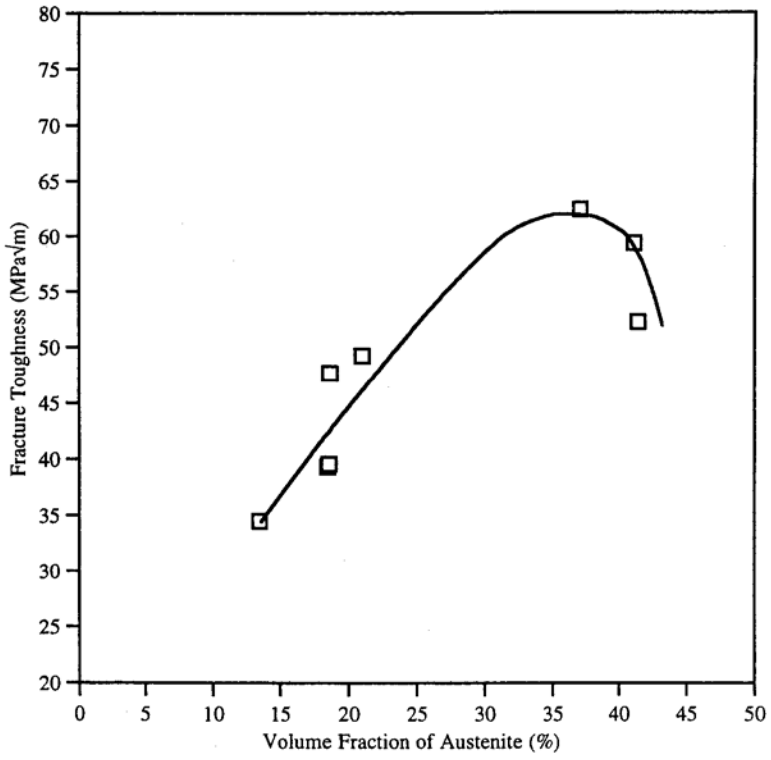

Fig. 2.25 Influence of volume fraction of austenite on the fracture toughness of HCHS steel [91]

The author found that the fracture toughness was found to depend on the parameter $\sqrt{\frac{X_\gamma C_\gamma}{d}}$ where X_γ is the volume fraction of the austenite, C_γ is the carbon content of austenite and d is the mean free path of dislocation motion in ferrite. C_γ is determined by the following equation 2-11 [92].

$$A_\gamma = 0.3548 + 0.0044C_\gamma \tag{2-11}$$

Where A_γ is the lattice parameter of austenite in nm.

With this investigated result, the author concluded that it will be possible to produce very high fracture toughness in HCHS steel by maximizing the parameter $\sqrt{\frac{X_\gamma C_\gamma}{d}}$, i.e. by an increase in ($X_\gamma C_\gamma$) product and a simultaneous reduction in d values.

Takeshi Iwamoto and Toshio Tsuta from Hiroshima University investigated the mechanism of strain-induced martensitic transformation toughening for TRIP steel due to crack extension in 2002 [93]. In their paper, It was recalled that McMeeking and Evans derived the following equation to evaluate the transformation toughening in the ceramics due to crack extension [94]:

$$K^{tip} = K^{far} + \Delta K \tag{2-12}$$

Where K^{tip} and K^{far} represent the stress intensity factors near the crack tip and in the far field, respectively. The value of ΔK is the toughness enhancement due to transformation. If ΔK <0 then transformation toughening occurs.

Then, Budiansky *et al.* [95] indicated that Eq. (2-12) can be derived from the viewpoint of energy conservation and can be rewritten using the *J*-integral as:

$$J^{tip} = J^{far} + \Delta J \tag{2-13}$$

Where J^{tip} and J^{far} are the crack tip and the far field *J*-integral. ΔJ is the amount of transformation toughening and possesses a negative value in the case of toughening.

Based on these two equations, the following equation 2-14 for evaluating toughness enhancement factor ΔJ_{te} due to strain-induced martensitic transformation (SIMT) can be derived in the form of the *J*-integral:

$$\Delta J_{te} = \frac{J^{tip}}{J^{far}} - 1 \leq 0 \tag{2-14}$$

Takeshi Iwamoto and Toshio Tsuta simulated the deformation behaviors of CT specimens of TRIP steel under mode I loading at various temperatures for the cases of stationary cracks and stable crack extensions. They introduced the nodal release technique and concept of pull-back force in the case of a stable crack extension. They proposed a thermo-elasto-viscoplastic constitutive equation [93] including transformation strain rate and the 3rd invariant of the deviatoric stress J_3.

Figure 2.26 is their result of the toughness enhancement ΔJ from Eq. (2-13) and difference of ΔJ between TRIP steel and austenite. It revealed that ΔJ for austenitic material has a peak near room temperature.

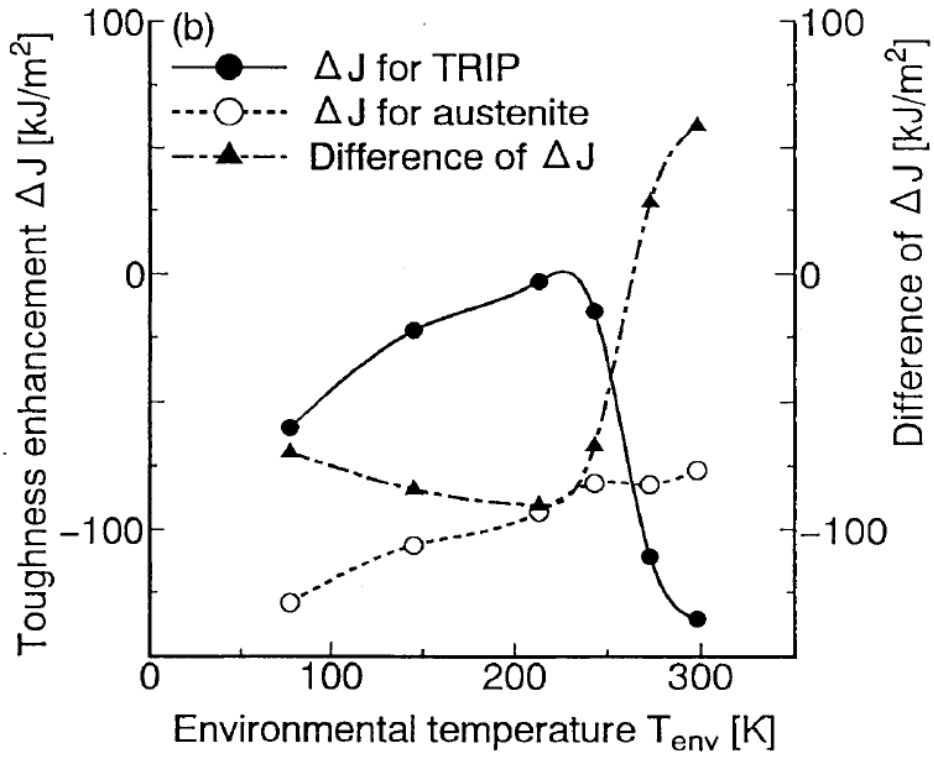

Fig. 2.26 The toughness enhancement ΔJ from Eq. (2-13) and difference of ΔJ between TRIP steel and austenite [93]

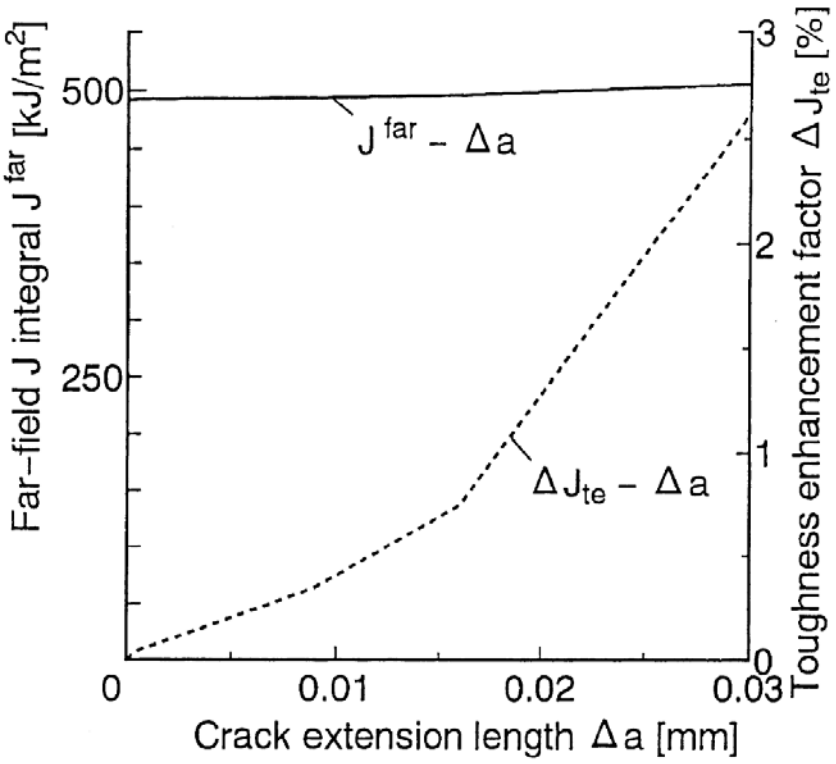

Fig. 2.27 The far-field *J*-integral J^{far} and toughness enhancement ΔJ_{te} defined by Eq. (2-14) during stable crack propagation of TRIP steel [93]

Fig. 2.27 shows the far-field *J*-integral J^{far} versus crack extension length Δa for TRIP steel. As can be seen in this figure, J^{far} tends to increase slightly with increasing Δa and the same tendency in the experimental results was observed. The toughness enhancement factor ΔJ_{te} defined by Eq. (2-14) during stable crack growth with a constant crack tip *J*-integral J_{IC} is also shown in this figure. ΔJ_{te} increases with crack propagation. It can be said that the transformation plasticity in TRIP steel is also a major source of toughness enhancement due to SIMT (Stress Induced Martensitic Transformation). The maximum fracture toughness enhancement effect is obtained in a very small length of crack propagation.

As a result, they concluded that the toughness enhancement for TRIP steel was larger than that for austenite near room temperature. The opposite relationship was observed in a lower temperature range. Therefore, the transformation toughening effect and fracture toughness are reduced when large amounts of martensite are formed. The transformation zone grows, and the high stress region moves and becomes larger during stable crack propagation. J^{far} tends to increase slightly and the toughness enhancement factor used by Okada *et al.* (1992) increases with crack extension. In the case of stable crack extension, the transformation toughening effect by SIMT was also reproduced.

K. Hase *et al.* in 2006 found that the use of a two-stage isothermal heat treatment (see figure 2.28) to generate a microstructure consisting of bainitic ferrite and retained austenite has been found beneficial to the mechanical properties of a particularly strong steel [97].

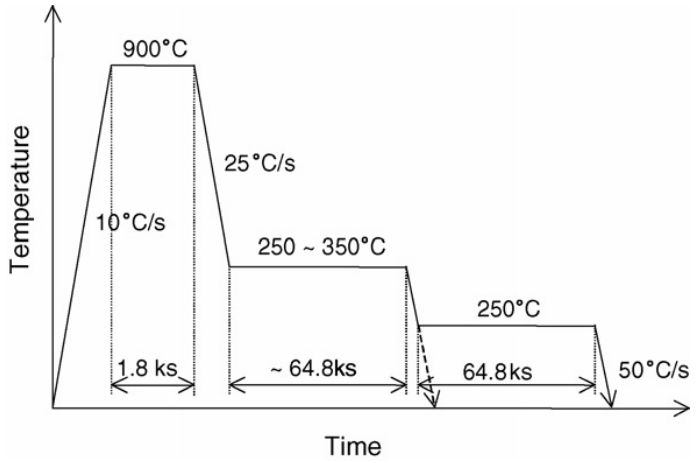

Fig. 2.28 The form of the 2-stage heat treatment

The following figure shows that the two-stage sample exhibits the best combination of strength and fracture toughness which is at least 30% higher than the normal one stage heat treatment method. They think the double isothermal treatment leads to a bimodal distribution of bainite plate size and a geometrical division of residual austenite in such a manner that the mechanical toughness of the austenite is improved.

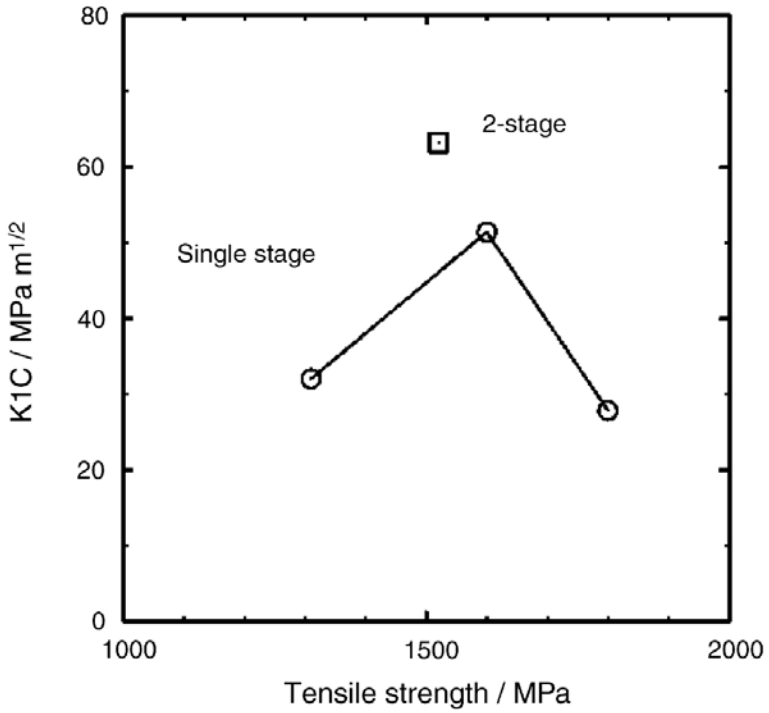

Fig. 2.29 Fracture toughness as a function of tensile strength [97]

In 2008, Archana Paradkar *et al.* investigated the effect of volume fraction of primary Ti_3Al (α_2) on fracture toughness of Ti–18Al–8Nb alloy, which undergoes stress-induced martensitic transformation (SIMT) [98]. They did a good materials characterization work with the tools TEM, SEM and XRD. The volume fraction of α_2 is varied by different heat treatment at different temperatures. They used the ASTM E399 Standard [99] to calculate the fracture toughness which is shown in equation 2-15.

$$K = \frac{P_Q}{B\sqrt{W}} f(\frac{a}{W}) \tag{2-15}$$

Where P_Q is the critical load, B is the thickness, W is the width of the sample and a is the crack length, $f(\frac{a}{W})$ is a geometry factor.

Then they got the relation between fracture toughness and the volume fraction of primary α_2 (see figure 2.30). Obviously the fracture toughness decreases with increase in volume fraction of primary α_2.

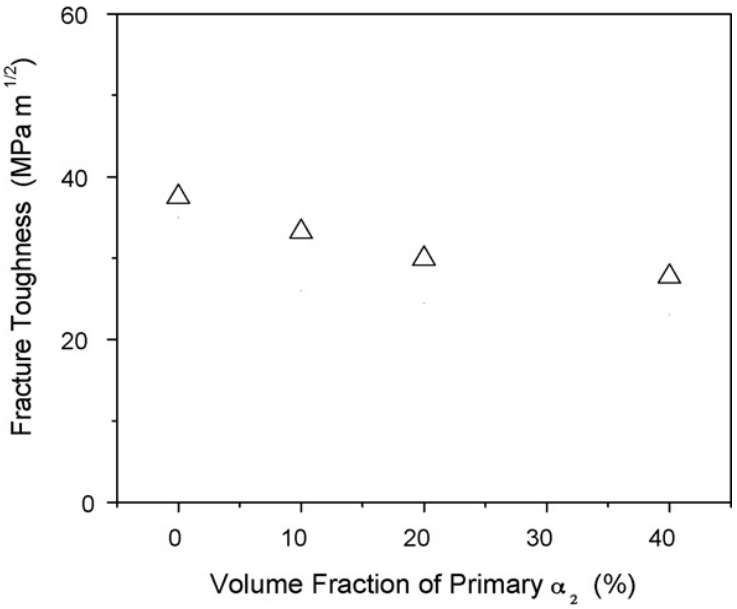

Fig. 2.30 Variation of fracture toughness of Ti-18Al-8Nb alloy with volume fraction of primary α_2 [98]

They think the model for the fracture toughness of two-phase alloys proposed by Richards [100] could explain well their investigated result in the above figure 2.30.

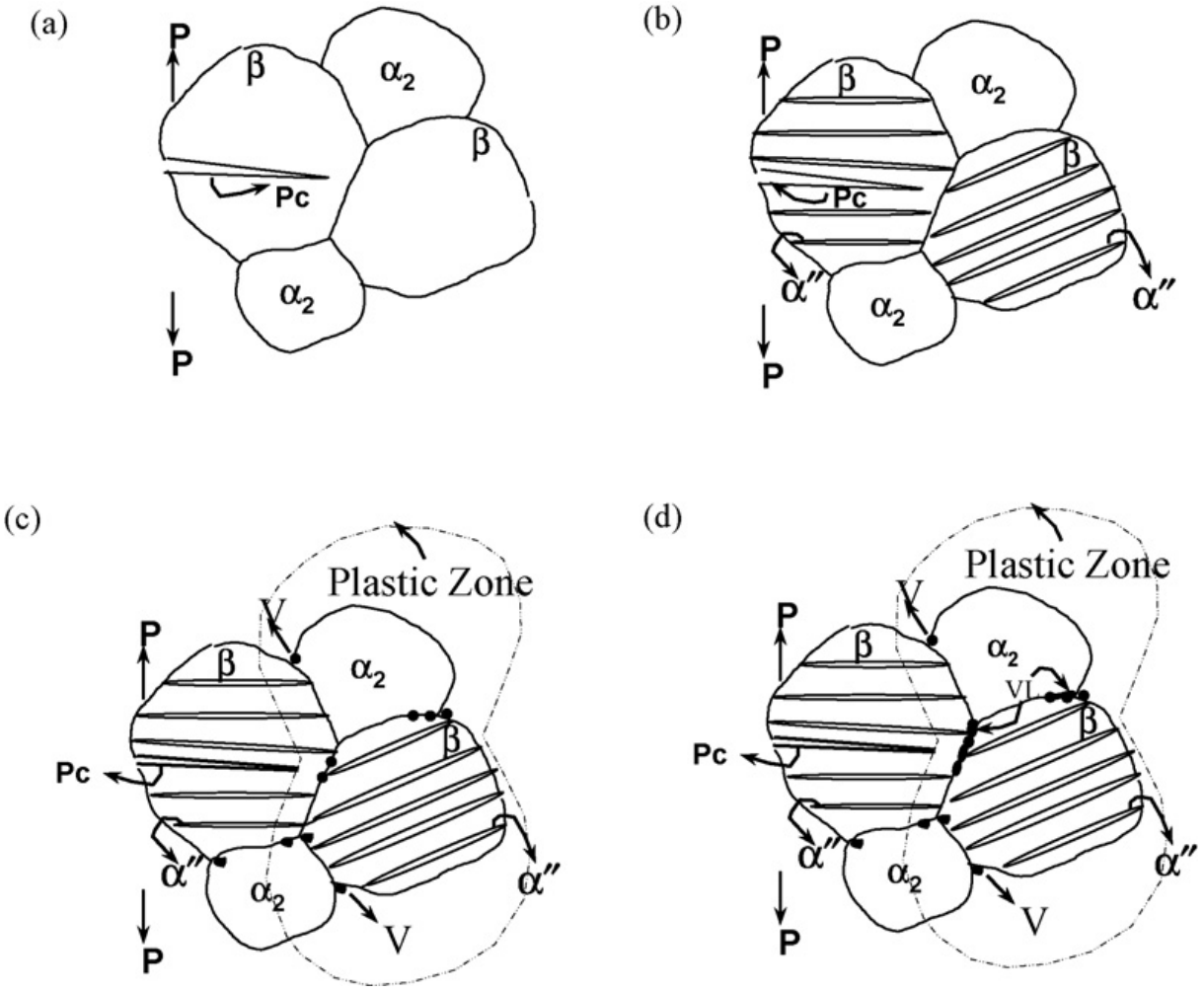

Fig. 2.31 Schematic of Richard's model [98][100]

Figure 2.31 is the schematic drawing showing various stages during fracture. (a) denotes the sample before loading showing initial microstructure and (b) austenite (γ) phase undergoes elastic deformation on loading resulting in SIMT, while in (c) void initiation (shown as V) at α_2 + γ interface and (d) void linkage (VL) leading to decohesion of precipitate and failure. Pc is fatigue pre-crack and P is the load.

They concluded that the reduction in enhancement of fracture toughness due to SIMT, and decrease in the inherent fracture toughness with increase in volume fraction of α_2 were found to be responsible for the reduction in fracture toughness of the alloy with an increase in volume fraction of primary α_2, latter playing a more dominant role.

Lifeng Ma from Xi'an Jiaotong University [101] derived the fundamental formulation for transformation toughening arising from martensitic and ferroelastic transformation by Green's

function method [95][102-104]. The transformation toughening problem geometry is shown in figure 2.32.

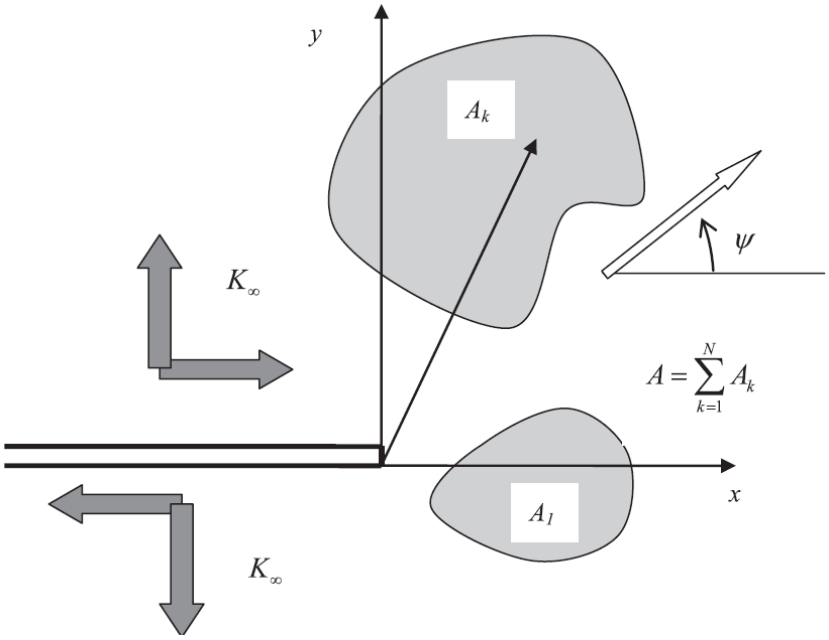

Fig. 2.32 Transformed zone in front of a crack tip under remote load [101]

In figure 2.32, $A = \sum_{k=1}^{N} A_k$ is the transformed zone area, K_∞ is the Stress Intensity Factor (SIF) in the infinite plane, ψ is the orientation angle. So the net SIF at the crack tip due to the presence of the martensitic transformation zone is given by

$$\Delta K = \Delta K_{\mathrm{I}} + \Delta K_{\mathrm{II}} = \iint_A f_4(x_s, y_s) D(x_s, y_s) dA \tag{2-16}$$

Where:

ΔK is the total transformation toughening amount while ΔK_{I} and ΔK_{II} is respectively the transformation toughening value in model Ⅰ and Ⅱ. $f_4(x_s, y_s)$ is the influence function of SIF and $D(x_s, y_s)$ is the transformation density function over the transformation zone.

And for the ferroelastic transformation case, The toughening mechanism of ferroelastic transformation results from the 90° ferroelastic domain switching (interchanging of the ferroelastic long and short axes) [105]. This procedure can be briefly illustrated with figure 2.33.

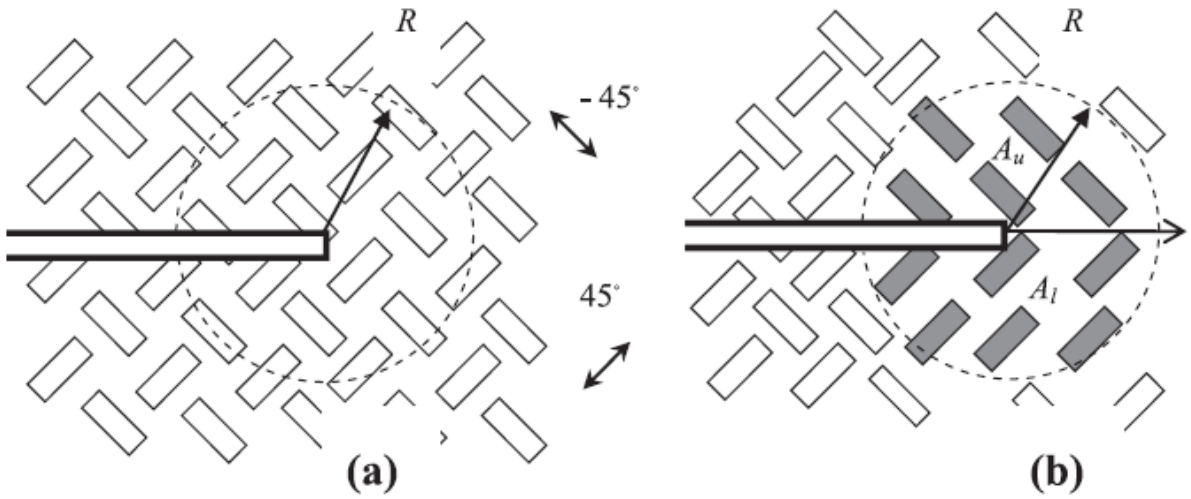

Fig. 2.33 Schematic demonstration of the toughening mechanism due to 90° ferroelastic domain switching near a crack tip: (a) Pre-switching; (b) Post-switching (in dashed circle) [105]

The similarly, the net SIF at the crack tip due to the presence of the ferroelastic transformation due to domain switching can be computed by the Green's function method:

$$\Delta K = \Delta K_{\mathrm{I}} + i\Delta K_{\mathrm{II}} = \iint_{A} f_5(r,\theta,\psi) D(r,\theta) dA \tag{2-17}$$

where $f_5(x_s, y_s)$ is the influence function for the net SIF due to the elementary domain switching and $D(r,\theta)$ is the transformation density function also. (r,θ) is the polar coordinates of the transformed circular region R.

The author set some simple examples to demonstrate the good validity and relevance of the fundamental formulations (2-16) and (2-17) which could pave the way for more rigorous studies of transformation toughening problems.

2.6 Evaluation of *J*-integral based fracture toughness

Characterization of crack propagation ability is done by fracture toughness. Even though *J*-integral based fracture toughness is more complex and difficult to deduce than the stress intensity factor K, but it will give us more accuracy result about the effect of phase transformation on crack propagation.

Now, we will review some remaining methods for the estimation of *J*-integral.

2.6.1 Some fracture specimens with typical geometry

Before we go into the *J*-integral and its evaluation, we make a brief introduction of the usual mechanical fracture samples with pre-crack. All these different specimens can be applied for *J*-integral estimation. Only the estimated result from the specimen with same standard geometry can be compared [106][107].

Figure 2.34 illustrates five conventional fracture specimens: CT, SENB, SENT, CCP and DECP. All in-plane sizes of these specimens are marked in this figure, in which *a* is the crack length, *W* is the specimen width and 2*H* is the specimen length. The specimen thickness is denoted by *B*. These specimens are used most commonly in the current fracture test [108].

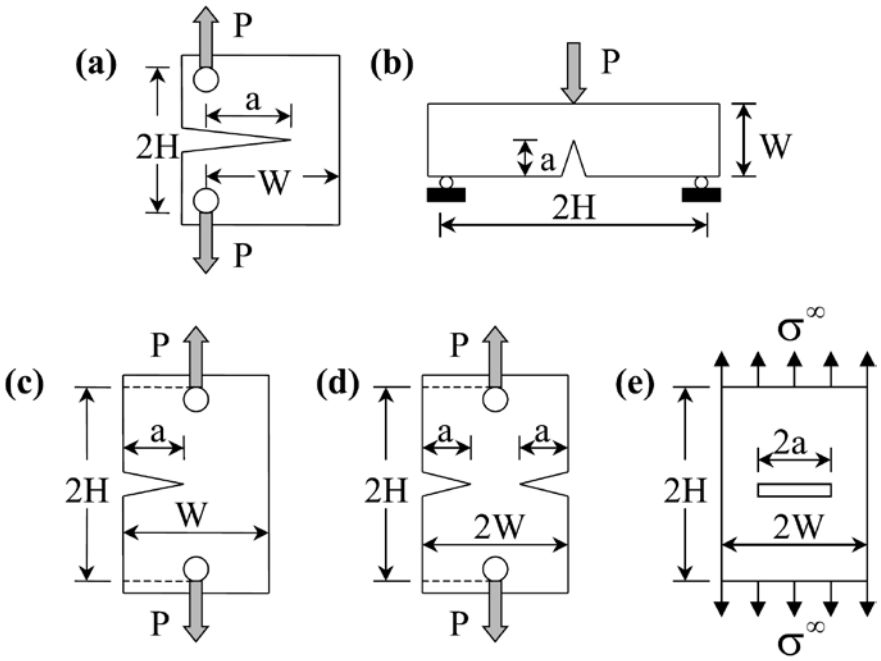

Fig. 2.34 Fracture test specimen geometries: (a) CT; (b) SENB; (c) SENT; (d) DECP; (e) CCP

2.6.2 *J*-integral and critical *J*-integral

2.6.2.1 Strain energy release rate

In 1920s, Griffith's crack theory was published [19][110], The basic idea of the Griffith theory is that at onset of unstable fracturing, one can equate the fracture work per unit crack extension to the rate of disappearance of strain energy from the surrounding elastically strained material [107]. Based of Griffith's crack theory, Irwin introduced his strain energy release rate concept which is also called The Griffith-Irwin Energy Balance.

Strain energy release rate (or energy release rate) is the energy dissipated during fracture per unit of newly created fracture surface area. This quantity is central to fracture mechanics because the energy that must be supplied to a crack tip for it to grow must be balanced by the amount of energy dissipated due to the formation of new surfaces and other dissipative processes. Actually, this energy rate can be regarded as composed of two terms: (1) the strain energy loss rate associated with extension of the fracture accompanied only by plastic strain local to the crack surface. This term is called G. (2) The strain energy loss rate associated with non recoverable displacements of the points of load application; however, this term is assumed to zero [107][111].

For the purposes of calculation, the energy release rate is defined as

$$G = -\frac{\partial U}{\partial A} \tag{2-18}$$

Where U is the potential energy available for crack growth and A is the crack area (crack length for two-dimensional problems). The unit of G is J/m^2.

The energy release rate failure criterion states that a crack will grow when the available energy release rate G is greater than or equal to a critical value G_C.

$$G \geq G_C \tag{2-19}$$

The quantity G_C is the fracture energy and is considered to be a material property which is independent of the applied loads or the geometry of the body.

The stress intensity factor K is a general way to deduce the strain energy release rate for linear elastic material, but J-integral has to be introduced when there is large-scale plastic strain for the elastic-plastic fracture mechanics.

2.6.2.2 J-integral

The J-integral represents a way to calculate the strain energy release rate, or work energy per unit fracture surface area in a material [112]. The path-independent J-integral proposed by James R. Rice [113] is a method of characterizing the stress-strain field at the tip of a crack by an integration path taken sufficiently far from the crack tip to be substituted for a path close to the crack-tip region [114] (Elastic-plastic situation under radial loading). It is defined as follows:

$$J = \int_{\Gamma} W dy - \vec{T}(\frac{\partial \vec{U}}{\partial x}) ds \tag{2-20}$$

in which:

Γ = any contour surrounding the crack tip as shown in Figure 2.35.

W = the strain energy density = $\int_0^{\varepsilon_{ij}} \sigma_{ij} d\varepsilon_{ij}$,

$\vec{T}$ = the traction vector defined according to the outward normal $\vec{n}$ along Γ , $T_i = \sigma_{ij} n_j$,

$\vec{U}$ = displacement vector,

s = arc length along Γ .

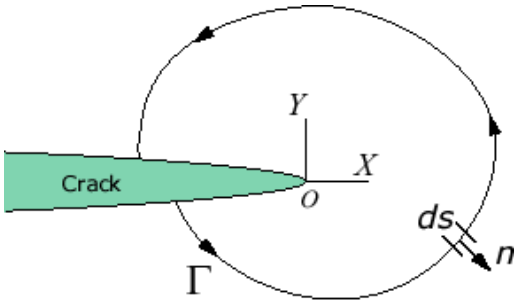

Fig. 2.35 Definition of *J*-integral

From a more physical viewpoint, *J*-integral can be interpreted as the different potential energy between two identically loaded bodies having different crack size.

$$J = -\frac{1}{B}\frac{\partial W}{\partial a} \tag{2-21}$$

In which, B is the thickness of the specimen, ∂W is the different potential energy in the two fracture tests, which is the shadow shown schematically in Figure 2.36, ∂a is the crack length difference between the two fracture samples.

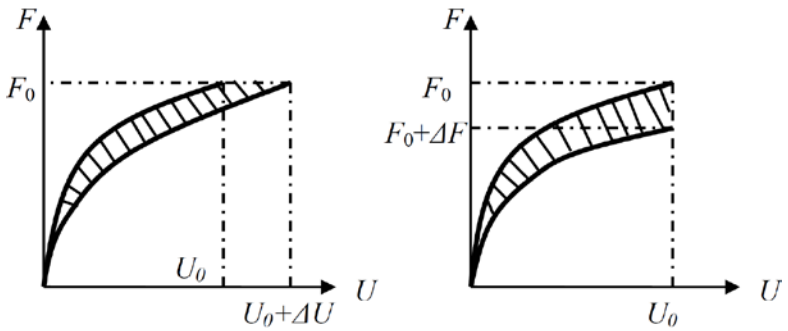

(a) Force loading (b) Displacement loading

Fig. 2.36 Schematically of *J*-integral determination by force (F) vs. displacement (U) curves [115]

In Figure 2.36, if the fracture test is entirely controlled by the loading with force, (a) could be applied to determine the *J*-integral, while the loading is displacement imposed, the shadow in (b) then is the different potential energy [115].

2.6.2.3 Critical *J*-integral J_{1C}

The critical *J*-integral J_{1C} defines the point at which large-scale plastic yielding during propagation takes place under mode I [113], it is taken when the crack extension was first encountered and regarded as the initiation toughness of crack propagation. So it is a criterion to assess quantitatively the toughness of one material.

2.6.3 Some current evaluation methods

In the latest paper of Xian-Kui Zhu and James A. Joyce from Battelle Memorial Institute, they made a systematic technical review of fracture toughness (G, K, *J*, CTOD, CTOA) testing and standardization [73]. In this section and based of this review, we will make a brief summary about the current evaluation methods for detecting the value of critical *J*-integral.

2.6.3.1 ASTM standard method

From the effort by many researchers and scientists worldwide for more than a half century, the ASTM fracture toughness test standards made a significant progress and grew step by step. The present versions of ASTM E399-09e2, E1820-11, E1921-11, and others have been developed and improved over the last several decades to provide consistent and economical procedures to measure estimates of fracture toughness designated as K_{1C}, K-R curve, J_{1C} and *J*-R curve etc. to meet the needs of practical engineering applications [116-136]. The mostly often used specimens in ASTM fracture test standards are C(T), SE(B) and M(T) specimens containing a through-thickness tensile crack, i.e., mode-Ⅰ crack. The mostly cited standard for the estimation of *J*-integral is E1820. While ASTM E399-09e2 and E1921-11 work well for brittle fracture situation which are not applicable for our case here.

We take single edge bend specimen for example to explain how the standard E1820 estimates the *J*-integral [137]. First of all, the total *J* will be separately calculated to elastic part and plastic part.

$$J = J_{el} + J_{pl} \tag{2-22}$$

Where:

J_{el} = elastic component of *J*, and

J_{pl} = plastic component of *J*.

The elastic part can be easily calculated by followed equation:

$$J_{el} = \frac{K^2}{E'} \tag{2-23}$$

in which:

K is the stress intensity factor, E' is equal to the elastic modulus E when plane stress and equal to $\frac{E}{1-\nu^2}$ when plane strain where ν is the Poisson ratio.

The plastic part is calculated:

$$J_{pl} = \frac{\eta_{pl} A_{pl}}{B_N b_0} \tag{2-24}$$

Where:
A_{pl} = area under force versus displacement records shown in Fig 2.37,

η_{pl} = 1.9 if the load-line displacement is used for A_{pl}, $= 3.785 - 3.101\frac{a_0}{W} + 2.018(\frac{a_0}{W})^2$ if the crack mouth opening displacement record is used for A_{pl} (if it is CT specimen, the expression of η_{pl} is different),

B_N = net specimen thickness (B_N = B if no side grooves are present), and

$b_0 = W - a_0$.

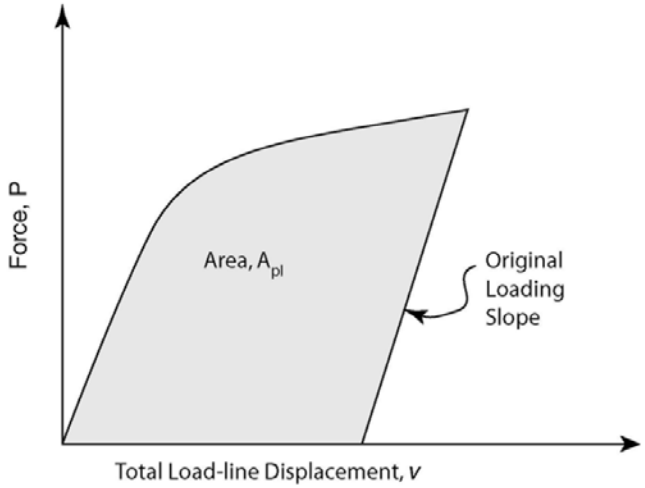

Fig. 2.37 Definition of area for J calculation using the basic method [139]

This method is widely used in all of the world and it can give the researchers a convince result, but unfortunately, it demands strictly the specimen structure and size, for example, $\frac{a_0}{W}$ is asked to be close to 0.5 and B_N is asked to be the same to or half of W. This geometry is very difficult for us to obtain an uniform phase field when there is phase transformation. Also, it only recommends the CT and SE(B) specimen but no SENT or other types of specimens.

Notice that this method was conducted using the 'maximum load'-based J_{1C} estimates, as done by Joyce [138] and Towers and Garwood [139]. Clearly, since the hardening masked crack initiation and growth in high strain hardening materials, the maximum load toughness did not give accurate J_{1C} results for these materials. On the other hands, it was required to determine J_{1C}, thus requiring the tests of plenty of specimens to obtain a resistance curve and then one material toughness value, this will definitely cost a lot [73].

2.6.3.2 EPRI solution

In the late 1970s and the early 1980s, Electric Power Research Institute (EPRI) in the United States sponsored a series of major projects for establishing a *J*-integral handbook. An engineering estimation scheme for elastic–plastic fracture analysis was thus developed, and the *J*-integral solutions for many specimens and simple geometries in plane stress and plane strain conditions were obtained by Kumar et al. [140] using finite element numerical calculations.

In this method, the SENP or SENT specimen was taken into account and the total *J* is also split to the elastic part and plastic part. The elastic part is the same as equation 2-23, and the plastic part is estimated by:

$$J_{pl} = \alpha\sigma_0\varepsilon_0 \cdot (W-a) \cdot \frac{a}{W} \cdot h_1 \cdot (\frac{P}{P0})^{n+1} \tag{2-25}$$

Where n and α are material constants defined by the pure stress-strain law, they can be very easily obtained by fitting the stress-strain curve according to the Ramberg-Osgood relation. σ_0 is the yield stress, ε_0 is the yield strain, h_1 is a function of a/W and n, it's value is given in Fig. 2.38 (for plane stress) and Fig. 2.39 (for plane strain) [107][140]. In these figures, the dimension b is the total width. P is the applied load per unit thickness, and:

$$P_0 = \dot{\psi} \cdot \eta \cdot (W - a) \cdot \sigma_0 \tag{2-26}$$

Where $\dot{\psi}$ = 1.072 for plane stress, $\dot{\psi}$ = 1.455 for plane strain, and:

$$\eta = \sqrt{1 + (\frac{a}{W-a})^2} - \frac{a}{W-a} \tag{2-27}$$

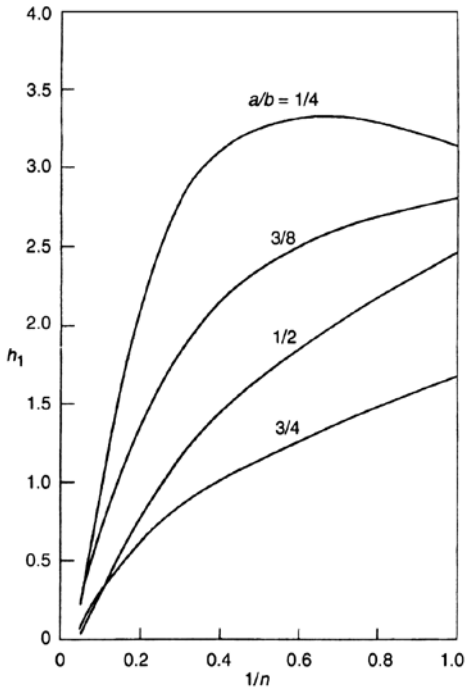

Fig. 2.38 h_1 versus 1/n for a SENT, plane stress

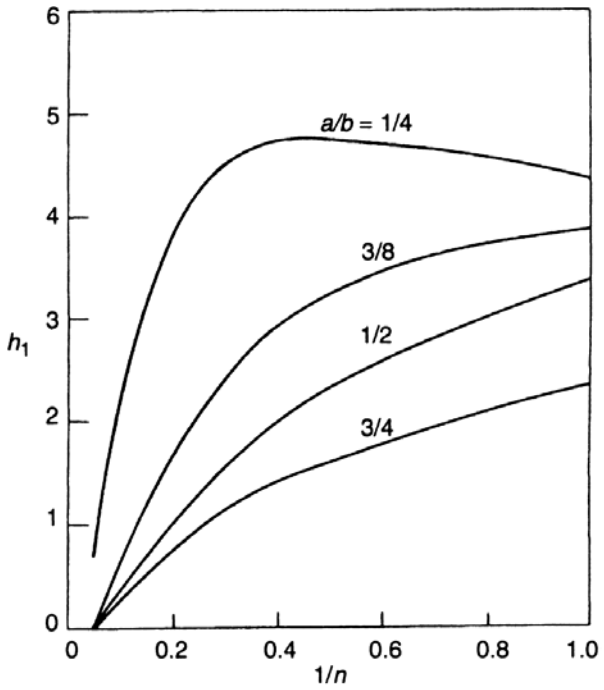

Fig. 2.39 h_1 versus 1/n for a SENT, plane strain

This method provided a solution of *J*-integral for many specimens and simple geometries such as SENT (SENP), CT, CCP, SENB, DECP and even cylinder pipes, it also made a good connection between the experimental result and finite element calculation.

But unfortunately, it only concerned the maximum hardening exponent n 20, and also if the material is nearly perfect plasticity, that is to say n is very big, equation 2-25 then has a very big error which cannot be accepted. Even for the material with a small value of hardening exponent n, this method still has a bad accuracy as it is always difficult to find a very accurate yield stress and this make the P_0 has a big error and further also the J_{pl}. Besides, not all stress-strain curves can be precisely approximated with the Ramberg-Osgood relation.

2.6.3.3 0.2 mm offset of J-Δa curve

As we emphasis the estimation of the critical J-integral but not the J-Δa curve or J-R curve, so we ignore the determination process of J-Δa curve here. The point is that when we have the J-Δa curve, how can we get the critical J-integral value? On the other hand, even the method we will mention is one partial content of the ASTM standard methods, but we still want to fetch it out as it is quite different to the ASTM E1820 method we have mentioned in 2.6.3.1.

From the J-Δa curve, ASTM E1820 adopts an engineering definition of J_{1C} at the intersection of a 0.2-mm offset construction line and the J–R curve, as shown in Fig. 2.40 [73]. This figure illustrates a typical construction procedure used to evaluate J_{1C}. At first, the J-R curve is defined as the test data in the region bounded by the coordinate axes and the J_{max} and Δa_{max} limits. To develop the construction lines, a blunting construction line is defined. Plot this blunting line, then draw an exclusion line parallel to the blunting line intersecting the abscissa at 0.15 mm. Draw a second exclusion line parallel to the blunting line intersecting the abscissa at 1.5 mm. Also draw a line parallel to the construction and exclusion lines at an offset value of 0.2 mm. The J-Δa data points that fall inside the region between the 0.15 mm and 1.5 mm exclusion lines are valid data that are used for fitting a power-law regression curve. The intersection of the power-law regression curve with the 0.2 mm offset line defines the provisional point-value J_Q that is subject to qualification criteria to see if it is an acceptable value. The basic one is to guarantee a sufficient specimen size: $B \geqslant 25 J_Q/\sigma_Y$, where σ_Y is the effective yield stress equal to the average of yield stress and tensile stress. If this qualification requirement and others defined in Section A9.8 of E1820 are met, the J_Q is J_{1C}.

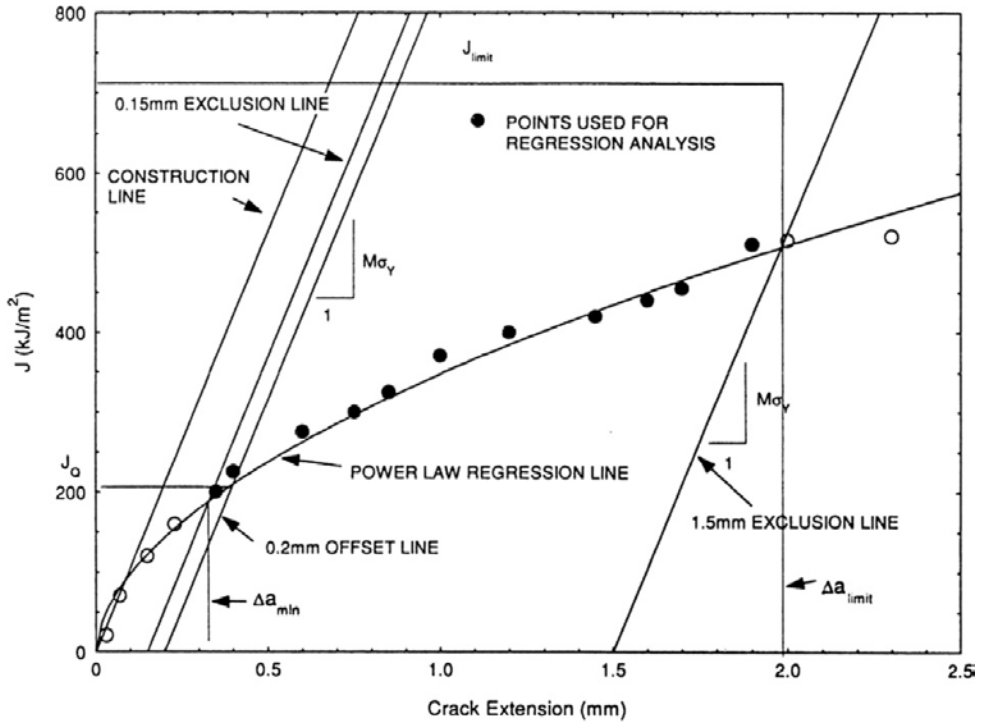

Fig.2.40 A typical *J*-Δa curve with test data points, construction lines and limitation bounds required [73]

This single specimen technique can also give us the estimation value of critical *J*-integral. But it implied two difficult questions. First, it didn't mention how to find the crack initiation moment and actually it is not easy. Second, it is not easy to find the accurate 0.2mm crack extension.

All above is the brief summary of the current methods to estimate the critical *J*-integral. Of course, there is surely other evaluation ways such as CTOD and CTOA methods, but we just introduce the most widely used ones. Details could be found in the reference [73]. All these methods have made a great contribution for the estimation of toughness parameters, while the work to improve test procedures has been a constant topic of interest, debate and incremental research is still on.

Chapter 3 A New Method of Toughness Evaluation

In this chapter, we will introduce one cost-save and effective method to estimate the critical *J*-integral with a sole Single Edge Notched Plate SENP (SENP) specimen. The Direct Current Potential Drop (DCPD) method is applied to obtain the initial fatigue crack length. DCPD is compared with Digital Image Correlation (DIC) at room temperature to evaluate the crack propagation initiation load. It is observed that slightly before the load drops, the crack starts to propagate. DIC will also help us to get the Boundary Conditions (BC) for Numerical Simulation in which the method G_theta will give us the critical *J*-integral.

3.1 A new method to evaluate the critical *J*-integral

We choose SENP specimen to do the fracture test. In the beginning, PD method is applied to control the fatigue crack fabrication. The fracture test will then be done on the pre-cracked SENP. The J_{1C} value is to chosen to be the *J* value when crack starts to propagate on the SENP specimen. The method is first tested at room temperature for which the material is more brittle. The global load displacement curve was correlated with the DIC measures which give the crack tip position, the image processing of the two faces of the specimen which are used to check the previous prediction and the PD method provides a third measure of the crack tip position. The comparison of these three measures permits to decide when the crack starts to propagate.

Meanwhile, the stress-strain curve is obtained by the round bar test. Notice that, the PD method will not be applicable when electrical induction coil is working, but the result of crack propagation initiation point we found in room temperature is applicable to other cases in high temperature. One observes at room temperature with those three means that the crack starts to propagate slightly before the maximum load.

The J_{1C} value then is extracted using a careful finite element analysis of the experiments. The finite element analysis was conducted as follows: DIC is used to define the real Boundary Conditions (BC) to be applied to the finite element model for the fracture test for the load level. The test has then been simulated by a refined finite element plane stress analysis, using the material properties extracted from the standard stress strain curve obtained at the corresponding thermal history. The load displacement curve predicted by FEM is compared to the experimental one to check the quality of the simulation as well as the adequate choice of

the stress strain curve. J_{1C} value is then extracted by the G_theta method using the elastoplastic evaluation of *J*. The original G_theta method provided in CAST3M couldn't be applied in our case, because the plastic zone was much larger than the region defined by the nine disks around the crack tip. Consequently we had to reprogram the G_theta method. Figure 3.1 is a sketch of the methodology.

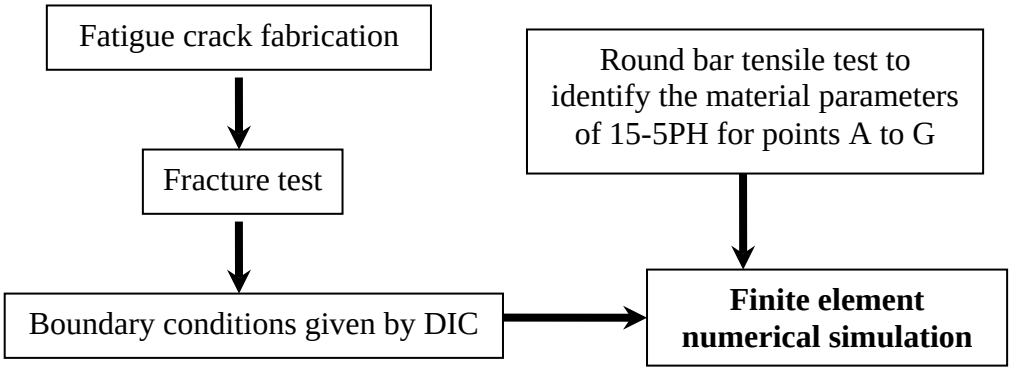

Fig. 3.1 The methodology to get J_{1C} from experiments

3.2 An example to obtain the J_{1C} value

In this section, we will introduce our method to evaluate the critical *J*-integral and illustrate with an example. In our study, all the fracture samples are designed as followed Figure 3.2 shows, the thickness is only 2 mm and the pre-crack length is 1.5mm or 2.5mm. The available supplied material (cylindrical bar of 25 mm diameter) imposed a size of the specimens, which is small. The benefits of this geometry are to provide cheap specimens, which are also easy to control on temperature. Associated with electrical induction heating, the rates of heating and cooling are higher than what you can impose in a furnace and so, much more representative of welding processes. On the other hand, the surface of gripping is small and the gradient of temperature along the axis of the specimen (far from the crack) does not allow imposing perfect boundary conditions. The two big holes of the SENP specimen are used to fix the sample, and the two small holes permit to input the current and produce a controlled fatigue crack using Potential Drop (PD) technology which is showed in Fig. 3.2. The notch has been enlarged in the Figure 3.2 and precisely defined in Detail B. The initial fatigue crack length is measured by the PD method using Johnson's formula [23] coupled with optical microscope and DIC (see annexe 2). Let’s also note that the crack length (around 2 mm) is large compared to the size of the microstructure (approx. 0.02 mm).

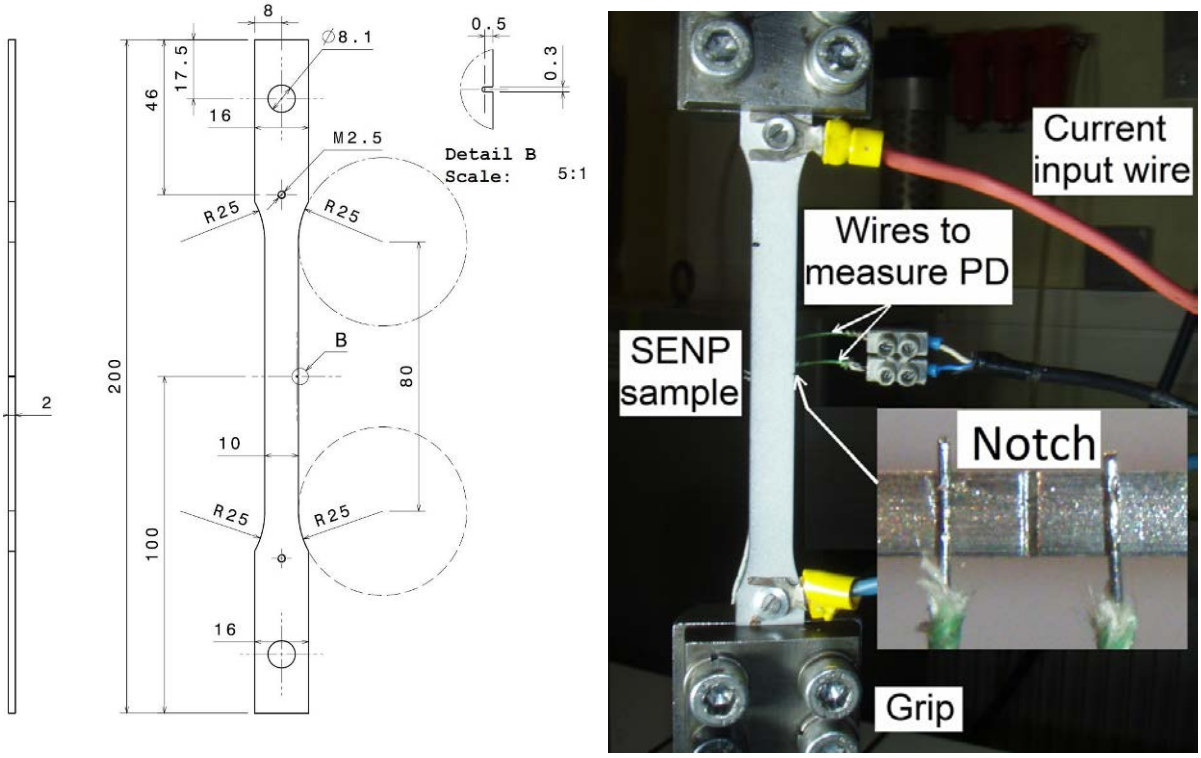

Fig. 3.2 Fracture test SENP specimen (left) and fatigue test set-up (right) in our investigation

This example is implemented on the 16MND5 low carbon steel at room temperature with a pre-crack length 2.5mm. When the fatigue crack (pre-crack) is produced, we will clean the pre-cracked SENP specimen and then do the painting on two faces in the central part. If the maximum temperature of later heat treatment is very high, it needs special paint which can stick to the face even the sample will be under tension after or during the heat treatment. The fracture test will be done by a displacement velocity (0.5mm/minute) until the crack propagates to the moment when final ligament is nearly half of the width. During the fracture test, Loading Line Displacement (LLD) and force together with potential drop will be acquired. The acquisition frequency is 10 points per second. The loading was released at the end of the fracture test when the crack has propagated a certain length. During the fracture test, PD was recorded and a series of photos have been taken (5 photos every 2 seconds) by a CCD (Charge Coupled Device) camera that can provide us the 1024 pixel × 1024 pixel photos.

Certainly it is impossible to process all the data we acquired. Frankly, we fetch some points from the beginning of the fracture test to the one the crack has propagated a lot. During elastic part, we fetch one point every 10 seconds, when there is the plastic strain, more and more points are selected around the maximum fracture force. At last, the density of points is decreased. Just as the following Fig. 3.3 shows, based on the selected experimental points and photos, we plot the curve of force versus displacement and the curve of PD versus

displacement. It is the fracture test result plotted versus time, blue curve denotes the force, pink curve is the measured potential drop which contains all the aspects induced PD such as change of y and width W in figure 2.3, also massive plastic strain etc. The green curve is the corrected PD curve which has taken the change of y into account (as proposed by Johnson [23]). The actual and real time value of y was obtained from DIC.

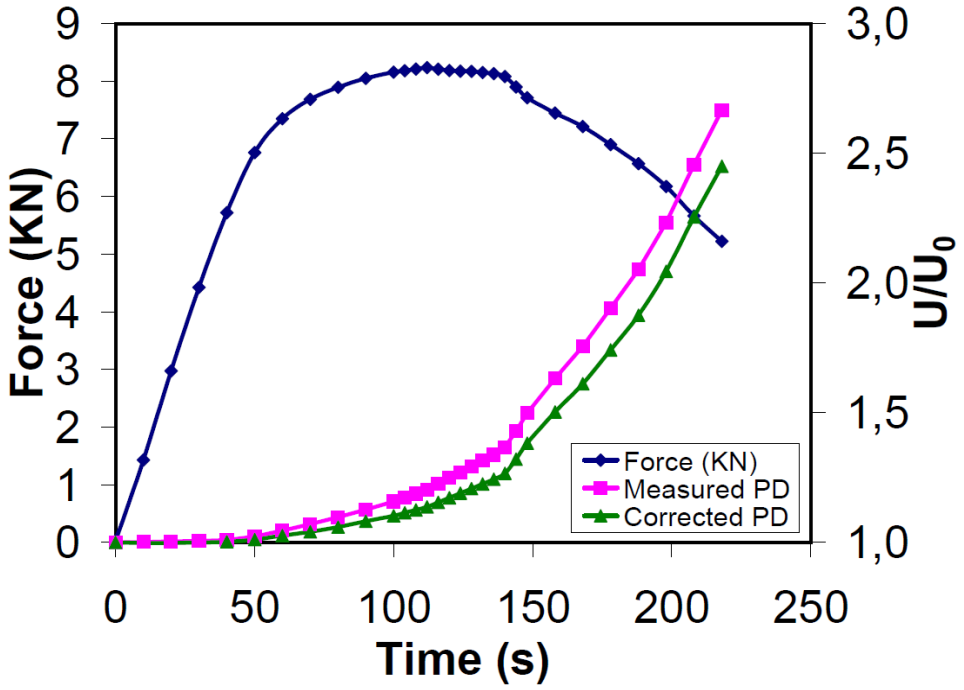

Fig. 3.3 Fracture test and potential drop acquisition

PD method is not applied widely to deduce the crack propagation length especially when the specimen has huge plasticity, but this method can tell the critical moment when the crack propagates by searching the mutational point of the slope of the potential drop curve.

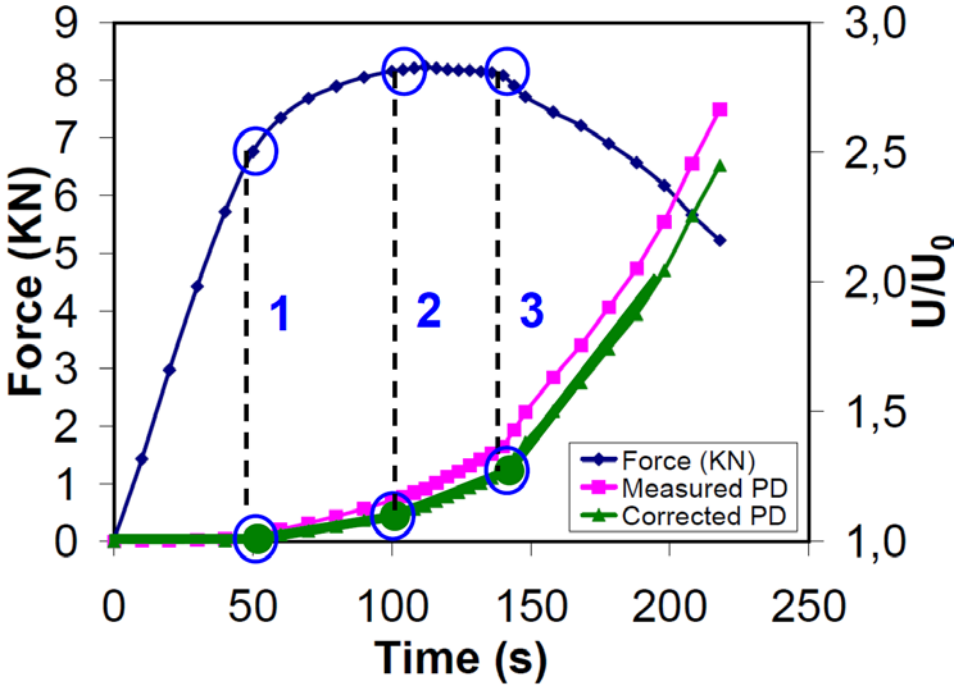

Fig. 3.4 Three mutational points on the potential drop curve

Figure 3.4 and 3.5 show that there are three significant critical points on the green curve. The first is at 50 second, it compares to the end of the elastic strain. Second critical point is around 100 second which is associated with the change of y value due to plasticity at crack tip or crack propagation initiation. These two points correspond very well with the blue load-time curve. The last critical point is at 140 second. It can be explained by two reasons. First, the crack starts to propagate. Second, the crack propagation rate suddenly increases. We then use DIC to better understand the load-displacement curve.

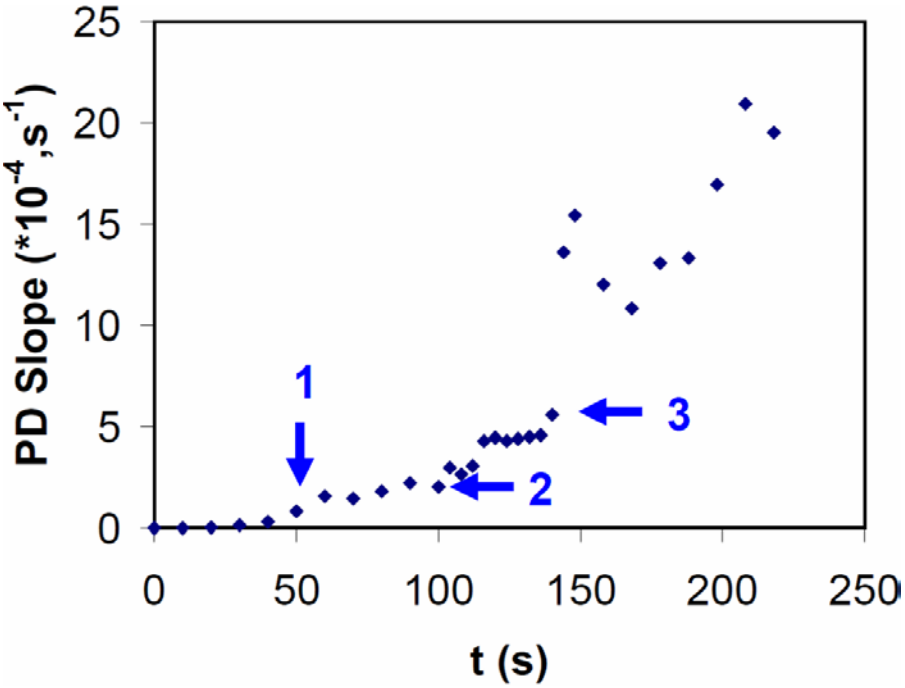

Fig. 3.5 Slope of the three mutational points on the potential drop curve

We choose a series of pictures from the beginning of the fracture test to the one where we are pretty sure that the crack has propagated. All the times of the pictures are consistent with the times of points from potential drop curves. One Zone Of Interested (ZOI) named E-PE-PF-F will be selected on every picture. Fig. 3.6 (a) is the initial picture of the fracture test, whereas (b) denotes the ZOI chosen.

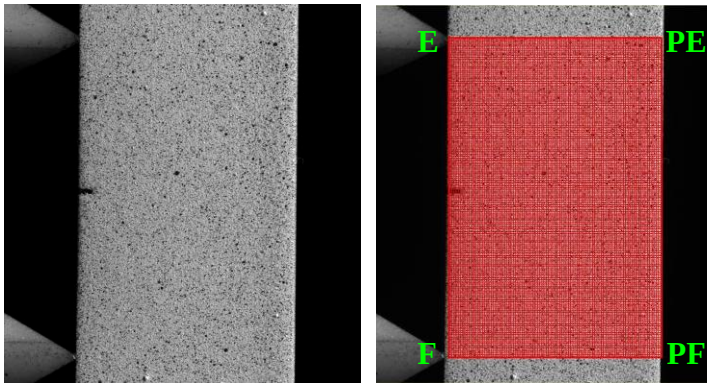

(a) (b)

Fig. 3.6 Initial photo and ZOI during DIC process

The software Icasoft can process and give us the displacement and local strain field of the entire series of pictures. Fig. 3.7 shows us the Green Lagrange strain field from the beginning of the fracture test until the point where the crack is surly propagating. The 28 pictures are the deformed ones, the initial picture is shown in figure 3.6. The time of every picture in figure

3.7 is marked below the picture and respectively related to the points at figure 3.5. We can see that the time difference between every selected picture around the maximum force point in figure 3.7 is 4 seconds. Note that the maximum force point in figure 3.4 is at 112 seconds. The red rectangle in figure 3.7 is the original selected ZOI for our reference. We can connect every picture's information with the mechanical information expressed in Fig. 3.3.

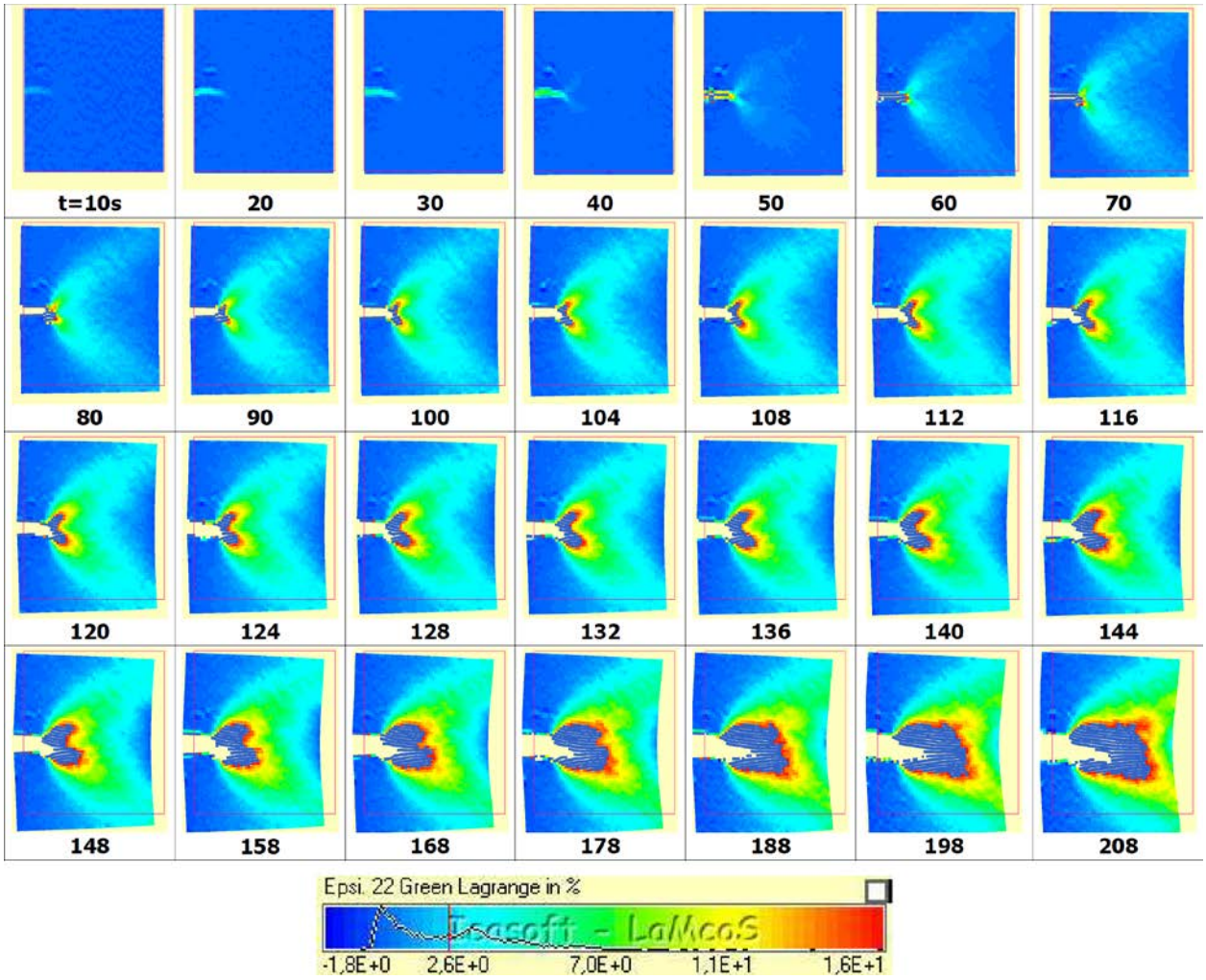

Fig. 3.7 The Green Lagrange strain field of one of our fracture tests given by DIC at room temperature

From figure 3.7, we can find from the first four deformed pictures that the axial strain is small. On the picture taken at time t=50s (which is related to the first mutational point in figure 3.4 or 3.5), there is visible butterfly strain field around the crack tip. While the picture at the third mutational point (140 seconds) shows that the crack has clearly propagated. The picture taken at time t=100s related to the second mutational point in figure 3.5 shows that crack start to propagate. Before this critical picture, we observe that the large strain zone becomes larger and larger, the crack mouth displacement becomes bigger and bigger, while there is no significant crack propagation. After this critical picture, the crack already grows significantly

and the butterfly has been entirely broken. On this critical picture at 100 seconds, we can see that the mesh around the crack tip is being teared but hasn't been yet broken, while it is broken by the lower crack tip in the next picture. From these observations we deduce that the second mutated point at 100 seconds is the critical time when crack starts to propagate. The shorter is the time between these pictures, the better DIC accuracy is.

By comparison the result given by DIC in figure 3.7 with the result from PD from figure 3.3 to 3.5, we can fix the critical moment. It is slightly before the maximum force. Note that this critical moment could be different for different materials. Once we know when the crack starts to grow, we can fetch the displacement field and boundary conditions from the initial picture to the critical picture by DIC again.

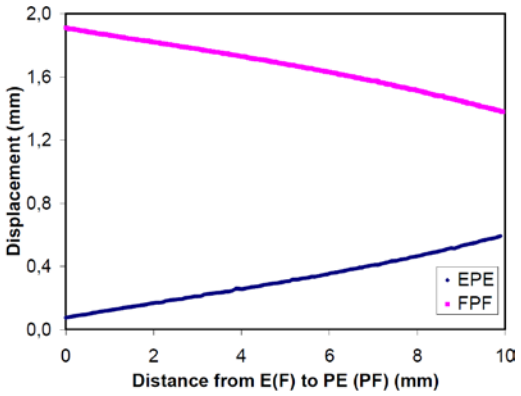

(a) Vertical displacement at critical moment along the boundaries E-PE and F-PF given by DIC

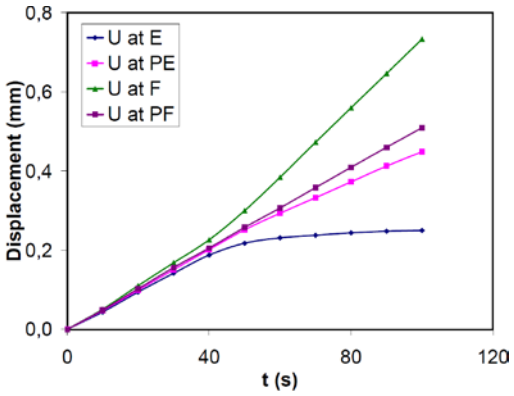

(b) Vertical displacement evolution for points E PE F and PF obtained from DIC

Fig. 3.8 Vertical displacements obtained from DIC, material is 16MND5 at room temperature, loading rate is 0.5mm/minute, pre-crack length is 2.5mm

As Fig. 3.8 shows the boundary conditions given by our method for 16MND5 material at room temperature (pre-crack length is 2.5mm). Figure 3.8 (a) shows that the displacement at critical moment along the segment E-PE or F-PF is almost a straight line, and the displacement at the four points E, PE, F and PF of ZOI is different at every moment before the crack propagation during the fracture test.

Now with the basic stress-strain curve of this specimen and the boundary conditions provided in Fig. 3.8, we can estimate the critical *J*-integral by finite element simulation. Elastoplastic plane stress analysis with large strain was performed using CAST3M [141-143] finite element software in order to evaluate J_{1C}. A special attention is taken to build an appropriate mesh. It consists of a circular part of 10 layers of elements around crack tip. Quadratic 6 and 8 nodes

finite elements in plane stresses are used elsewhere. Top and bottom sides are described by 10 elements as we can see in figure 3.9 where the mesh has 1358 elements.

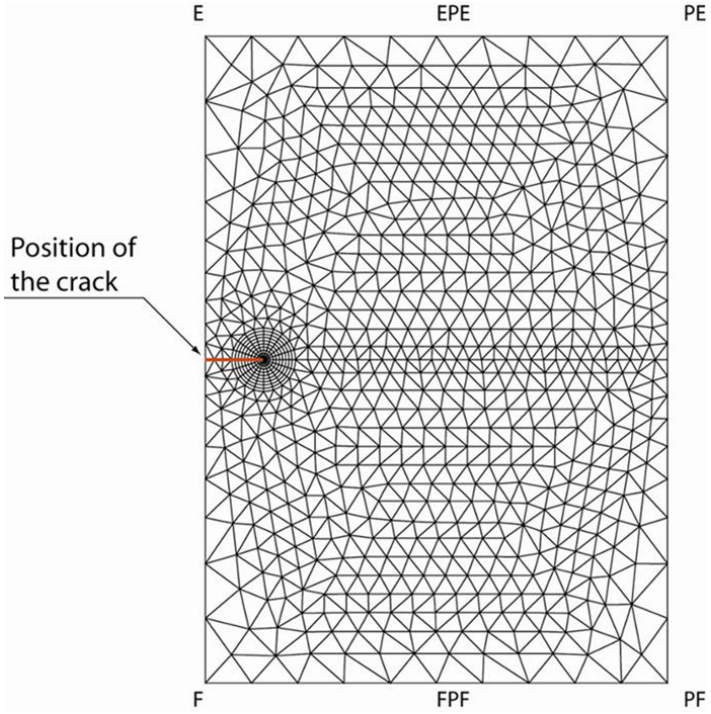

Fig. 3.9 Mesh constructed in CAST3M for our finite element simulations

The size of the simulated zone is 15 mm height per 10 mm width which is exactly the same to the ZOI in DIC processing. The material is considered to be elastoplastic with isotropic hardening. Translations and rotations are extracted from the experimental measured displacements histories of lines E-PE and F-PF in Fig. 3.8 and applied to the finite element points E, PE, F and PF.

Figure 3.10 shows the simulation result of displacement and accumulated plastic strain field. (a) displays the Uy displacement which is just in the same direction to the loading, (b) presents the accumulated plastic strain around the crack tip. Figure 3.11 compares the simulation result of force vs. mean displacement between two top segments of the ZOI with the experimental result for our example. The agreement is very good which confirms the quality of the numerical simulation and validates the methodology as well as stress strain characterization.

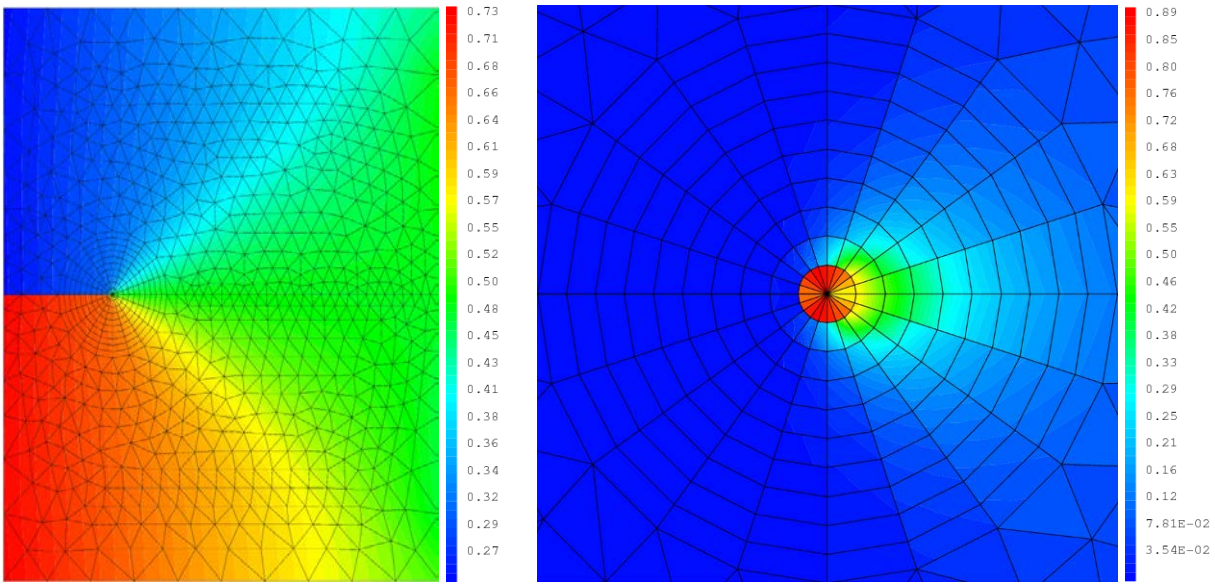

(a) (b)

Fig. 3.10 Simulation result, (a) is Uy displacement field (unit: mm), (b) is the accumulated plastic strain around crack tip

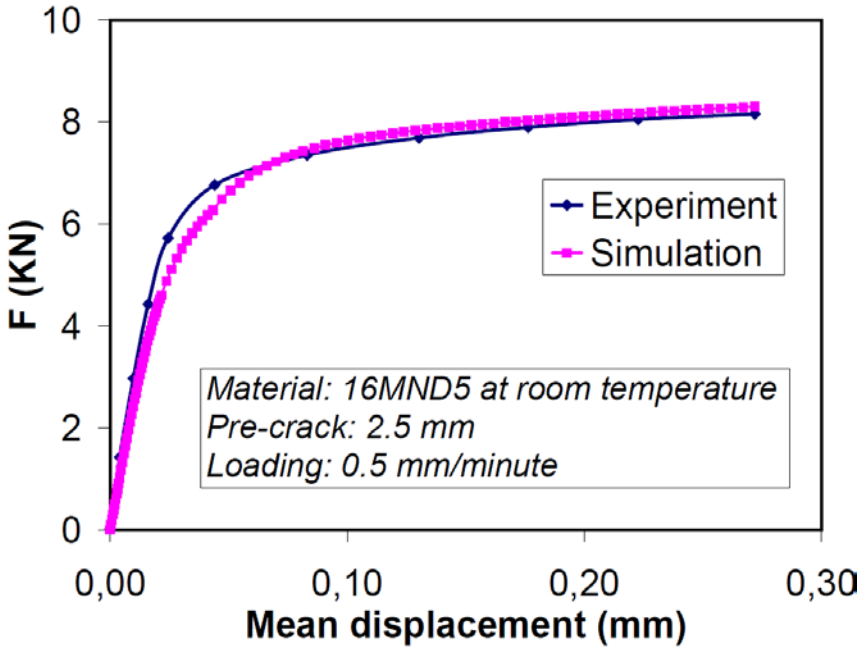

Fig. 3.11 Simulated force versus mean displacement between E-PE and F-PF

After the simulation, J_{1C} is extracted using the modified G-theta method [144][145], which permits to compute the energy release rate for elasto-plastic radial loading. As we know, the original G-theta method in CAST3M works well for J_{1C} evaluation when there is no plastic strain or when plastic zone is confined into the inner domain. When the plastic zone is larger than the nine disks, the J_{1C} estimated by the CAST3M G-theta method is no longer valid because it is no longer path independent.

Hence, for our elastic-plastic fracture mechanics situation, we have to reprogram the original CAST3M G-theta method. We change the integration path to a large domain shown in figure 3.12. Second, we calculate the strain energy density or work by the actual strain in the integration domain which is shown in Eq. (3-1).

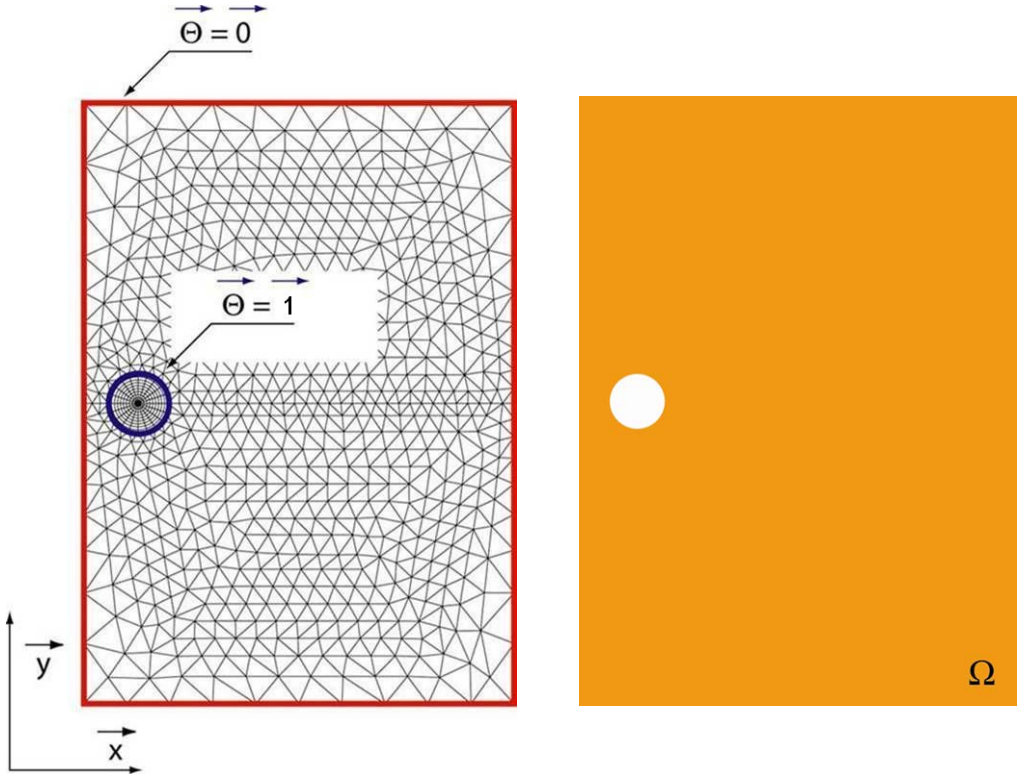

(a) (b)

Fig. 3.12 Integration domain of modified G-theta method, (a) is the G-theta field on the boundary and (b) is the integration domain.

$$J = \int_{\Omega} \sigma_{ij} U_{i,k} \Theta_{k,j} dS - \int_{\Omega} W.\Theta_{p,p} dS \tag{3-1}$$

In equation 3-1,

$\underline{\underline{\sigma}}, \vec{U}$: are solutions of the mechanical problem with true boundary conditions,

and the theta components:

$$\Theta_{k,j} = \frac{\partial \Theta_k}{\partial x_j} \tag{3-2}$$

$$\Theta_{p,p} = \sum_{p} \frac{\partial \Theta_p}{\partial x_p} = \Theta_{1,1} + \Theta_{2,2} \tag{3-3}$$

and,

$$\sigma_{ij}U_{i,k}\Theta_{k,j} = \begin{matrix} \sigma_{11}\left[U_{1,1}\Theta_{1,1}+U_{1,2}\Theta_{2,1}\right]+ \\ \sigma_{12}\left[U_{1,1}\Theta_{1,2}+U_{1,2}\Theta_{2,2}\right]+ \\ \sigma_{12}\left[U_{2,1}\Theta_{1,1}+U_{2,2}\Theta_{2,1}\right]+ \\ \sigma_{22}\left[U_{2,1}\Theta_{1,2}+U_{2,2}\Theta_{2,2}\right] \end{matrix} \tag{3-4}$$

While W is the strain energy density:

$$W = \int_0^{\underline{\underline{\varepsilon}}} \underline{\underline{\sigma}} : d\underline{\underline{\varepsilon}} \tag{3-5}$$

It is practically calculated incrementally by:

$$W \cong \sum_{i=1}^{n}\left(\frac{\sigma_{i-1}+\sigma_i}{2}\right)\times\left(\varepsilon_i-\varepsilon_{i-1}\right) \tag{3-6}$$

dS is a surface element and equal to $dS = dx\cdot dy$.

Equation 3-1 in a compact writing is:

$$J = \int_\Omega \underline{\underline{\sigma}} : \underline{\underline{\underline{\underline{grad}}}}\left(\vec{U}\right).\underline{\underline{\underline{\underline{grad}}}}\left(\vec{\theta}\right)dS - \int_\Omega W.div\left(\vec{\theta}\right)dS \tag{3-6}$$

With this G_theta method, we can numerically evaluate the critical *J*-integral value. Annexe (5) gives the "Gibiane" program of this method. Now we show the verification of path independence of *J*-integral obtained by this method. We highlighted three paths in figure 3.13 where blue one is contour 1, green one is contour 2 and red one is contour 3.

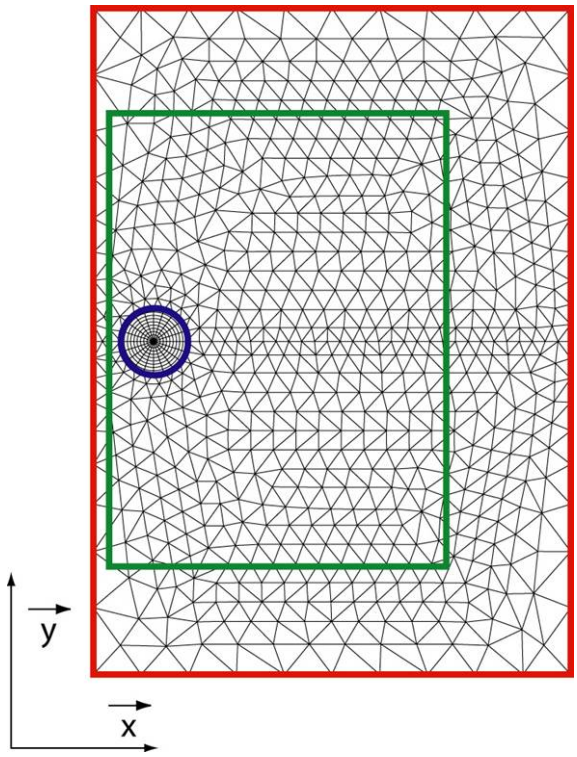

Fig. 3.13 Verification of path independent of J_{1C} obtained by modified G-theta method

We can see in two figures 3.14 and 3.15, the result of J_{1C} obtained by our G-theta method is good and path independent.

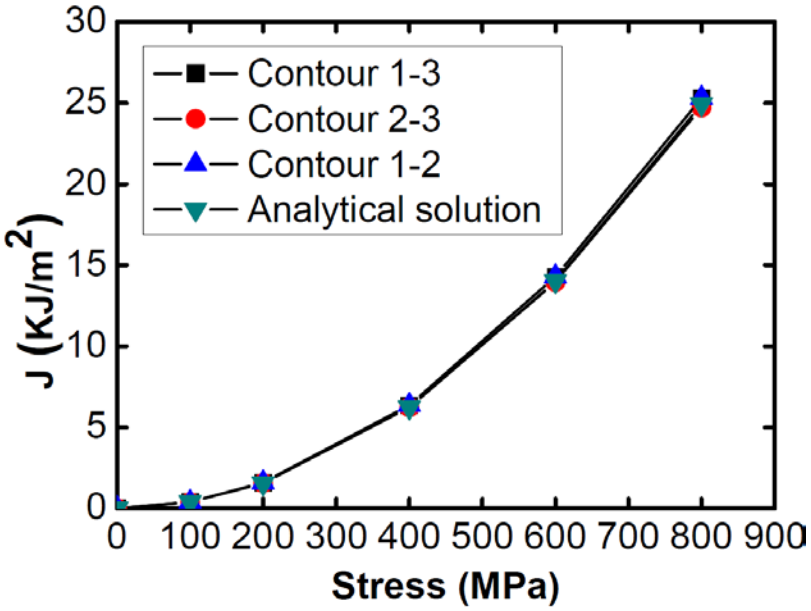

Fig. 3.14 *J* obtained by modified G-theta method for elastic situation

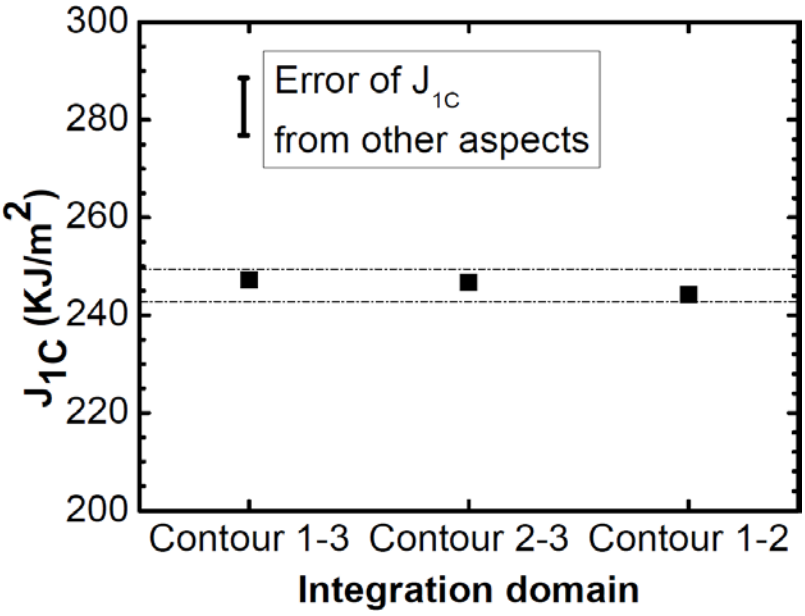

Fig. 3.15 J_{1C} obtained by modified G-theta method for plastic situation (Material: as received 16MND5 low carbon steel)

In figure 3.14, the analytical solution is calculated by equation (3-7):

$$J = \frac{K^2}{E} = \frac{\left(\varphi\sigma\sqrt{\pi a}\right)^2}{E} \tag{3-7}$$

In which, the geometrical coefficient φ is given by equation (3-8) [107].

$$\varphi = \sec\beta \cdot \sqrt{\frac{\tan\beta}{\beta}} \cdot [0.752+2.02 \cdot \frac{a}{W} + 0.37\ (1-\sin\beta)^3] \tag{3-8}$$

and

$$\beta = \frac{\pi a}{2W} \tag{3-9}$$

Results from figure 3.14 and 3.15 are from the as received material 16MND5 whose geometrical data can be found in figure 3.2 and pre-crack length is 1.5mm. Hence the geometrical coefficient φ calculated by equation (3-8) is 1.268.

The method has also been successfully compared with the basic G_theta produce of CAST3M with a small plastic zone.

All above is an example to show how our method to estimate the critical *J*-integral coupled the DIC/PD technology and FEA. With this method, we can now investigate the effects of phase transformation on *J*-integral based fracture toughness of material 15-5PH and 16MND5.

3.3 Some comments on our J_{1C} estimation method

Those experimental approaches we mentioned in section 2.6.3 impose to have specified specimen geometries and most of them are associated with rather expensive experiments. Moreover all these experimental methods can't be applied to the determination of J_{1C} in case of phase transformations situations, because one cannot ensure, with thick specimens that the temperature fields around the crack tip region within the specimen is uniform. This implies that one do not know what is the material state within the specimen and along the crack front without making complex 3D computations, which is heavy and debatable if not compared with ad hoc measures. Besides, the EPRI method has a big error when the material hardening exponent is big and when the yield stress is not evaluated precisely (see the exponential equation 2.26).

It was then decided to use our non conventional method to extract the J_{1C} value. The J_{1C} value is determined on the base of observation of crack propagation on thin cracked plane specimen. We applied the thin and small Single Edge Notched Plate (SENP) as our fracture samples. Later after the fracture test, the J_{1C} value is extracted using a careful finite element analysis of the experiments. One could argue that this finite element computation can be avoided because DIC contains all the information. This is an interesting and efficient processing of the results but, in case of elastoplastic response, this method relies on the input of a stress strain law. It has been measured in our case and hence a purely experimental method could be directly applied. The interest of the chosen method is to cross check the use of the bar specimen stress law choice for the cracked plate specimen response, the quality of the choice of the stress strain curve is checked by the quality of the global force displacement law.

Another point is that the pre-crack length is too short to get a comparable and reference critical *J*-integral value as there is the effects of crack-tip constraint on that fracture toughness parameter. And some standards demand the pre-crack length should be more or less 1/2 of the width of the fracture sample (see figure 3.16).

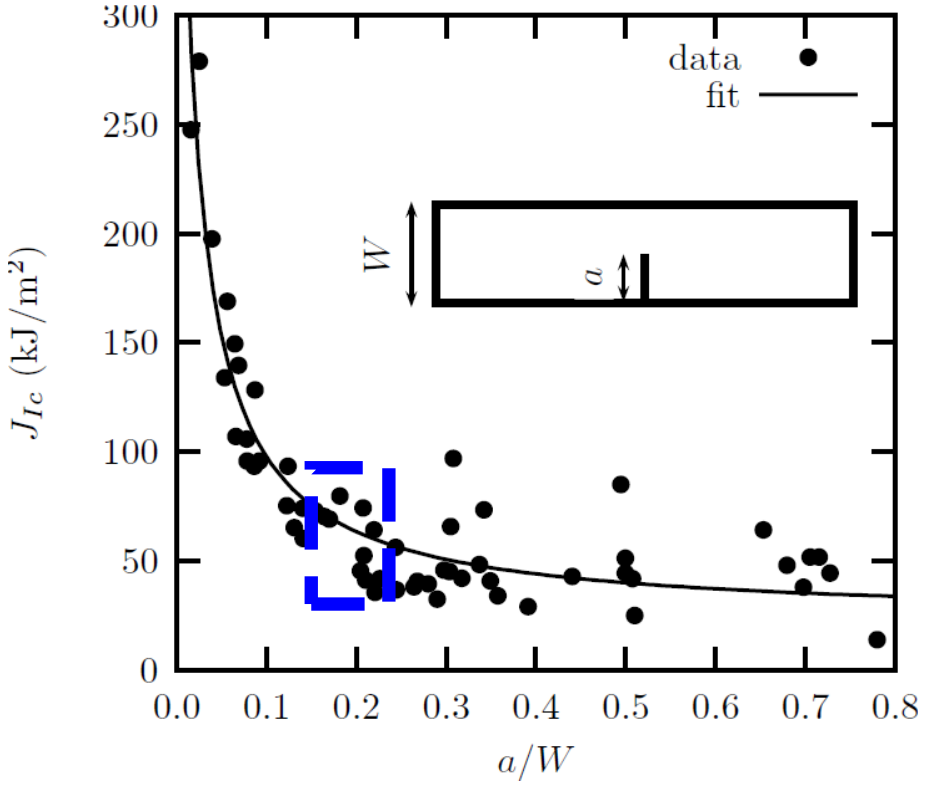

Fig. 3.16 Relation between J_{1C} with the pre-crack length [146]

In our case here, the pre-crack length is 1.5mm or 2.5mm which means the value of a/W is 0.15 or 0.25, the blue rectangle in figure 3.16 is the area of our a/W. We can see that there is no big error induced by the non-standard pre-crack length compared to the value from the standard a/W=0.5. let's step one foot back, our investigation purpose is to look for the effect of phase transformation on the critical *J*-integral based fracture toughness, so we applied same specimen with same pre-crack length and same geometry, that means, for our study purpose, the J_{1C} valued estimated by our method is comparable and enough to find the answer to our thesis.

This method was then used to get the J_{1C} at room temperature. The value we obtained has been compared with others from some literatures [147-152]. The critical *J*-integral was converted to critical stress intensity factor by the equation (3-7).

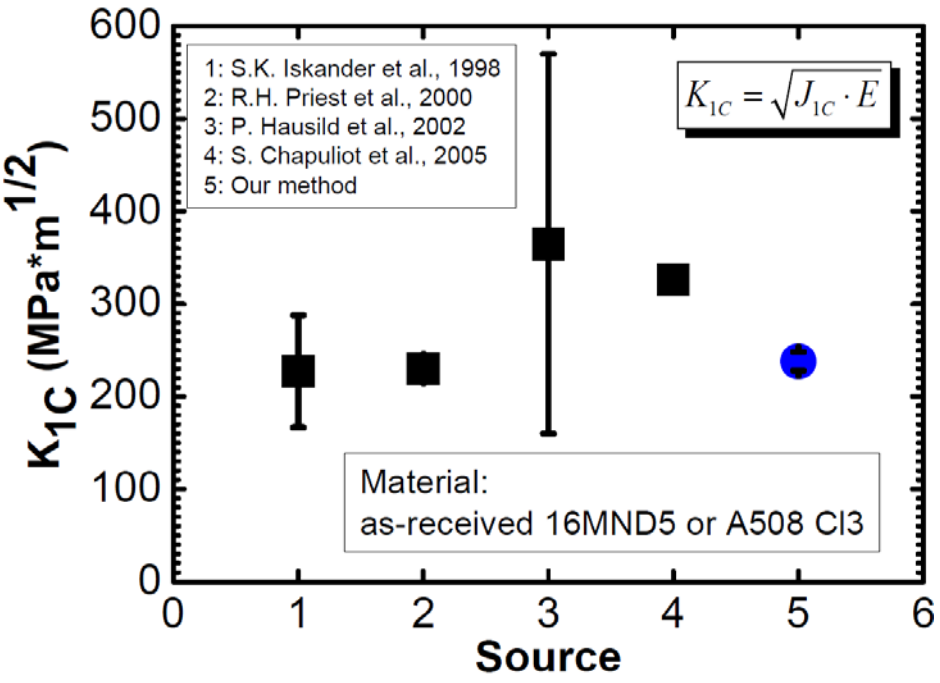

Fig. 3.17 Comparison of stress intensity factors from different sources [147-152]

In 3.17, the four black squares are the values from others, our value is the blue cycle point. We observe the results are consistent. Another aspect is that the error of our method is rather small.

Chapter 4 Effect of Martensitic Transformation on 15-5PH Fracture Toughness

In this chapter, we applied our method for the estimation of fracture toughness for 15-5PH stainless steel after different kind of heat treatments. When we get the critical *J*-integral values, we will discuss the influences of phase transformation on material fracture toughness together with the investigation of fractography and metallography.

4.1 Specimens

There are two kinds of specimens for 15-5PH, one is the SENP for fracture test and it has been shown in Fig. 3.2, another one is the round bar sample for the tensile test which is shown in Fig. 4.1.

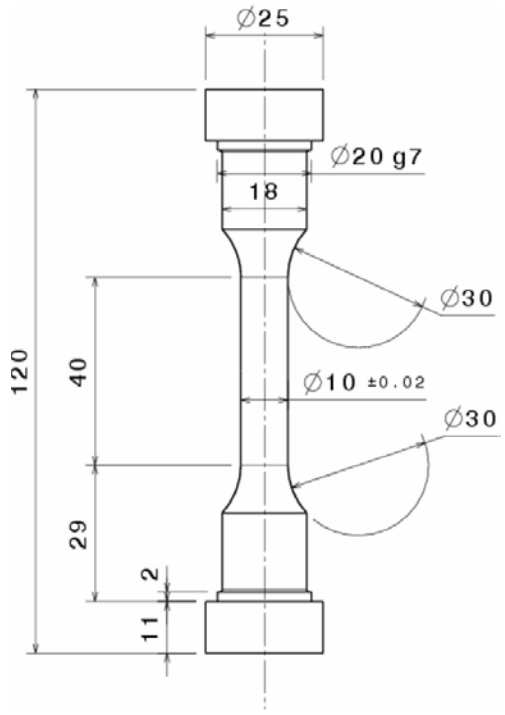

Fig. 4.1 15-5PH round bar sample for tensile tests

4.2 Experimental apparatus

Two servo-electro-hydraulic tension-compression machines are applied for the mechanical experiments. One with maximum capacity of 10KN is used for the fatigue test, another one with maximum 250KN is used for the fracture test and round bar tensile test. Type K thermal couples are connected to a converter TEPI (model BEP304) for signal amplification and conversion. The force, strain, displacement and temperature signals are collected by a digital

acquisition system with an acquisition rate of 10 Hz. The strains on the round bar specimen are measured by an extensometer (stick distance 15mm, see figure 4.2). Heating is generated by electromagnetic induction, and power is supplied by a 6KW generator (See figure 4.3). The automated configuration includes the controller, a PC, and the system software bundle. For DIC, two 4 Mpx cameras were placed in front of each face of the specimen to record digital images of the two sample surfaces (5 pictures every 2 seconds, see figure 4.4).

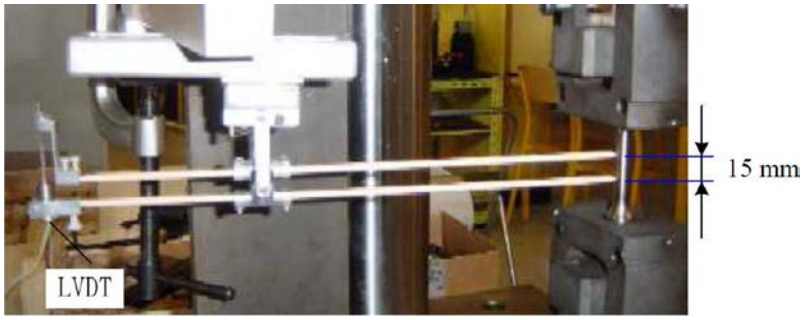

Fig. 4.2 Extensometer with 15mm distance between two sticks

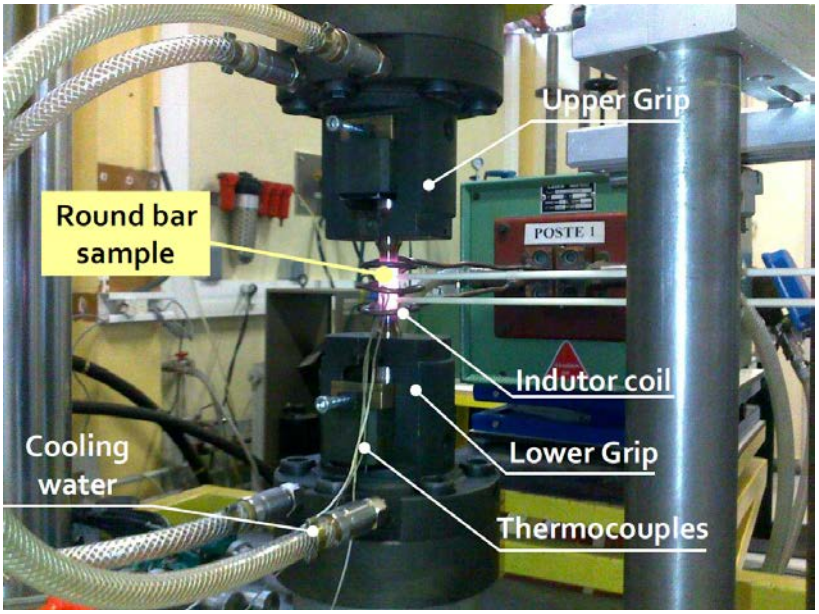

Fig. 4.3 Setup of devices for round bar tensile test

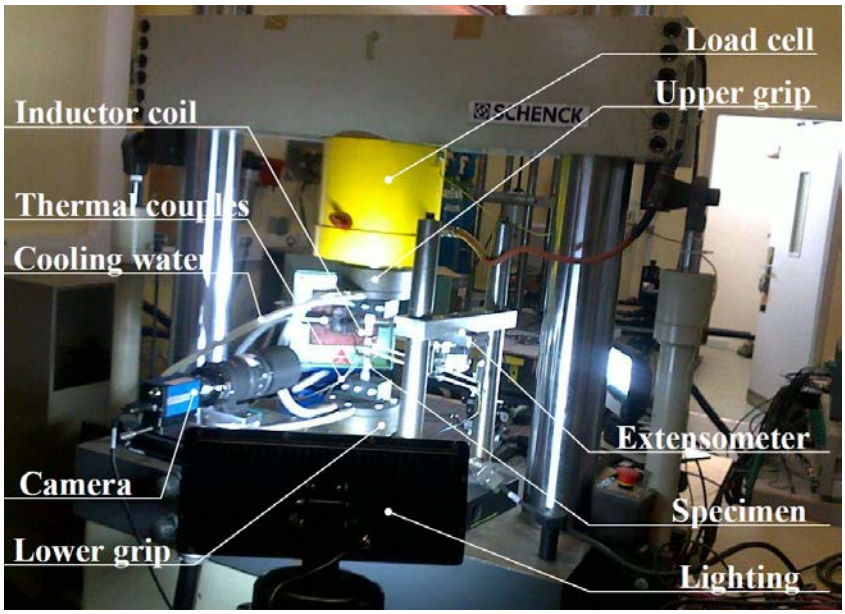

Fig. 4.4 Setup of devices for fracture test

Figure 4.5 is the schematic of the set-up of thermocouples welded on the specimen and the position of the electro-magnetic induction coil for tensile test or fracture test. Three thermocouples were used to record the temperature field (error: ±5°C). For the tensile test, the centre thermocouple is in the center of the specimen. For the fracture test, the centre thermocouple is in the same horizontal line with the pre-crack. Another two thermocouples are symmetrically welded in the two sides of the central thermocouple, the distance between each thermocouple is around 7.5mm.

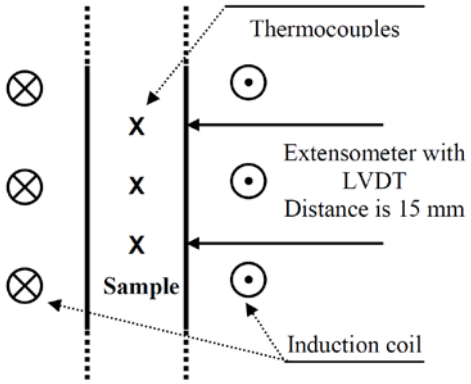

Fig. 4.5 Position of thermocouples and induction coil devices for mechanical tests

Figure 4.6 shows the central part of the SENP specimen for fracture test in the set-up shown in figure 4.4, the left one of figure 4.6 is one side surface of the fracture specimen, right one is another side.

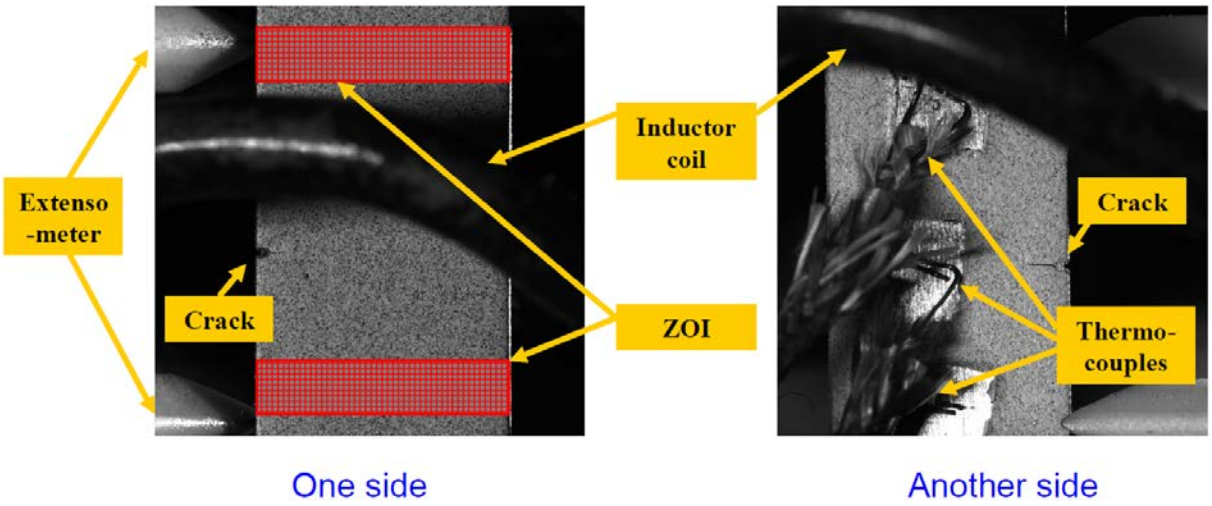

Fig. 4.6 Central part of the specimen for fracture test in the set-up, left one is one side of the specimen, right one is another side

4.3 Experimental results

4.3.1 Tensile tests results

The tensile tests were done by a displacement rate of 0.5mm/min. As we already described in figure 2.14 at section 2.4.3, we did the tensile tests after different heat histories marked from point A to G. Figure 4.7 shows the engineering stress-strain curves of 15-5PH after different heat treatment histories.

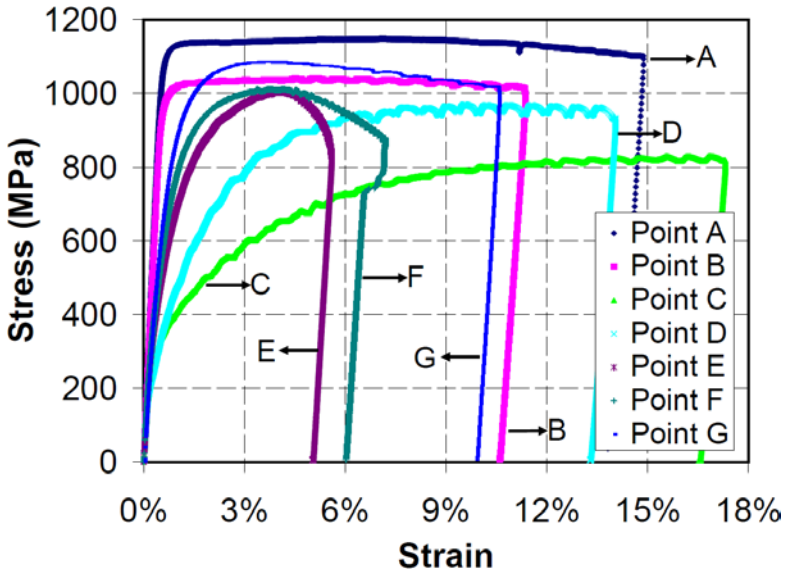

Fig. 4.7 Stress-strain curves of 15-5PH after different heat treatment history

One may observe that the ultimate stress at point G is smaller than original material which is point A. Comparing curves for point B and C, the pure austenite at 200°C (point C) is more

ductile but lower strength than pure martensite (point B) at the same temperature. For point D, E and F, as more austenite is transformed to martensite and temperature is decreasing, the material has a higher strength. The difference between points A, B and the rest of the experiments (C to G) is that A and B have a nearly "perfect plasticity" behaviour type while the other fives show much more hardening. We made a summary of the tensile test results of 15-5PH at different cases in the following table 4.1.

Table. 4.1 Tensile test result of 15-5PH at every experimental point

Experiment point	Yield stress (Mpa)	Yield strain	Ultimate stress (Mpa)	Ultimate strain	Hardening exponent n	Material constant α′
A	899	0,44%	1148	7,07%	29,97	0,0014
B	827	0,44%	1041	5,05%	29,37	0,0028
C	174	0,11%	829	15,57%	3,89	0,1637
D	143	0,10%	969	9,55%	3,00	0,1671
E	208	0,14%	1006	4,28%	3,62	0,0578
F	245	0,16%	1012	3,71%	4,16	0,0291
G	302	0,19%	1085	3,72%	4,69	0,0196

4.3.2 Fatigue crack fabrication

For each testing conditions (points A to G) at least two samples with different pre-crack length were produced. We make use of a sine loading to fabricate a fatigue crack, the maximum loading is calculated by equation (4-1), the minimum loading is 1/10 of the maximum, and the frequency of the sinus loading is 20HZ. In equation (4-1), σ_y is yield stress of 15-5PH, a is the crack length and actually is equal to the size of notch, W and B are the width and thickness separately of the SENP.

$$F_{\max} = 0.6\sigma_y \cdot (W - a) \cdot B \tag{4-1}$$

Johnson's formula [23] in equation (2-9) was applied to control the fatigue crack fabrication as we expected to produce a 2.5mm pre-crack. Here a_0 is the notch size, $U_{(a_0)}$ is the original potential before the fatigue test while $U_{(a)}$ is the potential during the fatigue test. y is the distance between two wires for measuring the PD in figure 2(b). Johnson's formula, DIC, and optical microscope observation after later broken by fracture test were used to get the mean value of fatigue crack length a.

Finally all the SENP samples are given in table 4.2.

Table. 4.2 Fracture test results of 15-5PH

Experimental Point	Temperature [°C]	Sample	Fatigue initial crack length [a ,mm]	Maximum force of the fracture test [KN]
A	20	A1	1.654	18.87
		A2	2.060	18.51
B	200	B1	1.579	16.78
		B2	1.264	16.73
C	200	C1	1.587	11.85
		C2	2.504	10.47
D	170	D1	1.557	13.83
		D2	2.486	11.67
E	140	E1	1.566	15.12
		E2	1.249	16.33
F	110	F1	1.693	15.54
		F2	1.265	16.93
G	20	G1	1.571	16.99
		G2	1.260	17.41

4.3.3 Fracture tests results

The fracture tests were also done by a displacement rate 0.5mm/min on pre-cracked SENP samples. Force vs. global displacement curves of the specimens which have the similar initial crack length are plotted in the figure 4.8. The abscissa and ordinate values are given by the electro-mechanical testing machine. Maximum forces of every fracture test have been shown in table 4.2.

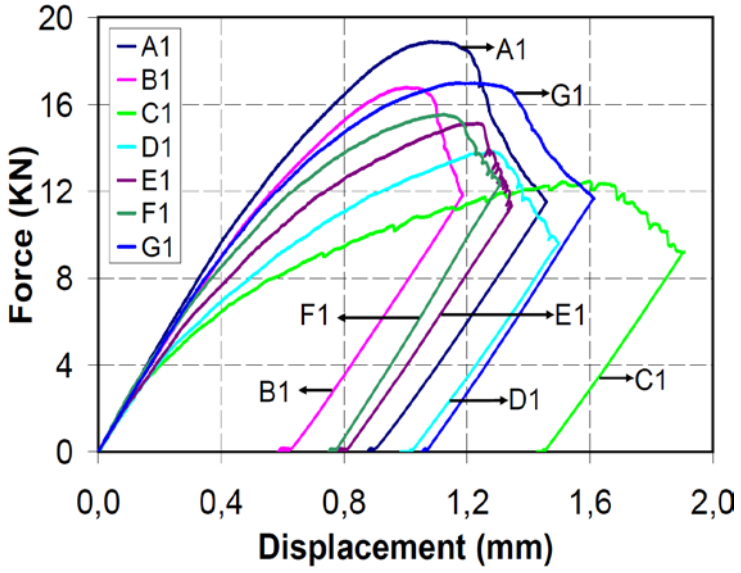

Fig. 4.8 Fracture curves of 15-5PH after different heat treatment history

One may be surprised about table 4.2 that the maximum force of the samples with different crack length are not always consistent with the initial crack length, for example, it needs bigger force to make the sample with longer pre-crack propagate. The reason has been found to be due to a difficult control of the “grip” conditions of the specimen into the machine. This difficulty is created by the extremely simple design of the specimen with small pre-crack difference but has been solved using DIC and finite element simulation of the experiments.

4.3.4 Boundary conditions from DIC for the FEM simulation

As we discussed in section 3.1, PD and DIC technologies are applied to confirm the crack initiation point, after that then we applied DIC again to detect the boundary conditions at seven experimental points from the beginning photo to the critical crack initiation photo which are shown in figure 4.9.

Point A

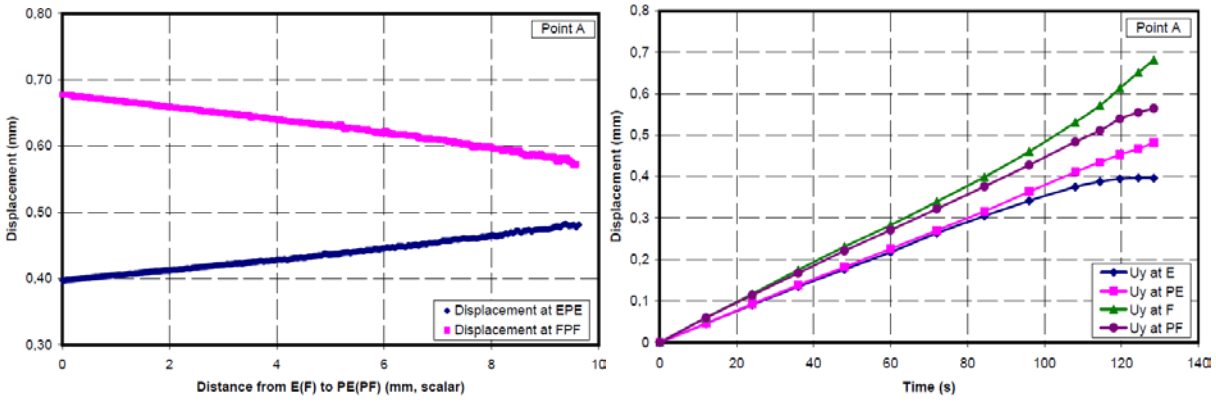

Point B

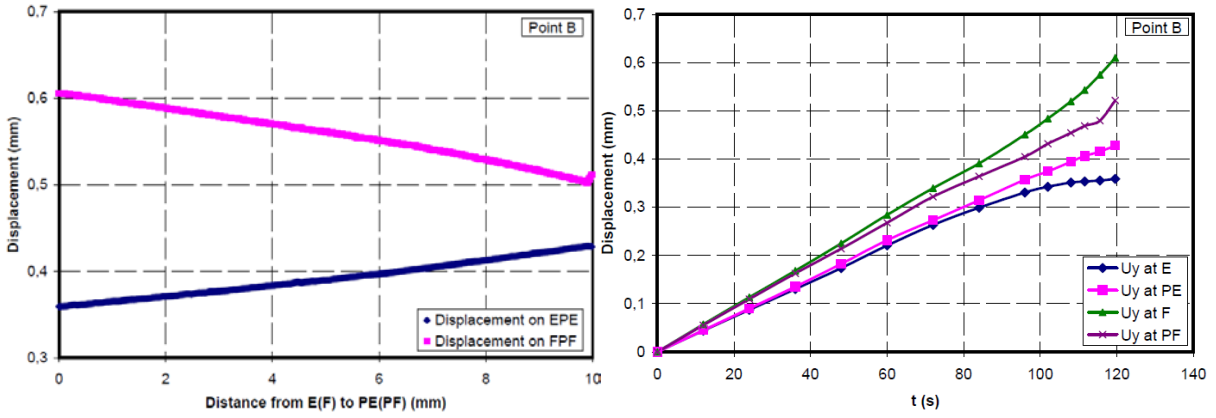

Point C

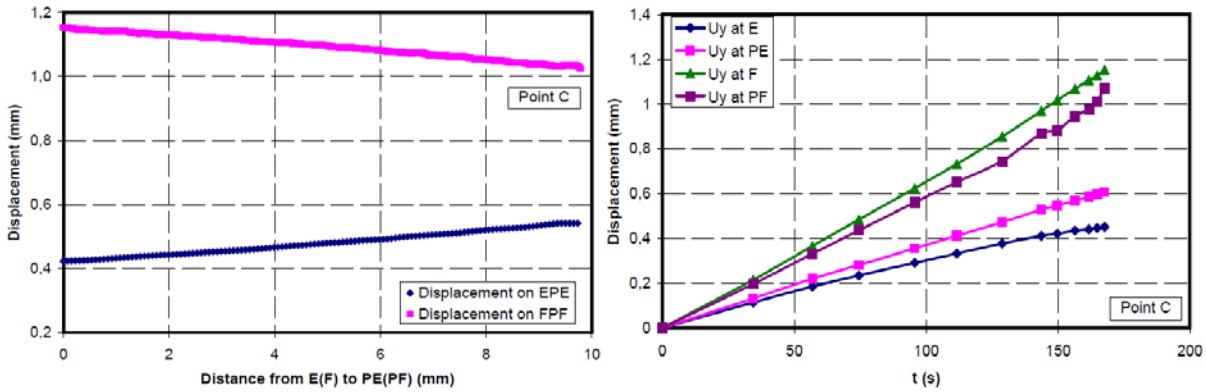

Point D

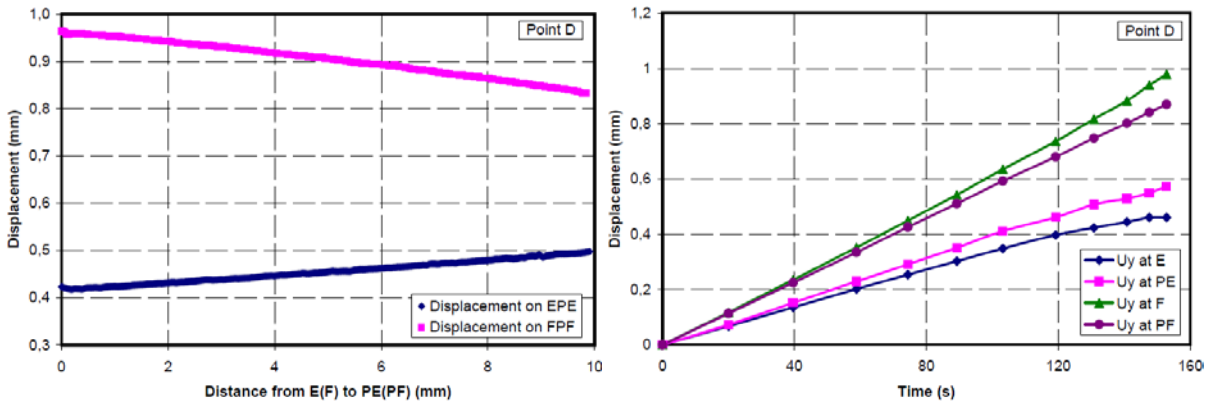

Point E

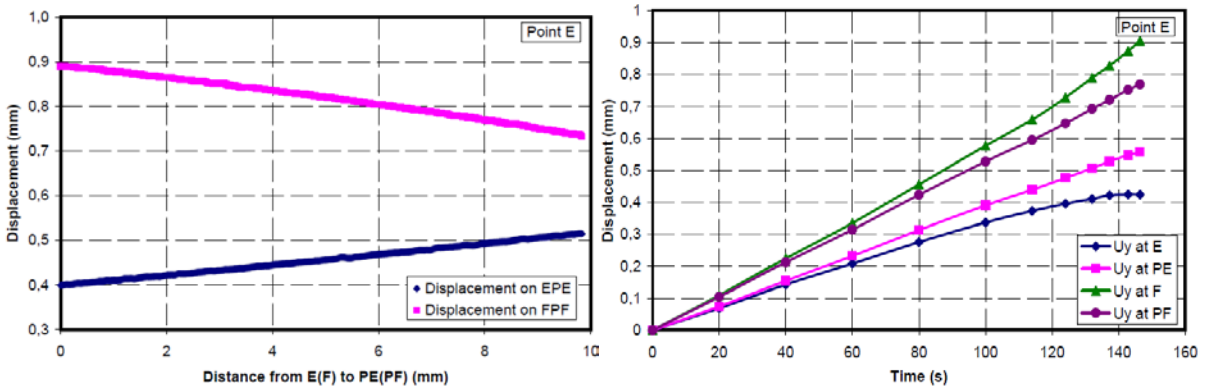

Point F

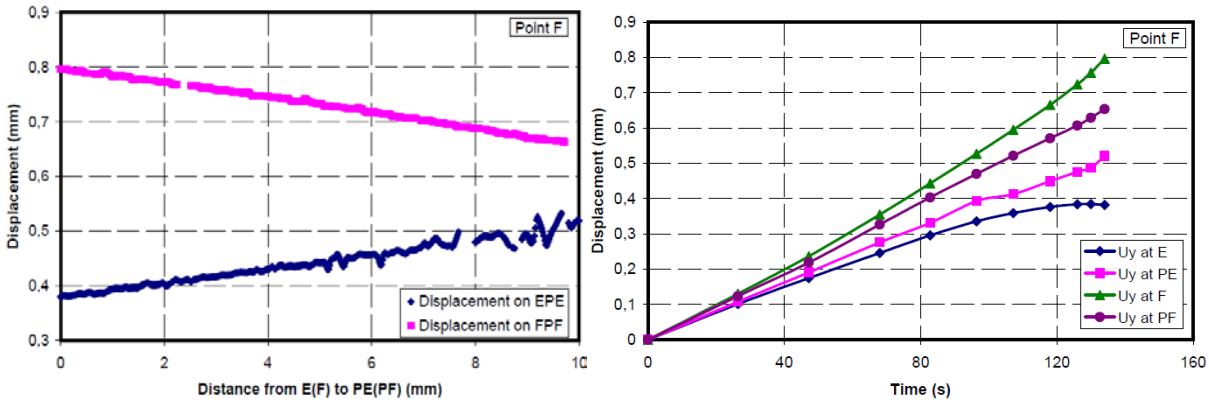

Point G

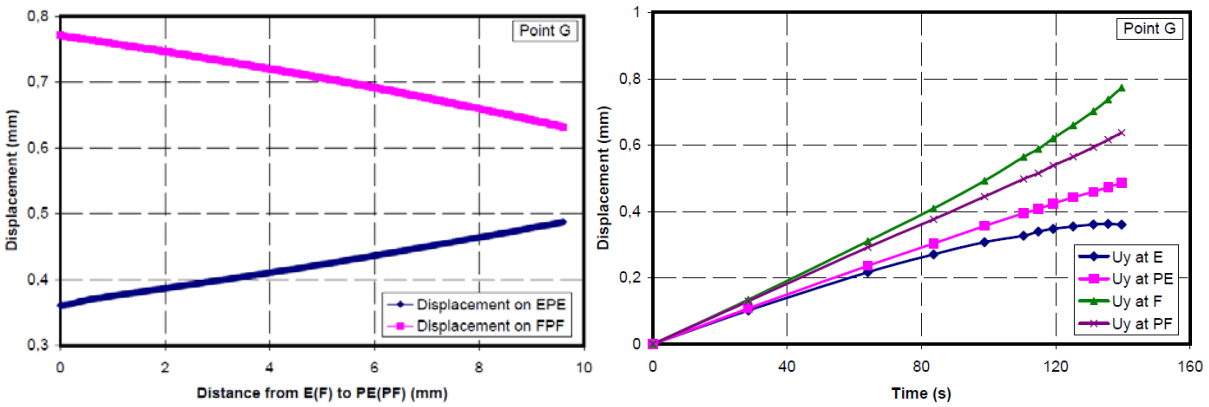

Fig. 4.9 Boundary conditions got by DIC of 15-5PH fracture tests at every experimental point

4.3.5 Fractography observation

A fractography of the fracture surfaces has been done by Scanning Electron Micrograph (SEM) for each specimen after failure to analyse the related fracture mechanism. It is displayed in figure 4.10.

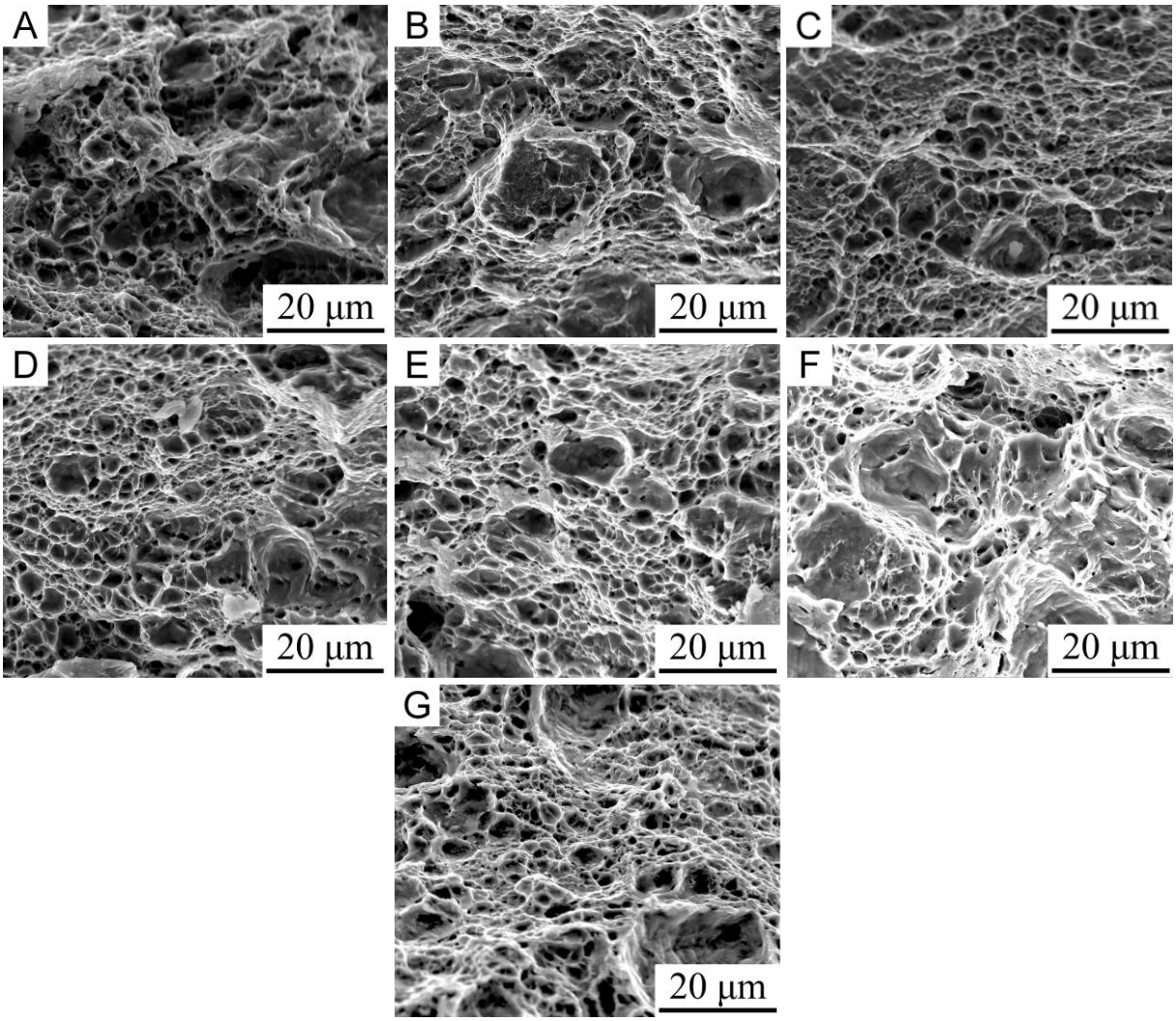

Fig. 4.10 Fractography of all specimens (A to G). Crack propagation direction is from the right to the left of the picture

The symbols A to G in figure 4.10 respectively are related to tests A to G. From the fractography, it is clear that each failure is characterised by a lot of microvoids. This denotes that they are all ductile fracture. 15-5PH is a high strength steel for any metallurgical state even at 200°C or during the martensite transformation period.

When one compares the size of the microvoids, A and B have larger microvoids than others. B has bigger dimples than A. For point G, the dimples are much smaller than for case A and their density is consequently higher.

Meanwhile, from the fractography, there are few inclusions, their influence on the fracture toughness should then be small.

4.4 Numerical simulation

When we have all the boundary conditions of every fracture test and stress-strain curves at every experimental point, we impose the boundary conditions to the finite element analysis, the re-programmed G_theta method will then give us the simulated result of critical *J*-integral. The comparison of experimental and simulated force vs. mean displacement at every point is shown in following figure 4.11.

Case A

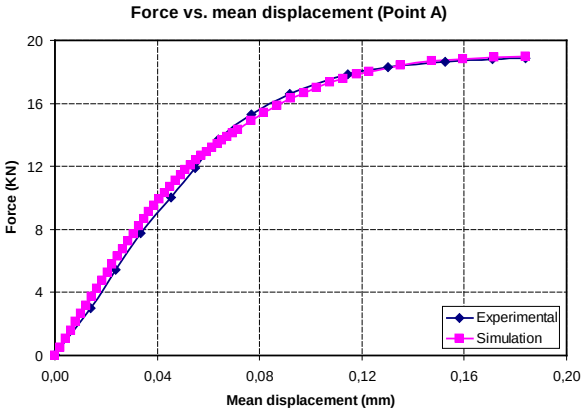

Case B

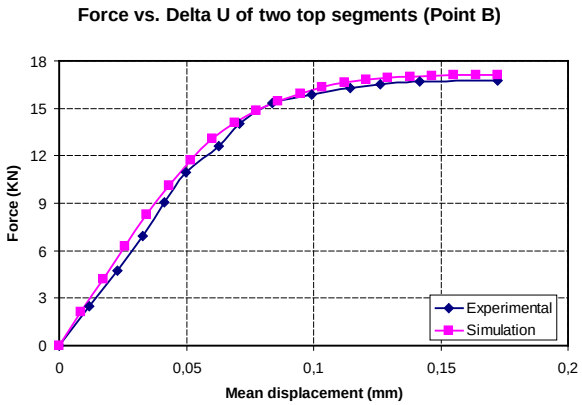

Case C

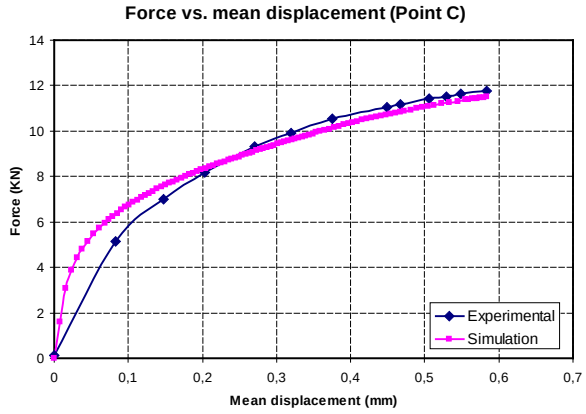

Case D

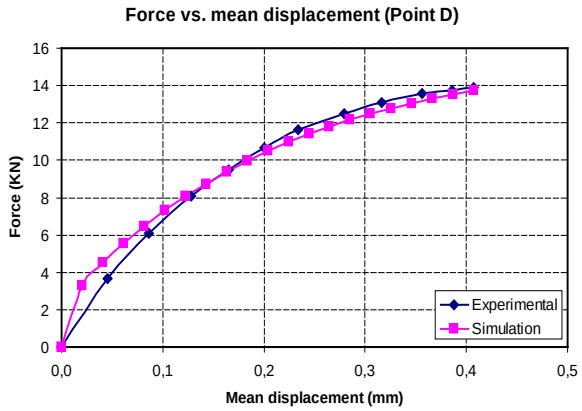

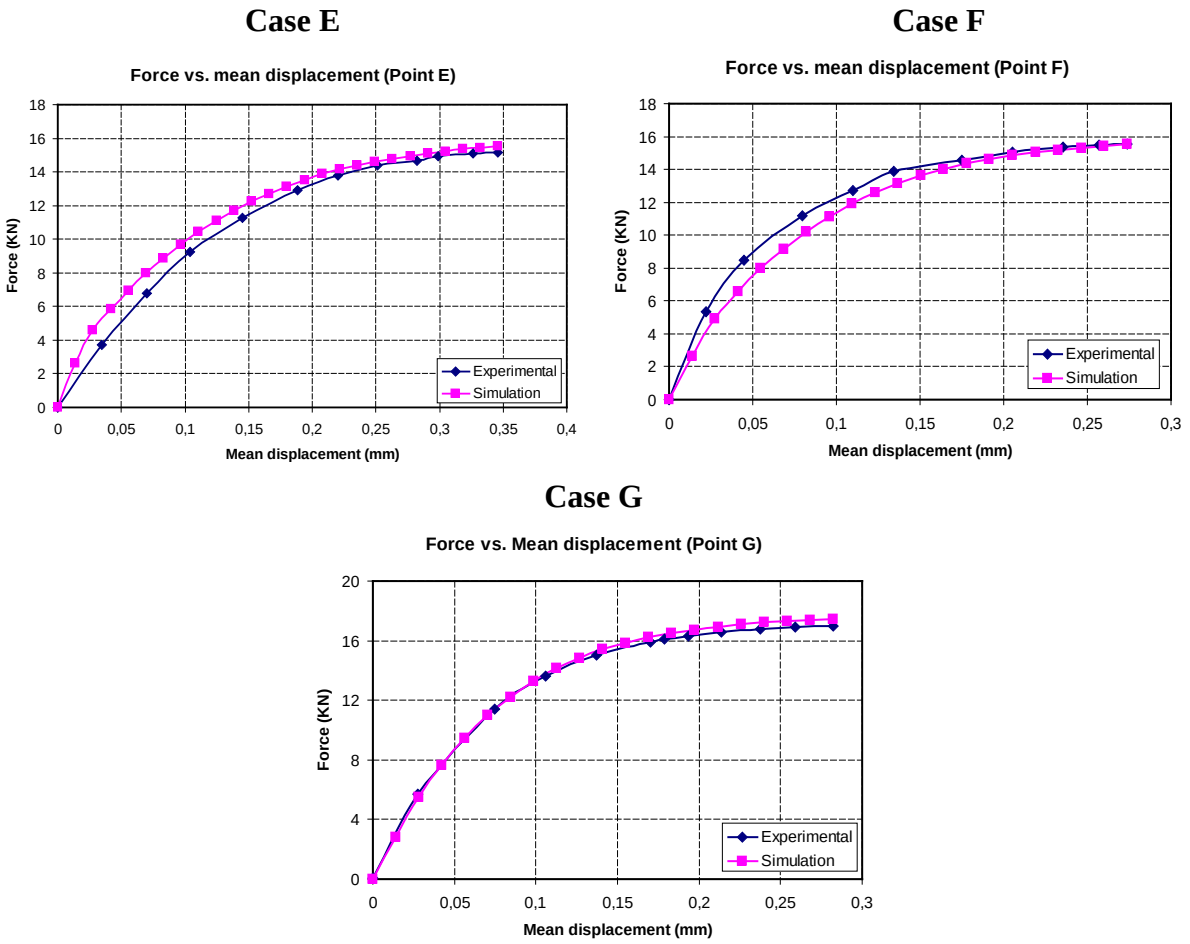

Fig. 4.11 Experimental and simulated comparison (force vs. mean displacement) for each point from A to G

The synthesis of the analysis is given on the following table 4.3. Figure 4.12 displays the J_{1C} estimated value for each experimental case (A to G)

Table. 4.3 Critical *J*-integral results of all samples given by the simulation

Experimental Point	Temperature [°C]	Sample	J_{1C} [KJ/m^2]	Mean J_{1C} [KJ/m^2]
A	20	A1	247	259
		A2	270	
B	200	B1	190	186
		B2	182	
C	200	C1	298	318
		C2	337	
D	170	D1	239	258
		D2	276	
E	140	E1	292	252
		E2	211	
F	110	F1	269	263
		F2	257	
G	20	G1	306	315
		G2	323	

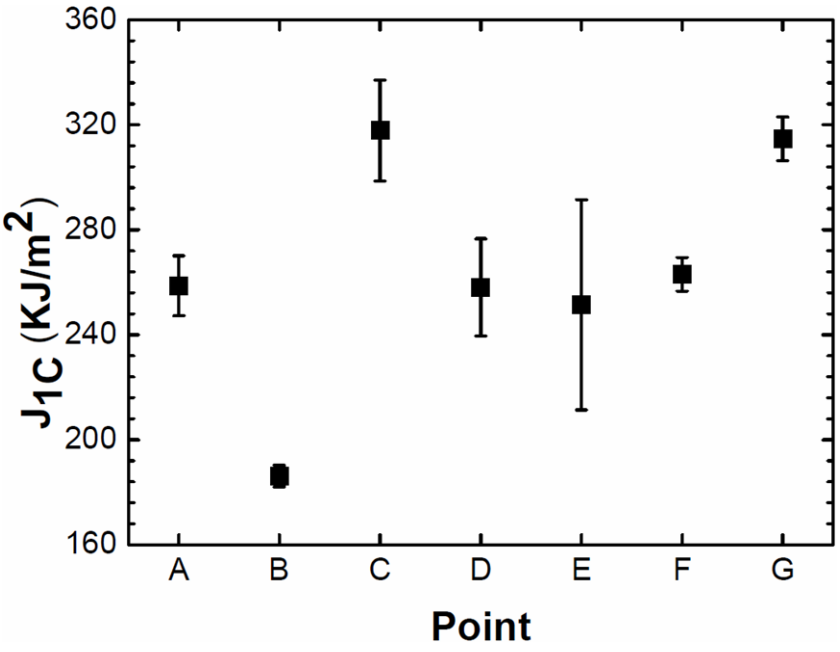

Fig. 4.12 J_{1C} of 15-5PH at different temperature

4.5 Results analysis

The results presented in figure 4.12 show that the heat treatment and metallurgic phase transformation has an influence on the fracture toughness of 15Cr-5Ni stainless steel.

We predict an as-received 15-5PH J_{1C} value of 259 KJ/m^2. If we convert this value to the stress intensity factor by equation (3-7) and compare it with the ASME recommended value or others in figure 4.13, we find that our value is very similar to the one given by I.I. Cuesta *et al.* (level 3 with $a_0 / B = 0.25$) [153], but higher (see figure 4.13) than the ASME recommended value [154] or the value from Kotoji Ando et al. [155].

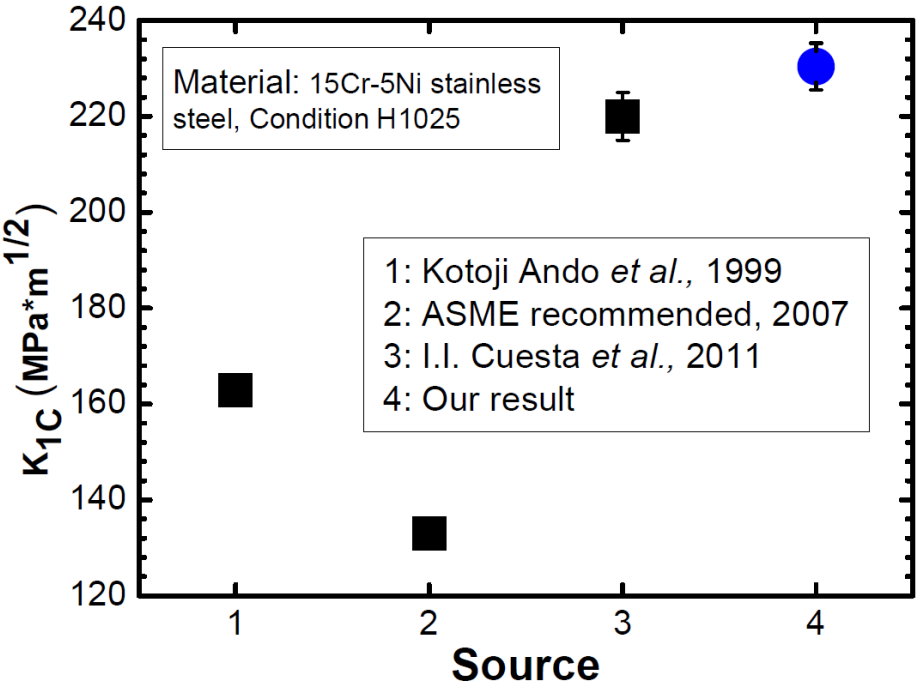

Fig. 4.13 Comparison of stress intensity factors of 15Cr-5Ni stainless steel from different sources [153-155]

If one now compares cases A and B, which are all fully martensitic, but at different temperature, A has a bigger J_{1C} value than B. The reason is not obvious. The difference is of about 20%. This observation should be confirmed by a larger number of experiments.

One now compares the toughness at 200°C but with two distinct metallurgic states: cases B (fully martensitic) and C (fully austenitic). J_{1C} for case B is clearly smaller than the one of case C. 15-5PH in austenitic phase is tougher than in martensitic one.

Comparing the toughness J_{1C} of cases A and G, the material after a whole cycle heat treatment has higher fracture toughness than the original material. This should be due to some residual austenite in the material after the heat treatment. This is confirmed by the fractographic analysis of the failure zone which shows a more ductile fracture mode.

For cases D, E and F, both martensite and austenite phase (their proportion is given in table. 2.3) exist in the specimens. Globally the toughness is smaller during the phase transformation than when it is finished or not started. But the decrease is not huge.

Overall, one can conclude that austenite enhance the ductility and then the toughness J_{1C} of the material. Let us also observe that these experiments do not give enough information for the evaluation of the pertinence of a mixture rule between austenite and martensite toughness.

Chapter 5 Effect of Bainite Transformation on Mechanical Properties and Fracture Toughness of 16MND5 Low Carbon Steel

In this chapter, we will firstly study more deeply about the bainite transformation especially the isothermal bainite transformation in 16MND5 low carbon steel, the good understanding of isothermal bainite transformation is useful to do the mechanical experiments at one isothermal temperature and to do the analysis of the influences of bainite transformation on fracture toughness. After that, we follow the same procedure as for 15-5PH stainless steel (chapter 3).

5.1 Detail research of bainite transformation in 16MND5

In section 2.4.5, we have mentioned some points about the transformation in the 16MND5 low carbon steel. We talked about the continuous cooling bainite transformation investigated by others, we have also shown the continuous cooling bainite transformation gotten from -5°C cooling condition. If we want to do the same mechanical experiments as what we did for 15-5PH stainless steel, we need to control that no phase transformation occurs at temperature higher than Bc. If there is no dilatation during temperature hold, we can start the mechanical tests at once. Otherwise, we need to wait for the end of isothermal transformation and then launch the mechanical test.

5.1.1 Isothermal bainite transformation at temperature higher than Bc

As what we did in 15-5PH, we will also choose seven points for the mechanical tests. Here we choose 600°C before continuous cooling bainite transformation and 573°C, 550°C, 530°C during the bainite transformation for the following isothermal bainite transformation investigation. Similarly the as received 16MND5 and the one after the whole heating and cooling process, together with one point with the same temperature at 600°C but before the austenitization are all selected also. These seven points are also named from A to G which is marked on the following figure 5.1. Notice that figure 5.1 is part of the figure 2.21.

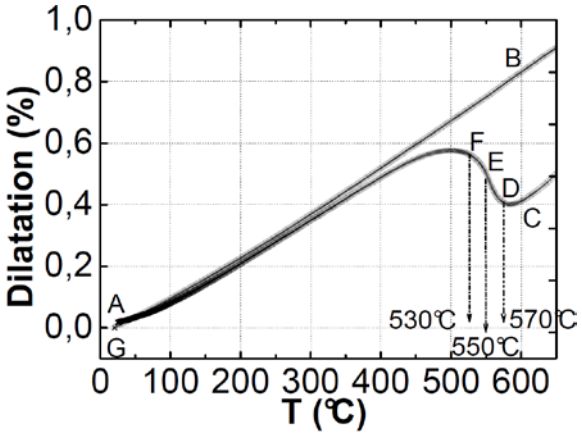

Fig. 5.1 Explanation of investigated points

We now need to confirm that when temperature is kept constant from continuous cooling at point C, D, E and F nothing happens. The free dilatation experiments show that there is a phase transformation when one keeps the temperature constant at these four points. We imposed the temperature loading illustrated in figure 5.2 to study the isothermal transformation. We did the same thing for heating and austenitization as what we did for pure continuous cooling bainite transformation. While during the austenite cooling period, we changed the cooling process to keep a constant temperature before and during the CCT bainite transformation starting temperature Bc.

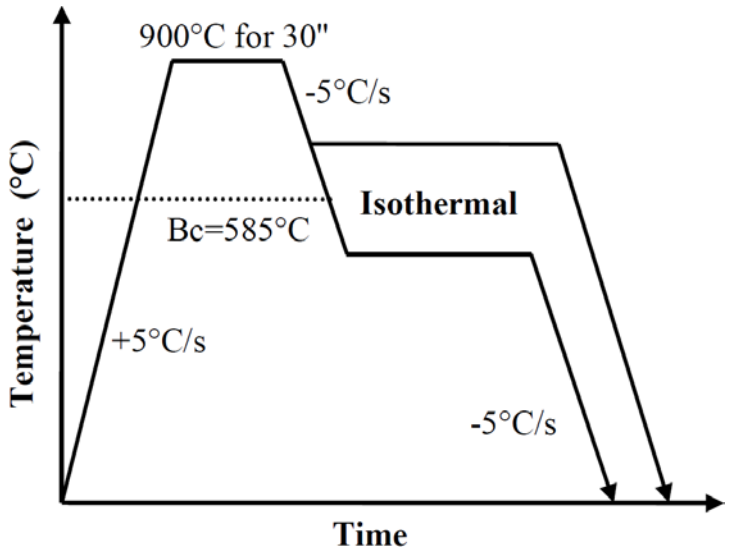

Fig. 5.2 Schematic of the heat treatment to study the isothermal transformation

On figure 5.3, we observe that the free dilatation curves also changed at constant temperature higher than Bc. Similarly the dilatation curves went higher at temperature lower than Bc during continuous cooling bainite transformation which will be discussed with more details in

section 5.1.2. For each point, isothermal phase transformation is finished after a certain hold time.

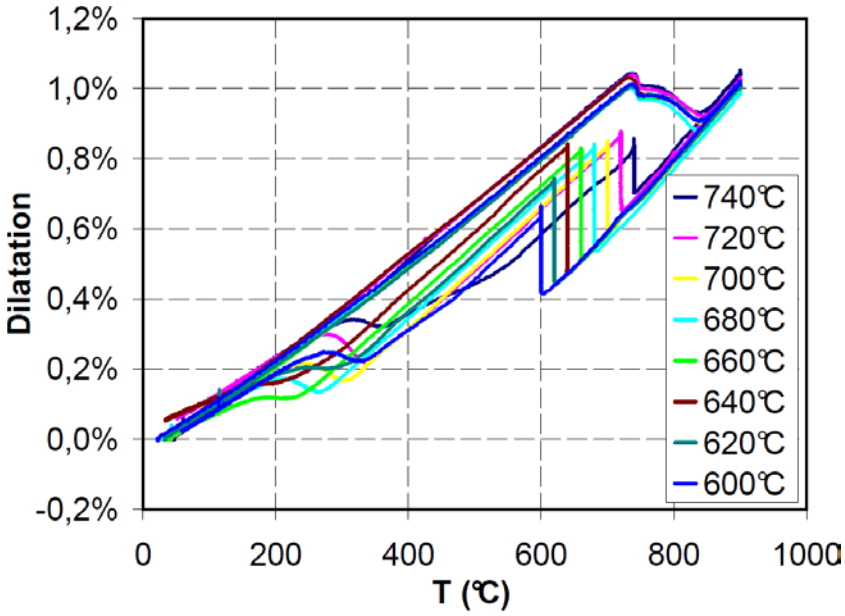

Fig. 5.3 Free dilatation curves of the isothermal transformation at temperature higher than Bc

For more convenience, we magnify the isothermal transformation part in figure 5.3 to have following figure 5.4. In figure 5.4, we can more easily observe what happens during the constant temperature hold at a temperature higher than Bc.

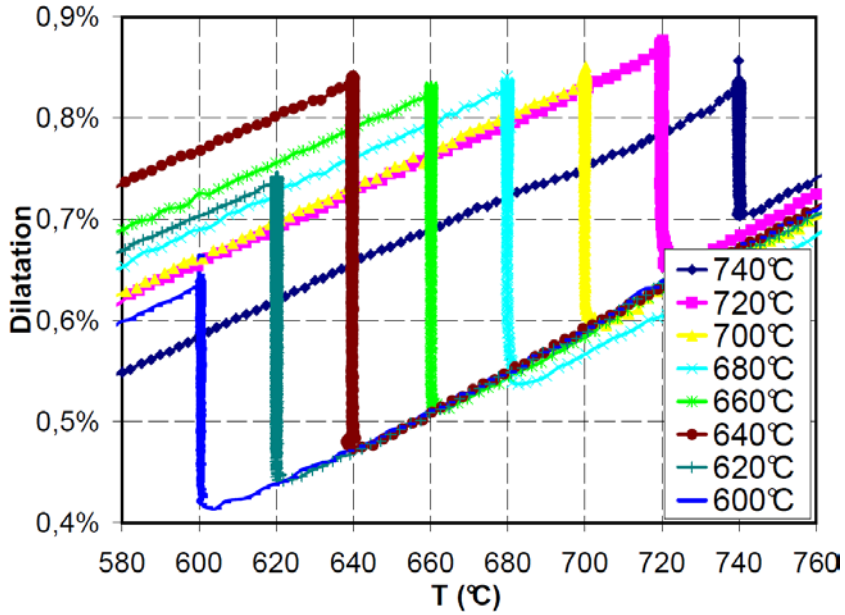

Fig. 5.4 Magnification of the free dilatation curves of the isothermal transformation at temperature higher than Bc

In figure 5.3, after the isothermal transformation, there is no further anisothermal bainite transformation as the following heat treatment condition can normally bring us bainite transformation. We also observe that the further martensite transformation starting temperature decreases. This is probably due to carbon movement induced by the isothermal transformation in the high temperature region. On the other hand, the upper limiting temperature of the bainite formation should be that of the eutectoid reaction which is 750°C in our material [156-160]. This can tell us that the reason why the dilatation curve at constant temperature went higher is due to the isothermal bainite transformation.

Let us observe the free dilatation experiment at isothermal temperature 680°C. The dilatation curve is shown in figure 5.5. In this figure, one observes three parts between the inflection points. Part 1 is due to the austenitization, part 2 is caused by the isothermal bainite transformation in our opinion. After part 2, when the sample is cooled again by -5°C/s, it gives part 3 which is martensite transformed from retained austenite after the isothermal bainite transformation (part 2).

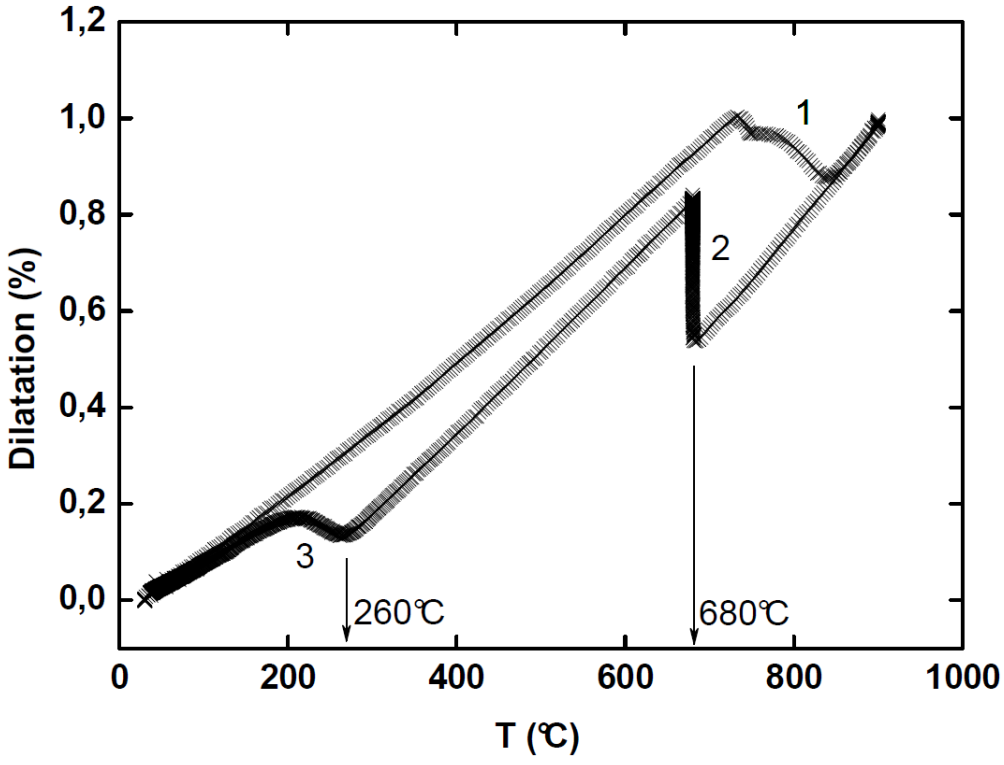

Fig. 5.5 Free dilatation curves of 16MND5 at the isothermal temperature 680°C and then cooling to room temperature by -5°C/s

Following figure 5.6 is the micrograph of 16MND5 at room temperature after isothermal temperature at 680°C. From this metallurgical photo, we may observe that there are lots of

bainitic ferrite plates which come from the isothermal transformation at 680°C, and the photo also shows that there is some martensite which comes from the later martensite transformation from the retained austenite after the earlier isothermal bainite transformation.

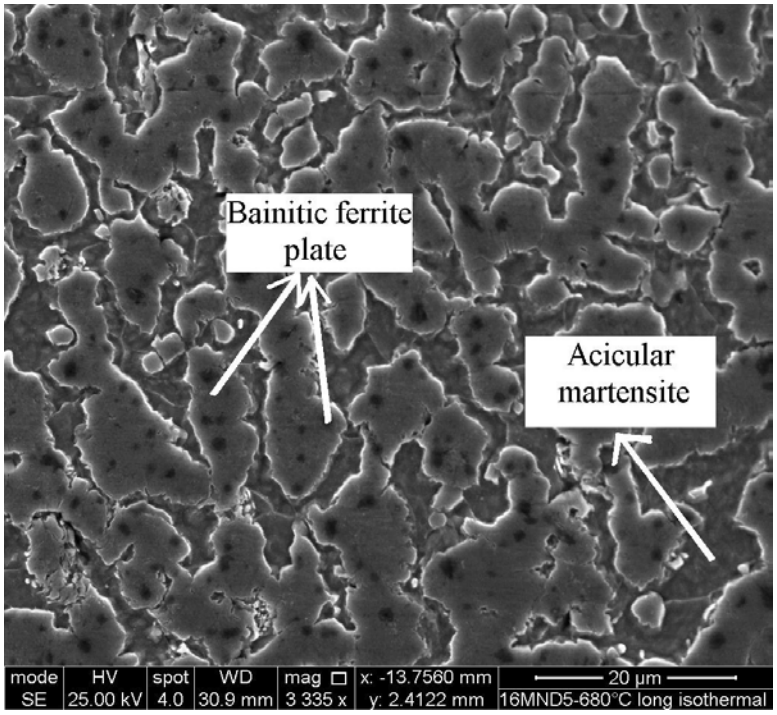

Fig. 5.6 Micrograph of 16MND5 at room temperature after isothermal temperature 680°C

The X-ray diffraction test result shown in figure 5.7 proves that there is no pearlite after the isothermal transformation at 680°C. As three peaks are typical peaks of BCC α-Fe.

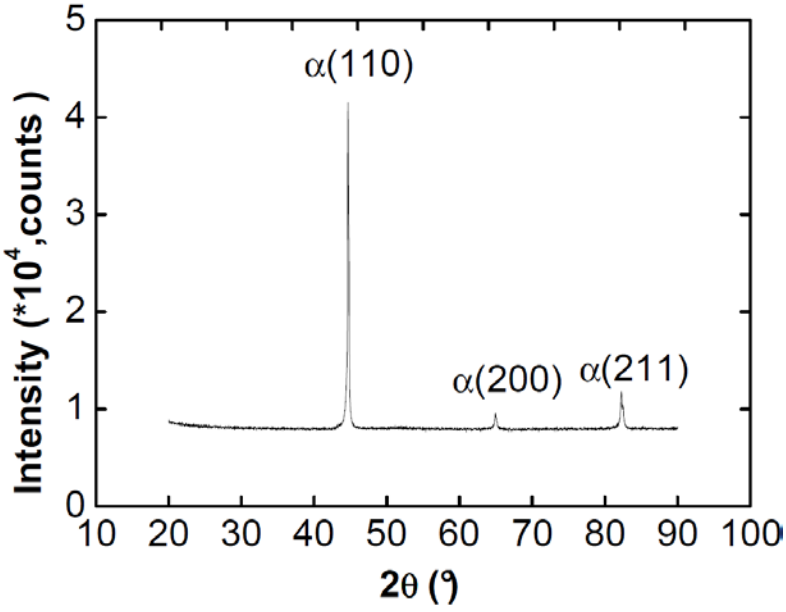

Fig. 5.7 X-ray diffraction test result of 16MND5 after isothermal transformation at 680°C

These two metallurgical observations confirm that the reason why the dilatation curve changed when applying a hold time is that there is the isothermal bainite transformation. The kinetic curve of the isothermal bainite transformation and following martensite transformation is given in figure 5.8 in which the phase fraction is calculated by equation (2-8).

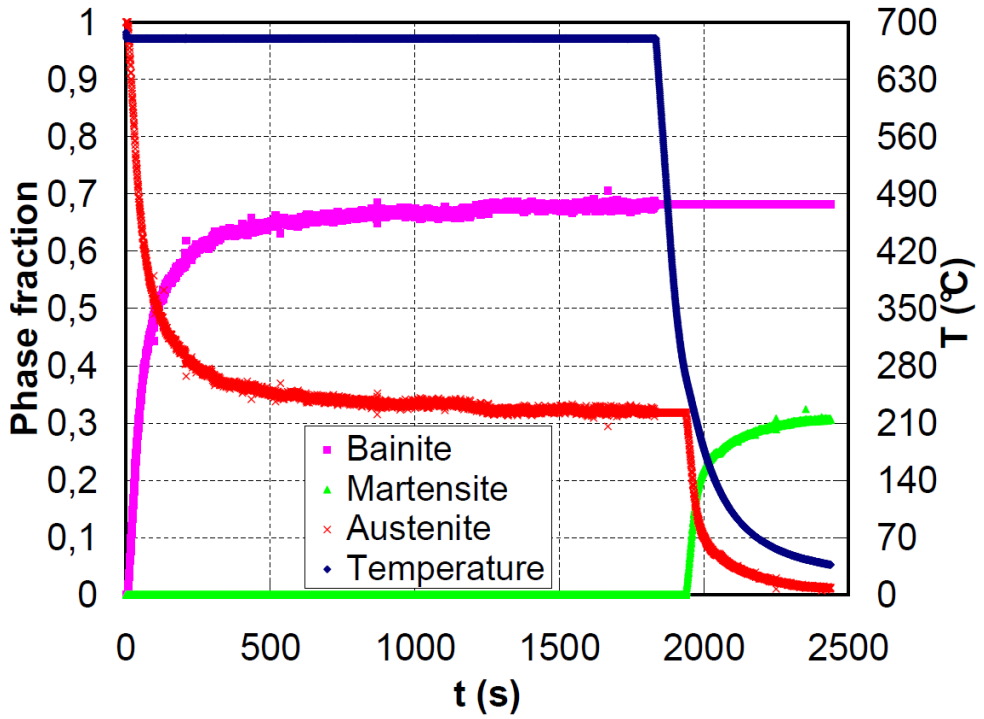

Fig. 5.8 Phase fraction changes with the temperature (for 680°C isothermal temperature)

In figure 5.8, we can find that nearly 70% austenite transformed to bainite (or bainitic ferrite), it is very well consistent with the metallography (see figure 5.6). The rest part is martensite transformed from 260°C in the following continuous cooling period.

Looking at figure 5.3, we observe that different isothermal temperature leads to different martensite transformation starting temperature (Ms). D. Quidort and Y. Bréchet explained in their paper [48] that the bainite transformation is the evolution of the carbon content of the austenite and the carbon enrichment of the untransformed austenite can decrease the Ms temperature. Figure 5.9 and 5.10 show the dilatation curves and fraction versus holding time at every constant temperature before Bc.

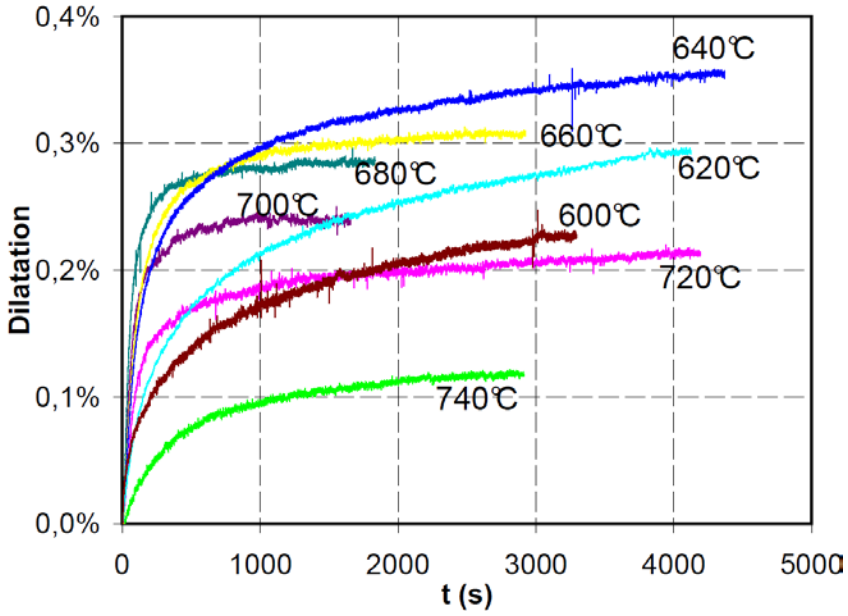

Fig. 5.9 Free dilatation curves of the isothermal transformation before CCT Bc

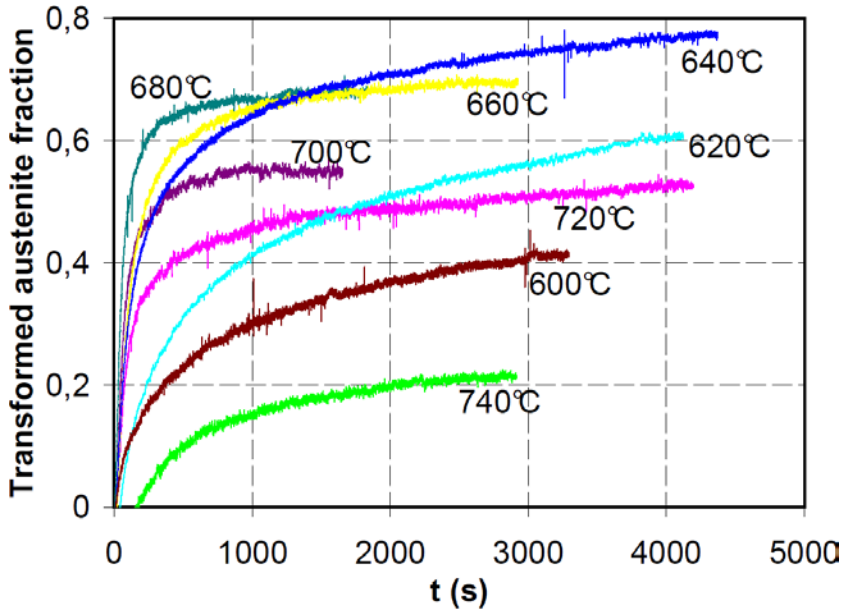

Fig. 5.10 Transformed austenite fraction versus time in the isothermal transformation before CCT Bc

Once we got all the final bainite fractions at every isothermal temperature (details are given in table 5.1), we plot the Ms temperature versus bainite fraction in figure 5.11. It clearly shows that more austenite transformed, lower Ms temperature is. This agrees very well with the experimental result of D. Quidort and Y. Bréchet.

Table. 5.1 Summary of martensite transformation temperature and bainite fraction after different isothermal temperature holding

Isothermal T(°C)	Bainite fraction	Martensite transformation T(°C)
740	0.21	354
720	0.53	328
700	0.55	302
680	0.68	260
660	0.70	229
640	0.80	210
620	0.66	300
600	0.49	310

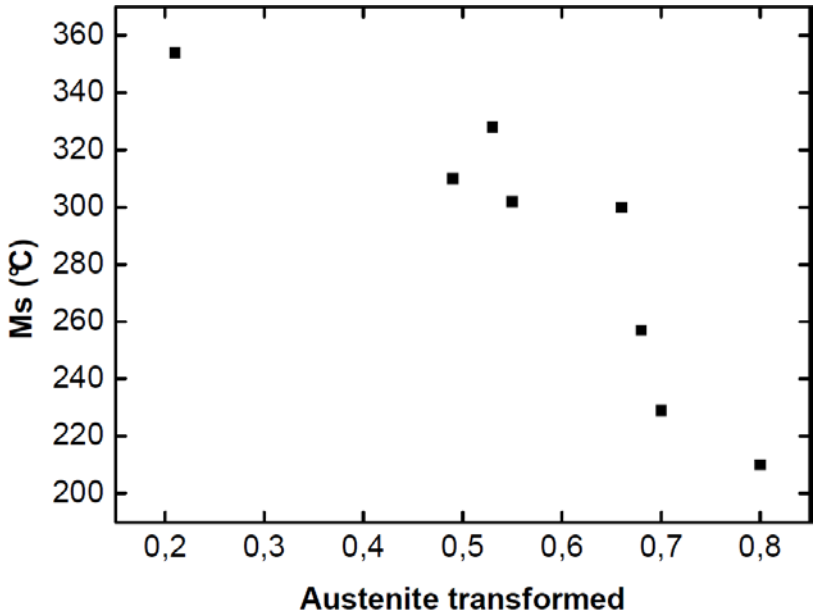

Fig. 5.11 Ms temperature decreases as more austenite transformed

Continuous cooling transformation shown in figure 2.22 needs no more than 100 seconds to finish. The isothermal bainite transformation is quite slower even if it happens at a high temperature region (Fig. 5.12). After 200 seconds in figure 5.12, the maximum bainite fraction is only 0.6.

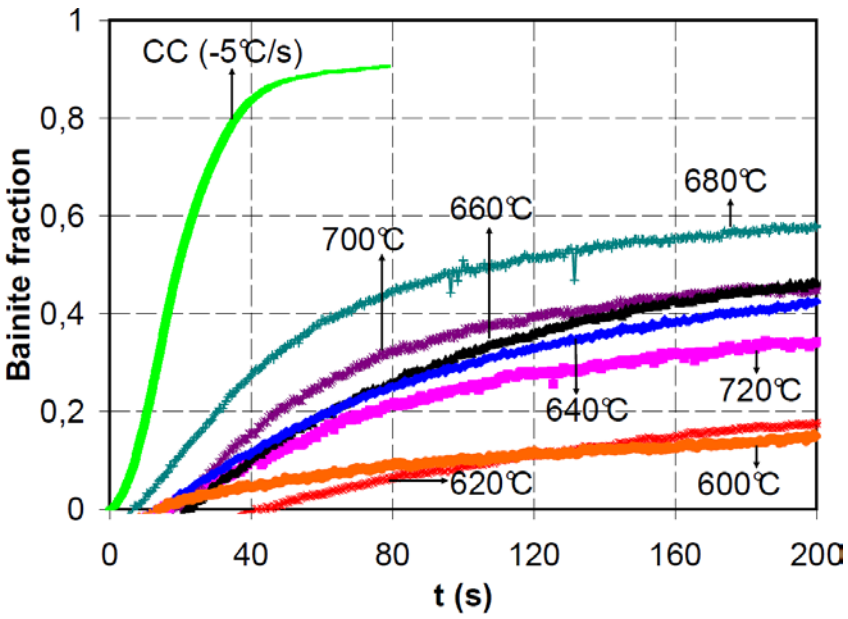

Fig. 5.12 Transformation rate comparison of continuous cooling (CC) and isothermal bainite transformation

In figure 5.12, we can also deduce that the bianitic ferrite ξlaths growth rate is not constant. It is first very quick then slow down, finally it proceeds very slowly. This is rather different from what D. Quidort and Y. Bréchet found in 0.5% C steels as they found the bainite growth rate is a constant [49]. Anyway, notice should be paid attention that the heat treatment procedure and material are all different. We will go deeper in this point later.

5.1.2 Isothermal bainite transformation at temperature lower than Bc

Similarly to the isothermal transformation happened at temperature higher than Bc, the dilatation curve went higher also when the cooling temperature is changed to be constant during the continuous cooling bainite transformation. In following figure 5.13, we observe that when the cooling temperature is kept constant at one temperature (point D at 570°C, point E at 550°C or point F at 530°C) lower than Bc, the dilatation curves is increasing. The whole transformation here will be called hereinafter 'continuous cooling-isothermal bainite transformation'. Note that the martensite transformation is going on after the former 'continuous cooling-isothermal bainite transformation': this is probably due to the retained austenite after the former bainite transformation.

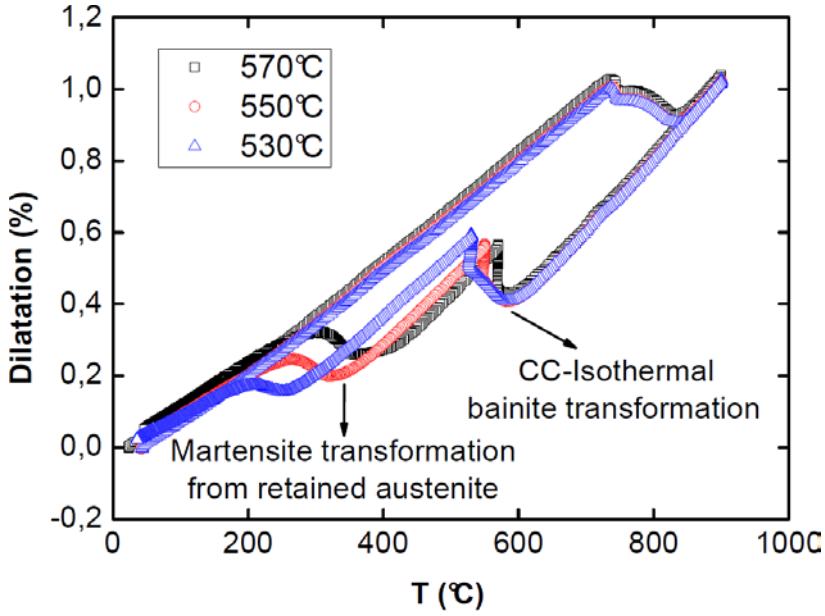

Fig. 5.13 Free dilatation curves of the continuous cooling-isothermal transformation at temperature lower than Bc

Figure 5.14 and 5.15 show the dilatation curves and bainite fraction evolution for these three complex bainite transformations. In all the figures, blue points denote the continuous cooling (CC) part occurring at the cooling rate -5°C/s. Pink points show what happens at the isothermal temperature. Time zero in figure 5.14 and 5.15 is chosen when the transformation started at Bc 585°C.

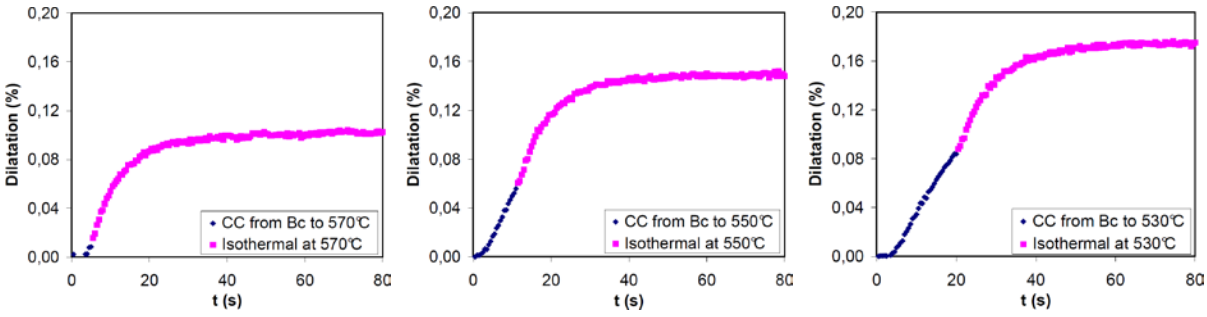

(a) (b) (c)

Fig. 5.14 Dilatation curves of the isothermal transformation after CCT Bc at 570°C, 550°C and 530°C

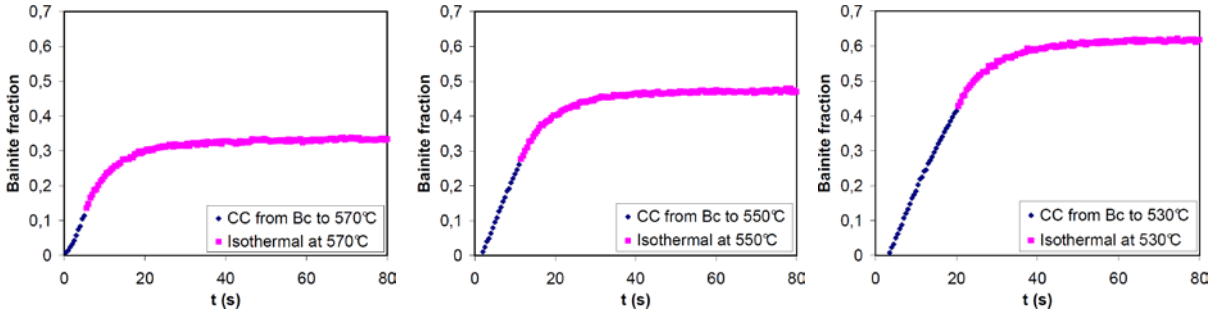

(a) (b) (c)

Fig. 5.15 Bainite fraction development versus time in the isothermal transformation after CCT Bc

On figure 5.16, we plot the bainite fraction development versus time which begins with the continuous cooling phase transformation from temperature Bc and until the end of the isothermal transformation at 530°C. The green curve displays the temperature history: firstly it cools by -5°C/s and then was held constant at 530°C. The blue and pink curves are dilatation curves due to different causes. There is also a t_{shift} marked in figure 5.16 to denote the shift time when the cooling temperature is shifted to be constant. When the temperature is continuous cooling (-5°C/s), it will give us the blue curve which shows us the continuous cooling bainite transformation from 585°C, once when the continuous cooling temperature is changed to be constant at 530°C, it gives the pink dilatation curve which denotes the isothermal bianite transformation at 530°C. The Transformation kinetics of continuous cooling and isothermal transformation at other two points (point D at 570°C and point E at 550°C) are similar to this one.

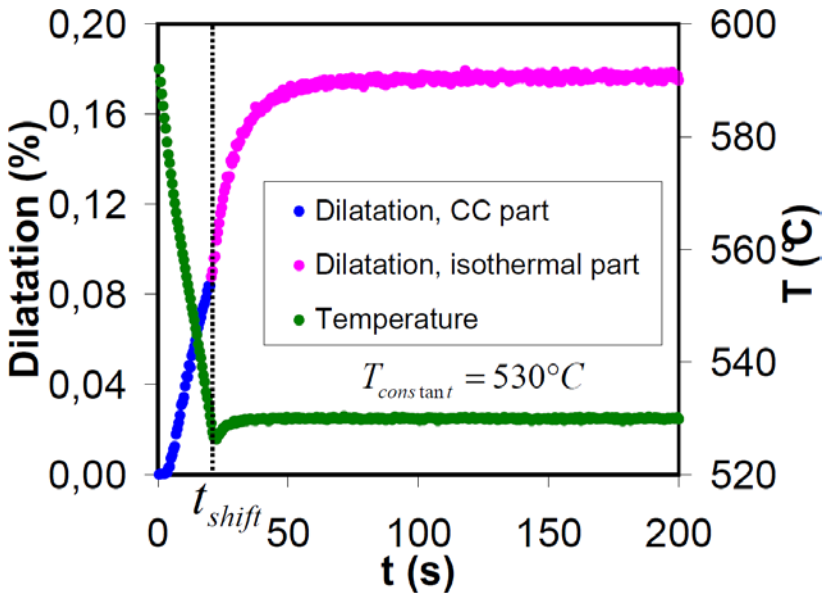

Fig. 5.16 Transformation kinetics of continuous cooling followed by an isothermal transformation at 530°C

Figure 5.17 shows the phase fraction of transformed bainite with this process. One observes that the lower isothermal temperature is, the more bainite is produced by anisothermal and consquentely less bainite is produced by isothermal bainite transformation.

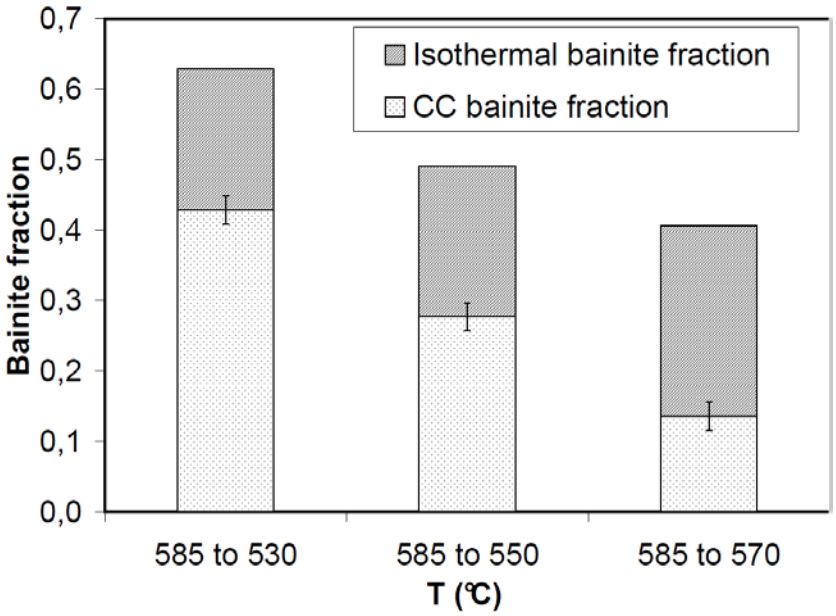

Fig. 5.17 Bainite transformed by continuous then isothermal transformation respectively

Figure 5.18 analyzes the relation between the bainite transformation after Bc in figure 5.15 and the following Ms temperature. We find that Ms temperature decreases perfectly linearly with bainite fraction produced.

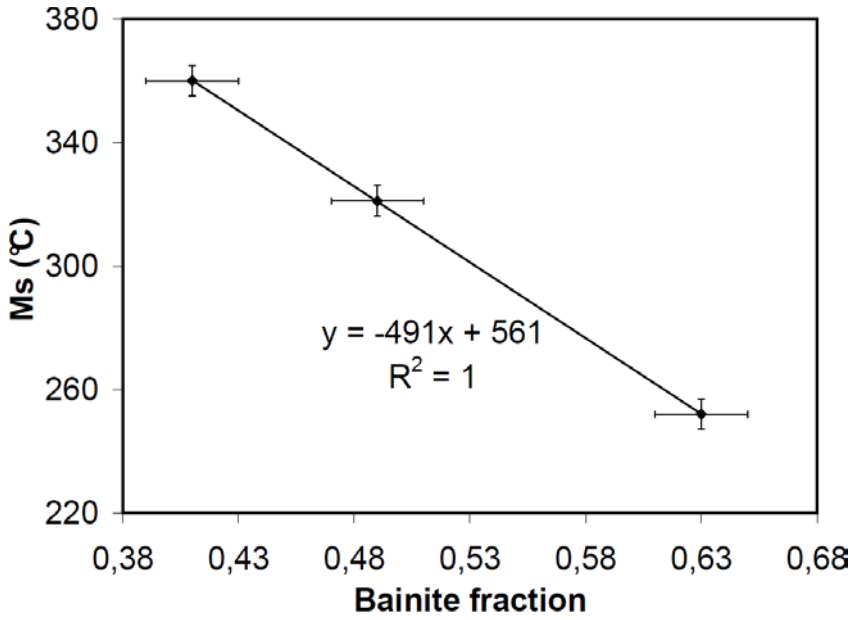

Fig. 5.18 Ms temperature decrease linearly with more bainite fraction produced (Error of T is +/- 5°C and error of fraction is +/- 0.02)

The results are summarized in the following table.

Table. 5.2 Summary of martensite transformation temperature and bainite fraction transformed by continuous cooling-isothermal bainite transformation

Hold temperature (°C)	**Bainite fraction**	**Ms temperature (°C)**
570	0.41	360
550	0.49	321
530	0.63	252

Micrography obtained by SEM is given in fig. 4.19. (a), (b) and (c) is respectively the metallographic of the specimen submitted to the isothermal transformation at 570, 550 and 530°C. Bright areas are bainite, the dark ones are residual austenite and a little martensite transformed from retained austenite after the bainite transformation. From (a) to (c), more and more austenite has been transformed and bainite becomes more and more fine due to increased nucleation rate. Small temperature difference makes the refinement be not very clear. Obviously, specimen (c) has more bainite than (a) and (b). More information needs to be found by XRD.

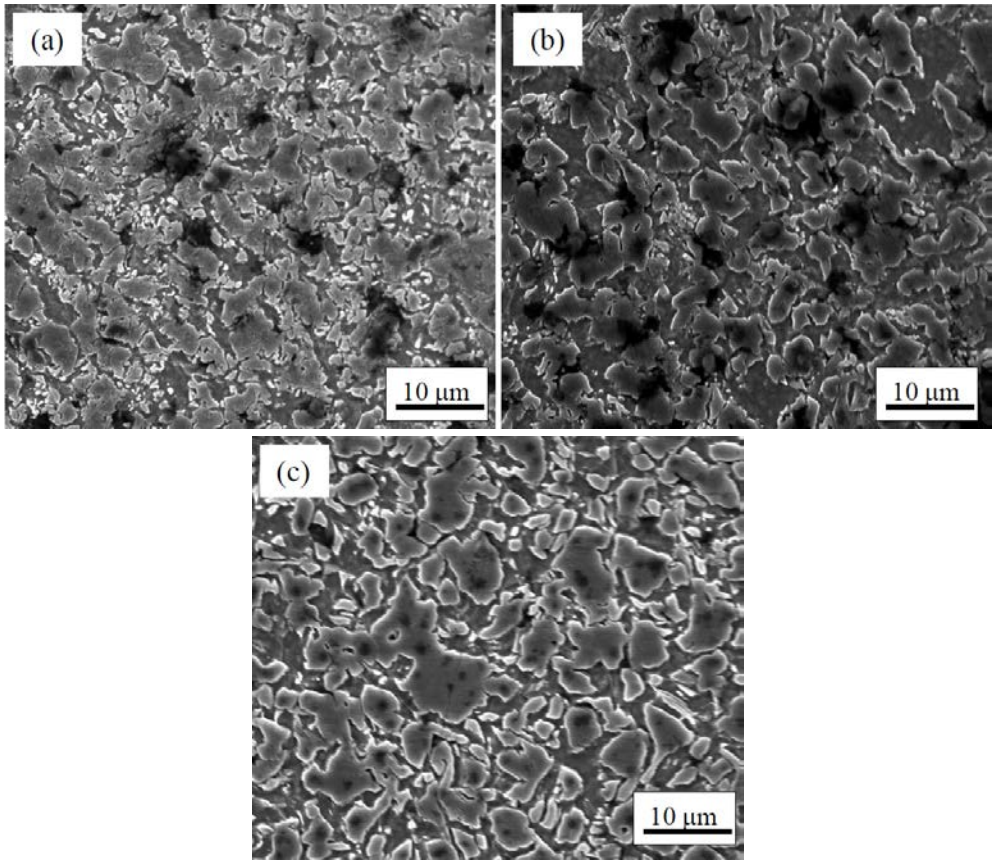

Fig. 5.19 Metallography of bainite given by continuous cooling-isothermal bainite transformation separately at (a) 570°C, (b) 550°C, (c) 530°C. Amplification: ×4000, etching in 2% Nital

As discussed before, in the continuous cooling-isothermal bainite transformation experiments, such as isothermal temperature 570°C, 550°C and 530°C, from both the dilatation curve or bainite fraction curve versus time, the transition from continuous cooling to isothermal bainite transformation was perfectly smooth, around the shifting time, the transformation rate didn't change also (see the slope of the dilatation curve around the shifting time). This point could give us the evidence that continuous cooling and isothermal bainite transformation in 16MND5 have the same transformation mechanism which is probably displacive, because continuous cooling and isothermal heat treatment have the essential difference: continuous cooling has over-cooling potential but isothermal hasn't. When the bainite transformation shifts from continuous cooling to isothermal, the bainitic subunit was continouly growing with the same rate without over-cooling induced diffusion. But why pure continuous cooling or continuous cooling-isothermal bainite transformation proceeds more faster than pure isothermal bainite transformation? In our understanding, there are several reasons: 1), pure continuous cooling and continuous cooling-isothermal have longer incubation time; 2), pure continuous cooling and continuous cooling-isothermal have more over-cooling energy; 3), Displacive movement has no strong dependence on high temperature; 4) austenite at high temperature is more stable. So, we can maybe conclude that the bainite transformation in 16MND5 is a transformation that obey the displacive theory but with the carbon evaluation.

5.1.3 Incomplete isothermal bainite transformation and it's half C-curve

As we all know that bainite transformation is an incomplete transformation. It was explained by Zener C. as when the bainitic ferrite formed the supersaturated carbon which would be expelled to the surrounding austenite thus thermodynamically stabilising it against further transformation [161]. Bhadeshia and Edmonds [57] explained that it is a manifestation of the formation of essentially supersaturated bainitic ferrite, so that the original bainitic ferrite retains much of the carbon content of the parent austenite [59]. In our material here also exists the situation especially the isothermal bainite transformation in high temperature region. The reason could be that the austenite in high temperature is stable as bainite transformation in our material implements at a high temperature (majority higher than 500°C, see figure 2.21). This temperature is normally regarded as the highest temperature of upper bainite. The alloy element in 16MND5 could be another reason, but silicon can be absolutely excluded. D. Quidort and Y. Bréchet said in their paper [49] that 0.5% in mass of silicon is not enough to prevent the cementite precipitation and further the bainite transformation. However there is

only 0.015% silicon in 16MND5. Hence we think that 1.3 wt% Mn in 16%MND5 can make the TTT-curves go to the right which means it needs more time to finish the transformation [162].

Figure 5.20 compares the results obtained with our experiments with half C-curve for 16MND5 low carbon steel, they are consistent. We have plotted the starting temperatures as 5% bainite transformation until 50% bainite fraction transformed. One observes that transformation is fastest at 680°C and that the curve is symmetric around the same 680°C.

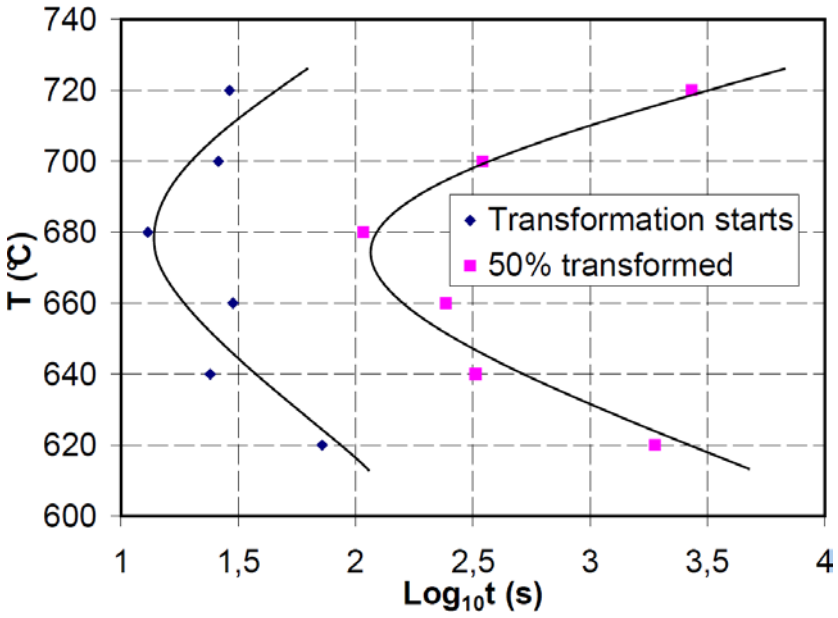

Fig. 5.20 Half C-curve of isothermal bainite transformation in 16MND5

5.2 Effect of bainite transformation on 16MND5 mechanical properties and fracture toughness

5.2.1 Specimens

Comparing with 15-5PH, we used the same fracture samples SENP but different round bar samples because we have used the Gleeble machine to study 16MND5 material. The geometrical plan for fracture test is the same to figure 3.2 and round bar samples were designed as shown in figure 5.21 and 5.22. A special design (displayed in figure 5.23) has to be done for point G because the yield stress at this point is too high after heat treatment.

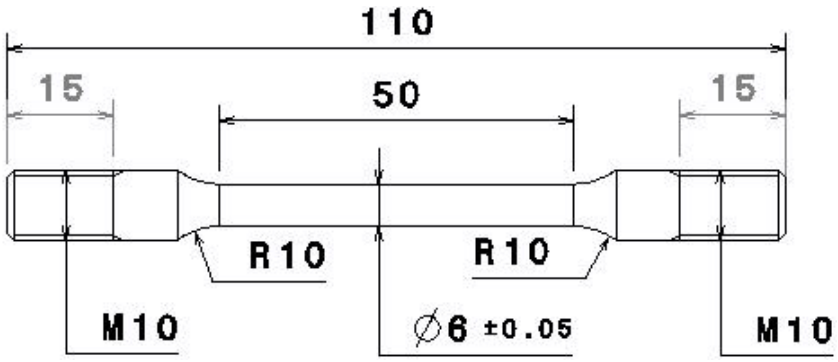

Fig. 5.21 16MND5 round bar sample for tensile test of point A on Gleeble machine

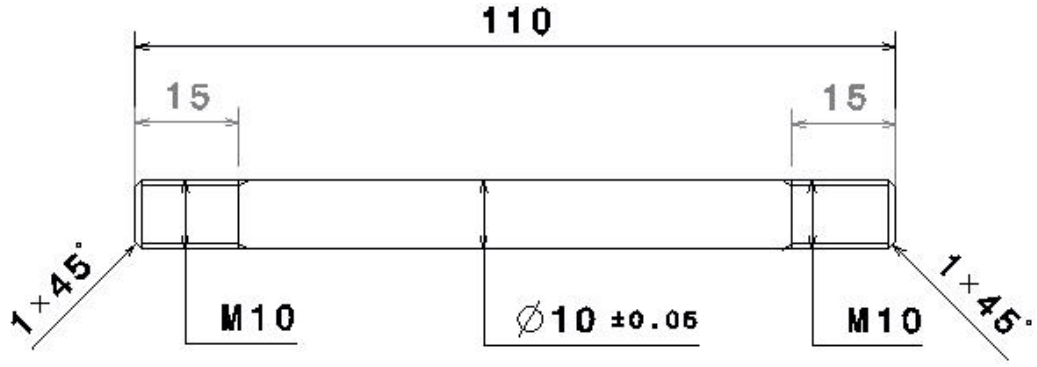

Fig. 5.22 16MND5 round bar sample for tensile test of point B to F on Gleeble machine

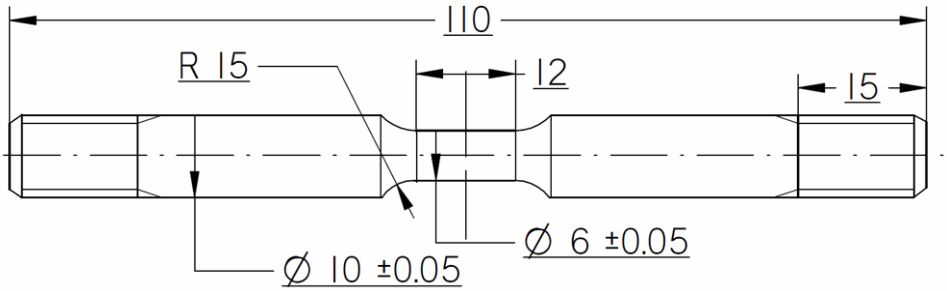

Fig. 5.23 16MND5 round bar sample for tensile test of point G on Gleeble machine

5.2.2 Experimental apparatus

Except the devices for round bar samples, we use the same apparatus for the mechanical tests i.e. fatigue crack fabrication and fracture test as for 15Cr-5Ni stainless steel. For a better accuracy, we did fracture test on the hydraulic tensile machine with maximum force 10kN when the maximum force of the fracture test is small. Otherwise, we did the fracture test on the machine which can provide maximum force 250KN. Figure 5.24 shows you the set-up of the Gleeble 3500 system. The upper picture is the overall view of the Gleeble system with

control panel, operating platform and experimental chamber. Lower left one is the front view of the experimental chamber while lower right one is the side view. During the tensile test of 16MND5 material at different heat treatment situation, dilatometer was used to measure the dilatation and transverse strain. Meanwhile extensometer measures the dilatation also and longitudinal strain, the distance between two sticks of the extensometer is 10 mm. Cooling Air was applied for cooling the measurement devices such as dilatometer and extensometer as the maximum temperature during the tensile test for majority points is 900°C.

For the heating control, three thermocouples were welded on the surface of the round bar specimen for tensile tests. The centre thermocouple is in the center of the specimen, the distance between every thermocouple is 5 mm. For the fracture test, we also used three thermocouples, the centre thermocouple is in the same horizontal line with the pre-crack. Another two thermocouples are symmetrically welded in the two sides of the central thermocouple, the distance between each thermocouple is around 7.5mm.

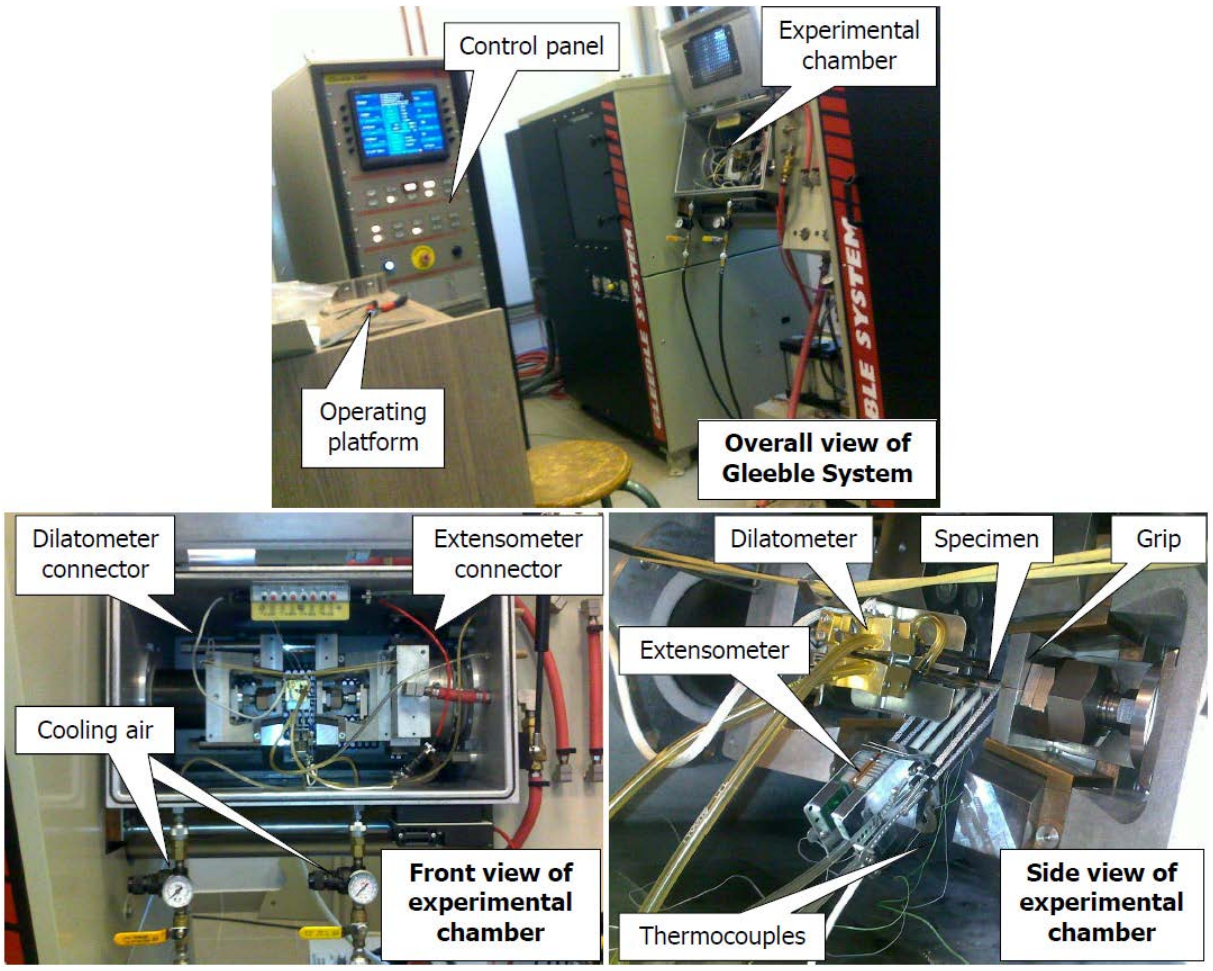

Fig. 5.24 Schematic of Gleeble 3500 system and setup of measuring devices

5.2.3 Stress-strain curves for different metallurgical states from point A to point G

Materials at point A, B are pure bainite, G is nearly pure bainite. Point C has 41% bainite after the isothermal bainite transformation while point D, E and F separately has 36%, 48% and 63% bainite. All the phase fractions can be easily read from figure 5.9 and 5.13.

Tensile tests were accomplished at a displacement rate of 2mm/min until the rupture, the mean strain rate is 2.5%/min (it can be calculated as: the displacement rate divided by the globe length of specimen). Summary of all the tensile tests of 16MND5 low carbon steel after different heat treatment history is shown in figure 5.25. This figure also contains the positions of the selected seven experimental points. Contrary to 15-5PH stainless steel, 16MND5 low carbon steel after whole heat treatment cycle has an ultimate stress which is almost 40% higher and a slightly larger ultimate strain than the as-received material. The other stress-strain curves are not surprising except point B. It has a pure bainitic microstructure at 600°C, we found creep phenomenon during the tensile test at point B. This creep induces stress relaxation at slow strain rate.

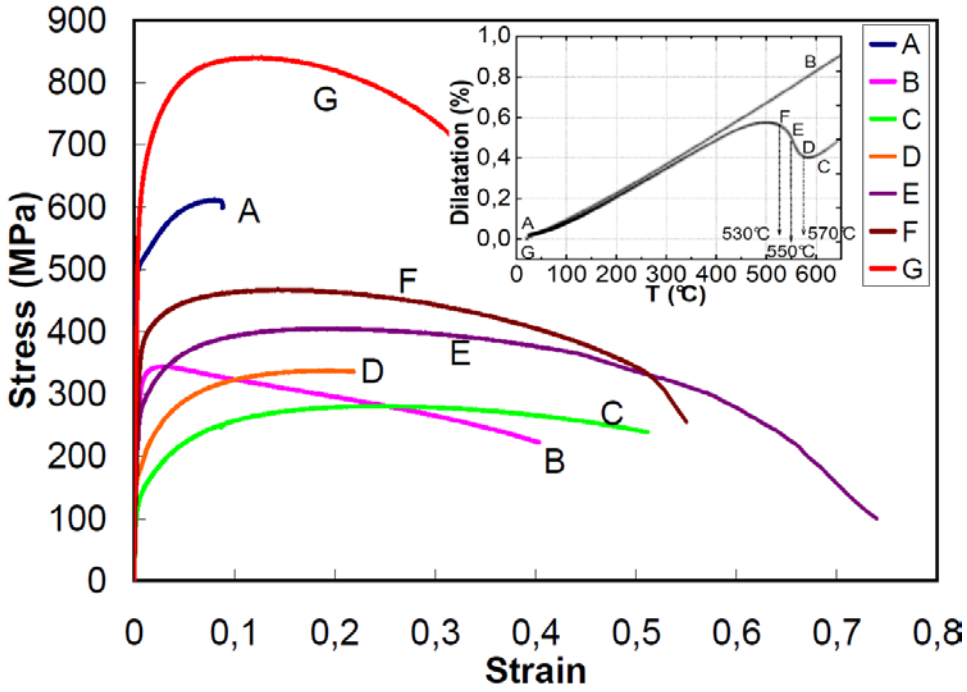

Fig. 5.25 Stress-strain curves of 16MND5 low carbon steel after different heat treatment

Figure 5.26 shows all the round bar specimens after rupture at different metallurgical states.

Fig. 5.26 Round bar samples after rupture

Table 5.3 summarizes all the material parameters of 16MND5 low carbon steel for the different experimental points. Strain at failure for experimental point A is not available because the rupture happened not in the centre. So when failure was happening, the strain given by the extensometer during the experiment is not meaningful. Strain at failure for point D is also not available because the extensometer lost the signal after the maximum force.

Table. 5.3 Summary of material parameters of 16MND5 at different temperature

Experimental point	Yield stress (Mpa)	Young's modulus (GPa)	Ultimate stress (Mpa)	Strain at failure (%)	Section shrinkage at failure (%)
A	420	210	610		67
B	198	141	344	40.33	67
C	101	51	280	51.13	76
D	153	96	338		74
E	194	123	405	73.97	70
F	162	93	467	55.02	68
G	364	203	840	32.53	48

5.2.4 Fracture toughness

5.2.4.1 Fatigue crack fabrication

Potential drop method was used again to produce the pre-crack for the later fracture tests on SENP specimen. Table 5.4 displays the pre-crack information of every SENP sample. One can find that for each experimental point, we produced two pre-cracked fracture samples, one shorter pre-crack length is around 1.5mm while the longer one is about 2.5mm.

Table. 5.4 Fatigue crack fabrication of 16MND SENP samples

Experimental point	Sample number	Fatigue crack length (mm)
A	A1	1.478
	A2	2.522
B	B1	1.494
	B2	2.509
C	C1	1.499
	C2	2.493
D	D1	1.482
	D2	2.517
E	E1	1.499
	E2	2.507
F	F1	1.486
	F2	2.501
G	G1	1.472
	G2	2.595

5.2.4.2 Fracture tests results

Fracture tests were also accomplished with a displacement rate of 0.5mm/min until the crack growth to about one half of the width. During the fracture test, PD and DIC were also recorded at room temperature. Figure 5.27 shows the fracture curves at every experimental point (from A to G). The abscissa is the total displacement in the loading direction and the ordinate is the applied loading, loading line displacements and forces are all given by the hydraulic machine.

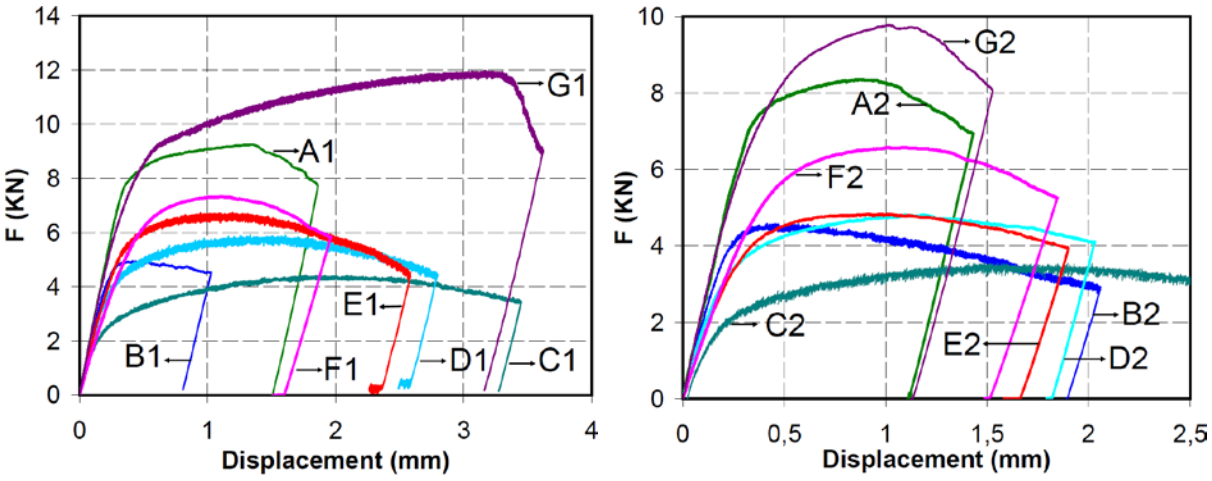

(a) short pre-crack length (b) long pre-crack length

Fig. 5.27 Fracture test results of all the 16MND5 SENP samples

Figure 5.27 (a) shows the result obtained with short pre-cracks (1.5 mm). The longer ones are shown in figure 5.27 (b).

5.2.4.3 Boundary conditions from DIC for the FEM simulation

Similar to what we have done for 15-5PH stainless steel, we used DIC again to find the boundary conditions for the finite element analysis. We only display the displacement at the four points E, PE, F and PF. 16MND5 is more ductile than 15-5PH which has the consequence that the displacement history of point E, PE, F and PF is no longer proportional. Once we have the displacement conditions at every picture on the four points, we will directly impose the boundary conditions on the mesh nodes in the simulation. Figure 5.28 compares the displacement at every point found by DIC and imposed to the corresponding nodes in the simulation. The abscissa is time proportion in the fracture experiment or step proportion in the simulation related to experimental time.

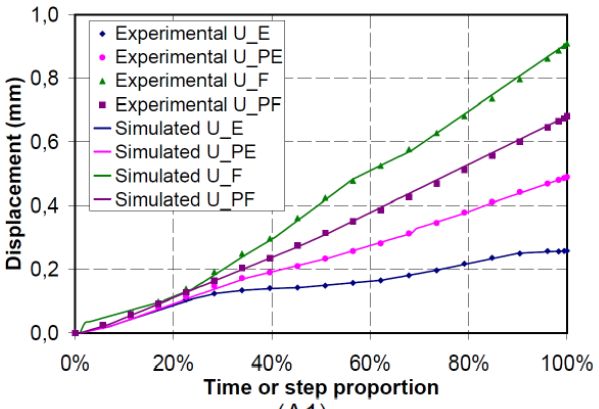

(A1)

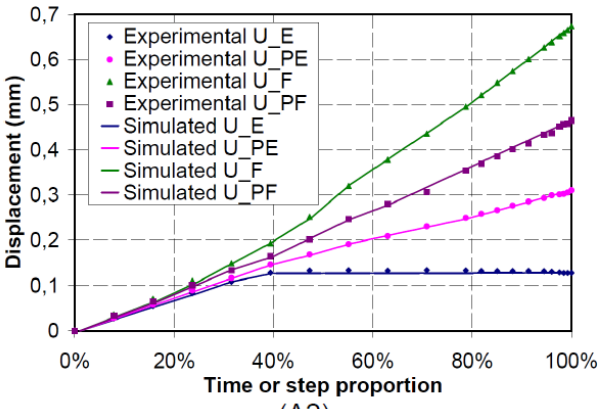

(A2)

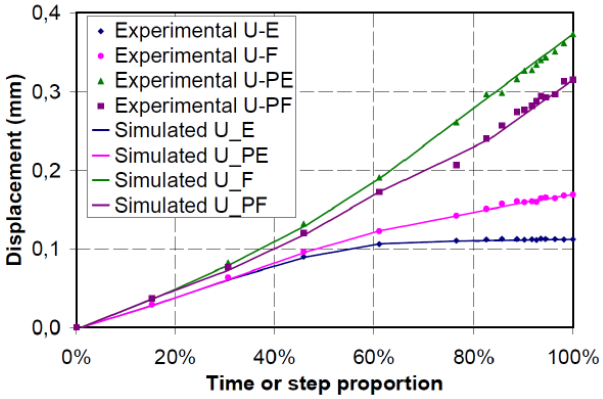

(B1)

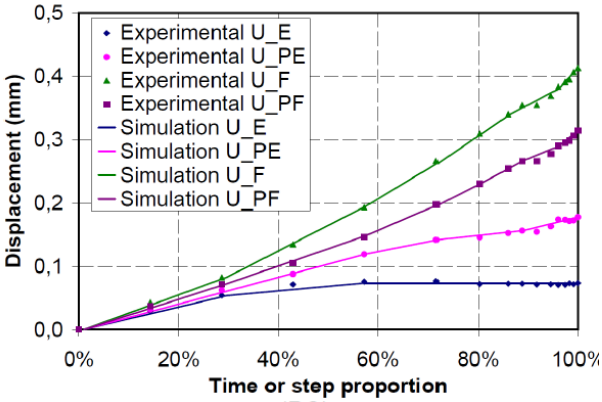

(B2)

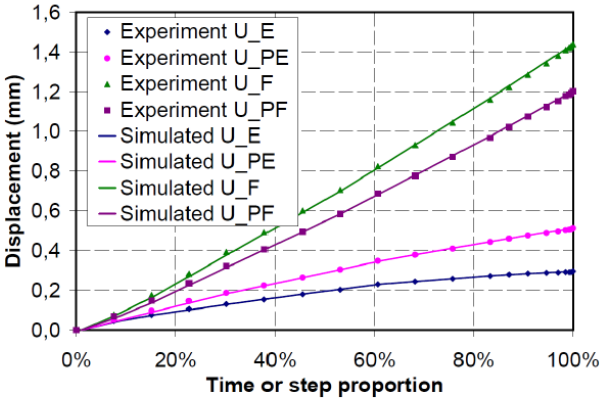

(C1)

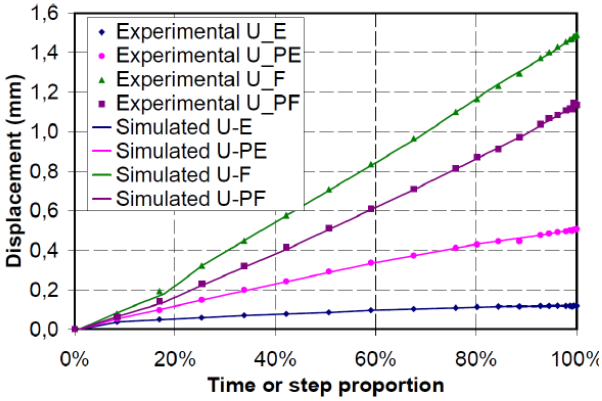

(C2)

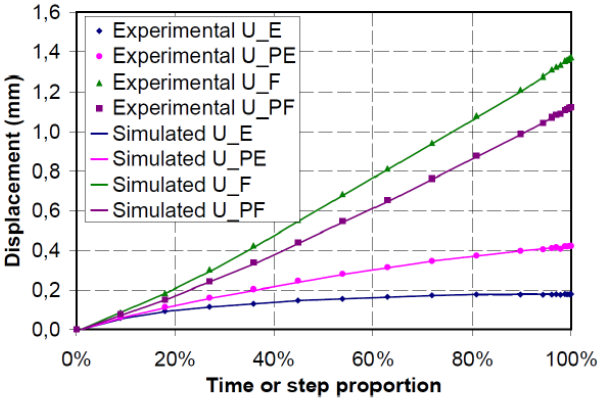

(D1)

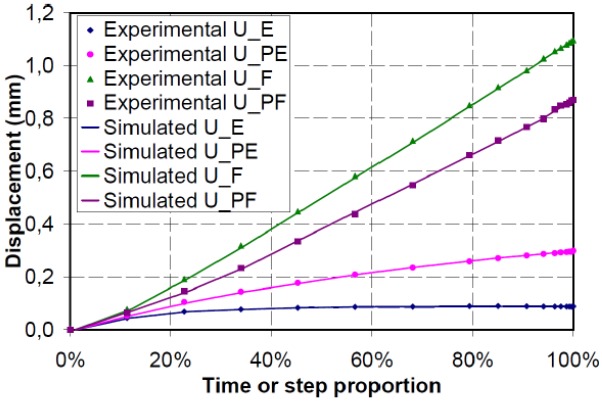

(D2)

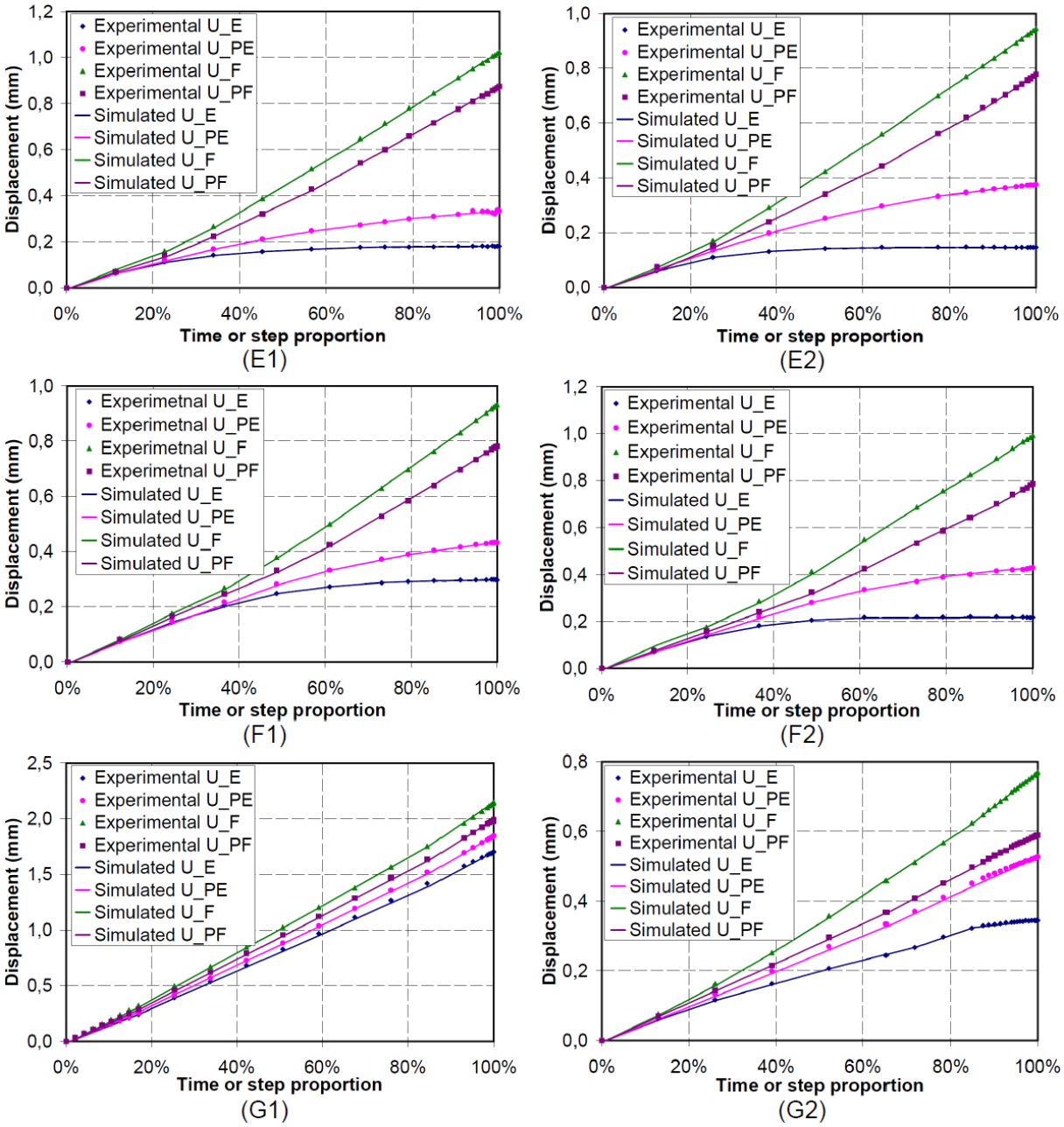

Fig. 5.28 Boundary conditions detected by DIC and imposed in the simulation

5.2.4.4 Fractography observation

Like the investigation on 15-5PH, we did fractography observation also. Following figure 5.29 displays all fractography at seven experimental points from A to G. The crack growth direction is from the left of the picture to the right. Now we analyze them one by one. Concering the fracture surface of point A i.e. as received condition of 16MND5 material, there are few dimples which are very shallow, while there are plenty of cleavage facets. Hence, at received condition, the fracture of 16MND5 appears by cleavage. Compared to A, there are more dimples on fractography G, and these dimples are much smaller and a little bit

deeper. While there are no obvious cleavage facets between these dimples. So, conclusion should be given to point G about the fractography of 16MND5 at room temperature after one whole cycle heat treatment: the fracture type is ductile fracture. Point B is pure bainite at 600°C while point C is dual phase (austenite and bainite) austenite at the same temperature, their fractography both have the big dimples which are much deeper than those from point G. We can find also there are inclusions in not only figure B but also C. So the fracture mechanism is ductile fracture for point B and point C. The fractography D, E and F all has lots of small dimples and no typical cleavage facets. So, they are also mainly ductile fracture.

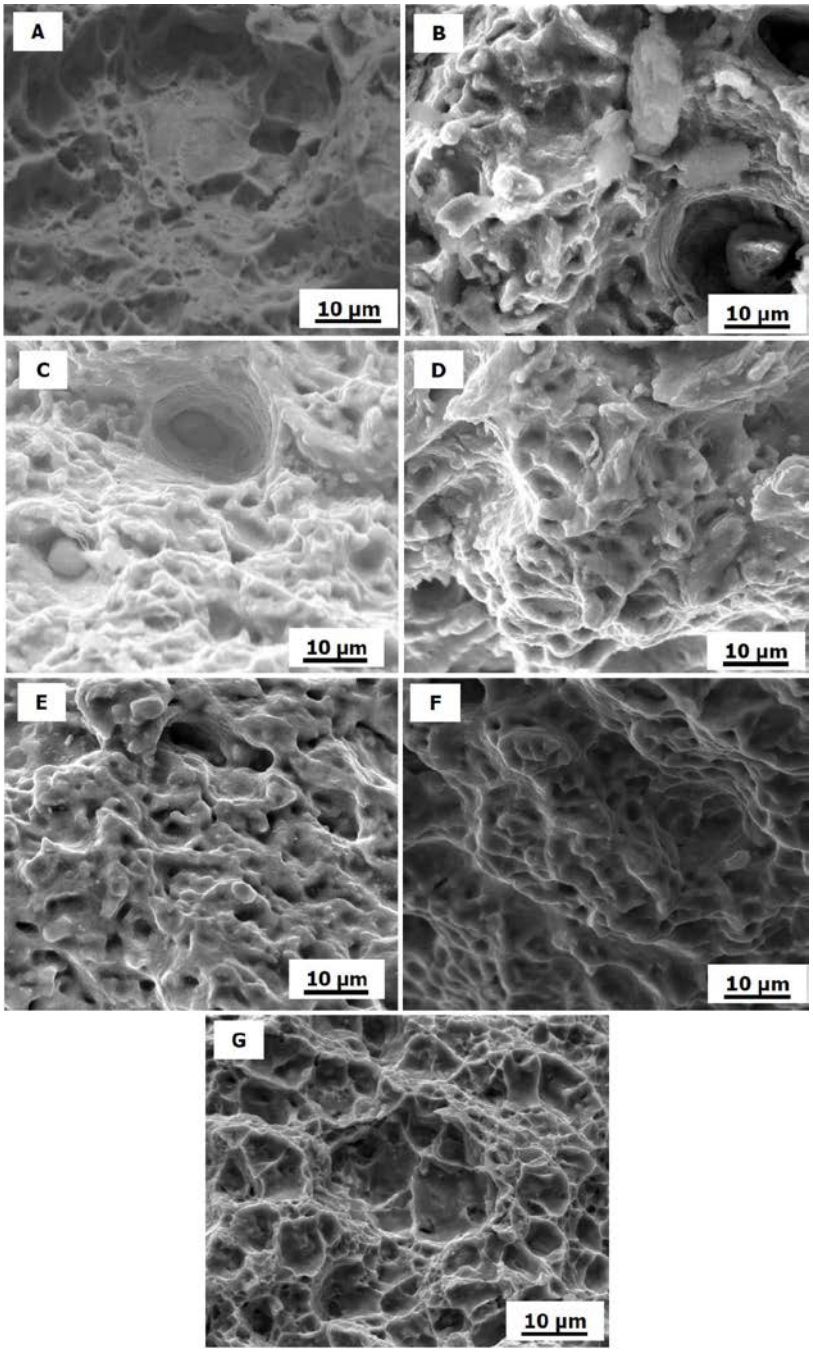

Fig. 5.29 Fractography of 16MND5 at different condition

Actually, during our tensile test at point B where the temperature is 600°C, we found that there was creep. We decided not to go deeper here for point B as said before.

5.2.4.5 Numerical simulation

Then we imposed the displacement loading which has been shown in figure 5.27 to the nodes E, PE, F and PF, figure 5.30 displays the comparison between experimental and simulated result about force versus mean displacement after the simulation.

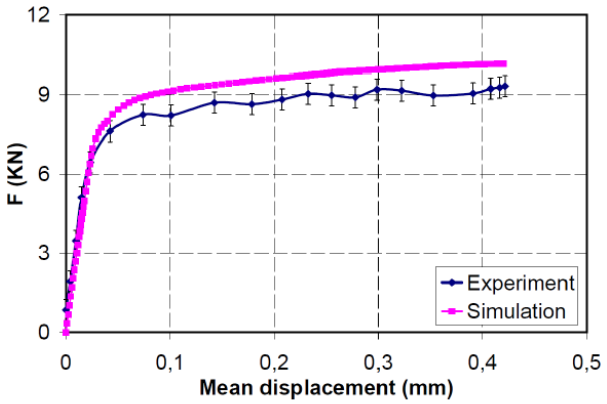

(A1)

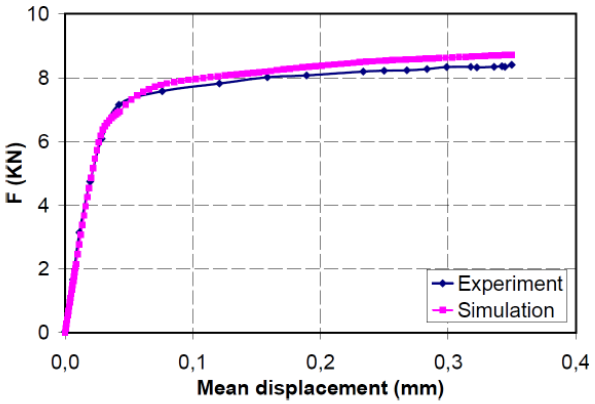

(A2)

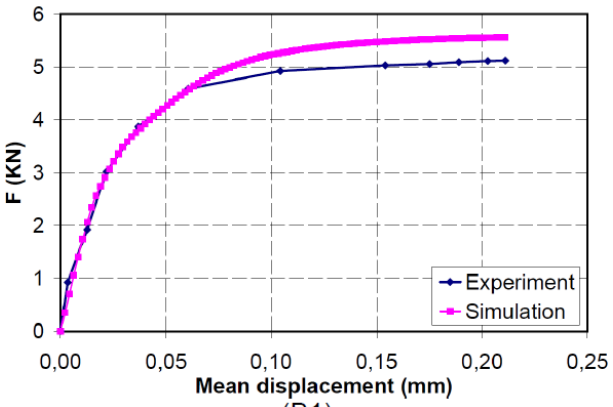

(B1)

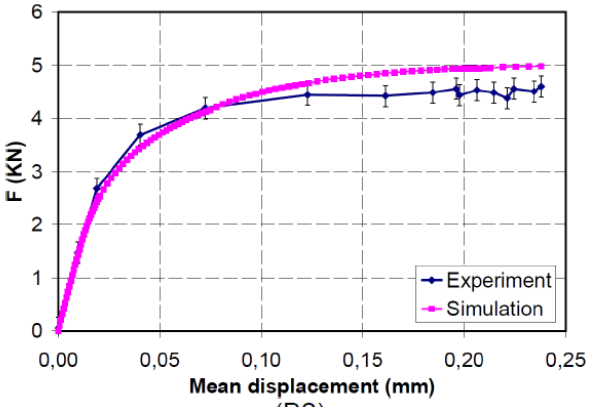

(B2)

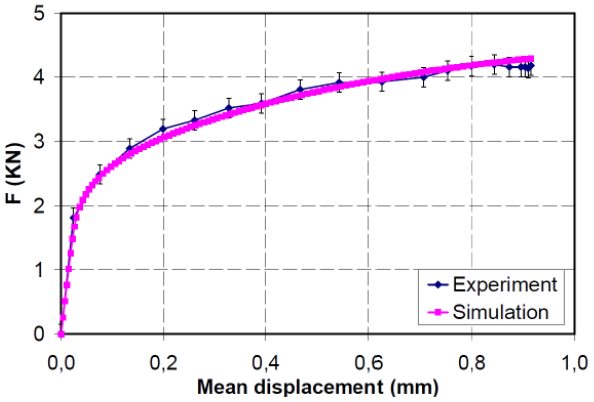

(C1)

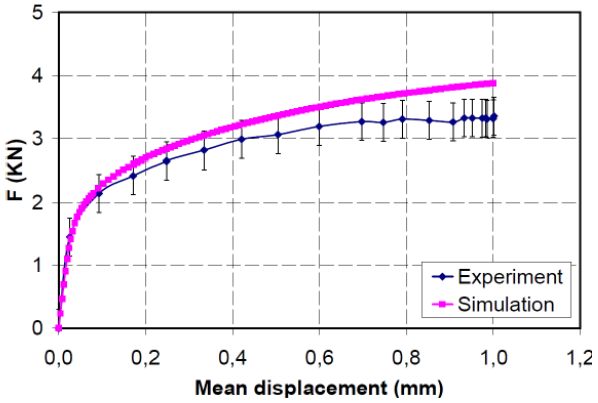

(C2)

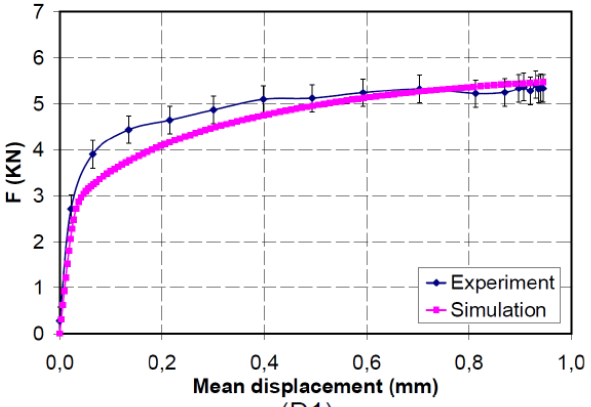

(D1)

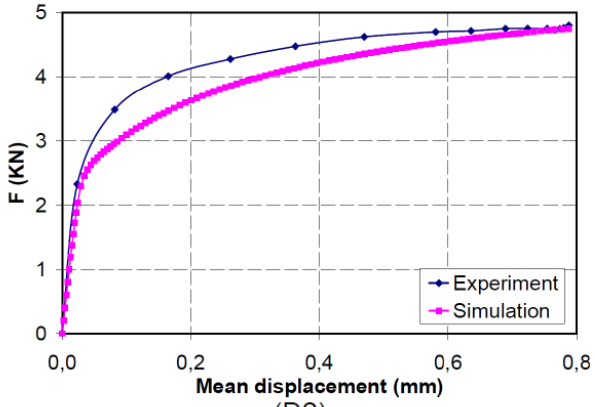

(D2)

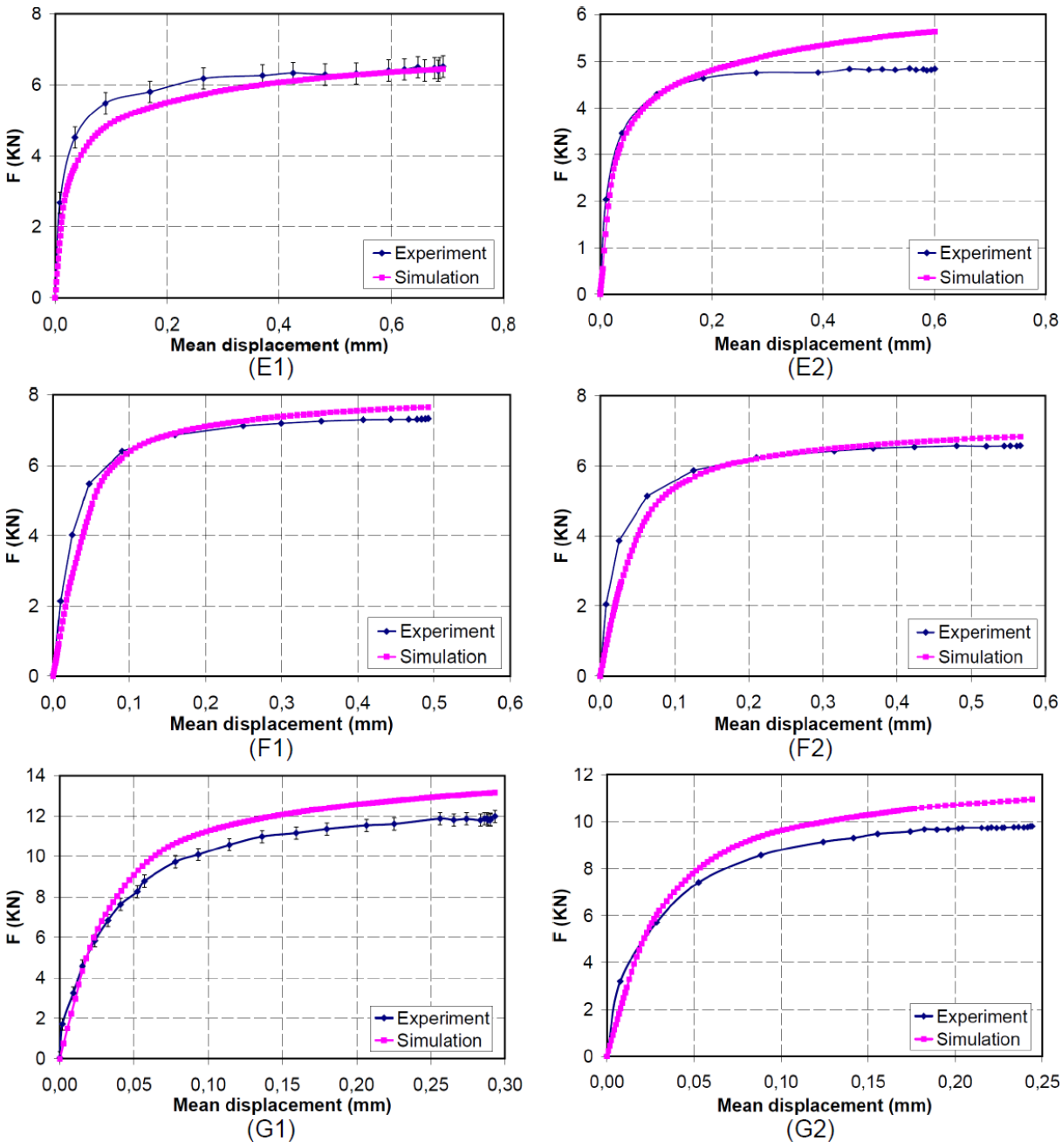

Fig. 5.30 Comparison between experimental and simulated result

Table 5.5 displays the finite element analysis result of every experimental point from A to G. Figure 5.31 is our result of critical *J*-integral estimation result of 16MND5 low carbon steel after different heat histories.

Table. 5.5 Critical *J*-integral results of all 16MND5 SENP samples

Experimental point	Sample number	Experimental temperature (°C)	Critical *J*-integral (KJ/m^2)	Mean J_{1C} (KJ/m^2)
A	A1	20	308	284
	A2		260	
B	B1	600	66	77
	B2		88	
C	C1	600	177	219
	C2		260	
D	D1	570	259	252
	D2		244	
E	E1	550	241	240
	E2		238	
F	F1	530	232	258
	F2		284	
G	G1	20	243	240
	G2		237	

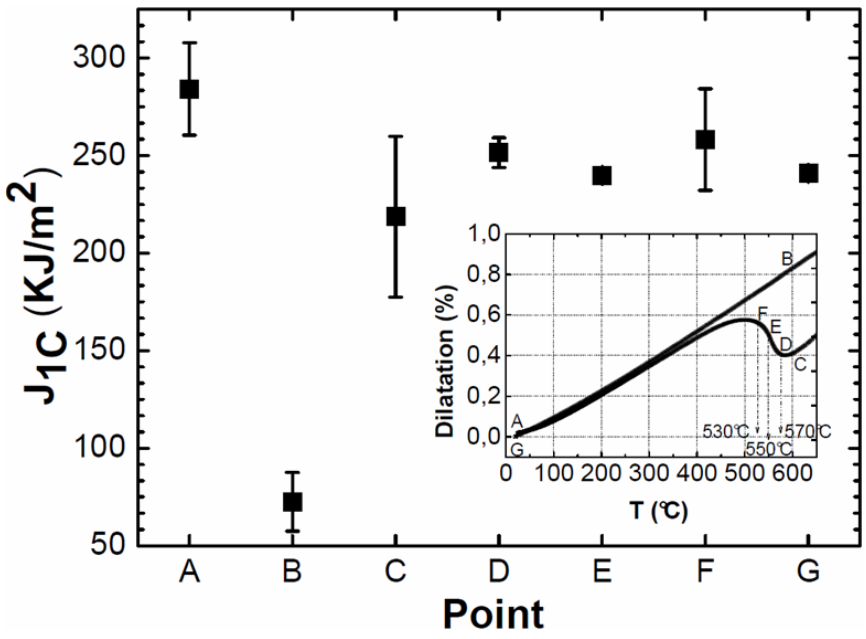

Fig. 5.31 Critical *J*-integral of 16MND5 after different heat treatment

5.2.5 Results analysis

The results presented in figure 5.31 also show that the heat treatment and metallurgic phase transformation has an important influence on the mechanical properties of 16MND5 low carbon steel. The material of 16MND5 after one cycle bainite transformation has a 40% higher strength than the original material (see figure 5.25 and table 5.1). This means that the

continuous cooling bainite transformation can refine the microstructure and hence enhance the strength of the original material. From figure 5.32, we can find that the grain size of the material after continuous cooling bainite transformation has been refined.

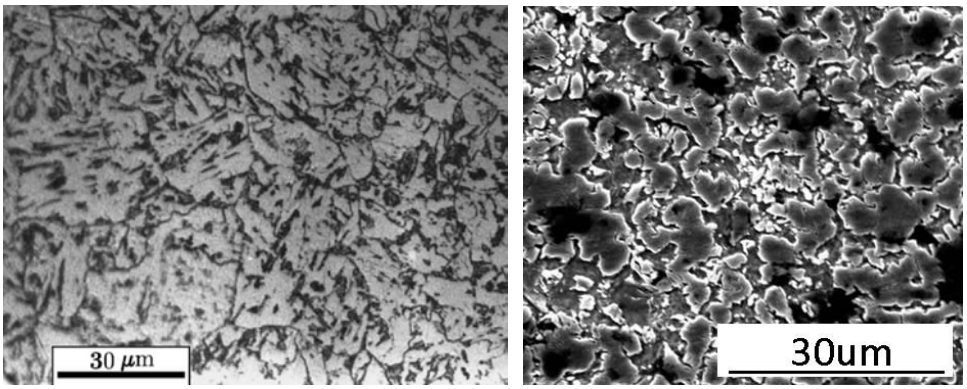

Fig. 5.32 Microstructure 16MND5 low carbon steel. The left one is the as-received condition [42] and the right one is the one after one cycle bainite transformation

If we compare point A and B, which are fully bainitic, but at different temperature, A has a much bigger J_{1C} value than B. This is consistent with the result of 15-5PH. If we look at the tensile curves of point A and B at figure 5.25, we found not only the ultimate stress became smaller but also ultimate strain. Concerning the potential influence of the creep phenomenon, this need to be done more deeply in the future.

For the toughness at the same temperature 600°C but with two different metallurgic status: cases B (fully bainite) and C (41% bainite + 59% austenite, see figure 5.9), J_{1C} for case B is clearly smaller than the one of case C. It means that 16MND5 with mixed phases of bainite and austenite at 600°C has a better fracture toughness than another one situation with pure bainite at same temperature. Let us observe that 16MND5 at point C at 600°C shows no creep.

Comparing the toughness J_{1C} of case A and G, the as received material has a slightly higher fracture toughness than the material after a whole cycle heat treatment, but if we take the estimation error of these two results, we can find that the difference between them is not significant. It means that one cycle heat treatment hasn't significant influence on the fracture toughness of the bainitic 16MND5 low carbon steel.

For cases D, E and F, both bainite and austenite phase co exist in the material and their proportion is given in figure 5.13. The J_{1C} value is similar to each other at these three cases, we think the effect from the phase proportion is neutralized with the influence from temperature change.

Overall, we can conclude that bainite transformation hasn't a huge influence on the fracture toughness of 16MND5 low carbon steel. This is not correlated to the stress-strain results which show that the material has a much higher ultimate stress at room temperature after a cycle heat treatment. The fact that fracture toughness at 600°C before austenitization is much lower could explain the crack propagation in parent material close to repair regions during the refilling operation. This point has to be checked with great care. The presented results showing the important effects of thermal history on material non linear properties clearly show that this topic should be investigated more deeply to ensure a good quality of the complex welding simulations. The observed loss of toughness during heating phase is of prime importance for the estimation of safety during severe accidents like the recent Fukushima accident.

Chapter 6 Conclusions and Perspectives

6.1 Conclusions

A lot of experiments and simulation works have been done in our study whose objective is dedicated to find the effects of metallurgical phase transformation on crack propagation. This may help us to better understand the change of fracture toughness of the material during the crack repair process by welding. Critical *J*-integral characterizes the fracture toughness which can express the resistance ability of crack initiation for the material. After comparing several current estimation method of critical *J*-integral, we proposed an economic and practicable method to evaluate J_{1C} with only one single edge notched plate specimen which combined digital image correlation, potential drop and finite element analysis technologies. First of all, potential drop method controlled the pre-crack fabrication and gives us the expected pre-crack length, then potential drop method was applied again with digital image correlation during the fracture test at room temperature, these two technologies could help and confirm to each other to find the crack initiation moment. We successfully did a good painting for the mechanical tension at higher temperature resisting to a maximum temperature 900°C and high mechanical test temperature 600°C. Once we found that critical moment, digital image correlation method was applied again to supply the local boundary conditions for the later finite element simulation. Meanwhile, the basic characteristic was provided to the simulation by the traditional tensile test. Then the critical *J*-integral value was computed using the G_theta method.

With this J_{1C} estimation method, we did our research on the 15-5PH martensitic stainless steel and 16MND5 low carbon steel. In 15-5PH, there exists only martensite transformation during cooling period, while there are pearlite transformation, bainite transformation and also martensite transformation in 16MND5 in different cooling conditions. Hence we studied in details phase transformations in these two materials at different situations, before doing the mechanical tests. Dilatometry technology was then applied to study the transformation kinetics and to calculate the phase fraction which could explain the effect of metallurgical phase transformation on fracture toughness. We found for 15-5PH steel that the martensite transformation starting temperature is around 185°C and the related martensite transformation ending temperature is nearly 80°C when the cooling rate is -5°C/s. While for 16MND5 low carbon steel, we did the similar heat treatment which (+5°C/s heating and -5°C/s cooling) the bainite transformation would take place around 585°C and finish around 450°C. The bainite

transformation kinetics found by dilatometry technology proved that the bainite transformation is an incomplete bainite transformation. Moreover there is no isothermal transformation in 15-5PH which implied that we can start the mechanical test just after control the temperature is obtained, while there exists isothermal bainite transformation in 16MND5. This forces us to wait for the end of the isothermal bainite transformation when we want to do the mechanical test.

After the transformation kinetics was studied for 15-5PH and 16MND5, we chose seven study points in each material which they are the receiving condition point, the one after one whole cycle heat treatment, three points during the martensite transformation in 15-5PH or three points during the bainite transformation in 16MND5, and two points with one just before the related transformation and another one at the same temperature but before the austenitization. Then we applied our J_{1C} estimation method to do the mechanical research.

Investigation result shows the influence of metallurgical phase transformation on the fracture toughness and further crack propagation.

For 15-5PH the influence is significant. The result of J_{1C} value shows that the pure martensitic 15-5PH has higher fracture toughness at room temperature than the one at 200°C. The toughness is also higher than the original material after one cycle heat treatment, which is probably caused by some residual austenite. Meanwhile, pure austenite 15-5PH has a higher fracture toughness than pure martensitic 15-5PH at 200°C. The J_{1C} value of the dual phase 15-5PH during the martensitic transformation also shows that possibly austenite can enhance the ductility of the material as well as fracture toughness.

For 16MND5 low carbon steel the influence is not large except at 600°C where creep occurs. The material at receiving condition has much bigger J_{1C} value than the situation where it was heated to 600°C. On the other hand, the material at 600°C just before isothermal bainite transformation after the austenitization during cooling process also has higher fracture toughness than the one at 600°C before austenitization. These two conclusions are consistent well with the result of 15-5PH. But 16MND5 after one cycle heat treatment has a slightly smaller J_{1C} value compared with the as received situation. It means that one cycle heat treatment hasn't a significant influence on the fracture toughness of the bainitic 16MND5 low carbon steel. When both bainite and austenite phase co exist in the 16MND5 material, the J_{1C}

value is similar to each other at these three cases during the bainite transformation, we think the effect from the phase proportion is neutralized with the influence from temperature change.

Conclusions of our research show that we should pay attention to the heating period before austenitization of the base material. When people weld for crack reparation, the high temperature will bring lower fracture toughness during this phase of the process. While during cooling period, the fracture toughness doesn't change a lot. 15-5PH martenstic stainless steel has even a better fracture toughness after the martensite transformation than the as-received condition.

6.2 Perspectives

This thesis concerns the critical *J*-integral estimation which is difficult to obtain and some problems need to be studied in the future.

The first one is the estimation method of J_{1C} for ductile materials. We proposed an economic and practicable method to evaluate the critrical *J*-integral value, but it still needs to be discussed even the comparison result has shown that the J_{1C} result obtained by our method is similar to others. What is the best geometry to be chosen for the experimental J_{1C} estimation and efficient numerical estimation? Can one reduce the difference between the simulated and experimental force versus mean displacement? Does the difference always exists or it is due to the pre-crack size and shape?

In the transformation kinetics aspect, does 15-5PH has some residual austenite after the martensite transformation at room temperature? This needs XRD examination.

What is the isothermal transformation before and during the anisothermal bainite transformation in 16MND5? The fact that bainite transformation takes place during the isothermal state when the cooling process is stopped is interesting. It could help to better understand the bainite transformation mechanism which is still in debate for many years provided that some in-situ observation and carbon movement tracking works could be done by some advanced machines and research methods.

Moreover, the reason which causes the change of the fracture toughness for all cases need to be understood more deeply. Does the residual austenite enhance the 15-5PH J_{1C} after one whole cycle heat treatment? In the three points we have chosen during the martensite or bainite transformation for these two materials, what's the relation between the temperature,

phase proportion and fracture toughness? Can we find a mathematical expression for J_{1C} as a function of temperature and phase proportion? Another problem is that, 16MND5 low carbon steel has a similar J_{1C} value after one cycle heat treatment compared to the original material. This is the opposite effect with the result of 15-5PH. We have explained some results we found by macroscopic point of view, but it should be better explained with some microstructure explanation.

One last interesting thing is the creep phenomenon at 600°C of 16MND5 low carbon steel. It was found that the tensile test in a short time and several creep experiments with constant stress provides the creep laws. The effect should be taken into account with a viscoplastic model for the fracture toughness evaluation for 16MND5 at 600°C. This has to be taken into account for a good control of crack propagation estimation during welding process for this important industry materal.

References

[1] Viswam Institute of Engineering & Technology, Gallery of welding, http://www.wildeck.com/about_us/manufacturing.html

[2] Pipe multi-jointing services, Onshore and offshore fabrication, http://photo.machinestogo.net/main.php/v/user/lincoln/pipe_welding_2.jpg.html

[3] Jonathan Atteberry, How welding works, http://science.howstuffworks.com/welding2.htm

[4] Peters WH, Ranson WF. Digital imaging techniques in experimental stress analysis, Optical Engineering, 1982; 21(3) : 427-31.

[5] Jinlong Chen, Ganmin Xia, Kebin Zhou, Guisuo Xia, Yuwen Qin, Two-step digital image correlation for micro-region measurement, Optics and Lasers in Engineering, 43 (2005) 836-846.

[6] Shun-Fa Hwang, Jhih-Te Horn, Hou-Jiun Wang, Strain measurement of SU-8 photoresist by a digital image correlation method with a hybrid genetic algorithm, Optics and Lasers in Engineering, 46 (2008) 281-289.

[7] S. Roux, J. Réthoré, F. Hild, Digital image correlation and fracture: an advanced technique for estimating stress intensity factors of 2D and 3D cracks, J. Phys. D: Appl. Phys., 42 (2009) 214004 (21pp).

[8] T.C. Chu, W.F. Ranson, M.A. Sutton, W.H. Peters, Applications of Digital.Image-Correlation Techniques to Experimental Mechanics, Experimental Mechanics, 25: (3) (1985) 232-244.

[9] S. Mugil-Touchal, F. Morestin, M. Brunet, Various experimental applications of digital image correlation method, CMEM 97 (Computational Methods and Experiental Measurements VIII), 1997, Rhodes.

[10] Zhengzong Tang, Jin Liang, Zhenzhong Xiao, Cheng Guo, Large deformation measurement scheme for 3D digital image correlation method, Optics and Lasers in Engineering, 50 (2012) 122-130.

[11] Chu, T. C., Ranson, W. F., Sutton, M. A., Peters, W. H., Application of Correlation Techniques to Experimental Mechanics, Experimental Mechanics, September 1985, 232-244.

[12] Computerized Measurement Products Services, Spring/Summer, 1994, 1223 People Avenue, TROY, NY 12180-3590.

[13] Julien Réthoré, François Hild, Stéphane Roux, Shear-band capturing using a multiscale extendeddigital image correlation technique, Comput. Methods Appl. Mech. Engrg., 196 (2007) 5016-5030.

[14] Jinlong Chen, Xiaochuan Zhang, Nan Zhan, Xiaoyan Hu, Deformation measurement across crack using two-step extended digital image correlation method, Optics and Lasers in Engineering 48: (2010), 1126-1131.

[15] Besnard G,Hild F, Roux S, finite element displacement fields analysis from digital images: application to Portevin-LeChatelier bands, Experimental Mechanics, 2006; 46(6): 789-803.

[16] Julien Réthoré, François Hild, Stéphane Roux, Extended digital image correlation with crack shape optimization. International Journal for Numerical Methods in Engineering, 2008; 73: 248-72.

[17] Stéphane Roux, François Hild, Digital image mechanical identification (DIMI). Experimental Mechanics, 2008; 48(4): 495-508.

[18] T. Belytschko, N. Moes, S. Usui, C., Parimi, Arbitrary discontinuities in finite elements, Int. J. Numer. Methods Engrg., 50 (4) (2001) 993-1013.

[19] N. Moes, J. Dolbow, T. Belytschko, A finite element method for crack growth without remeshing, Int. J. Numer. Methods Engrg., 46: (1), (1999), 133-150.

[20] S.V. Lomov, Ph. Boisse, E. Deluycker, F. Morestin, K. Vanclooster, D. Vandepitte, I. Verpoest, A. Willems, Full-field strain measurements in textile deformability studies, Composites: Part A (2007), doi:10.1016/j.compositesa.2007.09.014.

[21] Rethore J., Gravouil A., Morestin F., Combescure A., Estimation of mixed-mode stress intensity factors using digital image correlation and an interaction integral. Int J Fract, 2005, 132: 65-79.

[22] Wu, T., Experiment and numerical simulation of welding induced damage of stainless steel 15-5PH. Ph.D. Thesis, INSA de Lyon, France, 2007.

[23] H. H. Johnson, Calibrating the electric potential method for studying slow crack growth, Materials research & Standards, 1965; 442-445.

[24] I.S. Hwang, R.G. Ballinger, A multi-frequency AC potential drop technique for the detection of small cracks, Meas. Sci. Technol., 3 (1992) 62-74.

[25] I. Cerny, The use of DCPD method for measurement of growth of cracks in large components at normal and elevated temperatures, Engineering Fracture Mechanics, 71 (2004), 837-848.

[26] H. Nayeb-Hashemi, D. Swet, A. Vaziri, New electrical potential method for measuring crack growth in nonconductive materials, Measurement, 36 (2004), 121-129.

[27] Yasumoto Sato, Takeo Atsumi, Tetsuo Shoji, Application of induced current potential drop technique for measurements of cracks on internal wall of tube-shaped specimens, NDT&E International, 40 (2007), 497-504.

[28] ZQ. Cui, BX. Liu, Metallurgy and heat treatment. HIT Press, 1998, 104-105.

[29] Aamir, Cubic Unit Cells, http://wikis.lawrence.edu/display/CHEM/Properties+of+Solids-----Aamir, 2007.

[30] Fe-Fe_3C diagram, http://www.metalvemalzeme.com/demir-celik-denge-diagrami/, 2007.

[31] J.S. Dong, Iron and Steel, http://www.josen.net/post/20-GangXianWeiZuZhi.html, 2011.

[32] J.S. Dong, Iron and Steel, http://www.josen.net/post/BeiShiTibainite-ZuZhiXingTai.html, 2011

[33] B.L. Yi, Observation and analysis of the balance organization of steel alloy, http://202.194.15.128/jxgc/vr/experiments/experiment2.htm, 2006

[34] H. K. D. H. Bhadeshia, Interpretation of the Microstructure of Steels, POSTECH Graduate Institute of Ferrous Technology (GIFT), http://cml.postech.ac.kr/2008/Steel_Microstructure/SM2.html

[35] Metal Ravne Steel Selector v.4.0, Transformation Diagrams (CCT & TTT), http://www.metalravne.com/selector/help/testing/ttt.html, 2011.

[36] Forging Knives, Heat Treatment, http://www.navaching.com/forge/heattreat.html, 2008.

[37] Time-Temperature Transformation (TTT) Diagram, Oyal Metal, http://www.oyalmetal.com/tablolar/100-osikrosp.html, 2011.

[38] T. Y. Hsu, Martensite transformation and martensite, edition 2. Beijing: Science Press, 556-564, 1999.

[39] Hamata N., Modelisation du Couplage Entre L'elasto-viscoplasticité Anisotherme et la Transformation de Phase D'un Fontr G.S. Ferritique, Thèse de Doctorat de L'université Paris 6, 1992.

[40] Hashin Z., Shtrikman S., A variational approach to the theory of the effective magnetic permeability of multiphase materials, J. Applied Phys., 33: 3125-3131, 1962.

[41] M. Coret, S. Calloch, A. Combescure, Experimental study of the phase transformation plasticity of 16MND5 low carbon steel under multiaxial loading, International Journal of Plasticity, 18: 1707-1727, 2002.

[42] B. Tanguy, J. Besson, R. Piques, A. Pineau, Ductile to brittle transition of an A508 steel characterized by Charpy impact test Part I: experimental results. Engineering Fracture Mechanics, 72 (2005) 49-72.

[43] P. Hausild, C. Berdin, P. Bompard, Prediction of cleavage fracture for a low-alloy steel in the ductile-to-brittle transition temperature range, Materials Science and Engineering A, 391,(2005),188-197.

[44] H.-G. Willschuetz, E. Altstadt, B.R. Sehgal, F.-P. Weiss, FEM-Calculation of Different Creep-Tests with French and German RPV-Steels. Transactions of the 17th International Conference on Structural Mechanics in Reactor Technology (SMiRT 17), Prague, Czech Republic, August 17-22, 2003.

[45] M. Martinez, Jonction 16MND5-INCONEL 690-316LN par Soudage Diffusion Elaboration et Calcul des Contraintes résiduelles de procédé. PhD thesis, ENSMP, 1999, France.

[46] Honeycombe, RWK (1981). Steels: Microstructure & Properties.

[47] Bhadeshia, H. K. D. H., Bainite in Steels. The Institute of Materials, London, 1992.

[48] Smith, Cyril Stanley (1960). A History of Metallography. University of Chicago Press. pp. 225. Annexes

[49] D. Quidort, Y. J. M. Brechet, Isothermal Growth Kinetics of Bainite in 0.5% C Steels, Acta Mater., 49, (2001), 4161-4170.

[50] Y. Ohmori, T. Maki, Bainitic Transformation in View of Displacive Mechanism, Mater. Trans. JIM, 1991, 32(8): 631.

[51] M. Hillert, L. Höglund, J. Ågren, Escape of carbon from ferrite plates in austenite, Acta Metallurgica et Materialia, 1993, 41(7): 1951-1957.

[52] M. Hillert, The nature of bainite, ISIJ Int., 1995, 35, 1134.

[53] M.A. Yescas, H.K.D.H. Bhadeshia, Model for the maximum fraction of retained austenite in austempered ductile cast iron, Mater. Sci. Eng. A., 333 (2002) 60-66.

[54] C. Garcia-Mateo, H.K.D.H. Bhadeshia, Nucleation theory for high-carbon bainite, Mater. Sci. Eng. A., 378 (2004) 289-292.

[55] R.P. Garrett, S. Xu, J. Lin, T.A. Dean, A model for predicting austenite to bainite phase transformation in producing dual phase steels, International Journal of Machine Tools & Manufacture., 44 (2004) 831-837.

[56] G. Sidhu, S.D. Bhole, D.L. Chen and E. Essadiqi, An improved model for bainite formation at isothermal temperatures, Scripta Materialia., 64 (2011) 73-76.

[57] Bhadeshia H.K.D.H., Edmonds D.V., The mechanism of bainite formation in steels, Acta Metall., 1980; 28: 1265.

[58] Bhadeshia H.K.D.H., Waugh A.R., Bainite: An atom-probe study of the incomplete reaction phenomenon, Acta Metall., 1982; 30: 775.

[59] F.G. Caballero, C. Garcia-Mateo, M.J. Santofimia, M.K. Miller, C. Garcia de Andrés, Acta Materialia, 57 (2009) 8-17.

[60] P.H. Shipway, H.K.D.H. Bhadeshia, The effect of small stresses on the kinetics of the bainite transformation, Mater. Sci. Eng. A., 201 (1995) 143-149.

[61] Manabu Takahashi, Recent progress: kinetics of the bainite transformation in steels, Current Opinion in Solid State and Materials Science., 8 (2004) 213-217.

[62] P. Jacques, E. Girault, T. Catlin, N. Geerlofs, T. Kop, S. van der Zwaag, F. Delannay, Bainite transformation of low carbon Mn–Si TRIP-assisted multiphase steels: influence of silicon content on cementite precipitation and austenite retention, Mater. Sci. Eng. A., 273-275 (1999) 475-479.

[63] D. Quidort, Y. Bréchet, The role of carbon on the kinetics of bainite transformation in steels, Scripta Materialia., 47 (2002) 151-156.

[64] L.C. Chang, Microstructures and reaction kinetics of bainite transformation in Si-rich steels, Mater. Sci. Eng. A., 368 (2004) 175-182.

[65] R. Mahnken, A. Schneidt, S. Tschumak, H.J. Maier, On the simulation of austenite to bainite phase transformation, Computational Materials Science., 50 (2011) 1823-1829.

[66] H.K.D.H. Bhadeshia, The bainite transformation: unresolved issues, Mater. Sci. Eng. A., 273-275 (1999) 58-66.

[67] F.G. Caballero, M.K. Miller, C. Garcia-Mateo, Carbon supersaturation of ferrite in a nanocrystalline bainitic steel, Acta Materialia, 58 (2010) 2338-2343.

[68] M. Martinez, Jonction 16MND5-INCONEL 690-316LN par Soudage Diffusion Elaboration et Calcul des Contraintes résiduelles de procédé. Ph.D. thesis, ENSMP, (1999).

[69] NDT Resouce Center, http://www.ndt-ed.org

[70] gbtimes, Cracked axle renews railway safety fears, News 22.08.2011-09:11, http://gbtimes.com/news/cracked-axle-renews-railway-safety-fears

[71] Irwin G.R., Analysis of stresses and strains near the end of a crack traversing a plate, J. Appl. Mech., 1957 ; 24 : 361-64.

[72] Landes J.D., Elastic-plastic fracture mechanics: where has it been? Where is it going? In: Fatigue and fracture mechanics. ASTM STP 1360, vol. 30. American Society for Testing and Materials; 2000. p. 3-18.

[73] Xian-Kui Zhu, James A. Joyce, Review of fracture toughness (G, K, J, CTOD, CTOA) testing and standardization, Engineering Fracture Mechanics, 85, (2012), 1-46.

[74] Rice J.R., A path independent integral and the approximate analysis of strain concentration by notches and cracks. J. Appl. Mech., 1968; 35: 379-86.

[75] Greenwood, G.W., Johnson, R.H., The deformation of metals under small stresses during phase transformation, Proc Roy Soc, 283: 403-422, 1965.

[76] Magee C.L., Transformation kinetics, microplasticity and ageing of martensite in Fe-3l-Ni, Ph.D. Thesis, Carnegie Mellon University, Pittsburg, 1966.

[77] J. P. Bressanelli, A. Moskowitz, Effects of Strain Rate, Temperature and Composition on Tensile Properties of Metastable Austenitic Stainless Steels, ASM Trans. Quart. 59, 1966, p.223

[78] V.F. Zackay, E.R, Parker, D. Fahr, R. Busch, The Enhancement of Ductility in High-Strength Steels, Trans. ASM 60, 1967, p.252

[79] W.W. Gerberich, P.B. Hemmings, M.D. Merz, V.F. Zackay, Preliminary Toughness Results on TRIP Steel, ASM Trans. Quart.61, 1968, p.843

[80] W.W. Gerberich, P.B. Hemmings, V.F. Zackay, E.R. Parker, Interactions Between Crack-Growth and Strain-Induced Transformation, Fracture, Chapman and Hall Ltd., London 1969, p.288

[81] S.D. Antolovich, B. Singh, On the Toughness Increment Associated with the Austenite to Martensite Phase Transformation in TRIP Steels, Met. Trans. 2, 1971, p.2135

[82] S.R. Pati, M. Cohen, Nucleation of the Isothermal Martensitic Transformation, Acta Met. 17, 1969, p.189

[83] V. Raghavan, M. Cohen, Measurement and Interpretation of Isothermal Martensitic Kinetics, Met. Trans. 2, 1971, p.2409

[84] H.K.D.H. Bhadeshia, D.V. Edmonds, Bainite in silicon steels: a new composition property approach Ⅰ, Metal Sci. 17 (1983) 411-419.

[85] H.K.D.H. Bhadeshia, D.V. Edmonds, Bainite in silicon steels: a new composition property approach Ⅱ, Metal Sci. 17 (1983) 420-425.

[86] Sun Q-P, Hwang K-C, Micromechanics modelling for the constitutive behavior of polycrystalline shape memory alloys, J. Mech. Phys. Solids, 1993 ; 41: 1-33.

[87] Hannink, R. H. J., Kelly, P. M., Muddle, B. C., Transformation toughening in zirconia-containing ceramics J. Am. Ceram. Soc., 83 [3] 461-87 (2000).

[88] Sung Yi, Shan Gao, Lianxi Shen, Fracture toughening mechanism of shape memory alloys under mixed-mode loading due to martensite transformation, International Journal of Solids and Structures, 38 (2001) 4463-4476

[89] Wenyi Yan, Chun Hui Wang, Xin Ping Zhang, Yiu-Wing Mai, Effect of transformation volume contraction on the toughness of super elastic shape memory alloys, Smart Mater. Struct., 11 (2002) 947-955.

[90] P. Yan, O.E. Gungor, P. Thibaux, M. Liebeherr, H.K.D.H. Bhadeshia, Tackling the toughness of steel pipes produced by high frequency induction welding and heat-treatment, Mater. Sci. Eng. A., 528 (2011) 8492-8499.

[91] Susil K. Putatunda, Fracture toughness of a high carbon and high silicon steel, Materials Science and Engineering A, 297 (2001) 31-43.

[92] C.S. Roberts, Trans. AIME, J. Met. 197 (1953) 203-205.

[93] Takeshi Iwamoto, Toshio Tsuta, Computational simulation on deformation behavior of CT specimens of TRIP steel under mode I loading for evaluation of fracture toughness, International Journal of Plasticity, 18 (2002) 1583-1606.

[94] McMeeking, R.M., Evans, A.G., Mechanics of transformation- toughening in brittle materials. J.Am. Ceram. Soc., 65, 1982, 242-246.

[95] Budiansky, B., Hutchinson, J.W., Lambropoulos, J.C., Continuum theory of dilatant transformation toughnening in ceramics. J. Solids Struct., 19, 1983, 337-355.

[96] Stringfellow, R.G., Parks, D.M., Olson, G.B., A constitutive model for transformation plasticity accompanying strain-induced martensitic transformations in metastable austenitic steels. Acta. Metall. Mater., 40, 1992, 1703-1716.

[97] K. Hase, C. Garcia-Mateo, H.K.D.H. Bhadeshia, Bimodal size-distribution of bainite plates, Materials Science and Engineering A, 438-440 (2006) 145-148

[98] Archana Paradkar, S.V. Kamat, A.K. Gogia, B.P. Kashyap, Influence of volume fraction of primary α_2 on the fracture toughness of Ti-Al-Nb alloy undergoing stress-induced martensitic transformation, Materials Science and Engineering A, 491, (2008), 390-396.

[99] ASTM Annual Book of Standards, Am. Soc. Test. Mater., E399, 2004.

[100] N.L. Richards, J. Mater. Eng. Perform., 13 (2004) 223.

[101] Lifeng Ma, Fundamental formulation for transformation toughening, International Journal of Solids and Structures, 47 (2010) 3214-3220

[102] Lambropoulos, J.C., Effect of nucleation on transformation toughening, J. Am. Ceram. Soc., 69, 1986, 218-222.

[103] Rose L.R.F., The mechanics of transformation toughening, Proc. R. Soc. Lond. A. 412, 1987, 169-197.

[104] Tsukamoto, H., Kotousov, A., Transformation toughening in zirconia-enriched composites: micromechanical modeling, Int. J. Fract. 139, 2006, 161-168.

[105] Jones, J.L., Motahari, S.M., Varlioglu, M., Lienert, U., Bernier, J.V., Hoffman, M., Uestuendag, E., Crack tip process zone domain switching in a soft lead zirconate titanate ceramic. Acta Mater., 55, 2007, 5538-5548.

[106] J. Besson, Local Approach to Fracture: Ductile Rupture, Centre des Matériaux, Mines Paris Tech, UMR CNRS 7633, 2011

[107] Alan F. Liu, Mechanics and Mechanisms of Fracture: An Introduction, ASM International, 2005.

[108] X.K. Zhu, S.K. Jang, *J-R* curves corrected by load-independent constraint parameter in ductile crack growth, Engineering Fracture Mechanics, 68, (2001), 285-301.

[109] A.A. Griffith, The Phenomena of Rupture and Flow in Solids, Philos. Trans. R. Soc.(London) A, Vol 221, 1920, p 163-198.

[110] A.A. Griffith, The Theory of Rupture, Proceedings, First International Congress of Applied Mechanics (Delft, The Netherlands), 1924, p55-63.

[111] Strain energy release rate, http://en.wikipedia.org/wiki/Strain_energy_release_rate, WIKIPEDIA.

[112] Van Vliet, Krystyn J. (2006); "3.032 Mechanical Behavior of Materials".

[113] J.R. Rice, A Path Independent Integral and the Approximate Analysis of Strain Concentration by Notches and Cracks, Journal of Applied Mechanics, Transactions, ASME, 35, June 1968.

[114] Stanley T. Rolfe, John M. Barsom, Fracture and Fatigue Control in Structures, Application of Fracture Mechanics. Prentice-Hall, INC., Englewood Cliffs, New Jersey, 1977.

[115] H. Liebowitz, Fracture, An Advanced Treatise. 1968, By Academic Press, Inc.

[116] Irwin GR, DeWit R. A summary of fracture mechanics concepts, J. Test Evaluat., 1983; 11: 56-65.

[117] Erdogan F., Fracture mechanics, Int. J. Solids Struct., 2000; 37: 171-183.

[118] Cotterell B., The past, present and future of fracture mechanics, Eng. Fract. Mech., 2002; 69: 533-53.

[119] Milne I, Ritchie R.O., Karihaloo B., Comprehensive structural integrity, vols 1-10 (print version). Elsevier; 2003 or vols. 1-11 (online version), Elsevier; 2007.

[120] ASTM E1823-10a. Standard terminology relating to fatigue and fracture testing. American Society for Testing and Materials; 2011.

[121] ASTM E399-09e2. Standard test method for linear-elastic plane strain fracture toughness K_{IC} of metallic materials. American Society for Testing and Materials; 2011.

[122] ASTM E561-10. Standard test method for K-R curve determination. American Society for Testing and Materials; 2011.

[123] ASTM E1820-11. Standard test method for measurement of fracture toughness. American Society for Testing and Materials; 2011.

[124] ASTM E1290-08e1. Standard test method for crack-tip opening displacement (CTOD) fracture toughness measurement. American Society for Testing and Materials; 2011.

[125] ASTM E2472-06e1. Standard test method for determination of resistance to stable crack extension under low-constraint conditions. American Society for Testing and Materials; 2011.

[126] ASTM E1921-11. Standard test method for determining of reference temperature T_0 for ferritic steels in the transition range. American Society for Testing and Materials; 2011.

[127] Heyer RH. Crack growth resistance curves (R-curves)-literature review. In: Fracture toughness evaluation by R-curve methods. ASTM STP 527. American Society for Testing and Materials; 1973. p. 3-16.

[128] Barsom J.M., In: Fracture mechanics retrospective - early classic papers (1913 to 1965). ASTM RPS1. American Society for Testing and Materials; 1987.

[129] Joyce J.A., Manual on elastic–plastic fracture: laboratory test procedures. ASTM Manual, Series: MNL27; 1996.

[130] Landes J.D., Elastic–plastic fracture mechanics: where has it been? Where is it going? In: Fatigue and fracture mechanics. ASTM STP 1360, vol. 30. American Society for Testing and Materials; 2000. p. 3-18.

[131] Landes J.D., Fracture toughness testing and estimations. In: Milne I, Ritchie RO, Karihaloo B, editors. Comprehensive structural integrity, vol. Elsevier; 2003 [Chapter 7.02].

[132] Schwalbe KH, Landes J.D., Heerens J., Classic fracture mechanics methods. In: Milne I, Ritchie R.O., Karihaloo B., editors. Comprehensive structural integrity, vol. 11. Elsevier; 2007.

[133] Zhu X.K., *J*-integral resistance curve testing and evaluation, J. Zhejiang Univ. Sci. A 2009; 10: 1541-60.

[134] Zhu X.K., Advances in development of J-integral experimental estimation, testing and standardization. In: Proceedings of ASME 2011 pressure vessels and piping conference, Baltimore, Maryland, July 17-21, 2011.

[135] Wallin K., Fracture toughness of engineering materials-estimation and application. Warrington, UK: EMAS Publishing Co.; 2011.

[136] Zehnder A.T., Fracture Mechanics. London; New York : Springer Science + Business Media, 2012.

[137] ASTM E1820-05a. Standard test method for measurement of fracture toughness. American Society for Testing and Materials; 2005.

[138] Joyce J.A., On the mechanisms and mechanics of plastic flow and fracture, Sc.D. thesis, Massachusetts Institute of Technology, May 1974.

[139] Towers O.L., Garwood S.J., Maximum load toughness, Int. J. Fract., 1980; 16: R85-90.

[140] Kumar V., German M.D., Shih C.F., An engineering approach for elastic–plastic fracture analysis, EPRI Topical report # NP-1931, Electric Power Research Institute; July1981.

[141] Andrei Constantinescu, An introduction to finite elements based on examples with Cast3m. Laboratoire de Mécanique des Solides CNRS UMR 7649, Département de Mécanique, Ecole Polytechnique, 91120 Palaiseau, France.

[142] E. Le Fichoux, Présentation et Utilisation de CAST3M 2000, ENSTA, 1998.

[143] J.S. Fleuret, Prise en main de CAST3M 2000 par l'exemple, CEA Saclay / DRN / DMT / SEMT / LAMS, 1996.

[144] P. Destuynder, M. Djoua, S. Lescure, Some remarks on elastic fracture mechanics. Journal de Mécanique Théorique et Appliquée, 2: 113-135, 1983.

[145] X.Z. Suo, A. Combescure. Second variation of energy and an associated line independent integral in fracture mechanics. European Journal of Mechanics, A/Solids, 11: 609-624, 1992.

[146] Jacques BESSON, Local approach to fracture, November 7-9 2011, Paris.

[147] Petr Hausild, Ivan Nedbal, Clotilde Berdin, Claude Prioul, The influence of ductile tearing on fracture energy in the ductile-to-brittle transition temperature range, Materials Science and Engineering A, 335 (2002) 164-174

[148] A. Rossoll, Fracture Toughness Determination of a Nuclear Pressure Vessel Steel by Instrumented Charpy Impact Test, Ph.D. Thesis, Ecole Centrale Paris, (1998).

[149] S. Renevey, Approches globale et locale de la rupture dans le domaine de transition fragile-ductile d'un acier faiblement allié, Ph.D. Thesis, Ecole Nationale Supérieure des Mines de Paris, (1998).

[150] S.K. Iskander, P.P. Milella, A. Pini, Results of Crack-Arrest Tests on irradiated A508 Class 3 steel, Oak Ridge National Laboratory, 1998.

[151] S. Chapuliot, M.H. Lacire, S. Marie, M. Nédélec, Thermomechanical analysis of thermal shock fracture in the brittle/ductile transition zone. Part I: description of tests, Engineering Fracture Mechanics, 72 (2005) 661-673

[152] R.H. Priest, W.P.A. Belcher C.M. Mendes, B.K. Neale, Irradiation surveillance data for an A508 forging and associated weld metal, International Journal of Pressure Vessels and Piping, 77 (2000) 621-628

[153] Transaction of the 15th international conference on Structural Mechanics in Reactor Technology (SMRT-15), Seoul, Korea, August 15-20, 1999.

[154] Determination of the fracture toughness by applying a structural integrity approach to pre-cracked Small Punch Test specimens, Engineering Fracture Mechanics, 78 (2011) 289-300

[155] ASME API 579-1/ASME FFS-1. In fitness-for-service. American Society of Mechanical Engineers; 2007.

[156] F.G. Caballero, C. Garcia-Mateo, M.J. Santofimia, M.K. Miller, C. Garcia de Andrés, New experimental evidence on the incomplete transformation phenomenon in steel, Acta Materialia, 57 (2009) 8-17.

[157] Aaronson HI. In: Zackary VF, Aaronson HI, editors. The decomposition of austenite by diffusional processes, New York: Interscience Publishers; 1962. p. 387.

[158] Aaronson H.I., The mechanism of phase transformations in crystalline solids. London: The Institute of Metals; 1969. p. 270.

[159] Aaronson H.I., Spanos G, Reynolds Jr, W.T., A progress report on the definitions of bainite, Scripta Mater., 2002; 47: 139-144.

[160] Reynolds Jr, W.T., Li F.Z., Shui C.K., Aaronson H.I., An investigation of the generality of incomplete transformation to bainite in Fe-C-X alloys, Metall. Trans., 1990; 21A: 1433.

[161] Zener C., Trans. AIME 1946; 167:50.

[162] H.K.D.H. Bhadeshia, Steels Microstructure and Properties, third ed., Butterworth-Hienemann, Oxford, 2006.

[163] Document No. 11302, http://www.vishaypg.com/docs/11302/700.pdf, Revision: 17-May-2011, Vishay Precision Group.

Annexes

(1) Some experimental apparatus

- Micro-welding machine

During our study, we used one micro-welding machine many times, for example, weld the thermocouples on the specimen or weld the electrical wires besides the crack mouth to measure the potential drop during the fatigue test. Hence, here we introduce the 700 Portable Strain Gage Welding and Soldering Unit from Vishay Precision Group [163]. Figure a1 is the overall appearance of our micro welding machine. The control panel is shown in figure a2. Details could be found in reference 154.

Fig. a1 overall appearance of 700 Portable Strain Gage Welding and Soldering Unit

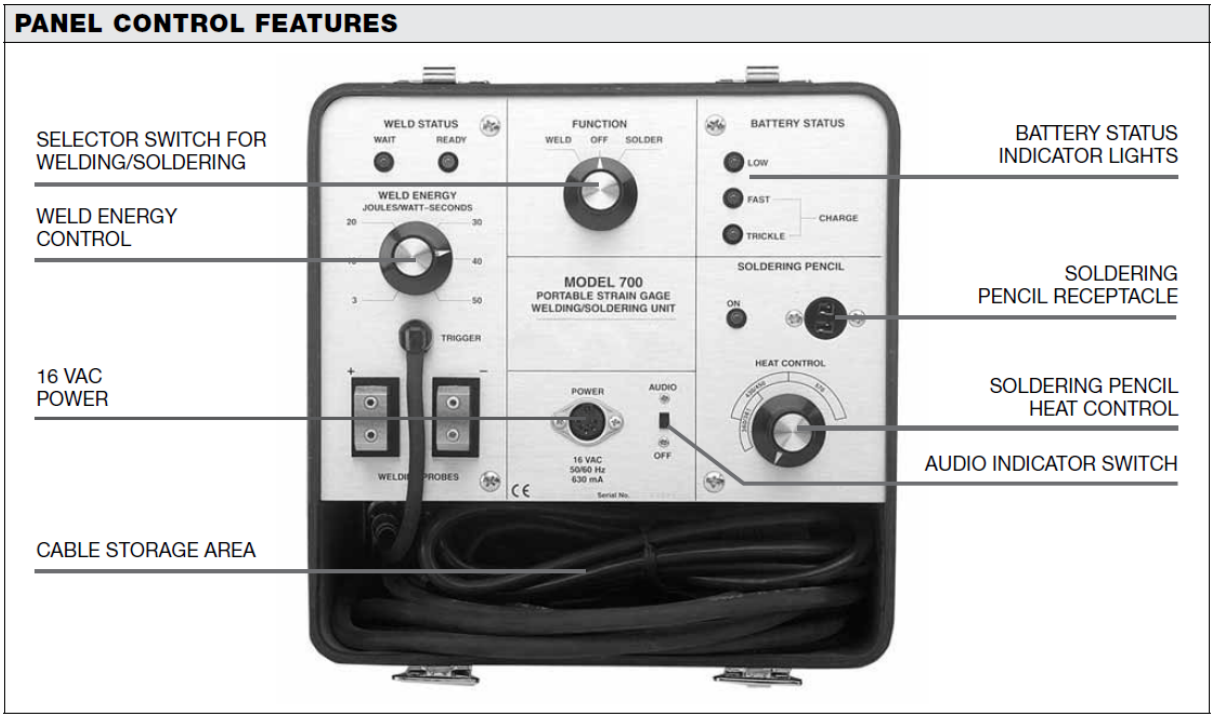

Fig. a2 Contraol panel of 700 Portable Strain Gage Welding and Soldering Unit

- Optical microscope

Two optical microscopes were used to study the metallography, measure the notch size, fatigue crack length and so on. One is ZEISS microscope which can provide maximum magnification ×500. It is shown in figure a3. Another one is Hirox microscope who can provide us a maximum magnification ×2500 (see figure a4).

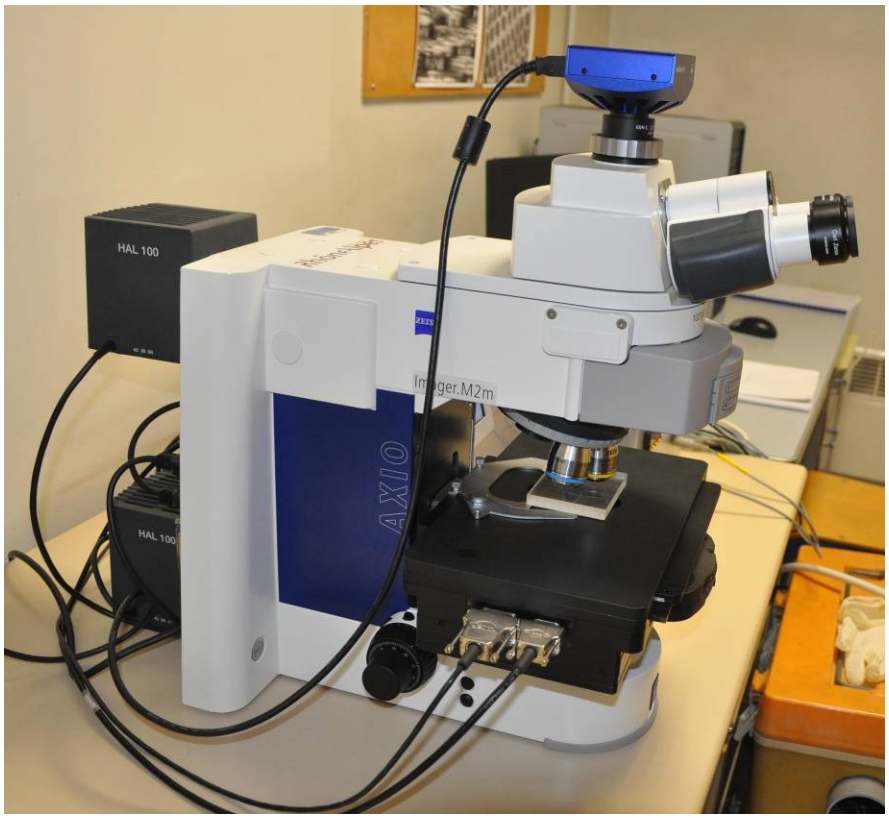

Fig. a3 SEISS optical microscope

Fig. a4 Hirox optical microscope

- SEM

FEI Quanta 600 SEM was applied also to study the metallography and fractography which are important for the investagation of transformation mechanism and fracture mechanism. The set-up of SEM is shown in figure a5.

Fig. a5 FEI Quanta 600 SEM

- XRD

X-ray Diffraction was carried out for studying the microstructure of 16MND5 after the isothermal transformation at very high temperature such as 600°C or 680°C.

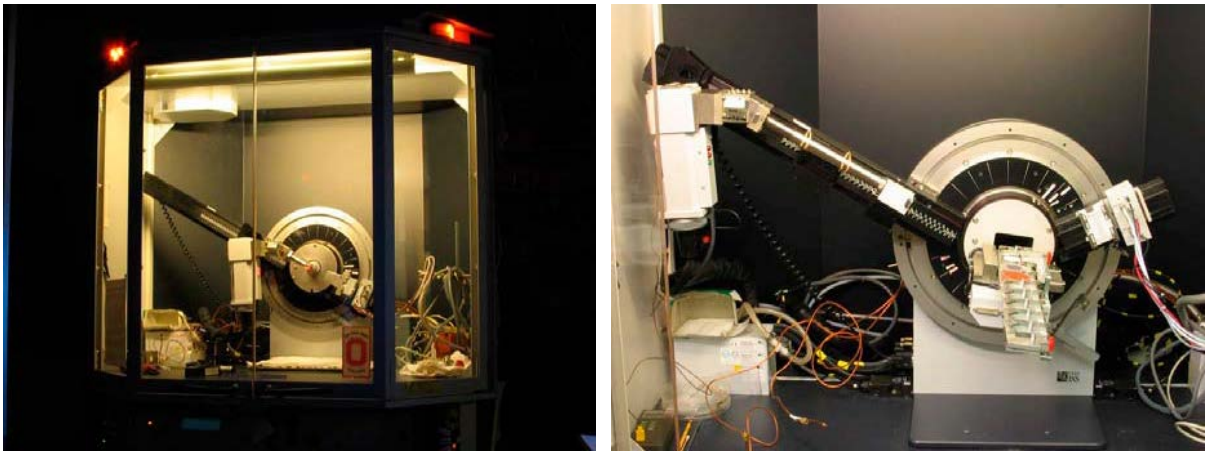

Fig. a6 Bruker X-ray Diffraction apparatus (In MATEIS)

- Potential drop recorder

A C3EM machine named in French 'Suiveur de Fissures' was applied to recorder the potential during the fatigue test and fracture experiment.

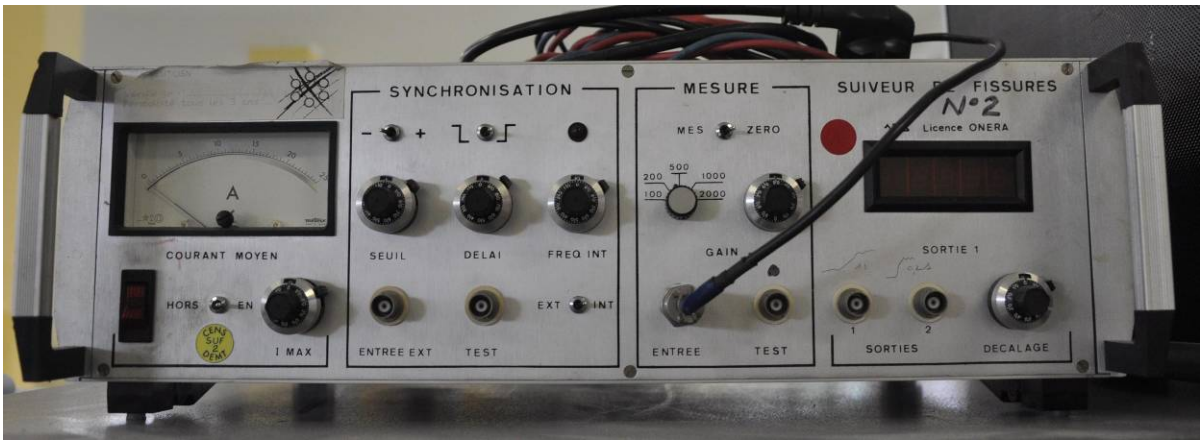

Fig. a7 Machine for recording the potential

(2) Pre-crack length definition

Annexe (2) shows how one can use potential drop and Johnson's formula to calculate the fatigue crack length a_{JF} (including the notch length). One may also use the microscope as well as DIC to "measure" the fatigue crack length a. We have then 3 different estimations (a_{JF}, a_{DIC}, a_{MICR}) of crack length. We decided that the crack length is the mean value of these 3 estimated values.

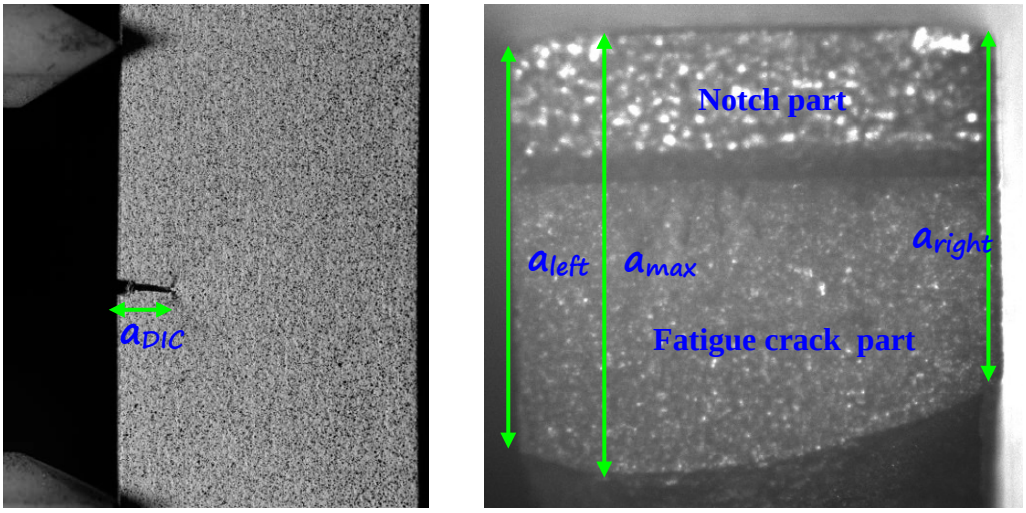

Fig. a8 The two "optical" crack length estimations: the left photo shows the DIC image used for initial crack length estimate a_{DIC}, the right one is the fatigue crack surface through the specimen observed after failure on which initial fatigue crack is easy to "see" with the microscope.

The pre-crack length is defined by:

$$a = \frac{a_{JF} + a_{DIC} + a_{MICR}}{3} \quad \text{(a-1)}$$

a_{MICR} is measured by the microscope after the test as shown in Figure a8 left. This initial crack length is a mean value of the 3 depth (a_{left} , a_{right} , $a_{\max}$) defined by:

$$a_{MICR} = \frac{a_{left} + a_{\max} + a_{right}}{3} \quad \text{(a-2)}$$

(3) Paint application for the fracture tests

For the Digital Image Correlation (DIC) technique, we need to do a painting on the sample surface. Concerning the high temperature during the heat treatment and fracture test process, a good painting is very important for the DIC method to obtain the boundary conditions for the further critical *J*-integral estimation.

Figure a9 shows three kinds of paint we applied in our study. The left one is the white paint and the middle one is the black paint. These two can be used in one maximum temperature 600°C. That means they can glued to the sample surface well at 600°C but it doesn't mean that when there is mechanical tension or compression, they can still well glued to the sample surface. The right one is the black 'Thermal Paint' (en Français: 'Peinture Thermique') which can stick well at a maximum temperature 900°C.

Fig. a9 Three kinds of paints we utilized

In our study here, the maximum temperature during one cycle heat treatment is 900°C, and the highest temperature for a mechanical test of 15-5PH is 200°C, for 16MND5 is 600°C. So for the fracture tests at room temperature or at 200°C before the maximum heat treatment temperature, the normal painting just can work well which white paint is in the bottom layer and the small black paint point is done on the upper layer. Otherwise, we made the black thermal paint as the bottom layer while the normal white one as the outside layer. Take the fracture test of 16MND5 low carbon steel at 600°C after the maximum temperature for example, figure a10 is the zone of interest for getting the displacement result of segment F-PF.

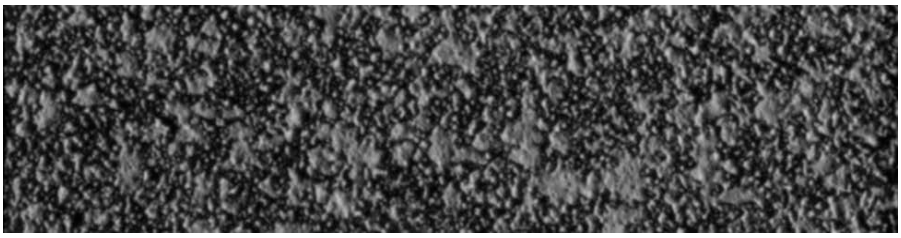

Fig. a10 Zone of interest with thermal painting in the bottom layer and white paint for outside layer

Figure a11 is the result processed by DIC software Icasoft. It shows that our painting method for the fracture test at high temperature works very well.

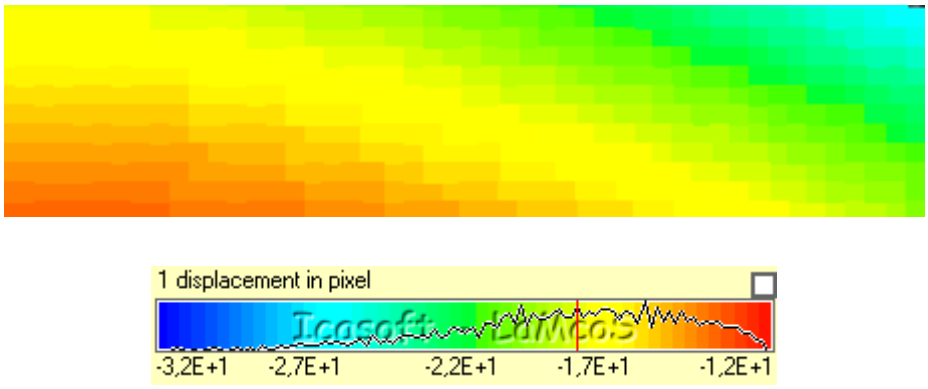

Fig. a11 Displacement field processed by Icasoft

(4) Effect of temperature and elastic strain on potential drop

As we talked in section 2.3 that the variation of temperature and the elastic strain can also bring a potential drop which can not be ignored. Here we make an adhesion to get knowledge about the quantitative influence temperature and elastic strain on potential drop. Figure a12 is the potential drop induced by the change of temperature for the material 15-5PH stainless steel.

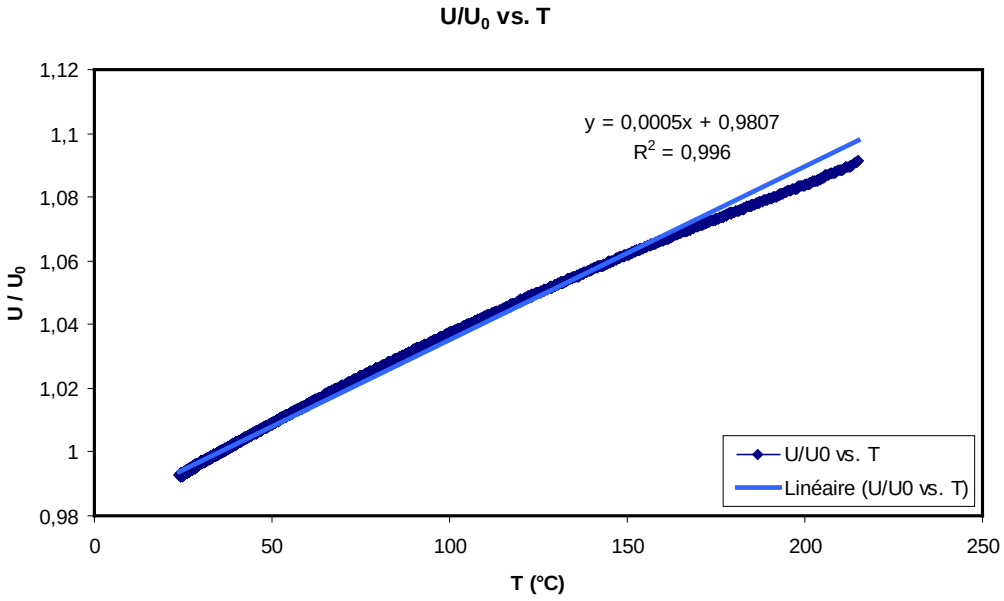

Fig. a12 Temperature gradient induced potential drop

Figure a13 shows the elastic strain induced potential drop of 15-5PH.

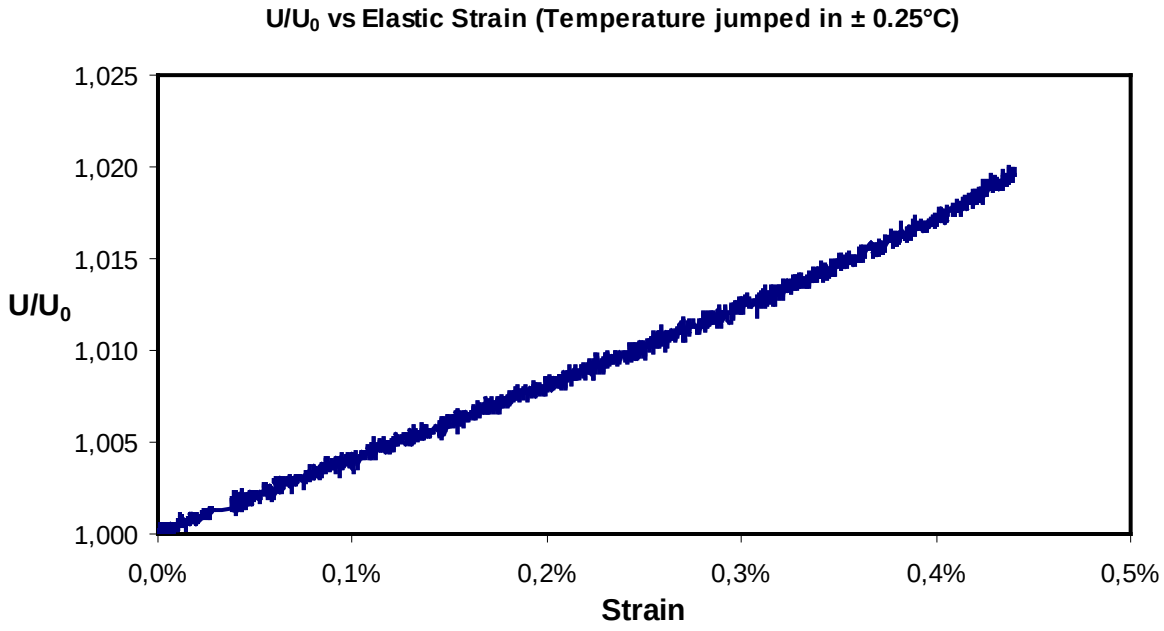

Fig. a13 Elastic strain induced potential drop

(5) One example of our programs

We put one example of our programs here, it is for J_{1C} estimation of 16MND5 at point A (as-received condition).

```
OPTION  DIME 2 ELEM QUA8 MODE PLAN CONT ;
*----------------------------------------*
* CONSTRUCTION DU MAILLAGE (RAYONANT)   *
*----------------------------------------*
*-----Largeur et longueur
lar1 = 10.;
lon1 = 80.;
P1 = 0.   (lon1/2);  P2 = 0.   (lon1/2) ;
*-----Define the crack length a,mm---------
lcrack1 = 1.462;
P3 = lcrack1 (lon1/2);
P4 = (lcrack1/2) (lon1/2);
P5 = lar1 (lon1/2)  ;
*----Define another two points for extensometer = 15 mm-------
yext = 15;
E = 0.  ((lon1/2)+(yext/2));
F = 0.  ((lon1/2)-(yext/2));
* maillage fond de fissure
SS COUR1 l1 l2 l3 l4 LVD LVG = @rayo P3 P4 10 ;
*OPTION ELEM QUA8 ;
den1 = 3;
den2 = 30;
*1ER CONTOUR
*OPTI ELEM TRI3;
P6 = L4 POIN 'INITIAL' ;
P7 = L3 POIN 'INITIAL' ;
PE = P5 PLUS (E MOIN P1);
P1E   = DROI P1 E 'DINI' 0.3  'DFINI' 1.5;
P6P1 = DROI den1 P6 P1;
P5P7 = DROI den2 P5 P7 ;
EPE  = DROI (den2/3) E PE;
P5PE = DROI P5 PE 'DINI' 0.3  'DFINI' 1.5;
CC1  = SURF (L3 ET L4 ET P5P7 ET P5PE ET
EPE ET P1E ET P6P1);
trac cc1;
*2EM CONTOUR
P4  = L1 POINT INITIAL ;
PF =  P5 PLUS (F MOIN P1);
P2F   = DROI P2 F 'DINI' 0.3  'DFINI' 1.5;
```

```
P4P2 = DROI den1 P4 P2;

FPF  = DROI (den2/3) F PF;

P5PF = DROI P5 PF 'DINI' 0.3  'DFINI' 1.5;
CC2 = SURF (L1 ET L2 ET P5P7 ET P5PF ET
FPF ET P2F ET P4P2);

trac cc2;

* Maillage total

mai1 = SS ET CC1 ET CC2 ;

trac mai1 ;

** // ** MODIF MC

mai1 = CHAN LINEAIRE mai1;

EPE = CHAN LINEAIRE EPE;
FPF = CHAN LINEAIRE FPF;
CC1 = CHAN LINEAIRE CC1;
CC2 = CHAN LINEAIRE CC2;
** // **

* PARTIE MECANIQUE

*=========================

* Modele et materiau

*=========================

* Modele

*-------

mo1 = MODE mai1 'MECANIQUE' 'ELASTIQUE' 'PLASTIQUE' 'ISOTROPE';

* Caracteristiques

*-----------------

you1 = 210000 ;

nu1 = 0.3 ;

*----courbe de traction, from the tensile curve of round bar---*

li_epsi = PROG 0. 0.002 0.004 0.005 0.007 0.01 0.014 0.02 0.03

0.05 0.07  0.1    0.5    1.  2. 5. 10. 50. ;

li_sigm = PROG 0. 420.  500.  505.  512. 520. 530. 545. 568.

597.  609.  610.  610. 610.  610. 610. 610. 610. ;

ev_t = EVOL MANU li_epsi li_sigm;

ma1 = MATE mo1 'YOUN' you1 'NU' nu1 'TRAC' ev_t ;

* Stiffener on EPE and FPF

mo_bord   = MODE (EPE ET FPF) 'MECANIQUE' 'ELASTIQUE' coq2;

ma_bord   = MATE mo_bord 'YOUN' you1 'NU' nu1;

car_bord  = CARA mo_bord EPAI 1000. ;

ma_bord   = ma_bord  ET car_bord;
```

```
** // **
*=========================
* Rigidite
* Cond. aux limites et
* chargement
*=========================
* Rigidite
*---------
*ri1 = (RIGI mo1 ma1) ;
** // ** MODIF MC
ri1 = (RIGI mo1 ma1) ET (RIGI mo_bord ma_bord) ;
** // **
* Cond. aux limites
*------------------
cl1 = BLOQ UY F;
cl2 = BLOQ UY PF;
cl3 = BLOQ UY E;
cl4 = BLOQ UY PE;
cl5 = BLOQ UX PE;
ri = cl1 ET cl2 ET cl3 ET cl4 ET cl5;
* Critical deplacement at four points
ut_E  = -0.26;
ut_PE = -0.49;
ut_F  = -0.91;
ut_PF = -0.68;
* Deplacement imposed
fo1 = DEPI cl1 ut_F;
fo2 = DEPI cl2 ut_PF;
fo3 = DEPI cl3 ut_E;
fo4 = DEPI cl4 ut_PE;
* Evolution en temps
ev1 = EVOL MANU (PROG 0. 6. 11. 17. 23. 34. 40. 56. 68. 100.)
(PROG 0. 0.03 0.07 0.11 0.15 0.27 0.33 0.53 0.63 1.);
ev2 = EVOL MANU (PROG 0. 6. 45. 51. 100.)
(PROG 0. 0.04 0.40 0.46 1.);
ev3 = EVOL MANU (PROG 0. 6. 17. 23. 28. 34. 40. 45. 62. 73. 90. 100.)
(PROG 0. 0.08 0.31 0.41 0.48 0.52 0.54 0.55 0.64 0.76 0.97 1.);
```

```
ev4 = EVOL MANU (PROG 0. 6. 11. 23. 28. 34. 51. 68. 79. 85. 100.)
(PROG 0. 0.04 0.10 0.23 0.30 0.35 0.48 0.64 0.77 0.84 1.);
cha1 = CHAR 'MECA' fo1 ev1;
cha2 = CHAR 'MECA' fo2 ev2;
cha3 = CHAR 'MECA' fo3 ev3;
cha4 = CHAR 'MECA' fo4 ev4;
*=========================
* Calcul incremental
*=========================
TAB1 = TABLE;
*    le temps
*    ---------
TAB1.TEMPS0        = 0. ;
p_lipas = PROG 0. PAS 1. 100.;
TAB1.TEMPS_CALCULES =  p_lipas ;
TAB1.TEMPS_SAUVES   =  p_lipas ;
*   les  modeles
*   ------------
** // ** MODIF MC
TAB1.'MODELE'             = mo1 ET mo_bord;
TAB1.'CARACTERISTIQUES'    = ma1 ET ma_bord;
TAB1.'CHARGEMENT'         = cha1 ET cha2 ET cha3 ET cha4;
TAB1.'BLOCAGES_MECANIQUES' = (cl1 ET cl2 ET cl3 ET cl4 ET cl5);
TAB1.'GRANDS_DEPLACEMENTS' = VRAI;
TAB1.'GRANDES_ROTATIONS'   = FAUX;
TAB1.'GRANDES_DEFORMATIONS' = FAUX;
** // **
* Calcul
* ------
PASAPAS TAB1;
*------Post process-----------------------
nb_pas = DIME (TAB1 . TEMPS_SAUVES);
last_pas = nb_pas-1;
dep1 = TAB1 . DEPLACEMENTS . last_pas;
sig1 = TAB1 . CONTRAINTES . last_pas;
* Tracer de la deformee
* -----------------------------
def1 = DEFO mai1 dep1;
```

```
TRAC def1;
* Tracer de champ de deplacement
* ------------------------------
depz = EXCO dep1 UY;
TRAC depz mai1;


* Tracer de deformations
* ----------------------
def1 = EPSI mo1 dep1 ;
TRAC def1 mo1;
*dess exx;
* Tracer des contraintes
* ----------------------
TRAC sig1 mo1 ;
*
* Mean disp versus force
*
mean_P = PROG 0.;
F_PROG = PROG 0.;
U_E = PROG 0.;
U_PE = PROG 0.;
U_F = PROG 0.;
U_PF = PROG 0.;
U_P1 = PROG 0.;
U_P2 = PROG 0.;
COD = PROG 0.;
*espe3 = PROG 0.;
*====================
* loop on time steps
*====================
REPE bou_pas  (nb_pas-1);
*REPE bou_pas  1;
* displacement time i-1
dep_ini = TAB1.deplacements . (&bou_pas);
*epse1 = TAB1 . VARIABLES_INTERNES . last_pas;
*epse1 = TAB1 . VARIABLES_INTERNES . (&bou_pas);
*==================================
* Uy displacement of points E,PE,F,PF
*==================================
```

```
UY_E  = EXTR dep_ini UY E;

UY_PE = EXTR dep_ini UY PE;

UY_F  = EXTR dep_ini UY F;

UY_PF = EXTR dep_ini UY PF;

U_E  =  U_E ET (PROG UY_E);
U_PE =  U_PE ET (PROG UY_PE);
U_F  =  U_F ET (PROG UY_F);
U_PF =  U_PF ET (PROG UY_PF);
* Crack Opening Displacement

UY_P1  = EXTR dep_ini UY P1;

U_P1   =  U_P1 ET (PROG UY_P1);

UY_P2  = EXTR dep_ini UY P2;

U_P2 =  U_P2 ET (PROG UY_P2);
U_COD=UY_P1-UY_P2;
COD=COD et (PROG U_COD);

*espe2 = EXCO epse1 EPYY P7;

*espe3 = espe3 ET (PROG espe2);

* Mean displacement (-1 is put to have a positive displacement)

meanDUY = -1*((0.5*(UY_F + UY_PF)) - (0.5*(UY_E + UY_PE)));

mean_P = mean_P ET (PROG meanDUY);

* Forces on EPE (per unit thickness)

ri_CL = cl3 ET cl4 ;

R_EPE_I = REAC ri_CL dep_ini ;

*list R_EPE_I ;

EPSE_P7= EXCO P7 dep_ini;

eyy    = EXCO def1 EPYY;

* Sum of forces  (MAXI is used to extract the value of the CHPOINT)

F_EPE = MAXI(RESU R_EPE_I);
F_PROG = F_PROG ET (PROG F_EPE);
FIN bou_pas;

*====================

MD_RF = EVOL MANU 'MEAN DISP' mean_P 'Force' F_PROG;

list MD_RF;

DESS MD_RF;
MD_E = EVOL MANU 'DISP U_E' U_E 'Force' F_PROG;

list MD_E ;

MD_PE = EVOL MANU 'DISP U_PE' U_PE 'Force' F_PROG;

list MD_PE ;

MD_F = EVOL MANU 'DISP U_F' U_F 'Force' F_PROG;

list MD_F ;
```

```
MD_PF = EVOL MANU 'DISP U_PF' U_PF 'Force' F_PROG;
list MD_PF ;
COD_COD = EVOL MANU 'DISP COD' COD 'Force' F_PROG;
list COD_COD ;
EPSE_33 = EVOL MANU 'EPSP P7' espe3 'Force' F_PROG;
list EPSE_33 ;
* data record
*@excel1 MD_RF 'dep_force.xls';
*Plot accumulated plastic strain :
**********
epse1 = TAB1 . VARIABLES_INTERNES . last_pas;
TRAC epse1 mo1 ;
*********
* Contour Mesh Outer
cont_ext = FPF ET P5PF ET P5PE ET EPE ET P1E ET P2F;
cont_int = L1 ET L2 ET L3 ET L4 ;
mai_thet = CC1 ET CC2;
*------------------------------- < Champ theta
* Imposed Theta field
cl_ext = BLOQ UX UY cont_ext;
cl_int  = BLOQ UX cont_int;
fo_thet = DEPI cl_int 1.;
* On bloque la fissure
cl_crack = BLOQ UY (P6P1 ET P4P2 ET LVD ET LVG);
* BC and Stiffness
ma2 = MATE mo1 'YOUN' you1 'NU' 0.  ;
ri_thet = RIGI mo1 ma2 ;
ri_thet = ri_thet ET cl_ext ET cl_int ET cl_crack;
* Resolution  theta field
dep_thet = RESO ri_thet fo_thet;
dd = DEFO dep_thet mai1;
trac dd;
trac (EXCO dep_thet UY) mai1 ;
* Gradient theta
gr_thet = GRAD mo1 dep_thet;
* on ne garde que la zone comprise ds le contour
gr_thetr = REDU gr_thet mai_thet;
```

```
gr_thetr = CHAN CONS gr_thetr 'TOTO';
gr_thetr = CHAN TYPE gr_thetr SCALAIRE;
* Components
gtxx = EXCO gr_thetr 'UX,X' 'SCAL';
gtyy = EXCO gr_thetr 'UY,Y' 'SCAL';
gtxy = EXCO gr_thetr 'UX,Y' 'SCAL';
gtyx = EXCO gr_thetr 'UY,X' 'SCAL';
* (theta)i,i
theti,i =(EXCO gr_thetr 'UX,X' 'SCAL') + (EXCO gr_thetr 'UY,Y' 'SCAL');
* Mechanical solution of the problem
*---------------------------------------------- < displacement
nb_pas = DIME (TAB1 . TEMPS_SAUVES);
last_pas = nb_pas-1;
* Final disp
dep1 = TAB1 . DEPLACEMENTS . last_pas;
dep1r = REDU dep1 mai_thet;
* Final disp gradient
gr_dep1 = GRAD mo1 dep1;
gr_dep1r = REDU gr_dep1 mai_thet;
gr_dep1r = CHAN CONS gr_dep1r 'TOTO';
gr_dep1r = CHAN TYPE gr_dep1r SCALAIRE;
* Components
gdxx = EXCO gr_dep1r 'UX,X' 'SCAL';
gdyy = EXCO gr_dep1r 'UY,Y' 'SCAL';
gdxy = EXCO gr_dep1r 'UX,Y' 'SCAL';
gdyx = EXCO gr_dep1r 'UY,X' 'SCAL';
*---------------------------------------------- < stresses
sig1 = TAB1 . CONTRAINTES . last_pas;
sig1r = REDU sig1 mai_thet;
sig1r = CHAN CONS sig1r 'TOTO';
sig1r = CHAN TYPE sig1r SCALAIRE;
* Components
ssxx = EXCO sig1r 'SMXX' 'SCAL';
ssyy = EXCO sig1r 'SMYY' 'SCAL';
ssxy = EXCO sig1r 'SMXY' 'SCAL';
aa = EXTR gtxx 'TYPE'  ;
bb = EXTR gdxx 'TYPE'  ;
```

```
list (aa et bb);
*=================================================================
*   Sum( s_ij.(u_k,i.theta_k,j))
*=================================================================
mo1r = REDU mo1 mai_thet;
llmo = MOTS 'SCAL';
* CAST3M 2009
*sprodxx = (gdxx '*' gtxx llmo llmo llmo mo1r) + (gdxy '*' gtyx llmo llmo llmo mo1r) ;
*sprodxy = (gdxx '*' gtxy llmo llmo llmo mo1r) + (gdxy '*' gtyy llmo llmo llmo mo1r) ;
*sprodyx = (gdyx '*' gtxx llmo llmo llmo mo1r) + (gdyy '*' gtyx llmo llmo llmo mo1r) ;
*sprodyy = (gdyx '*' gtxy llmo llmo llmo mo1r) + (gdyy '*' gtyy llmo llmo llmo mo1r) ;
* CAST3M 2010
sprodxx = (gdxx '*' gtxx) + (gdxy '*' gtyx) ;
sprodxy = (gdxx '*' gtxy) +  (gdxy '*' gtyy) ;
sprodyx = (gdyx '*' gtxx) + (gdyy '*' gtyx) ;
sprodyy = (gdyx '*' gtxy) + (gdyy '*' gtyy) ;

*sij_U_T = (ssxx '*' sprodxx llmo llmo llmo mo1r) +
*          (ssxy '*' sprodxy llmo llmo llmo mo1r) +
*          (ssxy '*' sprodyx llmo llmo llmo mo1r) +
*          (ssyy '*' sprodyy llmo llmo llmo mo1r) ;
* CAST3M 2010
sij_U_T = (ssxx '*' sprodxx ) +
          (ssxy '*' sprodxy ) +
          (ssxy '*' sprodyx ) +
          (ssyy '*' sprodyy ) ;
*---------------------------------------------- < Sum
S_sUT = INTG mo1r sij_U_T;
list S_sUT;
*=================================================================
*   The strain energy density
*=================================================================
nb_pas = DIME (TAB1 . TEMPS_SAUVES);
REPE bouW (nb_pas - 1) ;
dep_I = TAB1 . DEPLACEMENTS . (&bouW - 1);
dep_F = TAB1 . DEPLACEMENTS . (&bouW);
sig_I = TAB1 . CONTRAINTES  . (&bouW - 1);
```

```
sig_F = TAB1 . CONTRAINTES  . (&bouW);
defor_Ir = REDU (EPSI mo1 dep_I) mai_thet;
defor_Fr = REDU (EPSI mo1 dep_F) mai_thet;
sig_Ir   = REDU sig_I mai_thet;
sig_Fr   = REDU sig_F mai_thet;
sig_mean = 0.5 * (sig_Ir + sig_Fr);
D_defor = defor_Fr - defor_Ir ;
  SI (&bouW EGA 1);
  WW = ENER mo1r sig_mean D_defor;
  SINON ;
  WW = WW + (ENER mo1r sig_mean D_defor) ;
  FINSI ;
FIN bouW;
*=================================================================
*   W.theti,i
*=================================================================
WW = CHAN CONS WW 'TOTO';
*Wthet = (WW '*' theti,i llmo llmo llmo mo1r);
* CAST3M 2010
Wthet = (WW '*' theti,i);
S_Wthet = INTG mo1r Wthet;
list S_Wthet;
*=================================================================
*   J...
*=================================================================
JJ = S_sUT - S_Wthet;
mess '  '  ;
mess 'J MC :' JJ    ;
```

FOLIO ADMINISTRATIF

THESE SOUTENUE DEVANT L'INSTITUT NATIONAL DES SCIENCES APPLIQUEES DE LYON

NOM : LIU Prénom: Jikai DATE de SOUTENANCE :le 7 Décembre 2012

TITRE :
Influence of metallurgical phase transformation on crack propagation of 15-5PH stainless steel and 16MND5 low carbon steel

NATURE : Doctorat Numéro d'ordre : 2012ISAL0120

Ecole doctorale : Mécanique, Energétique, Génie civil, Acoustique (MEGA)

Spécialité : Génie Mécanique

RESUME :
Cette thèse porte sur l'influence des transformations de phases solide-solide sur la propagation de fissure. On souhaite ainsi mieux comprendre les variations de ténacité en cours de soudage par exemple, ou bien pendant la réparation d'une fissure. Dans ce travail, la ténacité est obtenue à partir de l'intégrale J. Il existe de nombreuses méthodes expérimentales permettant d'obtenir la ténacité critique J_{IC} mais qui sont difficilement applicables pour des essais se déroulant pendant une transformation de phase. C'est pourquoi nous avons proposé une méthode couplant essai mécanique et mesure par corrélation d'images avec de la simulation par éléments finis. Les essais sont réalisés sur de simples éprouvettes plates pré fissurées, faciles à usiner et simple à chauffer par induction. Les essais sont conduits pour différentes températures et jusqu'à rupture. En sus des mesures d'efforts et déplacements de traverse, la corrélation d'images nous fournit également les champs de déplacement sur chaque face de l'éprouvette. Chaque essai est ensuite simulé par éléments finis où la ténacité critique est calculée par la méthode G-Theta au maximum de la charge supportée par l'éprouvette. Les simulations précédentes intègrent les conditions aux limites obtenues par corrélation et le comportement mécanique considéré est celui que nous avons identifié sur des essais de caractérisation.

Deux nuances de matériau ont été étudiées avec cette méthode: l'acier inoxydale 15-5PH ainsi que l'acier ferritique 16MND5. L'acier 15-5PH est toujours sous forme martensitique alors que le 16MND5 peut être bainitique ou martensitique selon le traitement thermique. On

notera que l'étude sur la transformation bainitique du 16MD5 dépendant du temps et de la température s'est révélée dans notre cas plus complexe que l'étude sur le 15-5PH dont la transformation martensitique ne dépend que de la température. Pour ces deux matériaux, différentes températures d'essai ont été choisies avant, pendant et après la transformation pour effectuer les essais de rupture ainsi que de caractérisation du comportement mécanique.

Les résultats de cette étude montrent que la transformation de phase peut avoir un impact non négligeable sur la ténacité. Ainsi, pour le 15-5PH, le taux d'austénite résiduelle est un facteur important et les essais pendant la transformation martensitique montrent que la ténacité critique peut être inférieure pendant celle ci à celle du matériau purement austénitique.

Dans le cas du 16MND5, la ténacité est beaucoup plus faible à 600°C (et bainitique) qu'à température ambiante ce qui est assez logique. Par contre, lors du refroidissement, depuis 600° (austénitique) jusqu'à la température ambiante (bainitique), nous avons obtenu une ténacité critique relativement constante.

En conclusion, cette étude apporte une solution quant à la mesure de la ténacité critique de matériau pendant des transformations de phases, ce que ne permettent pas forcément les essais normalisés. Pour le 15-5PH, la ténacité critique semble évoluer pendant la transformation martensitique et est assez dépendante du taux d'austénite résiduelle. Il semble par contre que pour le 16MND5, la ténacité critique soit assez peu dépendante de la fraction volumique d'austénite et la valeur obtenue varie peu au cours du refroidissement du matériau depuis 600°C.

MOTS-CLES :
Propagation de fissure, Ténacité à la rupture, Transformation martensitique, Transformation bainitique, Intégrale *J* Critique, Condition limite, Corrélation d'image numérique, Analyse par éléments finis

Laboratoire (s) de recherche :
LaMCoS (Laboratoire de Mécanique des Contacts et des Structures), CNRS UMR5259

Directeur de thèse: Alain COMBESCURE

C- directeur de thèse: Michel CORET

Président de jury : Helmut KLOCKER

Composition du jury :

Rapporteur: Stéphane MARIE, Hervé LOUCHE,

Examinateur:
Philippe GILLES, Helmut KLOCKER, Jean-Yves GUEDOU, René BILLARDON